

OPTIMIZATION OF CONTRAST AGENTS FOR HIGH MAGNETIC FIELDS

By

HEATHER H. CORNNELL

A DISSERTATION PRESENTED TO THE GRADUATE SCHOOL  
OF THE UNIVERSITY OF FLORIDA IN PARTIAL FULFILLMENT  
OF THE REQUIREMENTS FOR THE DEGREE OF  
DOCTOR OF PHILOSOPHY

UNIVERSITY OF FLORIDA

2009

© 2009 Heather H. Cornell

To my Mom and Dad, the best parents in the world

## ACKNOWLEDGMENTS

For the first of my academic acknowledgements, I would like to extend my deepest gratitude to Dr. Arthur Edison and Dr. Glenn Walter. They have both been invaluable, without their help none of this work would be possible. Dr. Edison was always insightful, not only in academics, but with an exceptional big-picture attitude that always made me think outside of my comfort zone. Dr. Walter always challenged me with an uncanny ability to recall details that inevitably were correct and essential. I believe this combination helped me produce better research, and to become a more well rounded scientist. They are two of the smartest people I have ever met; I will always admire and respect both of them. I will always be grateful.

I thank my committee members Dr. Huabei Jiang and Dr. Rosalind Sadleir for their time and contributions. I thank Dr. Sherry for introducing me to PARACEST, for his material contributions to my research and for many insights which significantly contributed to my research. I thank Dr. Merritt for the CESTFIT MATLAB program, without which a large portion of this project could not have been completed.

I thank the staff of the Advanced Magnetic Resonance Imaging and Spectroscopy (AMRIS) and National High Magnetic Field Laboratory (NHMFL) faculty and staff including (but not limited to) Barbara Beck, Gary Blaskowski, Sam Grant, Kelly Jenkins, Victor Schepkin and Xeve Silver. I especially thank Dan Plant and Jim Rocca for all of their time and assistance, and Dr. Joanna Long for insight and recommendations. I thank all of my current and past labmates, especially Omjoy Ganesh, Seth McNeill and Cherian Zachariah.

On a personal level, first and foremost I thank my parents; without their decision to procreate, I would not exist. More importantly, they have always provided love and support, and allowed me to choose my own path. I admire my mom's determination and spirit, and thank my mom for her willingness to listen, even if she didn't always understand. I admire my dad's

dedication and his unique perception of life, and I thank my dad for the bed time stories and pretending to understand. They are the best parents I could ever have asked for, and they have my undying gratitude and love.

I also thank my sister, and although I did not include her version of my research, I certainly wanted to. She has always been there when I needed her and always knew exactly what to say to make me feel better. Haley has always been, and will always be my best friend. She too has my eternal thanks and love.

I want to specify that my next acknowledgements are in alphabetical order. I thank Upohar Haroon and Andrew Rudd.

Upohar Haroon has been my closest friend, and my most long lasting friendship. Although she hated me in fifth grade, I suckered her into friendship in eighth grade and we've never looked back. I think when you are friends with someone that long, they start to change the type of person you are. Upohar is caring, intelligent, and loyal to a fault. Being friends with Upohar for all these years has made me a better person, and I am forever grateful.

Andrew Rudd has been a huge part of my adult life. His pragmatic take on my problems may not have been what I wanted to hear, but it was always what I needed to hear. I thank him for balancing my occasional impetuosity; for being the calm in my storm. I appreciate everything that Andrew has done for me, and for the wonderful person he is. He has my love and thanks forever.

I would like to thank my friends. I thank Regina Wolper for her emotional support, and for the treats and coffee. I thank Matthew Peterson for being such a great friend, I couldn't imagine a better person for Upohar to spend the rest of her life with. I thank Vishal Patel for road trips, I thank Carly Dionne Williams for rock band, and I thank Elizabeth Van Wagner for

commiseration. I thank all the people in this section most importantly for being my friends, my life would not be as full of fun, love and laughter without anyone of you.

Last but certainly not least, I thank Billy.

## TABLE OF CONTENTS

	<u>page</u>
ACKNOWLEDGMENTS.....	4
LIST OF TABLES.....	10
LIST OF FIGURES.....	11
ABSTRACT.....	16
CHAPTER	
1 INTRODUCTION.....	17
Introduction.....	17
Alternate Imaging Modalities.....	18
Optical Microscopy.....	18
Computed Tomography.....	19
Ultrasound.....	21
Nuclear Magnetic Resonance and Magnetic Resonance Imaging.....	23
Introduction.....	23
Background.....	24
Theory.....	26
T <sub>1</sub> Relaxation Agents.....	30
Background.....	30
Clinical Use.....	32
T <sub>2</sub> Relaxation Agents.....	33
Background.....	33
Clinical Use.....	34
Chemical Exchange Saturation Transfer Agents.....	35
Background.....	35
Chemical Exchange.....	37
CEST versus Magnetization Transfer.....	39
High Field Advantage.....	39
2 METHODS.....	50
Contrast Agent Preparation.....	50
Multimodal Quantum Dots.....	50
PARACEST Agents.....	51
Iron Oxides.....	51
Phantom Preparation.....	51
Magnetic Resonance Imaging and Spectroscopy.....	53
Set Up.....	54
Relaxation Parameters.....	55
PARACEST Agents.....	56
CEST Spectra.....	57

Quantification of Contrast.....	58
Simulations.....	59
Rationale and Design.....	59
CESTFIT.....	60
Cell Labeling.....	60
3 RESULTS.....	68
Relaxation Agents.....	68
Multimodal Quantum Dots.....	68
Iron Oxides.....	68
PARACEST Agents.....	69
Multiple Lanthanide Ion Complexes.....	69
Field Strength.....	70
Concentration.....	70
pH.....	71
Temperature.....	72
Effect of Signal to Noise.....	73
Presaturation Power and Duration.....	73
Cell Labeling.....	74
Simulation.....	74
Relaxation Times.....	74
Chemical Shift Difference.....	74
Chemical Exchange Rates.....	75
Presaturation Power.....	75
Concentration.....	75
Temperature Fit.....	75
Number of Acquisitions Fit.....	76
4 DISCUSSION.....	102
Relaxation Agents.....	102
Multimodal Quantum Dots.....	102
Iron Oxides.....	103
PARACEST Agents.....	104
Multiple Lanthanide Ion Complexes.....	104
Field Strength Dependence.....	105
Concentration Dependence.....	107
pH Dependence.....	107
Temperature Dependence.....	108
Effect of Signal to Noise.....	109
Presaturation power and Length.....	110
Cell Labeling.....	110
Simulation.....	112
Relaxation Times.....	112
Chemical Shift Differences.....	114
Chemical Exchange Rates.....	114

Presaturation Power .....	115
Concentration .....	115
Temperature Fit.....	116
Number of Acquisitions Fit.....	116
Conclusions .....	116
5 FUTURE PERSPECTIVES .....	121
APPENDIX	
A IRON OXIDES DATA.....	125
B PARACEST AGENTS DATA AND CALCULATIONS.....	129
Ytterbium, Thulium and Europium PARACEST .....	129
Europium PARACEST Field Dependence.....	129
Europium PARACEST Concentration .....	129
Europium PARACEST pH.....	130
Europium PARACEST Temperature.....	130
Europium PARACEST Signal to Noise .....	131
Europium PARACEST Presaturation Power and Duration .....	131
C MATLAB SIMULATION.....	166
MATLAB Code Format.....	166
Modified Bloch Equations.....	166
Variable Chemical Shift Difference.....	172
Variable Chemical Exchange .....	175
Variable Presaturation Power .....	177
Temperature Fit MATLAB Code.....	180
Number of Acquisitions Fit MATLAB Code.....	184
LIST OF REFERENCES .....	193
BIOGRAPHICAL SKETCH .....	206

## LIST OF TABLES

<u>Table</u>		<u>page</u>
3-1	T <sub>1</sub> Relaxation values for 10 mM Eu-2 at multiple temperatures, measured at 14.1 T.....	93
B-1	CNR calculations for 4.7 T.....	138
B-2	CNR calculations for 17.6 T.....	139
B-3	CNR calculations for 21.1 T.....	139

## LIST OF FIGURES

<u>Figure</u>	<u>page</u>
1-1 Nuclear magnetic moment bar magnet representation.....	41
1-2 Precession in presence of $B_0$ .....	41
1-3 Nuclear magnetic moment alignment .....	42
1-4 Nuclear magnetic moment with orthogonal magnetic field $B_1$ .....	42
1-5 Net x-y magnetization immediately after $B_1$ is turned off.....	43
1-6 Spin lattice relaxation ( $T_1$ ).....	43
1-7 Spin-spin relaxation ( $T_2$ ).....	44
1-8 Gadolinium ( $T_1$ relaxation) contrast. ....	45
1-9 Common gadolinium based contrast agents .....	46
1-10 Iron Oxide ( $T_2$ relaxation) contrast. ....	46
1-11 Chemical Exchange Saturation Transfer (CEST) .....	47
1-12 Example CEST spectrum.....	48
1-13 PARACEST Imaging.....	49
2-1 Multimodal Gadolinium Quantum Dots.....	63
2-2 Chemical Structures of three europium Complexes .....	64
2-3 Chemical structures of the thulium and ytterbium complexes .....	65
2-4 Contrast to Noise Ratio (CNR) calculation region of interest diagram .....	66
2-5 Percent Decrease (%Decrease) calculation region of interest diagram for Eu-2 .....	66
2-6 Example CEST spectra, with the %Decrease calculation shown.....	67
3-1 Quantum Dot $T_1$ relaxation times. ....	77
3-2 Quantum Dot $T_2$ relaxation times.....	77
3-3 Quantum Dot $T_2^*$ relaxation Times.....	78
3-4 Iron oxide $T_2^*$ relaxation times.....	79

3-5	Europium PARACEST images at 17.6T .....	80
3-6	Thulium based PARACEST agents at 21.1T .....	80
3-7	Ytterbium based PARACEST agents at 21.1T .....	81
3-8	PARACEST contrast as a function of magnetic field strength .....	81
3-9	Difference images of europium complexes at 17.6 and 21.1 T.....	82
3-10	CEST spectra with variable magnetic field strength.....	83
3-11	Eu-2 serial dilutions .....	83
3-12	Eu-2 concentration phantom images at 14.1 T, with a presaturation power of 8 $\mu$ T.....	84
3-13	Eu-2 concentration phantom images at 14.1 T, with a presaturation power of 128 $\mu$ T ....	85
3-14	Concentration versus contrast for serial dilutions of Eu-2 at 14.1 T, with presaturation power of 64 $\mu$ T .....	86
3-15	CEST spectra at 14.1 T for Eu-2 serial dilutions .....	87
3-16	Eu-2 (10 mM) at two different pH's, and in SM.....	87
3-17	Eu-2 pH phantom at 17.6 T .....	88
3-18	Difference images of Eu-2 pH phantom at 14.1 T color enhanced to represent the corresponding CNR.....	88
3-19	Eu-2 at pH values from 3 – 13 at 14.1T.....	89
3-20	Presaturation offset versus normalized signal intensity for Eu-2 at multiple pHs at 14.1 T.....	89
3-21	Difference images of Eu-2 at multiple pHs at 14.1 and 17.6 T.....	90
3-22	CEST spectra for Eu-2 at multiple temperatures. ....	91
3-23	CEST spectra for Eu-2 with increasing number of scans .....	92
3-24	Number of acquisitions versus CNR.....	93
3-25	Varying presaturation power difference images .....	93
3-26	Presaturation power versus CNR for serial dilutions of Eu-2 at 14.1 T .....	94
3-27	Bulk water signal as a function of number of presaturation pulses .....	94

3-28	Cell labeling image results at 17.6 T.....	95
3-29	Simulated $T_1$ relaxation variation.....	96
3-30	Simulated $T_2$ relaxation variation.....	96
3-31	Simulated $\Delta\omega$ variation.....	97
3-32	Simulated variation in chemical exchange.....	98
3-33	Simulated presaturation power variation.....	99
3-34	Simulated concentration variation.....	99
3-35	Variable temperature data and fit.....	100
3-36	Variable number of acquisitions data and fit.....	101
4-1	Number of acquisitions versus CNR.....	120
A-1	Iron oxide images at 4.7 T.....	125
A-2	Iron oxide images at 4.7 T.....	126
A-3	Iron oxide images at 14.1 T.....	126
A-4	Iron oxide images at 14.1 T.....	127
A-5	Iron oxide images at 21.1 T.....	127
A-6	Iron oxide images at 21.1 T.....	128
B-1	Thulium complexes at 14.1 T.....	132
B-2	Ytterbium complexes at 14.1 T.....	133
B-3	Thulium complexes at 17.6 T.....	134
B-4	Thulium complexes at 17.6 T.....	135
B-5	Ytterbium complexes at 17.6 T.....	136
B-6	Ytterbium complexes at 17.6 T.....	137
B-7	Europium complexes CEST spectra at 14.1 T.....	138
B-8	Serial dilutions at 14.1 T.....	140
B-9	Serial dilutions at 14.1 T.....	141

B-10	Serial dilutions at 14.1 T.....	142
B-11	Serial dilutions at 17.6 T.....	143
B-12	Serial dilutions at 17.6 T.....	144
B-13	Serial dilutions at 21.1 T.....	145
B-14	Serial dilutions at 21.1 T.....	146
B-15	CEST spectrum of Serial Dilutions at 21.1 T.....	147
B-16	Variable pH phantom at 14.1 T.....	148
B-17	Variable pH phantom at 14.1 T.....	149
B-18	Variable pH phantom at 14.1 T.....	150
B-19	Variable pH phantom at 14.1 T.....	151
B-20	Variable pH phantom at 14.1 T.....	152
B-21	Variable pH phantom at 14.1 T.....	153
B-22	Variable pH phantom at 14.1 T.....	154
B-23	Variable pH phantom at 14.1 T.....	155
B-24	Variable pH phantom at 17.6 T.....	156
B-25	Variable pH phantom at 21.1 T.....	157
B-26	Variable pH phantom at 21.1 T.....	158
B-27	Variable pH with media phantom at 17.6 T.....	159
B-28	CEST spectrum of 10 mM Eu-2 at 14 °C.....	160
B-29	CEST spectrum of 10 mM Eu-2 at 20 °C.....	160
B-30	CEST spectrum of 10 mM Eu-2 at 26 °C.....	161
B-31	CEST spectrum of 10 mM Eu-2 at 32°C.....	161
B-32	CEST spectrum of 10 mM Eu-2 at 38 °C.....	162
B-33	CEST spectrum of 10 mM Eu-2 for one acquisition.....	162
B-34	CEST spectrum of 10 mM Eu-2 for two acquisitions.....	163

B-35.	CEST spectrum of 10 mM Eu-2 for four acquisitions.....	163
B-36	CEST spectrum of 10 mM Eu-2 for eight acquisitions. ....	164
B-37	CEST spectrum of 10 mM Eu-2 for 32 acquisitions.....	164
B-38	CEST spectrum of 10 mM Eu-2 for 64 acquisitions.....	165
B-39	Presaturation power and duration effect on CNR.....	165
C-1	CEST spectrum and fit for one scan. $R^2 = 0.995$ .....	190
C-2	CEST spectrum and fit for two scans. $R^2 = 0.989$ .....	190
C-3	CEST spectrum and fit for four scans. $R^2 = 0.990$ .....	191
C-4	CEST spectrum and fit for eight scans. $R^2 = 0.991$ .....	191
C-5	CEST spectrum and fit for 32 scans. $R^2 = 0.985$ .....	192
C-6	CEST spectrum and fit for 64 scans. $R^2 = 0.989$ .....	192

Abstract of Dissertation Presented to the Graduate School  
of the University of Florida in Partial Fulfillment of the  
Requirements for the Degree of Doctor of Philosophy

OPTIMIZATION OF CONTRAST AGENTS FOR HIGH MAGNETIC FIELDS

By

Heather H. Cornell

August 2009

Chair: Arthur S. Edison  
Major: Biomedical Engineering

Magnetic Resonance Imaging is one of most popular medical imaging modalities with the advantages of noninvasive and nondestructive high resolution images. Utilizing high magnetic fields can provide increased signal to noise resolution, but current contrast agents are not optimized for use in fields above 3 T. Several types of contrast agent were investigated to evaluate their potential application for cellular or molecular imaging at high magnetic fields in the future. The results indicated that  $T_1$  relaxation agents (gadolinium-based) were best used at lower magnetic field strengths, but two others,  $T_2$  relaxation agents (iron oxides) and PARACEST agents, hold great promise for high field contrast generation. These results could be applied to future studies to enhance contrast, gain higher resolution, advance understanding of cellular or molecular function, and contribute towards a dual anatomical-metabolic imaging modality of the future.

## CHAPTER 1 INTRODUCTION

### **Introduction**

The purpose of this project was to optimize contrast for high field magnetic resonance imaging, with the ultimate goal of enhancing molecular imaging. Molecular imaging enables the visualization of cellular function and molecular processes in living organisms. Alternate imaging modalities were considered, but due to its advantages and accessibility, magnetic resonance was chosen. Currently MRI is widely used in hospitals at 1.5 and 3 T to provide excellent anatomic information. Using higher field (4.7 – 21.1 T) magnets can increase the resolution for even better anatomical images. Unfortunately, no functional or physiologic information can be obtained using traditional MRI. If improvements in MRI contrast could allow functional and physiological information to be obtained, the results would have nearly limitless possibilities. Advances towards imaging cell function and/or physiologic processes could aid in earlier disease detection and diagnosis, as well as evaluation disease progression and possibly disease prevention by detecting very early signs. It could also be useful for developing better treatments through optimized clinical trials, targeted treatment and better treatment evaluation. This improvement in imaging could have long range economic effects due to earlier and more precise diagnosis, extended life span and better quality of life. The myriad of possible benefits from molecular imaging was the driving force in the investigation of high field magnetic resonance imaging contrast.

## Alternate Imaging Modalities

### Optical Microscopy

When discussing molecular imaging, the topic of microscopy inevitably arises, as it is well known for imaging on a cellular level, and remains a major method to verify other imaging modalities. Traditional optical imaging uses visible light and a system of lenses to produce a magnified image of an object, sample or specimen [1]. Microscopy literally refers to image visualization on a microscopic ( $10^{-6}$  m) level and light microscopy has a maximum resolution which is limited to the wavelength of the light source used [2]. However scanning electron microscopy and transmission electron microscopy have resolutions on the order of  $10^{-10}$  m [3].

There are several types of optical imaging contrast agents. Stains or dyes can be used provide contrast or change the color of the desired sample. Fluorescent dyes or proteins can also be used to cause the object of interest to fluoresce when excited with a specific wavelength of light. In recent years the ease and specificity of fluorescent staining or labeling has increased substantially [4] and fluorescent labeling cells or tissues has become one of the most important research methods available [5]. Methods employing multiple fluorescence sources can study reaction mechanisms, nearest protein neighbors, and interaction sites using fluorescence energy transfer (FRET) which uses the excitation of one fluorochrome to excite the second if the two are within a molecular distance of each other [1]. The methods using gene constructs like enhanced green fluorescent protein (eGFP) are especially promising for molecular imaging, because only the labeled cells which are expressing eGFP will fluoresce, providing a highly specific gene marker which effectively doubles upon cell division.

Microscopy currently has very high resolution, but suffers from the general limited depth penetration (due to absorbance or scattering of the excitation light and scattering of the reflected/emitted light). This is often circumvented by thinly slicing the sample, which has the disadvantage of invasive sample removal and destruction. These are the main disadvantages to choosing optical microscopy as an option for molecular imaging. Investigation of MRI as a potential molecular imaging modality was chosen as a noninvasive alternative to optical imaging, but optical imaging will be used for verification for the foreseeable future.

### **Computed Tomography**

Computed Tomography (CT), also known as Computerized Axial Tomography (CAT), is a clinical imaging modality which utilizes x-ray images, taken at different angles, to create a 2D axial slice of the object being imaged. The axial view allows better visualization than conventional x-ray images. As such, use of CT is growing as a popular clinical imaging tool, with 62 million scans completed in 2008 [6]. CT provides anatomical images with resolutions on the order of  $10^{-7}$  m or better [7,8], which can be used to differentiate between bone and soft tissue, including organs, muscles and tumors. Software is used to manipulate the signal to increase resolution for different tissues, allowing the visualization of the lung airways, blood vessels or the visualization of bone [9]. Methods of multi-planar reconstruction combine multiple axial (transverse) slices to create a 3D image [7], which can then be used to create an image in alternate orientations (e.g. sagittal or coronal). The different orientations can be used to aid in diagnosis, pre-surgical planning or other treatment, including radiation therapy where effective dosage is highly dependent on precise density, size and location of the tumor.

X-ray, and therefore CT, images are created by transmitting x-rays through the patient, and detecting the remaining x-ray signal on the opposite side of the body. Inherent contrast is generated in CT images due to the differential attenuation of the x-ray signal between tissues [10]. For additional contrast, radiopaque dyes including barium sulfate or iodine are administered most often orally (barium or iodine) or intravenously (iodine) depending on the area where contrast is desired. These contrast agents provide positive contrast by increased attenuation of the x-ray signal [11]. The toxicity of the iodine agents is low, but contraindications may arise from known allergic reactions, which can increase the risk of severe reaction from fourfold for patients with a history of nonspecific allergy up to 11-fold for patients with a history of reaction to contrast media [12]. Additional contraindications include hyperthyroidism (as increased amounts of iodine in the system may, especially in patients with hyperthyroidism, cause increased production of thyroid hormones which can be toxic) and impaired renal function (as the patients would have difficulty eliminating the contrast) [11].

Recently, CT has been combined with Positron Emission Tomography (PET) to create images with anatomical and metabolic information. In contrast with CT and other traditional anatomical imaging modalities, PET images the "spatial distribution of radiopharmaceuticals introduced into the body [10]." The radiopharmaceuticals or 'radiotracers' consist of an isotope that decays by releasing positrons linked to a chemical substrate. The structure of the substrate determines the distribution of the tracer throughout the body, and often take advantage of the increased metabolic activity of malignant tumors [13]. The radiotracer decays and each releases a positron, which upon encountering an electron is annihilated and releases a pair of photons ( $\gamma$ -rays). PET

detects the pairs of photons, and generates an image showing the distribution of the radiotracers, and thereby the general location of metabolic activity. But PET alone does not result in anatomic information, and therefore is often combined with another imaging modality. The combination of CT and PET allows for good spatial localization of metabolic information [13], but suffers from increased radiation.

CT can also be combined with single photon emission computed tomography (SPECT), which like PET uses radio pharmaceuticals. The main difference is that the radiopharmaceutical in SPECT releases a single  $\gamma$ -ray upon decay. Because PET results in two  $\gamma$ -rays, it has an increase in sensitivity two to three orders of magnitude greater than SPECT [10].

In the New England Journal of Medicine, Brenner and Hall [6] report that the radiation doses administered during repeated CT scans may actually increase the risk of those patients developing cancer further down the line, with a possible 0.4% of all cancers in the United states attributable to the radiation from CT studies [14,15]. CT also requires patients to lie still for the duration of the scan, and can therefore suffer from motion, or breathing related image distortions. MRI shares motion related distortions with CT, and maintains similar resolution and neither have depth penetration issues.

### **Ultrasound**

Ultrasound works by transmitting sound waves from a transducer into the body. The sound waves travel through tissue until they hit an interface that reflects the sound wave back to the probe (called a "reflector") [16]. By assuming that the speed of sound in biological tissue is 1540 m/s [16] and that the sound wave travels in a straight line to and from the transducer, the ultrasound machine can calculate the distance from the

transducer to the reflector. Ultrasound images are formed by transmitting very thin beams of sound waves then receiving the reflected sound waves repeatedly and assembling the resulting data [17].

Contrast within an ultrasound image is caused by the interface between two tissues. The interfaces reflect sound because different types of tissue propagate sound at different speeds and have different tissue density (combined, these are referred to as Impedance [16]). Most soft tissues have similar impedance values, with bone and air having much higher and much lower values, respectively [10]. The small differences cause detectable reflections while the large differences cause near total reflection (as with bone) or negligible reflection (as with air). The large impedance of bone and air, cause their presence to hinder ultrasound imaging. Resolution depends on the size of the ultrasound pulse, with typical axial (parallel to the US pulse) resolution values of 0.5 to 1 mm and typical lateral (perpendicular to the US pulse) resolution values of 2 to 5 mm [8]. The depth penetration is limited by the pulse repetition period (time between pulses), which is limited by the potential for an echo to return from a large depth to the transducer after the next pulse has occurred. The depth penetration depends on the pulse frequency, but is limited to 38.5 cm (for a pulse frequency of 2 kHz and a corresponding pulse repetition time of 500  $\mu$ s) [8].

To obtain greater sensitivity, contrast is used to enhance the ultrasound signal. Microbubbles are  $<10 \mu\text{m}$  in diameter (thus can safely cross capillary beds) and are generally injected intravenously where they remain in the vasculature [17]. In this way they can be used to obtain better visualization of vascular abnormalities or tumor vasculature. Specifically, microbubbles work to enhance the signal using harmonics [18].

This phenomenon is accomplished through the reverberation of the bubble walls. The ultrasound pulse causes the bubble to initially contract, in response to the increased pressure due to the ultrasound wave. After the initial contraction, the bubble expands, then contracts, and expands again, in a harmonic fashion. This reverberation causes an increase in the signal received by the ultrasound instrument. The bubbles are stabilized with a biodegradable shell to ensure they do not burst or merge into larger bubbles. As with contrast agents used for other types of imaging modalities, there is currently a trend in research towards targeting the ultrasound microbubbles to specific molecules [19-21]. By adding functionalized groups to the surface of the microbubble, these groups can be used to make the bubble stick to specific surfaces. This functionality could possibly be used for disease diagnosis, drug delivery, and potentially molecular imaging.

Ultrasound is currently a widely used technology for imaging human beings, with the advantages of being easily portable, noninvasive and relatively inexpensive [10]. Ultrasound is an extremely safe method of imaging with no limits on the number of patient examinations over a given amount of time set forth from the FDA [10]. Despite the safety, it suffers from relatively poor resolution and limited depth penetration.

## **Nuclear Magnetic Resonance and Magnetic Resonance Imaging**

### **Introduction**

The concept of Nuclear Magnetic Resonance (NMR) was first described in 1938, by Isidor Rabi, as a direct measurement of nuclear magnetic moments [22], and he was awarded the Nobel Prize in Physics in 1944 for this discovery. In 1946, the first NMR experiments were conducted independently by Felix Bloch [23], at Stanford University, and Edward Purcell [24], at Harvard University. These experiments led to development of NMR as a new spectroscopic technique that has since proven to be a versatile, accurate

and dependable method of chemical research [25]. Bloch and Purcell were jointly awarded the Nobel Prize in physics in 1952 for their work in NMR. Richard Ernst made the observation that sensitivity could be greatly enhanced by computing the spectrum from a free induction decay (the resulting recorded response to a short r.f. pulse) by means of a numerical Fourier Transformation (FT) [26,27]. He was then able to apply this transformation to develop 2D FT NMR methods [27]. For his contributions Ernst received the Nobel prize in Chemistry in 1991, and he is often recognized as one of the major early contributors to MRI. The principles of NMR spectroscopy were utilized by Paul Lauterbur and Peter Mansfield to develop a technique for noninvasive MR imaging. Paul Lauterbur incorporated a weaker gradient magnetic field for spatial localization [28], and Peter Mansfield introduced the k-space formalism [29] and the concept of transversing reciprocal space [30]. The two were major contributors to the development of Magnetic Resonance Imaging (MRI), and were jointly awarded the Nobel Prize in Medicine in 2003 for their discoveries.

## **Background**

Magnetic Resonance Imaging has become one of the most powerful imaging modalities in biomedical research [31]. Some of its advantages include being nondestructive and noninvasive; there are no known long-term negative side effects on human beings (unlike the radiation exposure in CT scans). Different tissues have inherent contrast differences based on their relaxation rates and special sequences can be used to enhance the detail of certain tissue types, or negate the effects of others. However, MRI is relatively slow and is sensitive to motion artifacts, which is to say if the patient moves during the scan it can affect the quality of the image. Additional disadvantages (which generally are outweighed by the advantages) include patient

discomfort. This discomfort can be due to confinement in the small space of the scanner during the imaging. Also, there are multiple sources of acoustic noise, which can be disconcerting or uncomfortable for the patient. Noise can arise from gradient or eddy currents, or radio frequency and slice select pulses [32], and higher fields can generate higher levels of noise [33]. In addition to patient discomfort, the noise can interfere with certain functional MRI studies [34]. Due to the small net magnetization (discussed below) the sensitivity of MR techniques are low when compared to the high contrast and sensitivity of PET.

MRI is widely considered to have a good safety profile, especially when compared to its main anatomical imaging alternative CT, which exposes the patient to large doses of radiation [35]. Side effects from MR imaging have been shown to be mainly transient, and can include a metallic taste, vertigo, nausea, and magnetosphenes (flickering lights) [36-38]. Despite this safety profile, there are patients who will always be contraindicated for MR imaging, mainly those with magnetic metal implants, shrapnel, or pacemakers. Six of seven reported fatalities associated with MR imaging in 1998 were caused by either movement of metal (aneurysm clip) or the presence of a pacemaker (the link between fatality and the MR scanning was uncertain in several of these deaths) [37]. There is some concern that increasing the static magnetic field strength may lead to increased side effects [37,39-41], but the results on humans in fields up to 8 T and animals up to 16 T indicate no decrease in the safety [37]. As it is used clinically today, MRI is generally considered safe and effective [39].

Currently there is a limit of the detail that can be seen using MRI. Higher resolution can be attained with longer scanning times, but this can lead to an increase in

motion artifacts and patient discomfort. One alternative is to use chemical agents to alter the signal and cause increased contrast. Currently, relaxation agents are commonly employed to alter the contrast at clinical field strengths of  $<1.0\text{-}3\text{ T}$ . Higher magnetic fields can be employed to increase signal, increase resolution, and decrease scan time [42]. The combination of increased signal from the higher field and increased contrast from the chemical agent may allow for much higher resolution than is currently available in clinical imaging. This increase in resolution would be beneficial for various medical reasons including reduced scan time and earlier disease detection. Also, increased resolution could contribute towards advanced research in disease treatment because it could be used for drug tracking or to obtain physiological information.

## **Theory**

In order to explain nuclear magnetic resonance, two main nuclear properties must be discussed: nuclear spin and nuclear magnetism. Spin is an intrinsic property of nuclei which is difficult to conceptualize but may be simplified to mean that the nucleus behaves as if it is spinning, similar to a planet rotating about its axis in space [43]. Classically, any object that rotates or spins about itself is said to have angular momentum, visualized as a vector pointing along the axis of rotation [43]. Nuclear momentum is quantized, resulting in distinct energy levels. Nuclear spin is a form of angular momentum which is not produced by the rotation of a particle but is an intrinsic property of the particle [43]. Nuclear spin can also be quantized resulting in separate energy levels which depend on the spin quantum number of the elemental particle. For protons, the quantized spin ( $S$ ) is  $\frac{1}{2}$  which results in a two state spin polarization which is oriented independent of any spatial dimensions. In the absence of an external field the two states are degenerate, but in the presence of an applied magnetic field the energy

levels split and the nuclear spins distribute between the energy levels according to the Boltzmann Distribution (Equation 1-1).

$$\frac{N_{\alpha}}{N_{\beta}} = e^{\frac{\Delta E}{k_B T}} \quad (1-1)$$

In Equation 1-1,  $N_{\alpha}$  refers to the number of spins in the lower energy state ( $\alpha$ ),  $N_{\beta}$  refers to the number of spins in the higher energy state ( $\beta$ ),  $\Delta E$  is the energy difference between the two states,  $k_B$  is Boltzmann's constant and  $T$  is the temperature. The energy difference causes a difference in the population of spins between the high and low energy states, and this causes the spin polarization to develop. The spin polarization determines the basic MRI signal strength. Spin polarization may be simplified by viewing it as classical angular momentum with the axis of rotation aligning either parallel or anti parallel to the applied magnetic field. While technically incorrect, the simplification is often employed to describe MRI. At room temperature this results in a polarization  $\sim 1$  ppm with an applied 0.3T magnetic field [44].

Nuclear magnetism refers to the interaction of the nucleus with a magnetic field. An additional simplification can be made by visualizing nuclear magnetism, usually expressed in terms of the magnetic moment ( $\mu$ ), as the particle being a tiny bar magnet (Figure 1-1). Nuclear magnetism and spin are proportional, as shown in Equation 1-2.

$$\mu = \gamma S \quad (1-2)$$

The proportionality constant  $\gamma$  is the gyromagnetic ratio and  $S$  is the spin angular momentum [43]. Because the spins have both angular momentum and magnetism, when they 'align' with the applied magnetic field, they precess (Figure 1-2) about an axis

aligned with  $B_0$  [43]. The frequency ( $\omega_0$ ) of this precession is called the Larmor frequency (Equation 1-3).

$$\omega_0 = -\gamma B_0 \quad (1-3)$$

The sign of the Larmor frequency refers to the direction of precession, clockwise or counterclockwise about  $B_0$  [43].

At room temperature in the absence of an external magnetic field, the spin states are degenerate and the magnetic moments in a given sample are uniformly distributed in all possible directions in space [43]. The sum of the randomly oriented nuclear magnetic moments is essentially zero, resulting in no net magnetization (Figure 1-3-A). MRI uses a static magnetic field ( $B_0$ ) to align the nuclear magnetic moments of the atoms in the sample (Figure 1-3-B).  $B_0$  causes the atoms in the sample with individual spins to align either parallel or antiparallel with the magnet, according to the Boltzmann distribution (Equation 1-1), with a small excess parallel. The resulting slight excess results in an overall net magnetization ( $M_0$ ), which aligns with  $B_0$  (referred to as along the z-axis).

The atoms' nuclear magnetic moments are aligned with  $B_0$ , but randomly distributed in the x-y plane (Figure 1-4-A). Radio frequency (RF) coils are used to induce an orthogonal magnetic field  $B_1$ , which changes the alignment of the nuclear magnetic moments into the x-y plane (Figure 1-4-B).

Once  $B_1$  is turned off, the nuclear magnetic moments return to alignment with  $B_0$  (the static field). This realignment with  $B_0$  causes a changing magnetic field, which induces a current in the receiver coils, as depicted in Figure 1-5. This signal is a sinusoidally dampened decay, called the Free Induction Decay (FID), and is converted into the frequency domain using the Fourier Transform. Gradient coils are used to

produce controlled variations in the main magnetic field ( $B_0$ ) which effect the Larmor frequency of the spins. By changing the frequency of precession, the resulting signals can be differentiated between different spatial locations within the image. The image is created through the difference in intensities in the peaks per pixel.

There are two mechanisms of nuclear spin relaxation. Spin-lattice relaxation refers to the mechanism by which the nuclear spin magnetization returns along the z axis (aligned with  $B_0$ ). The interaction between the spin and its environment causes this relaxation, which is characterized by a time constant  $T_1$ . Any time the magnetization is not in equilibrium,  $T_1$  relaxation occurs. For example, after the application of an appropriate  $B_1$  the system equilibrium was disrupted and the net magnetization along the z axis is approximately zero and the spins are not in equilibrium. Through spin lattice relaxation the spins recover to the equilibrium net magnetization (Figure 1-6). In general anything that can give rise to fluctuating magnetic fields can contribute to this relaxation including chemical shift anisotropy, magnetic dipole-dipole and electric quadrupole interactions [31]. Temperature and field strength also have an effect on  $T_1$  [45].

The second relaxation mechanism is spin-spin relaxation, characterized by  $T_2$ . Spin-spin relaxation refers to the mechanism by which the nuclear magnetization disappears (dephases) in the x-y plane (orthogonal to  $B_0$ ). While  $T_1$  refers to the net magnetization returning on the z axis,  $T_2$  refers to the dephasing of the spins in the x-y plane. At equilibrium, all the spins in the x-y plane are out of phase (Figure 1-4-A); they cancel each other resulting in a net magnetization with only a z component. When a 90 degree pulse is applied, the net magnetization is in the x-y plane (Figure 1-4-B). After  $B_1$  is turned off, the spins begin to dephase, and eventually the net magnetization in the x-

y plane returns to zero (Figure 1-7). This relaxation occurs because of the interaction of the spins with each other, but may also be due to inhomogeneities in the  $B_0$  field [31].

$T_2^*$  refers to the relaxation caused by both effects, and varies between instruments.

Differences in  $T_1$  and  $T_2$  between samples (or regions within samples) cause different signal intensities, and create contrast within images. Different pulse sequences can be used to increase the contrast effects due to these inherent differences. Chemical agents containing paramagnetic ions have been described for contrast generation as early as 1978 by Maria Helena Mendonça-Dias and Paul C. Lauterbur [46]. Since then research using chemical agents to increase these differences in signal intensity resulting in image enhancement has grown significantly.

## **$T_1$ Relaxation Agents**

### **Background**

There are a myriad of uses for increased resolution, and one promising path to obtain this resolution is through contrast agents used at high magnetic fields. Caravan, Ellison, McMurry and Lauffer [47] published a detailed description of paramagnetic agents used for MRI contrast generated through the interaction of the paramagnetic agents with water. This interaction changes the local magnetic environment to which the water protons are exposed. This alteration induces a change in the relaxation properties of water, resulting in modifications of signal and contrast. Relaxation contrast agents can cause concentration dependent changes in  $T_1$  or  $T_2$ .

Gd (III) can be used to induce a change in the local magnetic environment resulting in a change in  $T_1$ . Free Gd (III) is toxic [48], but chelating ligands greatly reduce the free Gd(III) toxicity [49]. Gd (III) based chelates are commonly used because when compared to other lanthanide ions, Gd (III) is more efficient at relaxing bulk water

protons [50]. This type of contrast is generally directly related to the amount of Gd present, which can be limited by stability of the chelating ligand and allowable concentration of injection [49]. Once present in the tissue, the contrast remains altered until all of the Gd has been eliminated from the system, which is usually around 24 hours [51] in healthy patients. Gadolinium has recently come under increased scrutiny as a result of a possible association with increased incidence of nephrogenic systemic fibrosis (NSF) [52]. While no direct link was found, the American Medical Association still recommended discontinuing the use of gadolinium based contrast agents in patients with renal disease. The safety profile of Gd chelate contrast agents is still considered especially good when compared to profiles of iodinated x-ray agents [53].

$T_1$  relaxation agents like those based on Gd work through inner and outer sphere relaxation as illustrated in Figure 1-8. The paramagnetic ion, in Figure 1-8 Gd-TSPETE, creates a fluctuating magnetic field which provides a relaxation pathway for the (inner sphere) water protons via electron-proton dipolar coupling, which drops off with distance [54]. The most efficient  $T_1$  relaxation agents have fast water exchange (characterized by a small  $\tau_M$ ) so that a large number of water protons experience the inner sphere relaxation. Inner sphere relaxation is also characterized by the rate of rotation (characterized by the rotational correlation time  $\tau_r$ ), and in general slowing down the tumbling rate increases the relaxation [55]. Slowing down the frequency of rotation of the Gd complex results in the fluctuations of the paramagnetic field being closer to the Larmor frequency, which causes more efficient relaxation [54]. The last factor in  $T_1$  relaxation is diffusion (characterized by the correlation time  $\tau_D$ ) which allows bulk water

molecules surrounding the Gd complex (in the outer sphere) to experience relaxation [54].

### **Clinical Use**

Magnetic Resonance Imaging (MRI) is a clinical imaging modality with many advantages including good spatial resolution, multiple intrinsic contrast mechanisms, chemical specificity and nondestructive analysis. Enhancements in contrast can be generated by the interaction of water with paramagnetic gadolinium (Gd) chelates, which change the local magnetic environment to which protons in water are exposed. This alteration induces a change in the relaxation properties of water, resulting in modifications of signal and contrast. An overwhelming majority of contrast enhanced clinical exams are performed with gadolinium complexes, with nearly 10 million MRI studies are performed with gadolinium each year [56]. Gadolinium is currently used in different forms as a contrast for MRI, including gadobenate dimeglumine (Multihance®), and gadopentate diglumine (Magnevist®) [57]. Both agents have similar chemical structures [58,59] (Figure 1-9) and work by changing the magnetic relaxation properties of water protons. This is accomplished through interaction of water in human tissue with the contrast agent. Since the tissue interacts with the Gd chelate, its relaxivities ( $r_1 = (\Delta(1/T_1))/[\text{Contrast Agent}]$  and  $r_2 = (\Delta(1/T_2))/[\text{Contrast Agent}]$  [60]) are altered. As such, any area that is imaged that contains the contrast agent will appear brighter on an MR image. Gd based agents are generally excreted partly by the kidneys and partly by the biliary system.

Contrast agents have been shown to enhance different types of lesions/disease differently. Some disease states do not require contrast. For example, conventional MRI

has been shown to demonstrate vascular malformations such as AVMs, capillary telangiectases, cavernous angiomas and venous malformations [57] because of the detail of the parenchyma shown while simultaneously showing the venous malformation. However, the use of contrast agents can help to further improve the delineation of feeding arteries and draining veins when trying to assess the presence and severity of brain aneurysms, venous thrombosis, central venous drainage, periventricular or deep location or occurrence of previous hemorrhage (within the brain). Also, contrast use is important to the diagnosis of several types of tumors. Contrast enhanced imaging is extremely useful in the evaluation of infectious types of lesions like meningitis, encephalitis, or abscess formation. Although the enhancement may be nonspecific, the contrast images used in conjugation with other special sequences (such as diffusion weighted imaging, as previously discussed) can still be used to diagnose the lesion.

In addition to the use for diagnosis of a disease/lesion contrast enhances MRI can be used pre-surgery to give the surgeon a better map of the area which needs treatment. MRI-guided biopsy is a growing area of clinical importance. This is due in part to the tissue contrast which can be provided using MRI (and contrast agents) which cannot be provided using ultrasound or CT.

## **T<sub>2</sub> Relaxation Agents**

### **Background**

In addition to T<sub>1</sub> relaxation agents, there are T<sub>2</sub> or T<sub>2</sub><sup>\*</sup> relaxation agents, which generally contain iron oxides. The iron-oxide agents are commonly ferumoxides (FeO<sub>1.44</sub>) and can be SPIOs (superparamagnetic iron oxides) and USPIOs (ultra-small superparamagnetic iron oxides) which are smaller in size.

Similar to gadolinium agents, iron oxides also induce a change in the relaxation properties of water, but instead of  $T_1$  relaxivity, the iron oxides influence  $T_2$  relaxivity. Unlike Gd contrast agents, iron oxides do not require chelating ligands, but they are dextran or carbodextran coated to prevent bioreactivity. They are not toxic at low concentrations, but the FDA has set guidelines to the amount of iron that can be administered during one time (.56 to .8 mg of iron/kg body weight depending on the type of agent) [61]. Like Gd based contrast agents, once present in the blood the contrast remains until all of the iron oxide has been eliminated (25hrs from blood, 7 days from system [62]).

Iron oxides affect the  $T_2$  relaxation parameters through outer sphere as shown in Figure 1-10. The iron oxides in superparamagnetic particles have a combination of  $Fe^{2+}$  and  $Fe^{3+}$  ions, which are aligned in one of two specific orientations. The  $Fe^{3+}$  ions cancel each other out, but there are some uncompensated  $Fe^{2+}$  ions, which result in a large magnetic moment [63]. This large magnetic moment induces strong local field gradients (Figure 1-10) which cause the surrounding water protons to quickly lose phase coherence (dephase) [54]. This rapid dephasing is not limited to close (inner sphere) water protons and can be seen at a considerable distance [54].

### **Clinical Use**

Contrast agents containing iron-oxides are useful in the liver and spleen because they efficiently accumulate in those areas within minutes of injection [64]. Their primary affect is on the  $T_2$  relaxivity of the tissue. SPIO particles are useful in the diagnosis of different liver lesions because lesions remain unchanged, while the SPIO particles are taken up by normal liver tissue, specifically the Kupffer cells [61]. This causes a reduction of the signal intensity in the normal liver while the lesion signal intensity

remains unchanged. This results in increased signal difference between the liver and the lesion, making the lesion appear bright and more easily distinguished; the use of iron oxide contrast has been shown to significantly improve the number of liver lesions detected compared to unenhanced MRI [65].

The safety profiles of iron oxides are slightly less desirable than those of the Gd chelates [53]. In a 1995 phase III clinical trial, a study involving 208 patients reported no serious reactions to ferumoxides, but reported adverse reactions in 15% of the patients [62]. The most common negative side effects are include mild to moderate back pain and flushing [61,62]. Other reported side effects included nausea, vomiting, diarrhea, headaches, body pain (neck, chest, abdomen), dry mouth, dizziness, muscle spasm, leg cramping and cold extremities [62]. Most symptoms were mild and resolved without additional complications. The disadvantages of the adverse reactions generally are outweighed by the increased detection of liver lesions.

Limitations of this contrast agent include a high incidence of false positives [53,66], cellular internalization of iron oxides may be metabolically unfavorable (to the cells) [67] and as with Gd agents, the contrast remains present in any images until the agent has been cleared from the system. However, iron oxides maintain the advantage of at least an order of magnitude greater in sensitivity than paramagnetic contrast agents.

### **Chemical Exchange Saturation Transfer Agents**

#### **Background**

Recent studies [68-70] have proposed an alternate method for contrast generation, adapting chemical exchange-dependent saturation transfer (CEST) methods along with a new type of chemical contrast agent. These agents contain paramagnetic lanthanide ions that have been shown to induce tremendous NMR hyperfine shifts in nearby NMR

nuclei [50,71]. Paramagnetic Chemical Exchange Saturation Transfer (PARACEST) uses a chelated paramagnetic lanthanide ion with an exchanging site which binds to water. This bound water is in constant exchange with the surrounding bulk water (Figure 1-11-A). The bound water is chemically shifted away from the bulk water through its interaction with the lanthanide ion. Supplying an RF pulse at the chemical shift induced by the paramagnetic lanthanide ion, saturates the bound water protons (Figure 1-11-B). Nuclei maintain magnetization through the process of chemical exchange, so when the bound water exchanges with a bulk water it retains saturation (Figure 1-11-C). Because the system is in constant chemical exchange, applying saturation at the chemical shift of the bound water protons for an amount of time allows the system to build up the number of saturated (or transfer the magnetization to the) bulk water protons (Figure 1-11-E), which results in a decrease in the overall water signal.

This phenomena can be utilized to measure chemical exchange in spectroscopy or produce contrast during imaging. A CEST spectrum (also referred to as Z spectrum) is the result of selectively presaturating a range of frequencies and plotting the remaining bulk water signal intensity as a function of presaturation offset (Figure 1-12). It can also be used to generate contrast in an imaging experiment. If the RF saturation is applied on the resonance of the bound water protons (Figure 1-13-A), a decrease in the bulk water signal will be observed, but only where the lanthanide complex is present (Figure 1-13-B). The same RF saturation is applied on the opposite side of water (Figure 1-13-A), and there is no decrease in the water signal (Figure 1-13-C). The contrast is further elucidated by taking the difference between the two images (Figure 1-13-D).

Despite resulting in a decrease in signal intensity similar to SPIO contrast agents, CEST images have the advantage that they can be turned on and off for different lanthanide (III) paramagnetic chelates (PARACEST agents) through the use of frequency selective presaturation pulses. PARACEST agents are particularly useful due to their large chemical shifts and long life times of bound water, which can result in a more efficient transfer of magnetization to bulk water.

### **Chemical Exchange**

By definition PARACEST agents rely on chemical exchange with water to carry the magnetization of the nuclei from the bound to the bulk water pool. An estimation of the effect of chemical exchange on the bulk water signal is given by Equation 1-4 [70].

$$\frac{M_{on}}{M_{opp}} \approx [1 - k_1 T_{1sat}] \quad (1-4)$$

$M_{on}$  is the magnitude of the bulk water signal with presaturation on the resonance of the bound water pool,  $M_{opp}$  is the magnitude when the presaturation is on resonance on the opposite side of water,  $k_1$  is the pseudo first order exchange rate constant and  $T_{1sat}$  is the spin-lattice relaxation rate of the bulk water signal with saturation of the bound water protons. The pseudo first order exchange rate ( $k_1$ ) can be simplified as the single exchange site rate constant ( $k_{ex}$ ) for simple reactions multiplied by the total number of exchange sites available (proportional to the concentration) [70].

The estimation of effect of chemical exchange (Eqn 1-4) shows that systems with longer  $T_1$  values allow for a larger range of viable exchange rates because the longer  $T_1$  values allow the spins to maintain their magnetization longer. It also shows that as long as the exchange is sufficiently rapid, the signal associated with exchanging sites can be detected through observation of changes in bulk water [70].

However, if exchange is too fast, and the system is in fast exchange, the spectral distance between the bulk and bound water proton pools would be too small, and the peaks would coalesce. In order for viable contrast generation, the chemical exchange must occur to fulfill the slow to intermediate exchange requirement as shown in Equation 1-5 [72].

$$\Delta\omega\tau_M \geq 1 \quad (1-5)$$

Equation 1-5 is alternatively written as Equation 1-6.

$$\frac{\Delta\omega}{k_{ex}} \geq 1 \quad (1-6)$$

$\Delta\omega$  is the frequency (or chemical shift) difference between the bound and bulk,  $\tau_M$  is the bound water lifetime which is the inverse of the single site exchange rate constant ( $k_{ex}$ ). The chemical exchange rate is dependent on other factors such as pH, temperature and ionic environment [70]. As a result PARACEST agents have been developed to monitor pH [73-76] and temperature [77-79], both of which are dependent on chemical exchange.

The slow to intermediate exchange requirement shows the dependence of CEST contrast generation on both exchange rate and chemical shift difference. The chemical shift difference in PARACEST is caused by the lanthanide ion, and each lanthanide has a difference  $\Delta\omega$ . Larger chemical shift differences have an advantage of allowing faster exchange rates while maintaining a discrete spectral difference between the bound and bulk water protons [72]. Large  $\Delta\omega$  (>2ppm) differences can also increase specificity by avoiding direct saturation of water [70]. They can also allow broad band excitation without direct saturation effects on water protons, which can avoid the magnetic susceptibility resulting from poor/inhomogeneous saturation.

## **CEST versus Magnetization Transfer**

CEST utilizes saturation similarly to Magnetization Transfer (MT) techniques, which uses a single off-resonance irradiation to generate contrast based on macromolecule-water proton interactions [80,81]. The macromolecules used to create MT are endogenous, and can sometimes be overproduced or in higher abundances in the brain as a result of white matter diseases; therefore MT can be used for creating contrast to help characterize white matter diseases [54]. The effect of the macromolecules is approximately symmetric about water (the center of symmetry is actually in the aliphatic region not exactly on water) and can be detected over a large range of frequencies (~100 kHz) [82].

Conversely, CEST uses proton chemical exchange between water and metabolites (or chemical agents with exchangeable protons) with bound water pools farther from water [70]. The CEST effect is asymmetric and has a much higher frequency specificity than MT [82]. Additionally, where MT is dependent on chemical exchange and cross relaxation, CEST is dependent on only chemical exchange [82].

### **High Field Advantage**

Higher magnetic field strengths in MRI have the inherent advantage of an increase in signal, which is shown in the Boltzmann Distribution (Eq. 1-1). The larger static magnetic field creates a greater energy difference between the two spin states, and results in a greater proportion of spins in the lower energy state ( $N_\alpha$ ) than the higher energy state ( $N_\beta$ ). This greater proportion of spins results in a larger MRI signal. The predicted increase in signal with field strength is proportional to  $B_0^{7/4}$  for small samples (dominated

by coil noise) [45,83] and proportional to  $B_0$  for large samples (dominated by sample noise) [45,84].

In addition to the increase in signal at high fields, CEST benefits from a greater chemical shift difference. The Larmor frequency of each nuclei increases proportionally with field strength (Eq. 1-3), which effectively increases the frequency difference between bulk water protons and the lanthanide chemically shifted water protons. For example, given an exchanging system where  $\Delta\omega$  is 50 ppm, this translates to 10 kHz at 4.7 T and 45 kHz at 21.1 T. This effectively lowers the  $\tau_M$  (increasing the possible exchange rate) needed to maintain the  $\Delta\omega\tau_M \geq 1$ . Therefore, while few lanthanide agents would be able to create PARACEST contrast at lower field strengths of 1.5 or 4.7 T, several lanthanide complexes (including praseodymium, neodymium, samarium, europium, terbium, dysprosium, holmium, erbium, thulium, and ytterbium ions [50]) should exceed the  $\Delta\omega\tau_M \geq 1$  requirement making contrast generation possible.

High magnetic fields offer an inherent increase in signal, which can be used to increase the resolution. This, coupled with the increase in contrast potential for PARACEST contrast, makes PARACEST at high fields an area with great potential for molecular imaging.

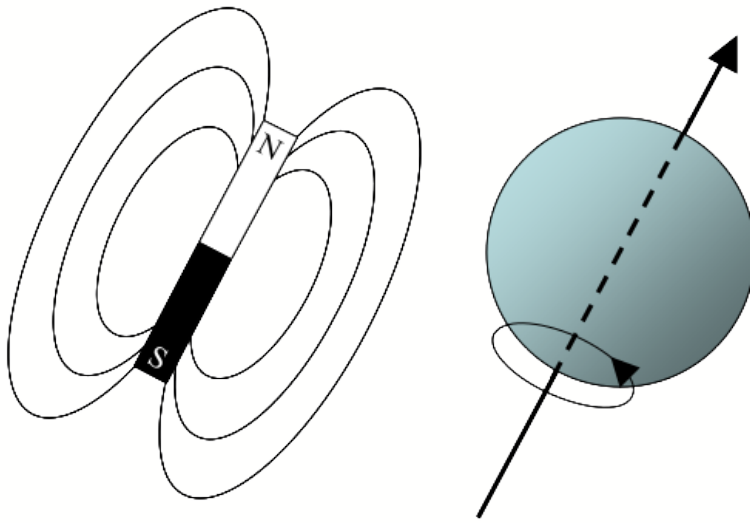


Figure 1-1. Nuclear magnetic moment bar magnet representation.

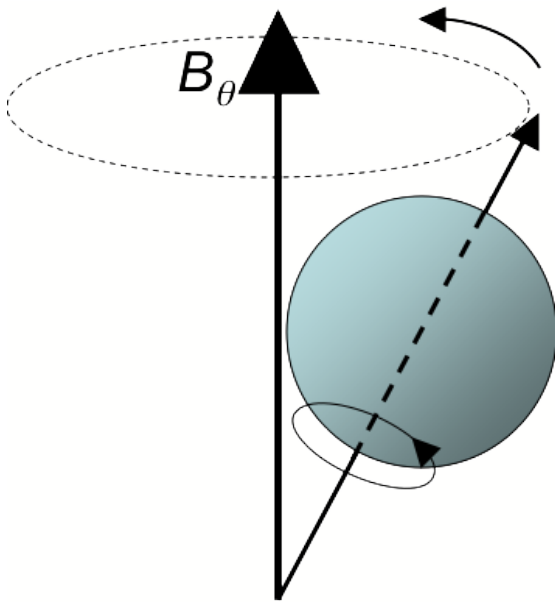


Figure 1-2. Precession in presence of  $B_0$ .

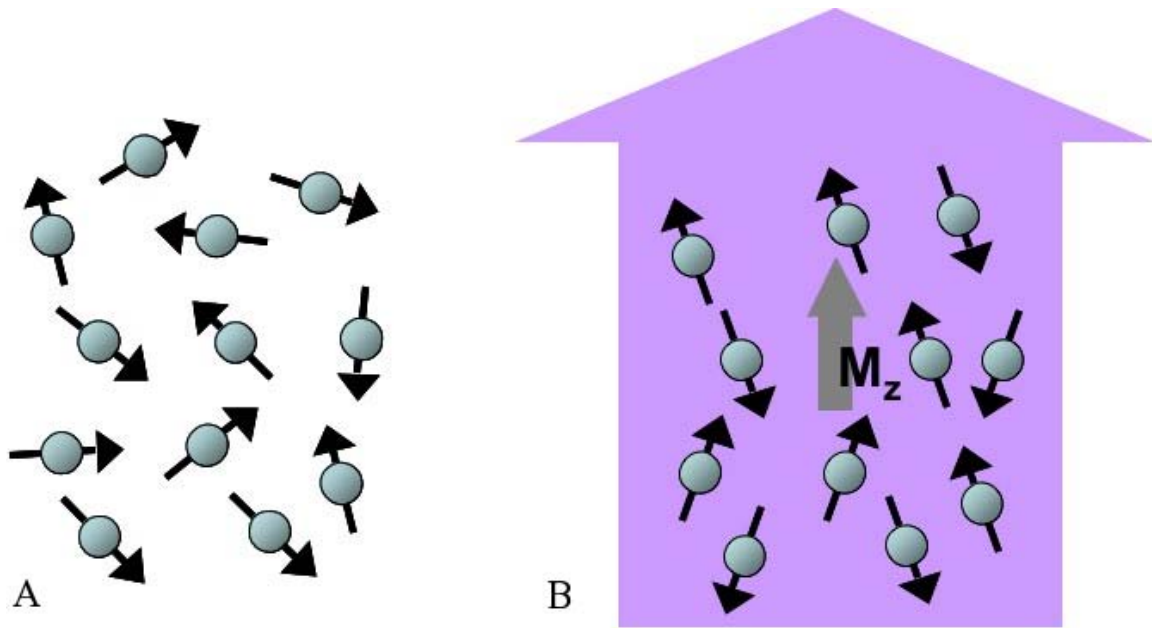


Figure 1-3. Nuclear magnetic moment alignment. A) The nuclear magnetic moments are randomly distributed in the absence of an external magnetic field. B) The nuclear magnetic moments are aligned (parallel or antiparallel) when placed inside the magnetic field.

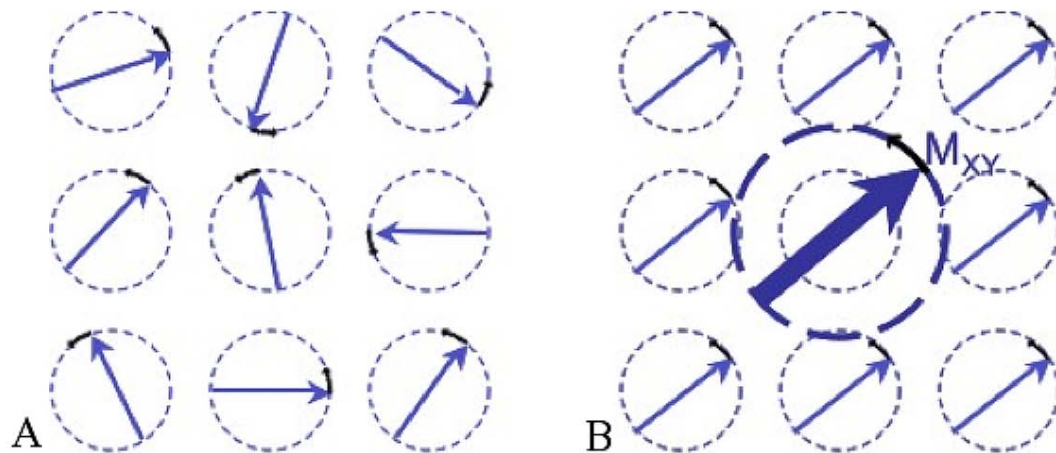


Figure 1-4. Nuclear magnetic moment with orthogonal magnetic field  $B_1$ . A) When the sample is in the magnetic field, initially all spins are randomly distributed and their x-y magnetization cancels out. B) The RF pulse creates the orthogonal magnetic field ( $B_1$ ) which orients them in one direction, for a net magnetization in the x-y plane.

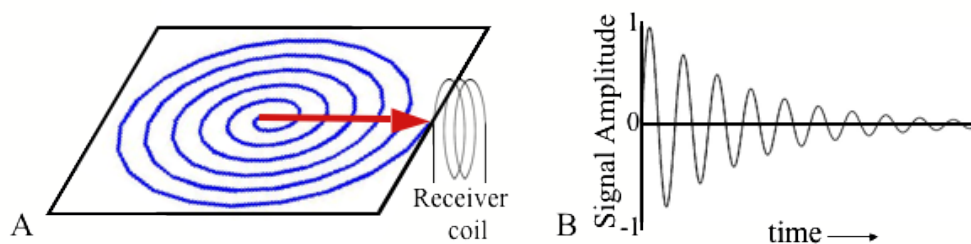


Figure 1-5. Net x-y magnetization immediately after  $B_1$  is turned off. A) Tracking the x-y magnetization from the top view. B) The resulting Free Induction Decay (FID).

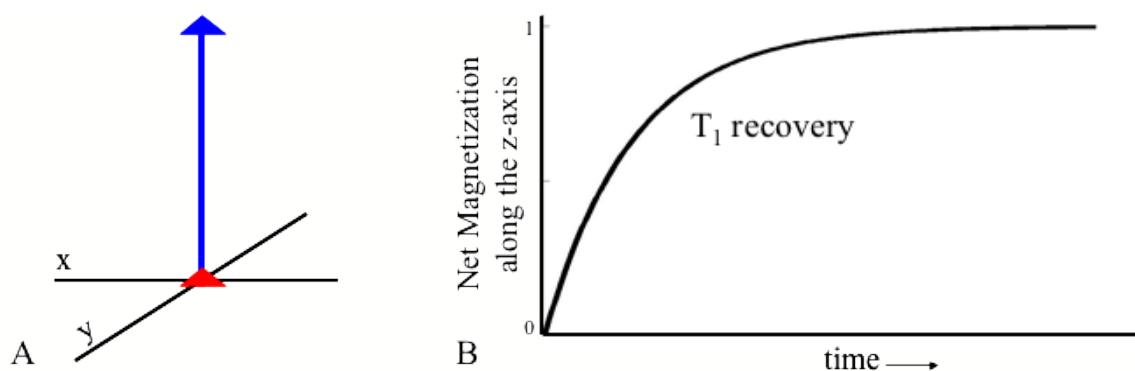


Figure 1-6. Spin lattice relaxation ( $T_1$ ). A) The net magnetization along the z-axis during application of the orthogonal magnetic field (shown in red) and after relaxation to equilibrium (shown in blue). B) The net magnetization along the z-axis shown as a function of time, showing  $T_1$  as the time it takes for the net z-axis magnetization to return to equilibrium.

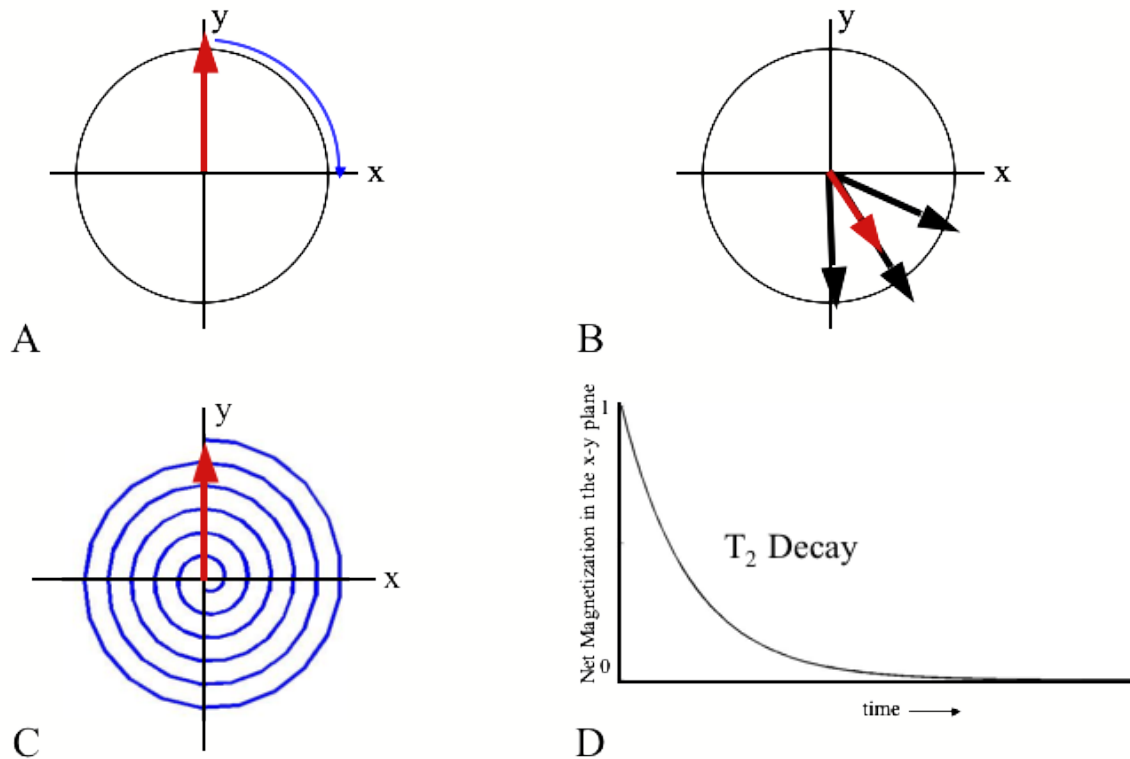


Figure 1-7. Spin-spin relaxation ( $T_2$ ). A) The net magnetization (in red) in the x-y plane during application of the orthogonal magnetic field, with the direction of precession in blue. B) The net magnetization (shown in red) in the x-y plane after some time  $< T_2$ , showing dephasing (individual magnetization vectors shown in black). C) The net magnetization in the x-y plane from the application of the orthogonal magnetic field (start point in red) until relaxation to equilibrium at zero. D) The net magnetization in the x-y plane shown as a function of time, showing  $T_2$  as the time it takes for the net magnetization in the x-y plane to return to zero.

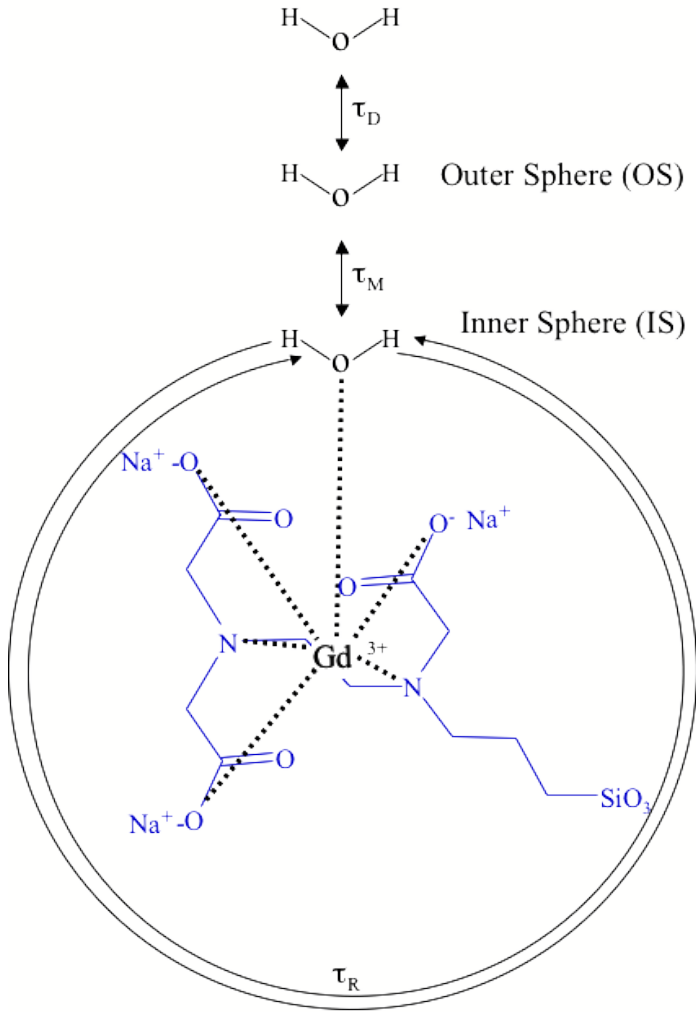


Figure 1-8. Gadolinium ( $T_1$  relaxation) contrast.

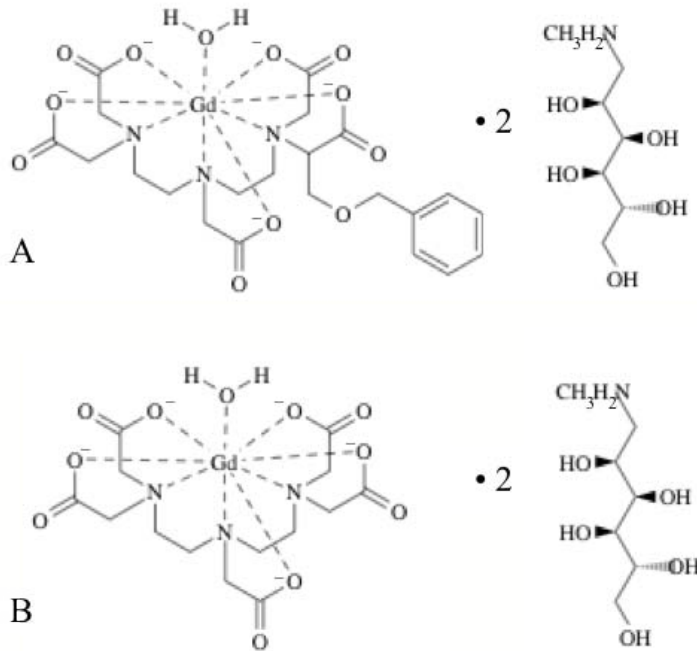


Figure 1-9. Common gadolinium based contrast agents. A) Multihance® [58]. B) MAGNEVIST® [59].

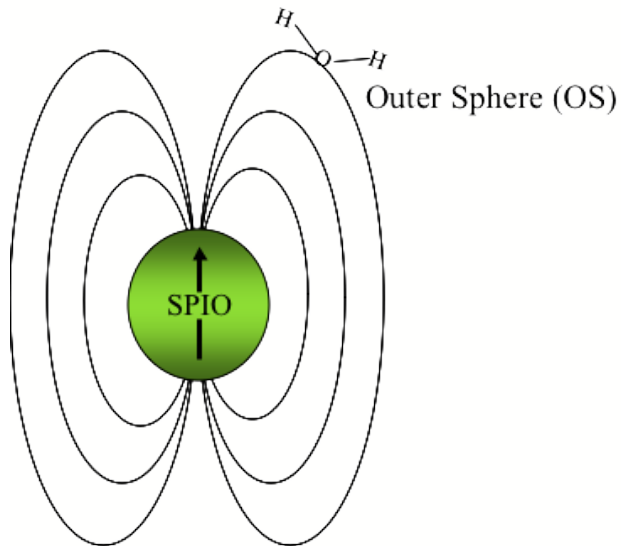


Figure 1-10. Iron Oxide ( $T_2$  relaxation) contrast.

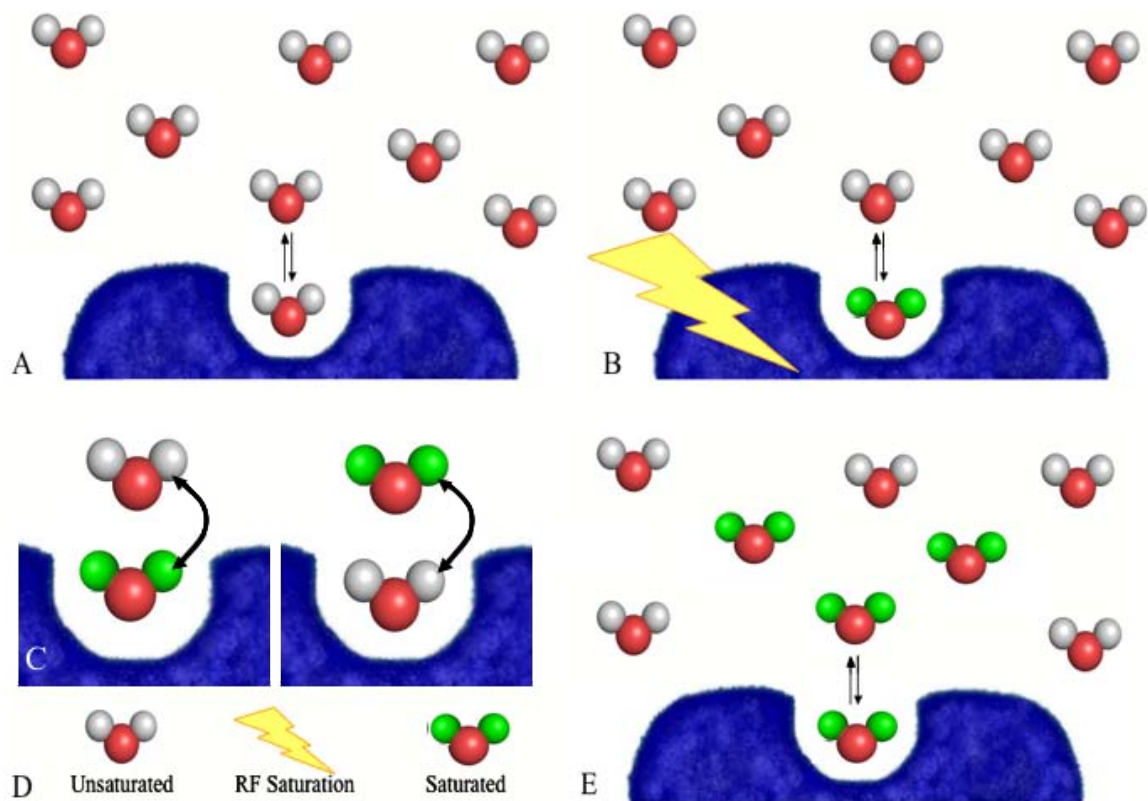


Figure 1-11. Chemical Exchange Saturation Transfer (CEST). A) Unsaturated bulk water protons exchanging with a bound water molecule. B) Once RF saturation is provided, the bound water proton becomes saturated. C) The saturated bound water proton exchanges with an unsaturated bulk water proton. D) Unsaturated, and saturated protons, and RF saturation labeled. E) After some time, the saturation has transferred to multiple bulk water protons.

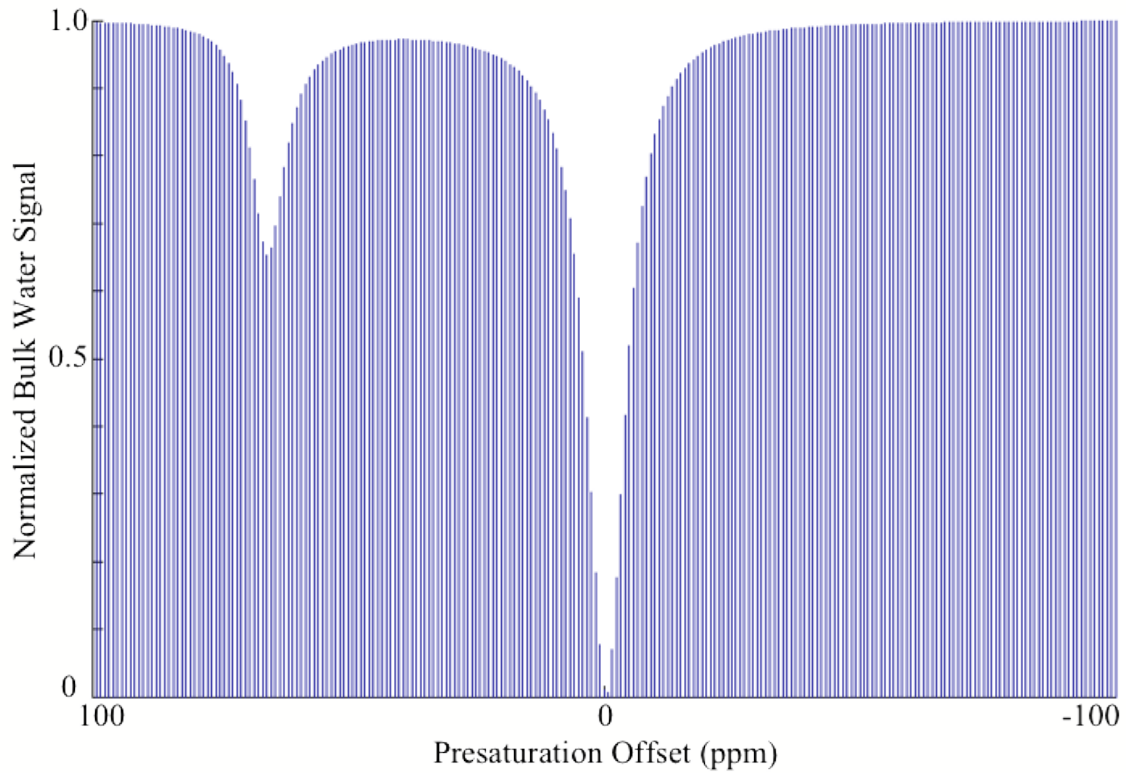


Figure 1-12. Example CEST spectrum. Each line represents the remaining bulk water signal with presaturation supplied at the offset on the x-axes; shown for a complex with the bound water pool located at  $\sim 50$  ppm, illustrated by the dip in the left side of the spectrum. The larger dip at 0 ppm is a result of the direct saturation of water.

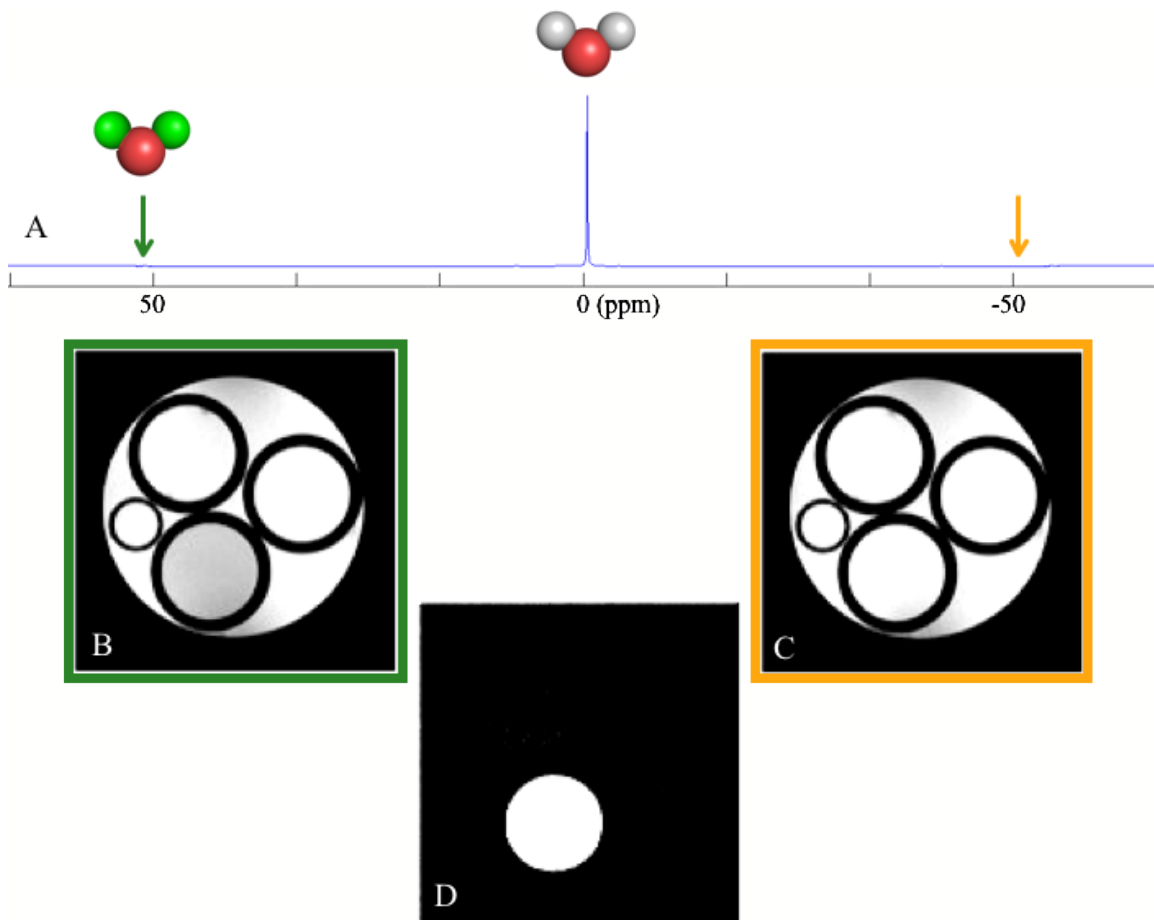


Figure 1-13. PARACEST Imaging. A) Example 1D proton spectra, with location of bulk (unsaturated) water and bound (saturated). B) Example image where RF saturation is supplied at the offset of the bound water protons. C) Example image where RF saturation is supplied at the offset on the opposite side of the bulk water. D) Example difference image showing the resulting contrast.

## CHAPTER 2 METHODS

In order to determine optimal contrast agents for use at high magnetic fields, various agents were tested to determine their contrast generation potential. The contrast agents were made into solutions, and put into phantoms for evaluation at several applied magnetic field strengths ( $B_0$ ). The type of testing varied depending on the type of contrast agent, but included both imaging and spectroscopy. As discussed in the previous chapter, three types of contrast agents were investigated:  $T_1$  relaxation agents, iron oxides and PARACEST agents. Relaxation agents and iron oxides both produce contrast that is dependent on their relaxation effects on water. In these cases, the relaxation parameters were measured done using imaging. For PARACEST agents the contrast is dependent on a presaturation RF pulse and chemical exchange, and can be seen using imaging and spectroscopy. In order to test PARACEST images with presaturation at varied offsets were taken to best illustrate the contrast generation via imaging. Alternatively, CEST spectra were obtained to show the PARACEST contrast as the decrease in bulk water signal. The methods for these procedures are included in the following Chapter.

### **Contrast Agent Preparation**

The chemical agents which were used to produce contrast were obtained from various sources, as detailed below.

#### **Multimodal Quantum Dots**

The Particle Engineering Resource Center at the University of Florida supplied this experiment with the fluorescent gadolinium contrast agent. Gadolinium functionalized quantum dots (Gd Qdots, Figure 2-1) were fabricated by as previously described by synthesizing water-soluble silica-coated ZnS-passivated CdS:Mn (CdS:Mn/ZnS/SiO<sub>2</sub> core/shell/shell) fluorescent

Qdots [85]. After aqueous stabilization, the Qdots were functionalized by adding n-(trimethoxysilylpropyl) ethyldiamine, triacetic acid trisodium salt (TSPETE) and Gd (III) acetate. Dysprosium quantum dots were fabricated in a similar manner.

### **PARACEST Agents**

Three europium (Figure 2-2), two ytterbium (Figure 2-3 A and B) and two thulium (Figure 2-3 C and D) PARACEST agents were investigated in this study. All PARACEST Agents were obtained from A. Dean Sherry (Department of Chemistry and Biochemistry, University of Texas, Dallas, TX) or purchased from Macrocyclics (2110 Research Row, Suite 425, Dallas, TX 75235 [www.macrocyclics.com](http://www.macrocyclics.com)).

### **Iron Oxides**

Ferumoxide ( $\text{FeO}_{1.44}$ ) was used as a representative dextran coated superparamagnetic iron oxide for this study. Specifically, Feridex® is manufactured by Bayer Healthcare Pharmaceuticals.

### **Phantom Preparation**

A phantom for MR imaging refers to an inanimate object which can be imaged. Phantoms can be used for many purposes, including testing the performance of an imaging system before imaging a living organism. Phantoms can also be used to image a specific type of tissue or chemical compound to optimize the imaging parameters. Phantoms were used to evaluate several chemical compounds for their efficacy as contrast agents. For this study phantom refers to a container consisting of a larger tube filled with liquid (usually water) containing several smaller tubes filled with different liquids (usually a contrast agent). Generally, a phantom was created by filling capillary tubes with different contrast agents, and closing off the capillary tubes with clay. The capillary tubes were put into the larger tube, and then the large tube was filled with double deionized water ( $\text{ddH}_2\text{O}$ ), and the large tube is closed with a plastic cap.

The Gd QDots were obtained already in solution of given concentrations. These solutions were often not entirely soluble, and therefore precipitated out of solution if left sitting for some time. The time for precipitation was dependent on the batch, but ranged from ten minutes to several hours. In order to avoid precipitation during an imaging experiment, the Gd QDots were suspended in agarose for imaging. A 2% agarose solution was prepared by mixing 0.50 mg of analytical grade agarose in 25 mL of ddH<sub>2</sub>O. This solution was microwaved on high, and swirled often, until the agarose completely dissolved. This agarose solution solidified when allowed to come to room temperature. Phantoms of Gd QDots were prepared by mixing equal parts aqueous Gd QDot solution with 2% agarose. The resulting solution (which was half the concentration of the original solution) was quickly transferred into capillary tubes and allowed to harden. Phantoms of PBS buffer, dysprosium quantum dots, and dysprosium DTPA were prepared in a similar manner. The tubes were capped and labeled.

The ferumoxide was obtained in solution, and was completely soluble. Because precipitation was not a concern, the ferumoxide was diluted by adding 900  $\mu$ L ddH<sub>2</sub>O with 100  $\mu$ L of the original solution, for a 1:10 dilution. This solution was then used for additional dilutions by taking 100  $\mu$ L aliquots of the 1:10 dilution and adding 100, 400 and 900  $\mu$ L of ddH<sub>2</sub>O for resulting 1:20, 1:50 and 1:100 solutions. These dilutions were then transferred to capillary tubes, capped and labeled.

The PARACEST agents were obtained as solid lanthanide ion complexes (powders) with their formula weights listed. These complexes have been shown to be extremely kinetically inert, even at very acidic conditions [86], so were assumed to be stable in solution. The solutions were created by dissolving the powder in ddH<sub>2</sub>O. The desired concentration of these solutions was obtained by weighing the appropriate amount of powder according to the formula weight of the

complex, in accordance to Equation 2-1. For example, Eu-2 has a formula weight of 890.94 g/mol. For 1mL of 10 mM solution of Eu-2:

$$\overbrace{\left(10 \times \frac{10^{-3} \text{ mol}}{L}\right)}^{\text{DesiredConcentration}} \times \overbrace{\left(890.94 \frac{\text{g}}{\text{mol}}\right)}^{\text{FormulaWeight}} \times \overbrace{\left(1 \times 10^{-3} L\right)}^{\text{VolumeWater}} = 0.0089094 \text{ g} = 89.1 \text{ mg} \quad (2-1)$$

In order to get 1 mL of 10 mM Eu-2, 89.1 mg of the solid Eu-2 powder was dissolved in 1 mL of ddH<sub>2</sub>O. Solutions of varied concentrations, or different lanthanide ion complexes were created in a similar manner using the desired concentration and formula weight for each. After the desired concentration solution was prepared, the pH was measured and noted.

In some cases, the pH was altered using small volumes of 10 – 100 mM KOH or HCl to respectively increase or decrease the pH. The dilutions phantom for investigation of concentration dependance was created by first making a 200 μL of 100 mM Eu-2 solution. Serial dilutions were prepared by taking 100 μL of the original solution, and diluting with 100 μL of ddH<sub>2</sub>O (resulting in 200 μL of 50 mM Eu-2 solution). This process was repeated to obtain concentrations of 100, 50, 25, 13, 6, 3, 1.5, 0.8 and 0.4 mM. One phantom was made using 1% agarose to test the viability of contrast generation in an environment with less free movement of water.

To complete the phantom, the capillary tubes were inserted into a larger NMR tube. The large tube was then filled with ddH<sub>2</sub>O, for multiple reasons including stabilizing the capillary tubes, avoiding imaging artifacts which would result from air, and to use as a comparison for contrast generation.

### **Magnetic Resonance Imaging and Spectroscopy**

The imaging and spectroscopy for this study were done at the National High Magnetic Field Laboratory (NHMFL), in Tallahassee or at the Advanced Magnetic Resonance Imaging

and Spectroscopy (AMRIS) at the McKnight Brain Institute at the University of Florida. The 4.7, 11, 14.1 and 17.6 T magnets are located in the AMRIS facility, and the 21.1 T magnet is located in the NHMFL Tallahassee. All systems have Bruker software, including different versions of Paravision (for imaging) and xwinnmr or topsin for spectroscopy. The procedure for operation varies slightly between magnets, and software versions. This method section outlines the basic procedure for the imaging and spectroscopy completed in this study.

### **Set Up**

For all experiments, the set up was the same; the phantom was first centered in the coil (for the 4.7, 11, 17.6 and 21.1 T magnets) or placed in the spinner with the sample in the desired region (for the 14.1 T magnet). For the 4.7 and 11 T magnet, the sample was tuned using a network analyzer and then placed in the magnet. A position scan was run to ensure that the sample was in the center of the magnet. The phantom in the spinner was dropped (slowly via air pressure) into the center of the 14.1 T magnet. For the 17.6 and 21.1 T magnets, the probe with the sample centered in the attached coil was placed into the magnet. For the 14.1, 17.6 and 21.1 T magnets, the sample was tuned once in the magnet.

Once the sample was in the center of the magnet and tuned, the shimming was completed. This was done either automatically, using the Paravision autoshim tool, or manually using xwin/topspin. After shimming, the basic frequency was set in Paravision. For imaging, the 90 degree pulse power was calibrated using the onepulse or singlepulse sequence (which uses an RF pulse to obtain 1D data). This was completed by determining the attenuator power required to maximize the signal, and then altering the gain to set the digitizer filling between 60 and 80%. For spectroscopy, the power level was set (usually 0-6 dB) and the duration of the pulse was varied using a Bruker sequence which repeats a pulse sequence keeping all but one variable constant (paropt). The duration of the power pulse was determined as the 90 degree pulse, where

the signal should be a maximum, but was also calculated as half of the pulse length when the signal was 0 (the 180 degree point). For imaging, a tripilot scan (which results in three 2D images in each of three orthogonal axes *i.e.* x,y and z) was run to ensure correct sample placement, and to set up the geometry for the remainder of the images. An axial image slice was selected from the tripilot, in a homogenous region with no artifacts from air bubbles or contaminants. The axial slice dimensions fit the largest of the phantom tube; for a 5 mm NMR tube, the field of view was set to 5 mm by 5 mm.

After the preceding set up procedure, individual imaging and spectroscopy experiments were performed depending on the type of contrast agent.

### **Relaxation Parameters**

Phantoms were imaged at magnetic field strengths of 4.7, 11.1, 17.6 and 21.1 T using spin-echo and gradient-recall echo sequences that quantify  $T_1$ ,  $T_2$  &  $T_2^*$  relaxation by varying either the repetition time ( $T_R$ ) or the echo time ( $T_E$ ).

In order to calculate the  $T_1$  relaxation time, a variable repetition time (VTR) or progressive saturation experiment was performed in which the repetition time was varied from 10s to the lowest repetition time allowable with eight intermediate time points (*ex*  $T_R = 10$  s, 6 s, 3 s, 1.5 s, 750 ms, 500 ms, 250 ms, 125 ms, 75 ms, and 50 ms). Each  $T_R$  resulted in one image which was used to calculate the  $T_1$ . This calculation was performed using Paravision software, through Image Sequence Analysis (ISA) in the Image Display Tool. The region of interest tool (ROI) was used to create circular regions of interest drawn large enough to encompass the area of the contrast while excluding the NMR tube. Within the ROI tool, "calculate" was chosen, and the average signal intensity for each  $T_R$  image was determined by the program. Using the ISA tool, the ISA fit function was set to 't1 vtr', and the program fit the ROI values to Equation 2-2.

$$M_z(t) = M_{z,eq} - [M_{z,eq} - M_z(0)]e^{-(T_R/T_1)} \quad (2-2)$$

The net magnetization along the z axis is given by  $M_z$  and is a function of time (t). At thermal equilibrium the net z magnetization is  $M_{z,eq}$ .

In order to calculate the  $T_2$  relaxation time, a multi-slice-multi-echo (msme)  $T_2$  experiment was performed, in which the  $T_R$  was held constant (5 s), and an echo image was taken at each echo  $T_E$ . The number of echo images was input as a sequence parameter, and the  $T_2$  calculation was performed as above. ROIs were created and calculated, the ISA fit function was 't2', and the ROI values were fit to Equation 2-3.

$$M_{xy}(t) = M_{xy}(0)e^{-(T_E/T_2)} \quad (2-3)$$

The net magnetization in the xy plane is  $M_{xy}$  and is a function of time (t).

$T_2^*$  relaxation times, were calculated by performing several multiple-slice-multi-echo or fast-low-angle-shot (FLASH) gradient echo images with a constant  $T_R$  (either 400 ms or 2000 s) and varied  $T_E$  (from the minimum value  $\sim 3$  ms to 90 ms). Each echo image was taken from one individual pulse sequence. The images were similarly processed, using the ROI tool in paravision, and the values were fit using Equation 2-3. The difference between measuring  $T_2$  and  $T_2^*$  was that the echo images for  $T_2$  are taken from the same image sequence, one after the other, all within the same  $T_R$ . The  $T_2^*$  images are taken from different sequences, with each echo image being taken in its own  $T_R$ .

### **PARACEST Agents**

Phantoms of the lanthanide ion complexes were imaged magnetic field strengths ranging from 4.7 to 21.1 T using spin-echo, gradient recall echo, and FLASH magnetization transfer (MT) "prepped" sequences. These MT sequences were created from traditional pulse sequences, but the user was set to expert, and under 'preparation', 'magnetization transfer' was set to 'yes'.

Several parameters were varied within the 'MT parameters' including the duration of presaturation, type of saturation pulse, length of pulse, inter pulse delay, number of pulses, and presaturation offset. The presaturation consisted of a 1 ms pulse that was repeated 2000 to 4000 times. The pulse type was either 3-lobe sinc or gaussian pulses, and there was a 10  $\mu$ s inter pulse delay for a total irradiation time of two to four seconds. The offset value for each set of images was varied between 0 and  $\pm$ 500 ppm, and the irradiation power was varied from 1 through 200  $\mu$ T. To maintain a consistent level of RF power deposition, the CEST image was generated from the difference between two images, one with a positive offset value and the other with the negative offset value.

Determining the amount of presaturation power applied in each experiment was not straight forward. Published values were up to 250  $\mu$ T [69], but these values were not obtainable on the systems tested (to avoid arcing and sample heating). Initial studies were done by fully saturating water on resonance, and doubling that power for the rest of the imaging. The value of the presaturation pulse in  $\mu$ T was appropriately set by determining the actual value for the MTC\_pulsegain (in the pulse program under the previously mentioned 'MT parameters'). This resulted in presaturation values of 4 to 128  $\mu$ T.

### **CEST Spectra**

1D  $^1$ H NMR on phantoms that contain only one sample were used to obtain the CEST spectra. 1D spectra were taken using a presaturation pulse over a range of chemical shifts in increments ranging from 1 – 10 ppm dependent on contrast agent. The europium agents have an optimal offset around 50 ppm, therefore 1 – 2 ppm increments were used. The thulium and ytterbium agents have optimal offsets of 250 and 500 ppm respectively, so 10 ppm increments were used. The water peak from each of the 1D spectra was plotted versus the chemical shift of

the presaturation pulse. For phantoms containing multiple samples, a similar CEST spectra were obtained by running sequential magnetization transfer pulse sequences, with the offset of the presaturation pulse varying over a range of chemical shifts by the aforementioned increments. A graph of the percent remaining bulk water signal (in each of the samples) versus offset frequency create the CEST spectra. CEST spectra illustrated two minima when the PARACEST agent demonstrated significant contrast generation; one minima at the resonant water frequency (a zero offset), and one at the optimal CEST frequency.

### Quantification of Contrast

The contrast generated by PARACEST agents was calculated in different ways. When using an imaging approach, the difference images were used to calculate the Contrast to Noise Ratio (CNR). This is a ratio of the Signal to Noise Ratio (SNR) of the contrast sample to the SNR of water. This is calculated with Equations 2-4 and 2-5, with representative images and regions of interest shown in Figure 2-4.

$$SNR = \frac{(I_{sample} - I_{Noise})}{\sigma_{Noise}} \quad (2-4)$$

$$CNR = SNR_{Sample} - SNR_{Water} \quad (2-5)$$

Where  $I$  is the average signal intensity within the region of interest, and  $\sigma$  is the standard deviation of the signal intensity within the noise region.

Contrast was also measured as percent increase or decrease the bulk water signal, in either imaging or spectroscopy. PARACEST contrast is inherently a decrease of signal, thus the percent decrease is calculated with Equation 2-6, and illustrated in Figure 2-5.

$$\%Decrease = \frac{(SNR_{opposite} - SNR_{on})}{SNR_{opposite}} \times 100 \quad (2-6)$$

Where  $SNR_{on}$  is the SNR of the region of interest with the presaturation applied at the offset of the bound water, and  $SNR_{off}$  is the SNR with the presaturation applied on the opposite side of the bulk water peak.

CEST Spectra are generally normalized to the bulk water signal (when the presaturation pulse is applied far away from the bulk and bound water). The y-value on the resulting normalized CEST Spectra can then be used to calculate the percent decrease, also known as the percent CEST effect. Because the CEST Spectra was already normalized, the percent decrease for the Spectra can be calculated from Equation 2-7.

$$\%Decrease_{Spectra} = (1 - NI_M) \times 100 \quad (2-7)$$

Where  $NI_M$  is the minimum normalized intensity at the bound water shift (identified in Figure 2-6).

## Simulations

### Rationale and Design

Computer models provide a method for simulating contrast agent behavior under various conditions. Computer simulations are less expensive and faster than performing each experiment on an MRI instrument. By developing a predictive model for PARACEST contrast, variables such as temperature and pH can be tested for without hours of spectrometer time; and different PARACEST agents can be simulated to determine to contrast behavior.

MATLAB was used to create a program to simulate the Bloch equations modified for chemical exchange. The CESTFIT MATLAB program (Appendix A), created by collaborators (M.E. Merritt, D.E. Woessner, S. Zhang, and A.D. Sherry) at the University of Texas Southwestern Medical Center, Dallas Texas [87], was used for the simulations in this project. This simulation assumes two pools of water protons: those in bulk water, and those bound to the

PARACEST agent. (It can be altered to include 3 pools, with an additional bound pool of protons, ie. bound to an amine group). The water protons bound to the PARACEST agent will be saturated when a presaturation pulse is applied at the chemical shift of the PARACEST agent. The chemical exchange occurs between these two pools and causes saturation transfer from the bound water to the bulk water, which results in a decrease in the bulk water signal. The simulation tracks the remaining bulk water signal as a function of presaturation offset, which should indicate a minimum at the optimal chemical shift offset for the presaturation pulse.

### **CESTFIT**

MATLAB was chosen as the program in which to run the simulation for several reasons. The CESTFIT program [87] was originally written in MATLAB, so it has already been shown to work well within MATLAB. This code was adapted slightly, to fit the desired data. CEST spectra were obtained in the previously discussed method, and then processed in MATLAB. The CEST spectra were loaded into MATLAB, and then the area under each peak was calculated. The resulting single point spectra (versus peak spectra) were then fit to the Modified Bloch Equations using the CESTFIT program. Input variables were altered until the simulations fit (via an unconstrained nonlinear minimization (Nelder-Mead) program included in the MATLAB software) the data to  $R^2$  values of .95 to .99.

### **Cell Labeling**

As a step towards molecular imaging, direct cell labeling with contrast was investigated. Mouse monocyte/macrophage J774 cells were chosen because of their ability to uptake exogenous compounds and maintain viability [88]. The cells were defrosted, washed with and then resuspended in a supplemented medium (SM).

The SM was made by mixing 450 mL Dulbecco's modified Eagle's medium (DMEM)(GIBCO, Grand Island, NY), 50 mL fetal bovine serum (FBS)(Summit Biotechnology,

Ft. Collins, CO), 5 mL glutamex (GIBCO), and 5 mL penicillin/streptomycin (GIBCO). After mixing, the SM was filtered through a millipore sterile cup and refrigerated before use.

The defrosting was completed by thawing a vial of J774 cells, adding 0.5 mL SM to thawed cells, and transferring all resulting liquid to a 10 mL conical centrifuge tube. The original vial was rinsed with 1 mL SM, and the contents added to the 10 mL tube. The 10 mL tube was then filled with SM for a total volume of 10 mL.

Washing was completed by spinning down (1100 rpm for 5 min) the 10 mL tube, and decanting off the liquid, leaving the cell pellet in the bottom of the tube. The cell pellet was resuspended in 10 mL of fresh SM, and then all liquid was transferred to a 50 mL tube. This tube was then filled with SM for a total volume of 30 mL.

Each of three large cell culture plates was then seeded with 10 mL of the washed cell containing liquid. The plates were then placed in an incubator. The media was replaced (by aspirating the old media and dead cells, and then replacing with fresh SM) 24h after initial plating, and the cells were allowed to attach and grow to confluency (usually 2-3 days). After confluency, the cells were split into new plates.

Replating was completed by manually detaching the cells from the bottom of the plate (by scraping). The resulting media/cell mixture was transferred to a 10 mL tube, and washed with SM as above. Cells were counted by first creating a 1:10 dilution (with 100  $\mu$ L of cell solution, 500  $\mu$ L phosphate buffer solution, and 400  $\mu$ L trypan blue stain). Ten  $\mu$ L of this dilution were transferred to a counting slide, the number of cells in each of 4 quadrants were counted. This number was used to calculate the number of cells through Equation 2-8.

$$N_{cell} = \frac{C_{cell}}{\underbrace{4}_{\#of\text{squares}}} \times 10^5 \times V_T \quad (2-8)$$

where  $N_{\text{cell}}$  is the total number of cells,  $C_{\text{cell}}$  is the cell count from above, and  $V_T$  is the total volume prior to dilution. The  $10^5$  factor takes into account the dilution and the volume fraction. The total number of cells was then used to determine the final volume, which was adjusted (by adding fresh SM) to achieve a specific concentration of approximately  $2 \times 10^5$  cells/mL. Ten mL aliquots of the  $2 \times 10^5$  cells/mL solution was pipetted onto fresh cell culture plates.

The first PARACEST labeling solution was made by adding enough Eu-2 to SM for a resulting 40mM solution [69]. For a 1 mL solution, this was done by adding 35.6 mg of Eu-2 to 1 mL SM. The second labeling solution was created by mixing 35.6 mg of Eu-2 with 100  $\mu$ L of SM, and bringing the pH of that solution to  $\sim 7$  before adding the additional 900  $\mu$ L of SM for a final volume of 1 mL and concentration of 40 mM.

After a small cell plate reached 70-80% confluency, cell labeling was completed by first aspirating the old media and dead cells and then adding 1 mL of the labeling solution. The cells were allowed to incubate in the labeling solution over night (12-14 hours), after this time the labeling media was aspirated off of the cells, and replaced with fresh SM. The cells were washed and counted as above.

After washing, the cells were spun down one final time, and resuspended in a small amount ( $\sim 200 - 400 \mu$ L) of 1% agarose for phantom preparation and imaging (as above).

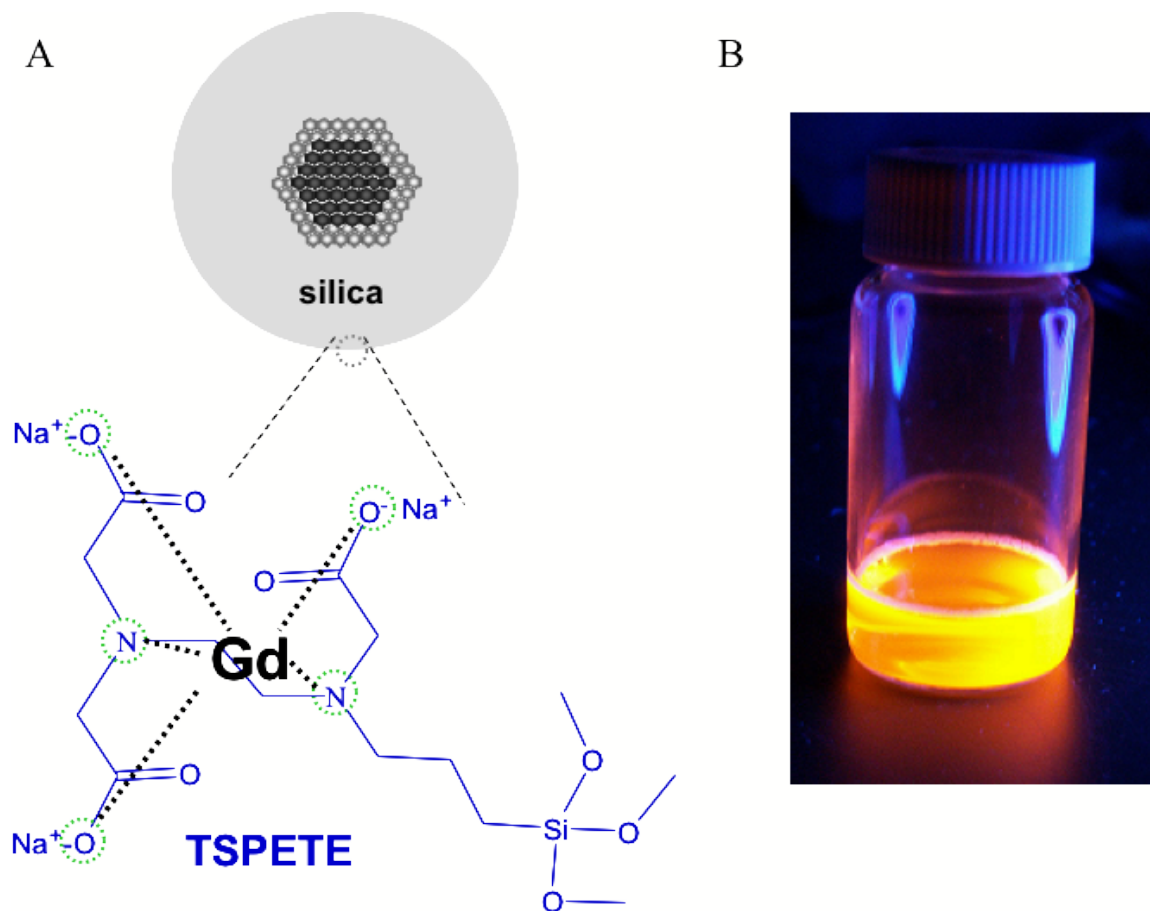


Figure 2-1. Multimodal Gadolinium Quantum Dots. A) Schematic representation. B) Image of sample of quantum dots under UV light (360nm), showing yellow fluorescence (590nm).

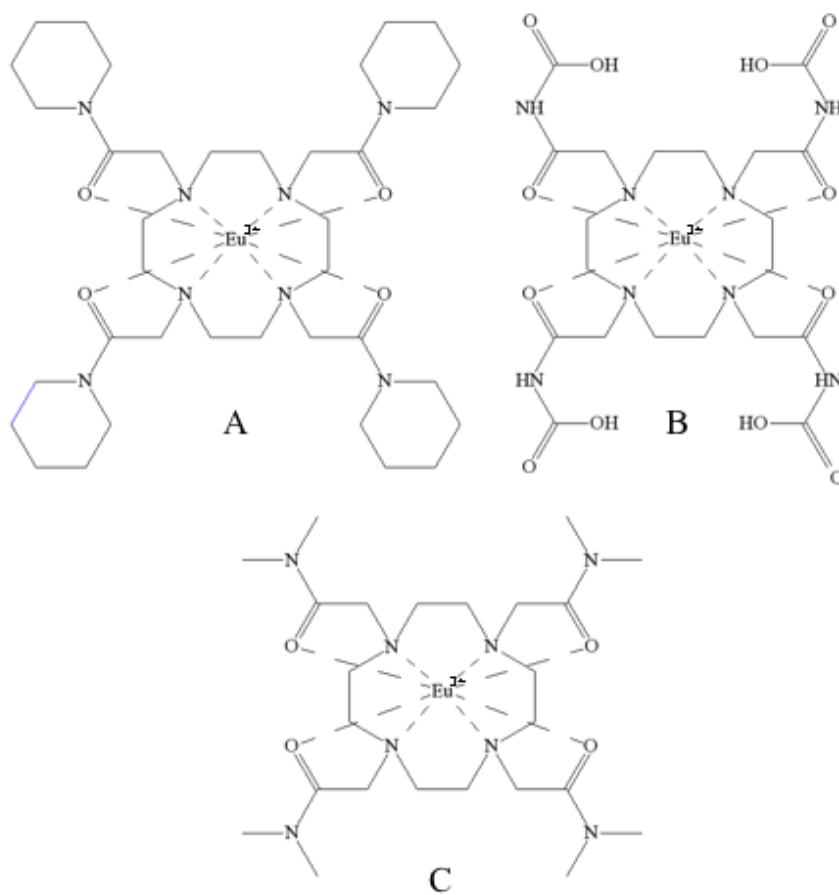


Figure 2-2. Chemical Structures of three europium Complexes. A)  $\text{C}_{34}\text{H}_{44}\text{Cl}_3\text{EuN}_8\text{O}_4$  Mol. Wt.: 931.27 g/mol. Referred to as Eu-1. B)  $\text{C}_{24}\text{H}_{40}\text{Cl}_3\text{EuN}_8\text{O}_{12}$  Mol. Wt.: 890.94g/mol. Referred to as Eu-2. C)  $\text{C}_{24}\text{H}_{48}\text{Cl}_3\text{EuN}_8\text{O}_4$  Mol. Wt.: 771.01g/mol. Referred to as Eu-3.

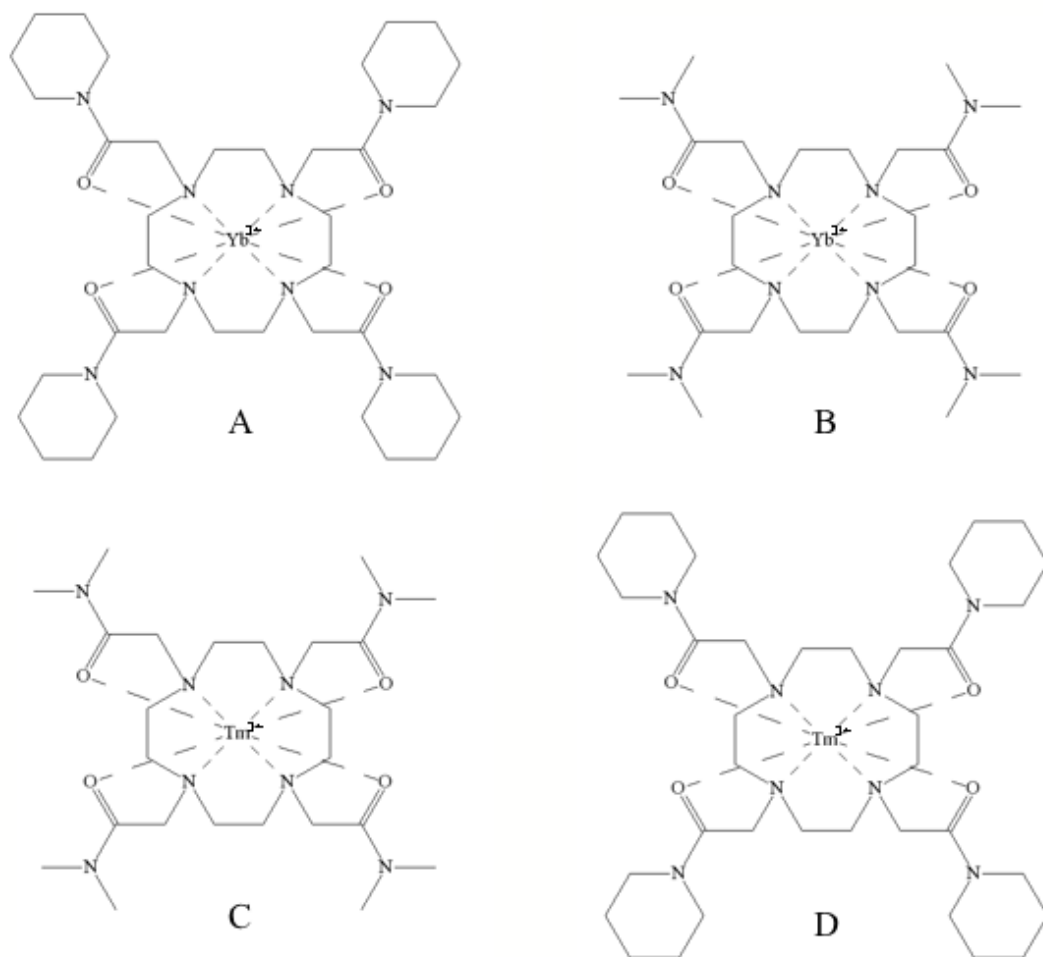


Figure 2-3. Chemical structures of the thulium and ytterbium complexes. A)  $C_{36}H_{64}YbN_8O_4$  Mol. Wt.: 952.34g/mol. Referred to as Yb-1. B)  $C_{24}H_{48}YbN_8O_4$  Mol. Wt.: 792.09g/mol. Referred to as Yb-2. C)  $C_{24}H_{48}TmN_8O_4$  Mol. Wt.: 787.98g/mol. Referred to as Tm-1. D)  $C_{36}H_{64}TmN_8O_4$  Mol. Wt.: 948.24g/mol. Referred to as Tm-2.

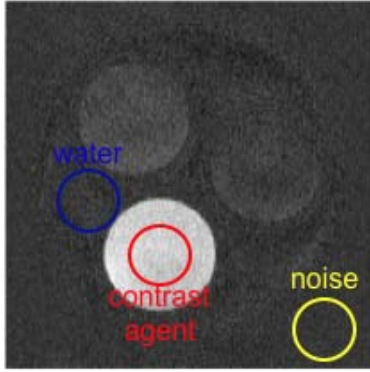


Figure 2-4. Contrast to Noise Ratio (CNR) calculation region of interest diagram. The difference image is shown with the water, contrast agent and noise regions indicated.

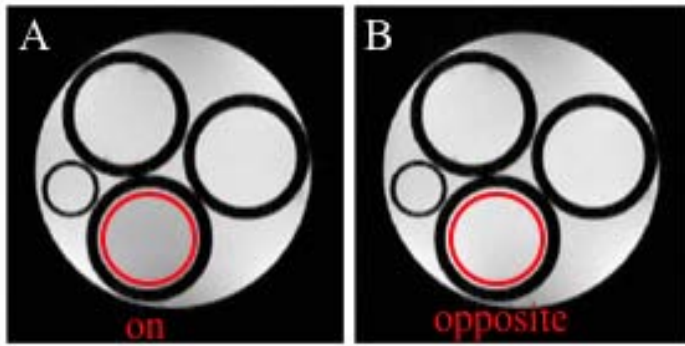


Figure 2-5. Percent Decrease (%Decrease) calculation region of interest diagram for Eu-2. A) The ROI for  $SNR_{on}$ , taken from the image at +53ppm. B) The ROI for  $SNR_{opposite}$  taken from the image at -53ppm.

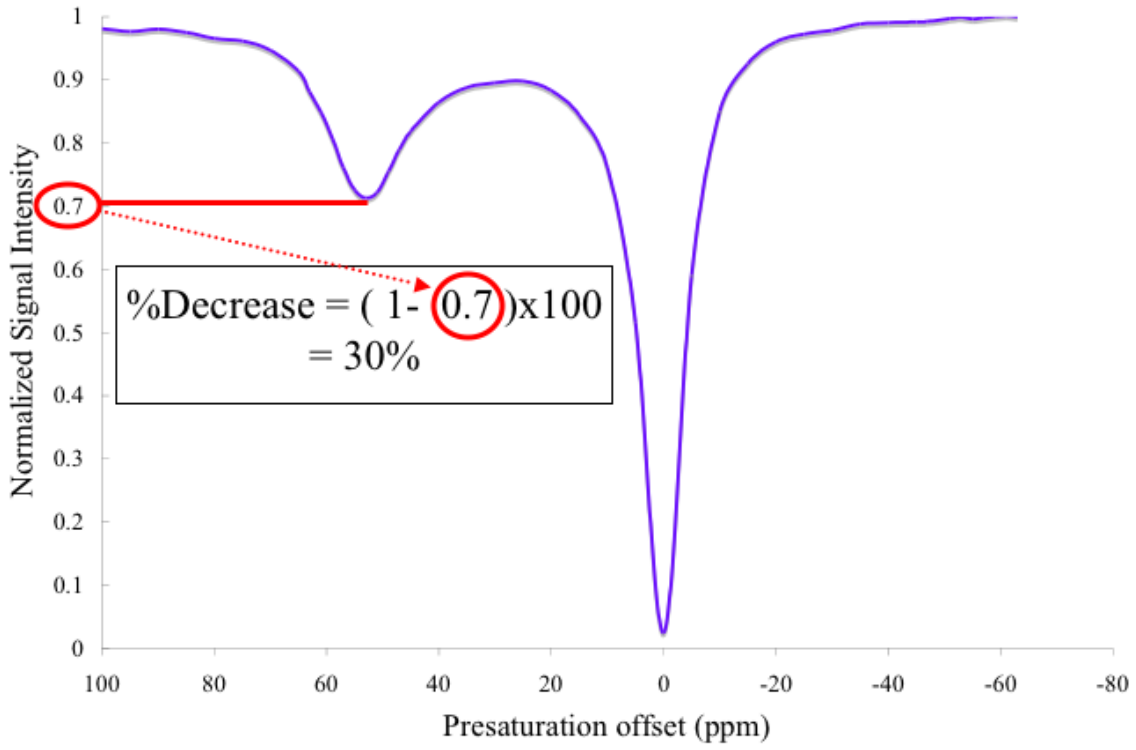


Figure 2-6. Example CEST spectra, with the %Decrease calculation shown.

## CHAPTER 3 RESULTS

### Relaxation Agents

#### Multimodal Quantum Dots

Gadolinium based contrast agents have been shown to cause favorable changes in relaxation properties [47] and the overwhelming majority of contrast enhanced clinical exams are performed with gadolinium complexes [56]. They are therefore a logical starting point for contrast agent investigation at high magnetic fields. Covalently attaching Gd-capturing ligands to CdS:Mn/ZnS quantum dots, should result in a multimodal contrast agent that produces strong MRI contrast and optical activity from the paramagnetic Gd-chelate conjugated quantum dots. In order to evaluate contrast potential as a function of field strength, the relaxation times were measured for Gd quantum dots, dysprosium chelate conjugated quantum dots and a dysprosium standard (Dy-DTPA-BME) at 4.7, 11.1, 17.6 and 21.1 T.

Spin-lattice relaxation times ( $T_1$ ) for all three agents are shown in Figure 3-1. The  $T_1$  relaxation times for both the dysprosium quantum dot and standard decrease with field strength, but increase for the gadolinium quantum dot. Spin-spin relaxation times ( $T_2$  and  $T_2^*$ ) for the agents are shown in Figure 3-2 and 3-3 respectively.  $T_2$  times remain approximately the same for quantum dots, but decrease slightly for the dysprosium standard. The  $T_2^*$  times remain approximately the same for the dysprosium quantum dots, but decrease with field strength for the gadolinium quantum dots and the dysprosium standard.

#### Iron Oxides

Iron oxides have also been shown to induce sizeable changes in relaxation properties [62,65,89]. The true  $T_2$  relaxation values are independent of field strength above 0.5 T [90,91] and were therefore not investigated. Similarly, the strong effect of iron oxides on

$T_2$  negates the need to evaluate  $T_1$  and results in the elimination of signal (negative contrast). The  $T_2^*$  values were measured (Figure 3-4) at 14.1 and 21.1 T. The data collected and used to calculate the  $T_2^*$  values are included in Appendix A.

## **PARACEST Agents**

### **Multiple Lanthanide Ion Complexes**

Three europium (Figure 2-2), two ytterbium and two thulium (Figure 2-3) PARACEST agents were investigated in this study. One europium complex (Eu-2) has previously been shown to generate contrast at lower field strengths [68,69], and therefore was expected to yield similar (if not better) results at higher field strengths. Thulium and Ytterbium were not useful as PARACEST contrast agents at lower field strengths, but were predicted to reach the slow-to-intermediate exchange requirement (Eqn 1-5) at higher field strengths [50].

Significant contrast was generated for all three europium compounds at different offsets for field strengths equal or greater than 14.1 T. Figure 3-5 shows this effect at 17.6 T. With RF presaturation applied at 53ppm, Eu-2 generates enough contrast to visibly identify in the presaturated image (Figure 3-5 A). However, the difference images (Figure 3-5 C and D) further elucidate this contrast. Eu-3 also demonstrates significant contrast at both 65 and 68 ppm, but this is best seen in the difference images. Eu-1 generates the least contrast of the europium complexes, but the difference images show a visible difference between the surrounding water and the Eu-1 tube at 68ppm. Contrast to noise measurements indicate CNR values of 8, 54, and 35 were calculated for Eu-1, Eu-2 and Eu-3 respectively at 17.6 T. Additional images are included in Appendix B.

The ytterbium and thulium compounds were tested at lower magnetic field strengths (14.1 and 17.6 T) without any significant contrast generation, sample images are included in Appendix B. These four compounds were imaged also at 21.1 T, and the results are shown in

Figures 4-5 (thulium) and 4-6 (ytterbium). Eu-2 was included in both phantoms as a positive control, to ensure the presaturation pulse was strong enough to elicit contrast. Both thulium complexes had the greatest contrast generation with a presaturation applied at 520 ppm. Both Tm-1 and Tm-2 (Figure 3-6 C) are visibly distinguishable from the surrounding bulk water (where the noise is not), but the contrast generation is not significant. The two ytterbium complexes had different optimal offsets, with Yb-1 generating the most contrast at 225 ppm, and Yb-2 at 210 ppm. As with the thulium complexes, the ytterbium complexes are visibly distinguishable from water (Yb-1 in Figure 3-7 D and Yb-2 in 3-7 C) but again without significant contrast generation.

### **Field Strength**

As previously mentioned, PARACEST contrast is predicted to increase with field strength. The results indicate an increase in contrast generation for all three Eu complexes with increased magnetic field strength (Figure 3-8). There was significant increased contrast between 4.7 and 17.6 T, and an additional increase at 21.1 T. The difference images at 17.6 and 21.1 T display the tunable contrast enhancement related to the PARACEST agent and saturation offset (Figure 3-9). The optimal offsets for each agent varied slightly; they were ~65 to ~53 to ~67 ppm for Eu-1, Eu-2, and Eu-3 respectively. The CEST spectra also illustrate the increase in CEST effect with field strength for 11.75 T (Figure 3-10-A), 17.6 T (Figure 3-10-B) and 21.1 T (Figure 3-10-C). This effect is highlighted by comparing the CEST spectra for Eu-2 at all field strengths (Figure 3-10-D). Additional images for the field dependence results are included in Appendix B.

### **Concentration**

Eu-2 was shown to have the greatest contrast generation potential, at all tested field strengths, so it was chosen for further studies. The concentration was serially diluted from 100 mM to 0.4 mM, and each dilution was included in the concentration phantom (Figure 3-11). The

contrast generated was dependent on the power supplied by the RF saturation pulse. At the high concentrations, low power (8  $\mu$ T) was needed to generate contrast (Figure 3-12). With higher power (128  $\mu$ T), even the low concentrations were able to generate significant contrast (Figure 3-13). The CNR for each concentration was calculated from difference images with 128  $\mu$ T and indicates an increase in contrast generation with concentration (Figure 3-14). The CEST spectra (Figure 3-15) also show increased CEST effect (shown as the decrease in the normalized bulk water signal at the offset of the bound water protons) with increasing concentration, agreeing with the imaging results. Additional images for the concentration results are included in Appendix B.

## **pH**

Because PARACEST is a chemical exchange dependent phenomenon, it is sensitive to both pH and temperature. Ten mM solutions of Eu-2 at different pHs were tested to verify the viability of contrast generation in different environments. A solution containing labeling media was also tested to see if there was any effect on the contrast due to the presence of ions in the media (which would then be likely in the cells) or the possible restriction of water movement by the agarose.

The first pH phantom (Figure 3-16) included a solution at pH 3, a solution at pH 7, and a solution of 50 % ddH<sub>2</sub>O and 50 % supplemented cell labeling media (SM; Chapter 2.5) at pH 7. This phantom was imaged for verification of contrast generation for different two pHs as well as an ionically rich environment. At a presaturation offset of +56 ppm at 17.6 T the image shows a significant decrease in signal for all three tubes compared to the surrounding water (Figure 3-17 A). The difference image further demonstrates the contrast generation, but also shows that the contrast is greater in the pH 7 solutions than the solution with a pH of 3 (Figure 3-17 C). The

difference images for +/- 53, 56 and 59 ppm were corrected (in MATLAB) to represent CNR maps (Figure 3-18). These corrected difference images demonstrate that all three solutions were able to generate contrast at all three offsets. These images also show that there is a shift of the optimal offset with pH. The Eu-2 at a pH of 3 has the greatest contrast generation at the offset of 53ppm, while both solutions at pH of 7 generate more contrast at 56ppm.

The second pH phantoms tests a larger range of pHs (from 3 – 13), and the difference images taken at 14.1T indicate contrast generation potential for pH 3, 7, and 10, but not 13 (Figure 3-19). These images similarly demonstrate a shift in the optimal offset, but also show that the pH of 10 has a lower overall potential than 3 or 7 (which both have comparable maximum CNR values). This was further investigated by generating a CEST spectrum. The close up of the 71-51 ppm region of the CEST spectrum shows that the minima of both pH 3 and pH 7 are approximately equal and result in a 45% decrease in signal (Figure 3-20). The sample with pH 10 does not have as distinct a dip as the pH 3 or 7 sample, but has a 5% decrease in signal compared to water. The pH of 13 sample is essentially indistinguishable from water at all points.

This pH sample was also tested at 17.6 T, and the results agree with the 14.1 T data. A comparison of the two field strengths show contrast generation for pH 3, 7 and 10, and a similar shift in maximum contrast potential and offset with pH (Figure 3-21). Both field strengths show no contrast generation for the pH 13 sample. Additional images for the pH results are included in Appendix B.

### **Temperature**

CEST spectra were taken for a 10 mM sample of Eu-2 at 14, 20, 26, 32 and 38 °C and the results are shown in Figure 3-22. The close up of the region from 35 to 75 ppm clearly show the

shift in the spectra with temperature (Figure 3-22 B). The warmer temperatures cause the exchange to speed up, which causes the dip to broaden and shift towards bulk water. Conversely, the colder temperatures cause the dip to sharpen and shift away from the bulk water. Individual spectra for the temperature results are included in Appendix B.

### **Effect of Signal to Noise**

Increasing the number of acquisitions should increase the signal to noise ratio as the square root of number of scans [44]. To test the effect of this increase on the CEST effect, the CEST spectra was taken for a 10 mM sample of Eu-2 with 1, 2, 4, 8, 32 and 64 scans and are shown in Figure 3-23. The close up of the region from 50 to 59 ppm shows an increase in CEST effect with increase in scans. Imaging experiments yielded similar results, showing an increased CNR with increasing number of acquisitions (Figure 3-24). Individual spectra for the multiple acquisition results are included in Appendix B.

### **Presaturation Power and Duration**

Both the power and the duration of the presaturation pulse affect the amount of contrast generation. The power was tested by imaging the same (serial dilutions) phantom at 14.1 T and varying the power from 8 to 128  $\mu$ T. The difference image from the +/- 53 ppm images show the change in contrast (Figure 3-25) and the CNR calculations indicate a nonlinear relationship between the power of the RF saturation pulse and the resulting contrast (Figure 3-26).

The duration of the presaturation for imaging was 2 s, because previous studies had published good contrast generation with that presaturation time [68,69]. The saturation time consisted of a loop of 1 ms pulses (2000 for the 2 s presaturation). The number of 1 ms pulses was tested at 14.1 T by monitoring the bulk water signal as a function of number of presaturation pulses applied at 53 ppm at 26 °C. The results show a decrease in bulk water signal with the

increase in number of presaturation pulses (Figure 3-27). The exponential increase in saturation can be used to determine the apparent exchange [92]. Additional temperatures were measured and show similar results. These and additional results are included in Appendix B.

### **Cell Labeling**

The first cell labeling solution was not pH balanced prior to cell labeling which resulted in total cell death. The second solution was balanced to a pH of 7, and was not toxic to the cells. The labeled cells were imaged at 17.6 T, and the results in the offsets of interest are shown in Figure 3-28. No viable contrast was generated. Additional images are included in Appendix B.

### **Simulation**

The CESTFIT [87] program uses the modified Bloch equations (Appendix C) to simulate the CEST effect. This program was adapted to simulate the effect of several variables, including field strength,  $T_1$  relaxation times, chemical shift difference and concentration. It was also used to fit variable temperature data. The MATLAB code which was used to create the following figures is included in Appendix C, and is summarized in Appendix C. The code for each specific simulation is included in the remaining sections of Appendix C.

### **Relaxation Times**

The effect of both the  $T_1$  and  $T_2$  relaxation times were simulated (Figures 3-29 and 3-30 respectively). The MATLAB code is included in Appendix C. Increasing  $T_1$  causes an increase in the CEST effect, but also increases the apparent direct saturation of water. Increasing  $T_2$  has no apparent effect on the CEST effect, but shows a broadening in the saturation around bulk water.

### **Chemical Shift Difference**

The effect of altering the chemical shift difference between bound and bulk water was simulated (Figure 3-31). The MATLAB code is included in Appendix C. Increasing  $\Delta\omega$

resulted in an increase in the distance between the two inverse peaks, but no apparent effect on the amount of CEST.

### **Chemical Exchange Rates**

To simulate the behavior of different PARACEST compounds, the chemical exchange rates were varied (by varying  $C_b$  the transition rate of the spins leaving bound water, also the inverse of the lifetime of a proton in the bound pool  $\tau_M$ .) The results of the simulation (Figure 3-32) indicate an optimum chemical exchange rate within a given set of variables (concentration, field strength, presat power,  $T_1$ ,  $T_2$  and chemical shift difference). The MATLAB code is included in Appendix C.

### **Presaturation Power**

The effect of increasing presaturation power was simulated (Figure 3-33). The MATLAB code is included in Appendix C. Increasing power resulted in an increase in CEST effect, but also resulted in a broadening of the saturation around bulk water.

### **Concentration**

The concentration varied by increasing the ratio of bulk to bound water protons ( $M_0^{\text{bulk}}$  and  $M_0^{\text{bound}}$ ).  $M_0^{\text{bulk}}$  was set to one and  $M_0^{\text{bound}}$  was incrementally increased from 0.0001 to 0.001. The results of the simulation are shown in Figure 3-34 and the MATLAB code is included in Appendix C. Increasing concentration resulted in an increased CEST effect.

### **Temperature Fit**

The modified CESTFIT simulation shows the agreement between the variable temperature data and the fit, for 14, 20, 26, 32 and 38 °C, with  $R^2$  values of 0.994, 0.993, 0.991, 0.997 and 0.998 respectively (Figure 3-35). The  $T_1$  relaxation times (Table 3-1) were measured via inversion recovery, and these values were used in the fit. MATLAB code and the individual temperature/fit plots are included in Appendix C.

### **Number of Acquisitions Fit**

The modified CESTFIT simulation shows the agreement between the variable data and the fit for spectra taken with 1, 2, 4, 8, 32 and 64 scans, with  $R^2$  values of 0.994, 0.989, 0.990, 0.991, 0.985 and 0.989 respectively (Figure 3-36). All spectra were obtained at 26 °C. There is an increase in the CEST effect with increased number of acquisitions. MATLAB code and the individual spectra/fit plots are included in Appendix C.

The discussion and conclusions of these results are presented in the next chapter.

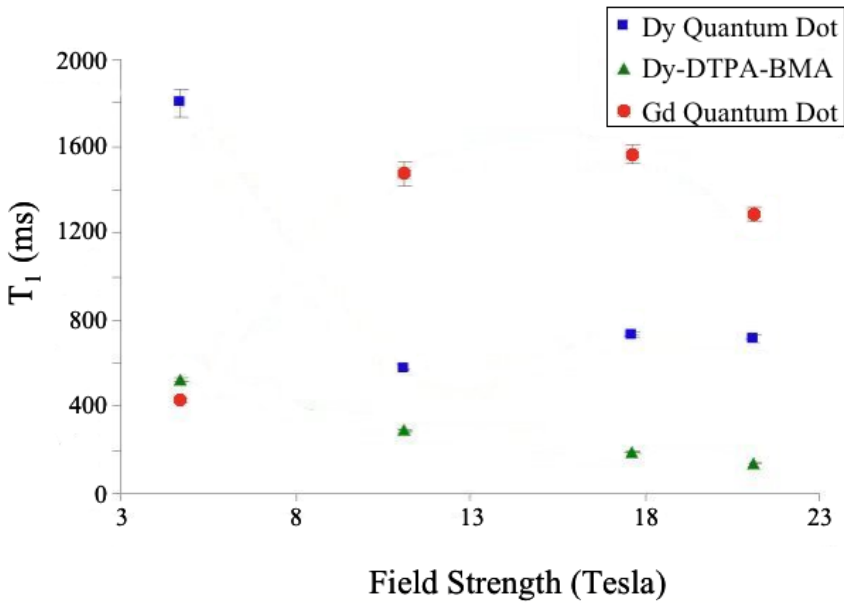


Figure 3-1. Quantum Dot  $T_1$  relaxation times. The  $T_1$  relaxation of gadolinium quantum dots (red), dysprosium quantum dots (blue), and Dy-DTPA-BMA (green) shown at magnetic field strengths of 4.7, 11.1, 17.6 and 21.1 Tesla.

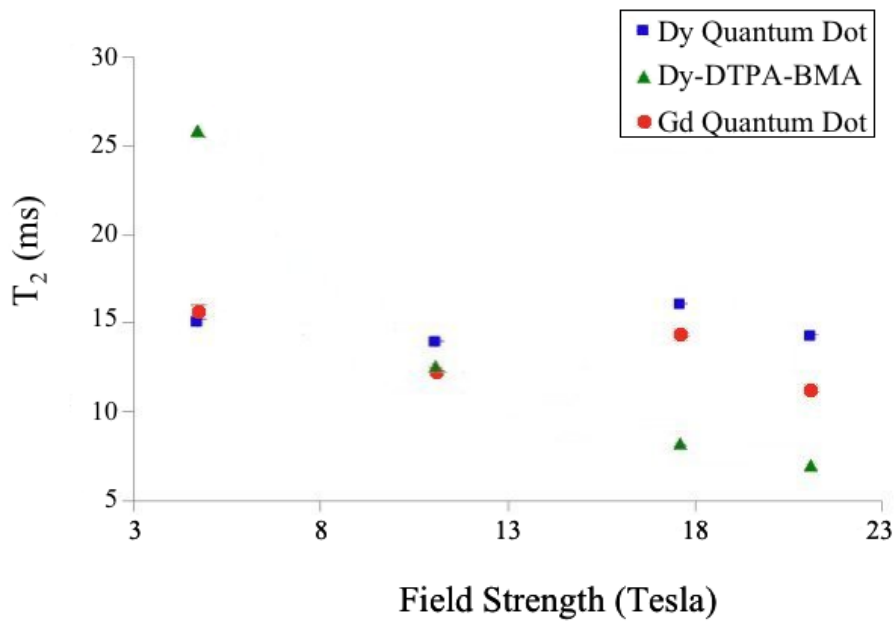


Figure 3-2. Quantum Dot  $T_2$  relaxation times. The  $T_2$  relaxation of gadolinium quantum dots (red), dysprosium quantum dots (blue), and Dy-DTPA-BMA (green) shown at magnetic field strengths of 4.7, 11.1, 17.6 and 21.1 Tesla.

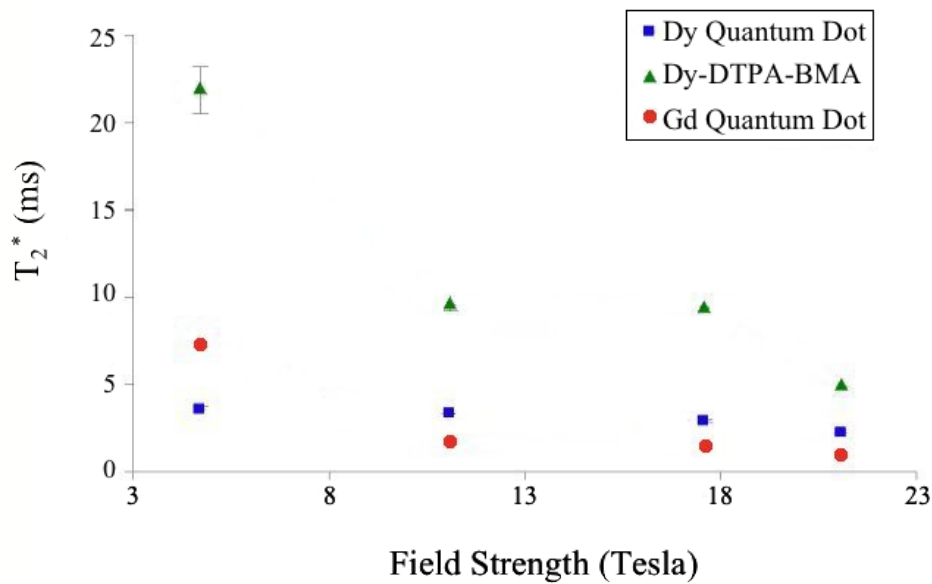


Figure 3-3. Quantum Dot  $T_2^*$  relaxation Times. The  $T_2^*$  relaxation times of gadolinium quantum dots (red), dysprosium quantum dots (blue), and Dy DTPA-BMA (green) shown at magnetic field strengths of 4.7, 11.1, 17.6 and 21.1 Tesla.

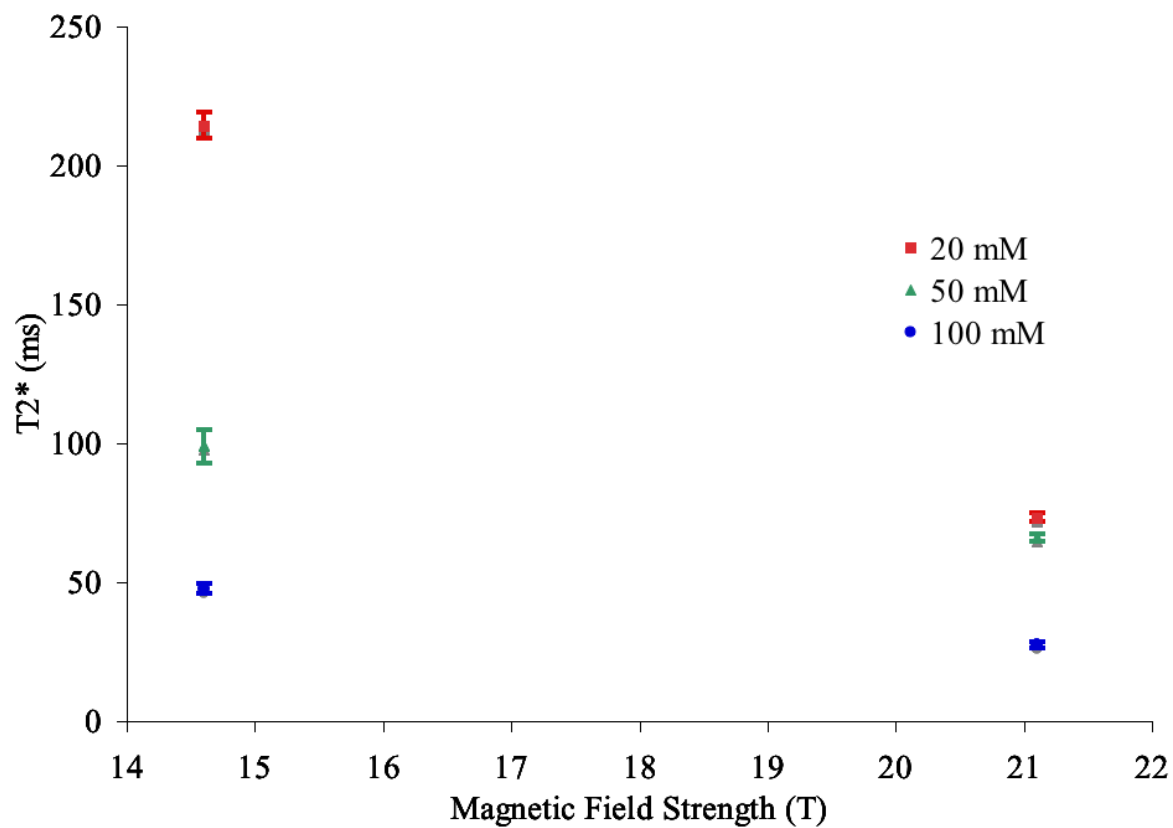


Figure 3-4. Iron oxide  $T_2^*$  relaxation times. The  $T_2^*$  relaxation times for ferumoxide at magnetic field strengths of 14.1 and 21.1T.

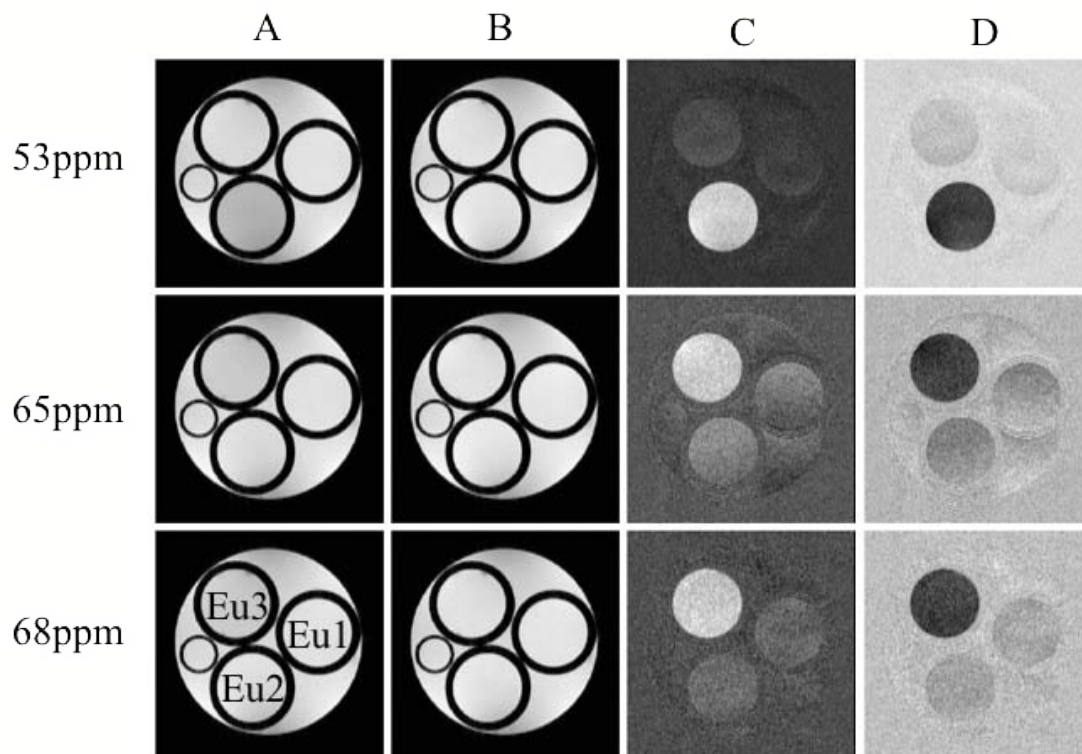


Figure 3-5. Europium PARACEST images at 17.6T. A) Images taken with presaturation offset at 53, 65 and 68 ppm (as indicated). B) Images taken with presaturation at -53, -65 and -68 ppm. C) Difference images taken to show positive contrast as  $B - A$ . D) Difference images taken to show negative contrast as  $A - B$ .

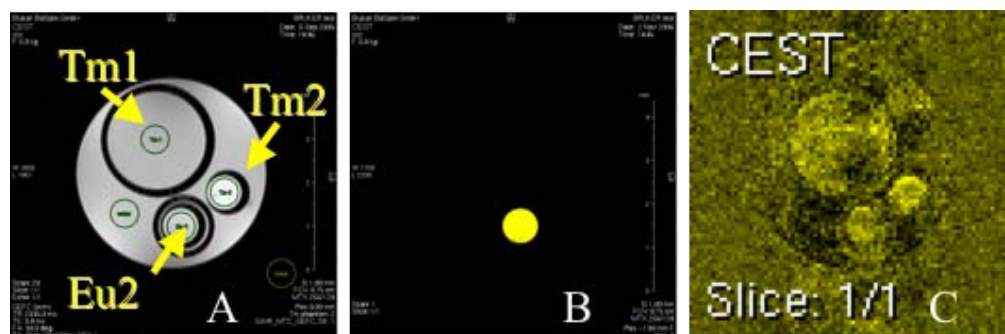


Figure 3-6. Thulium based PARACEST agents at 21.1T. A) Image without presaturation shows where each contrast agent is located, and also the lack of inherent contrast in Eu-2 and Tm-1. Both thulium agents show a slight chemical shift artifact, and Tm-2 shows a slight  $T_1$  weighting (as evidenced by the increased signal). B) The difference image between  $\pm 53$ ppm, shows significant contrast generation by Eu-2. C) The difference image between  $\pm 520$ ppm, shows the most contrast that was generated by both Tm-1 and Tm-2.

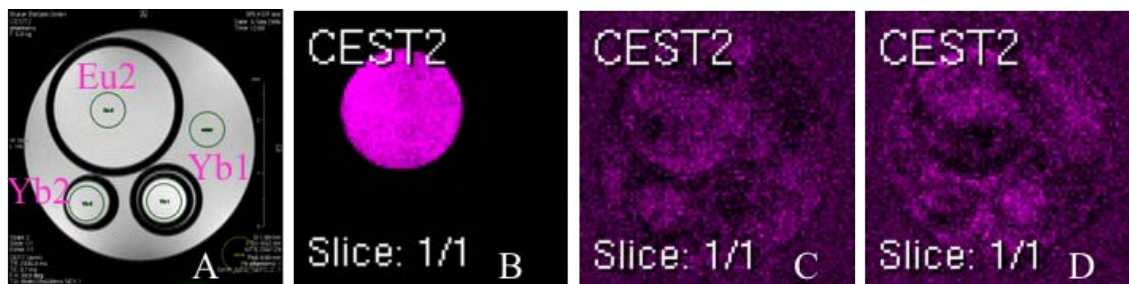


Figure 3-7. Ytterbium based PARACEST agents at 21.1T. A) Image without presaturation shows where each contrast agent is located, and also the lack of inherent contrast in Eu-2 and Yb-2. Both ytterbium agents show a slight chemical shift artifact, and Yb-1 shows a slight  $T_1$  weighting (as evidenced by the increased signal). B) The difference image between  $\pm 53$ ppm, shows significant contrast generation by Eu-2. C) The difference image between  $\pm 210$ ppm shows the most contrast that was generated by Yb-2. D) The difference image between  $\pm 225$ ppm shows the most contrast that was generated by Yb-1.

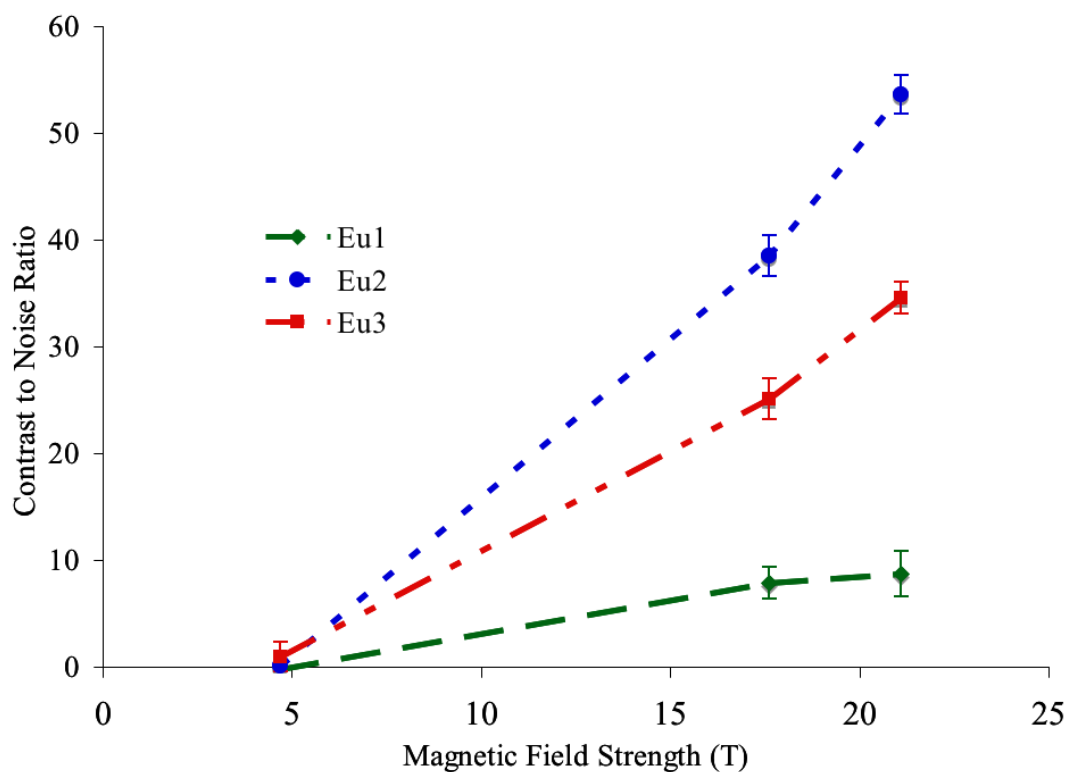


Figure 3-8. PARACEST contrast as a function of magnetic field strength. CNR was calculated from the difference image and was shown to increase for all tested compounds with field strength.

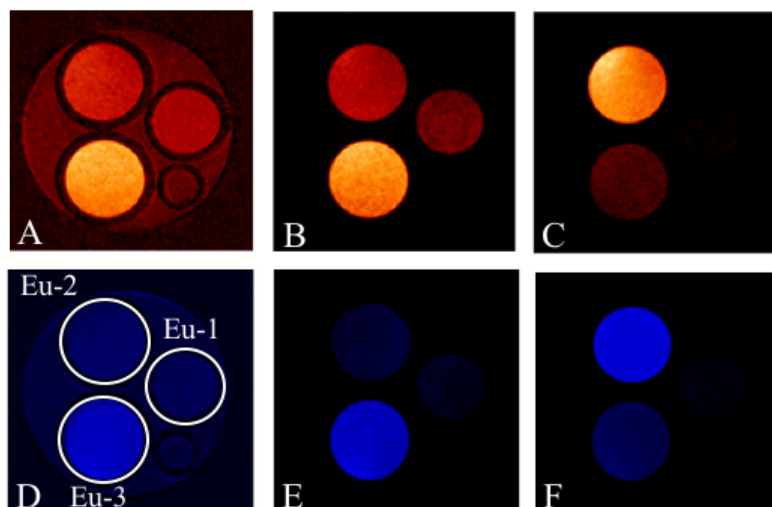


Figure 3-9. Difference images of europium complexes at 17.6 and 21.1 T. Difference images at 17.6 T with presaturation offsets of A) 67, B) 65 and C) 54 ppm, and at 21.1 T with presaturation offsets of D) 67, E) 65 and F) 54 ppm. The images illustrate the increase in contrast with field strength, as well as the shift of optimum offset with agent.

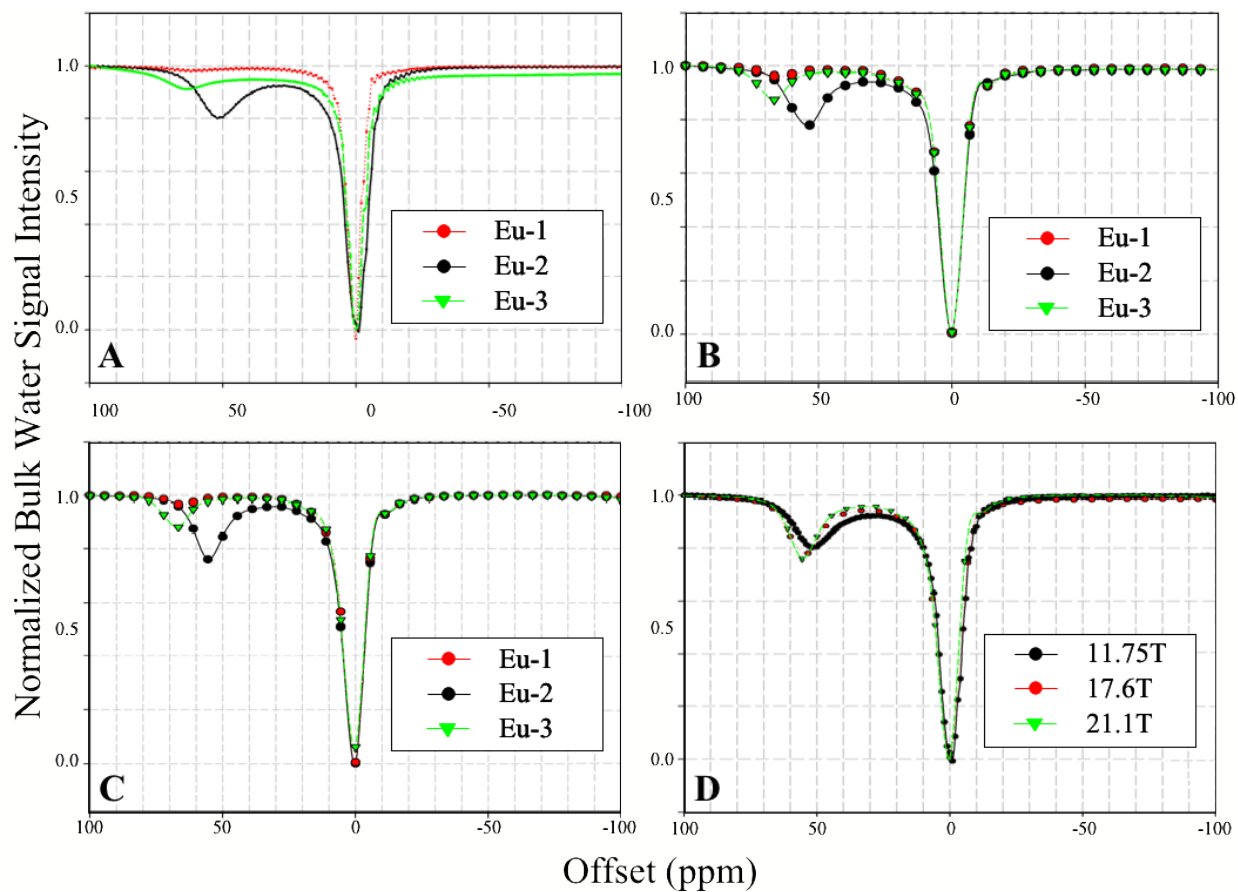


Figure 3-10. CEST spectra with variable magnetic field strength. CEST spectra shown for three europium complexes taken at A) 11.75 T, B) 17.6 T and C) 21.1 T. CEST spectra shown for Eu-2 at all three field strengths.

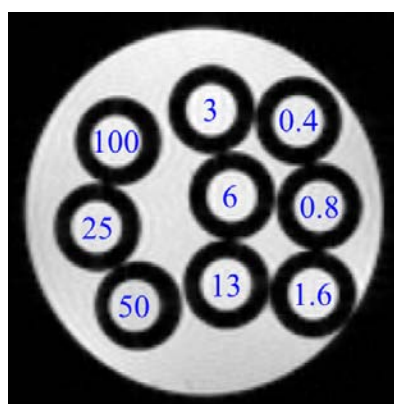


Figure 3-11. Eu-2 serial dilutions. Concentrations from 100 mM to 0.4 mM locations indicated.

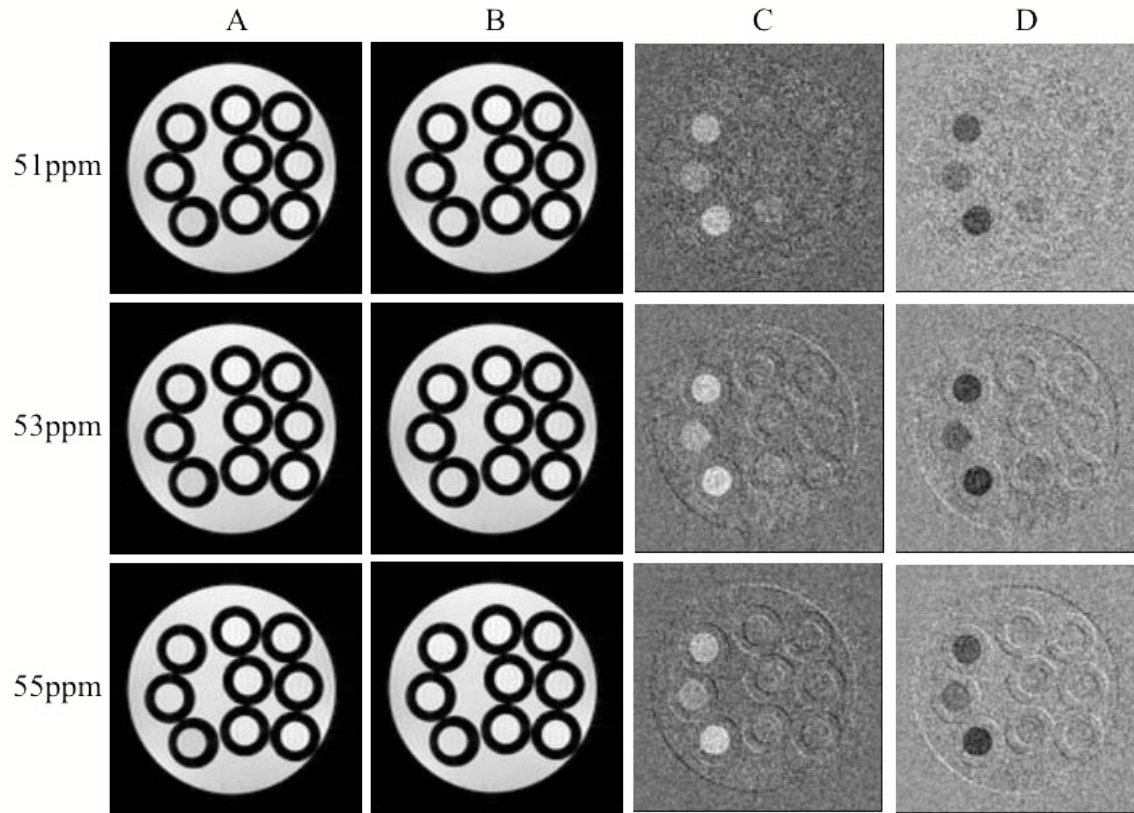


Figure 3-12. Eu-2 concentration phantom images at 14.1 T, with a presaturation power of  $8 \mu\text{T}$ . A) Images taken with presaturation offset at 51, 53 and 55 ppm (as indicated). B) Images taken with presaturation offset at -51, -53 and -55 ppm. C) Difference images taken as  $A - B$ . D) Difference images taken as  $B - A$ .

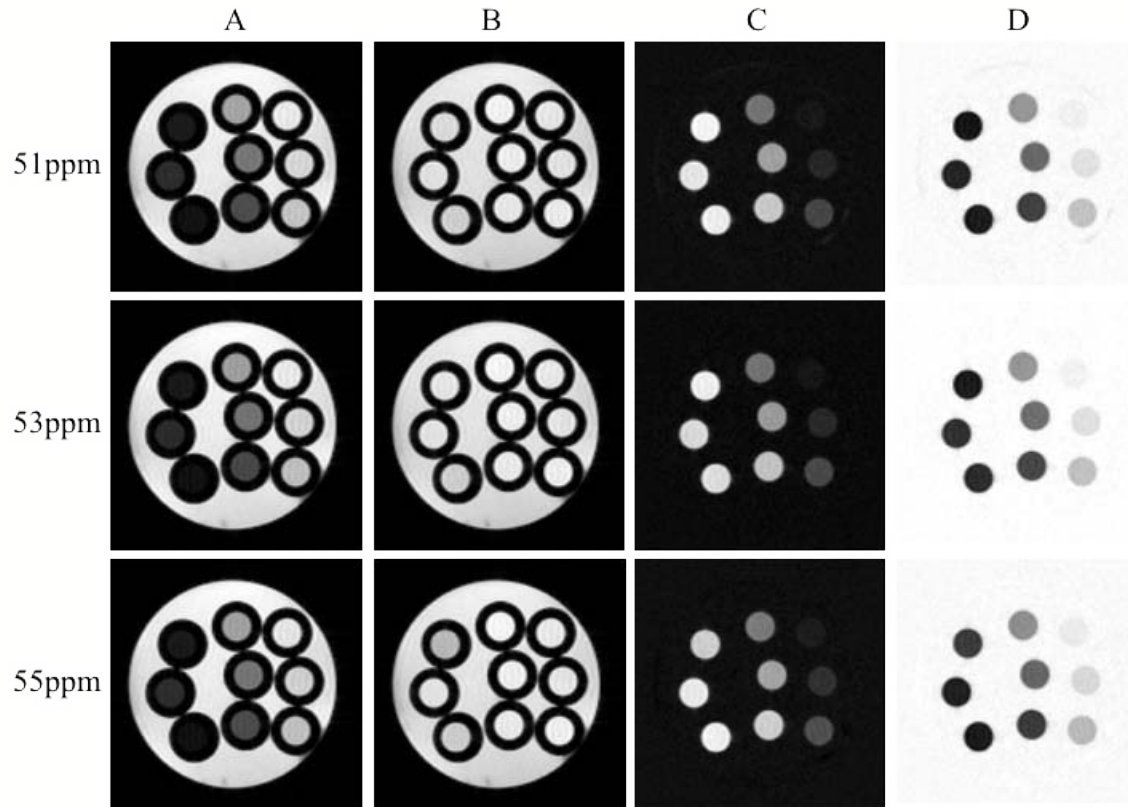


Figure 3-13. Eu-2 concentration phantom images at 14.1 T, with a presaturation power of 128  $\mu$ T. A) Images taken with presaturation offset at 51, 53 and 55 ppm (as indicated). B) Images taken with presaturation offset at -51, -53 and -55 ppm. C) Difference images taken as A - B. D) Difference images taken as B - A.

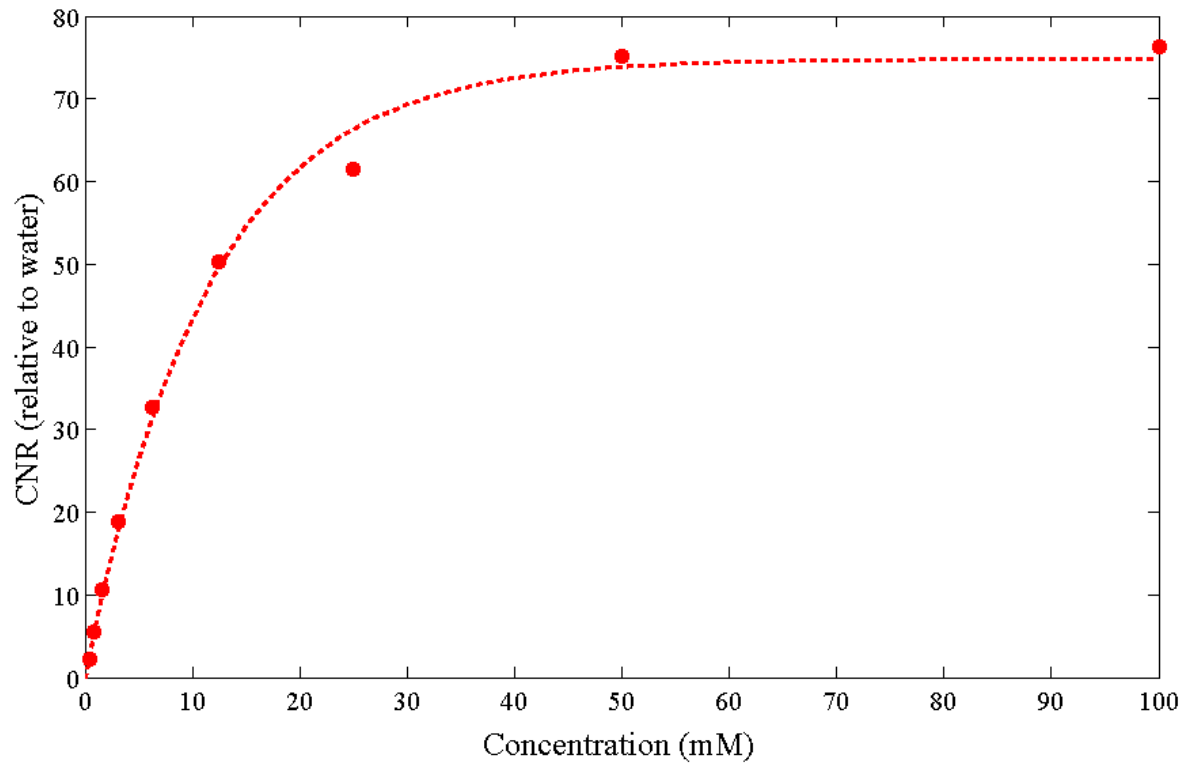


Figure 3-14. Concentration versus contrast for serial dilutions of Eu-2 at 14.1 T, with presaturation power of  $64 \mu\text{T}$  and a total presaturation time of 4 s. CNR was calculated from the difference image at  $\pm 53\text{ppm}$ .

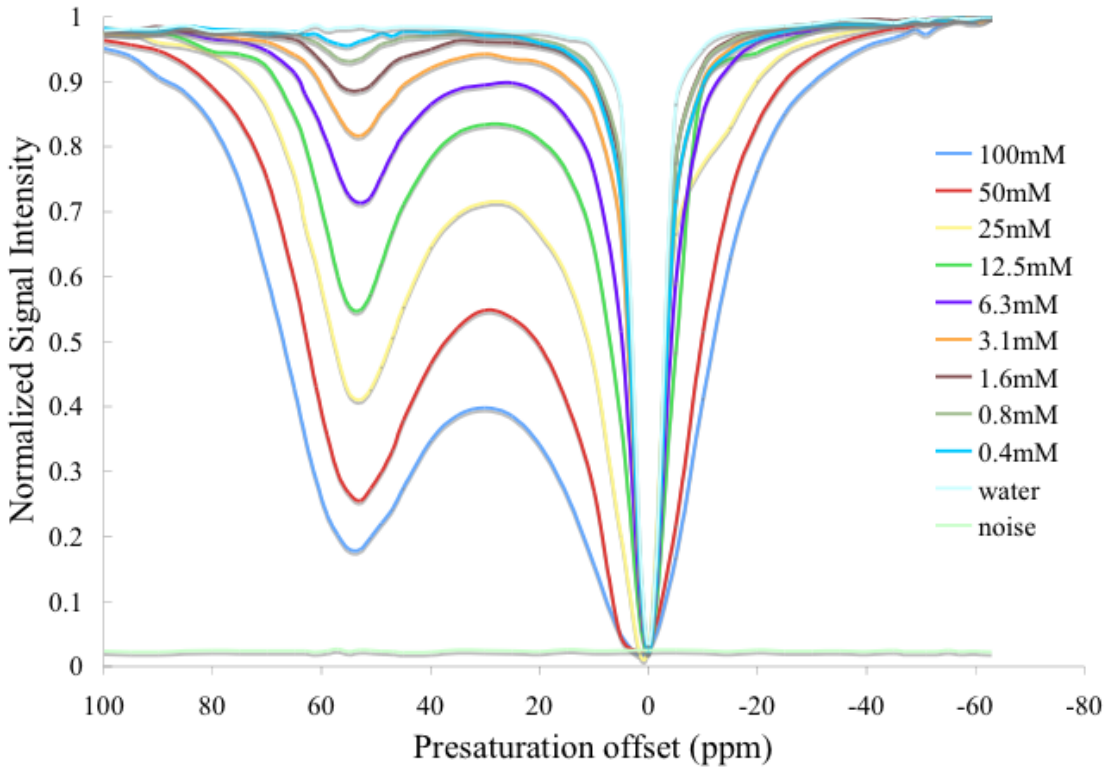


Figure 3-15. CEST spectra at 14.1 T for Eu-2 serial dilutions. The spectra further illustrate the increase in contrast generation with concentration.

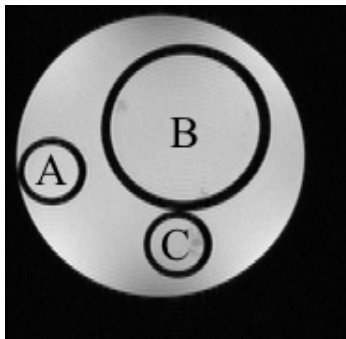


Figure 3-16. Eu-2 (10 mM) at two different pH's, and in SM. A) Eu-2 at a pH of 3. B) Eu-2 at a pH of 7. C) Eu-2 in a 50% water 50% SM solution at a pH of 7.

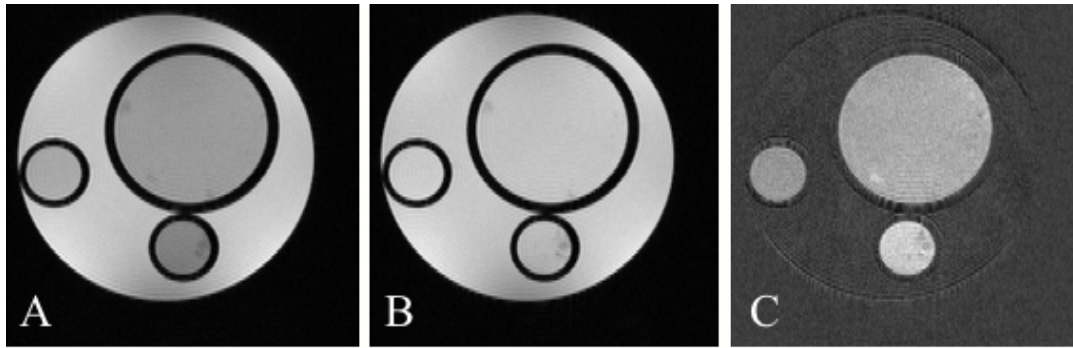


Figure 3-17. Eu-2 pH phantom at 17.6 T. A) Image taken with presaturation at 56 ppm. B) Image taken with presaturation at -56 ppm. C) Difference image of B – A.

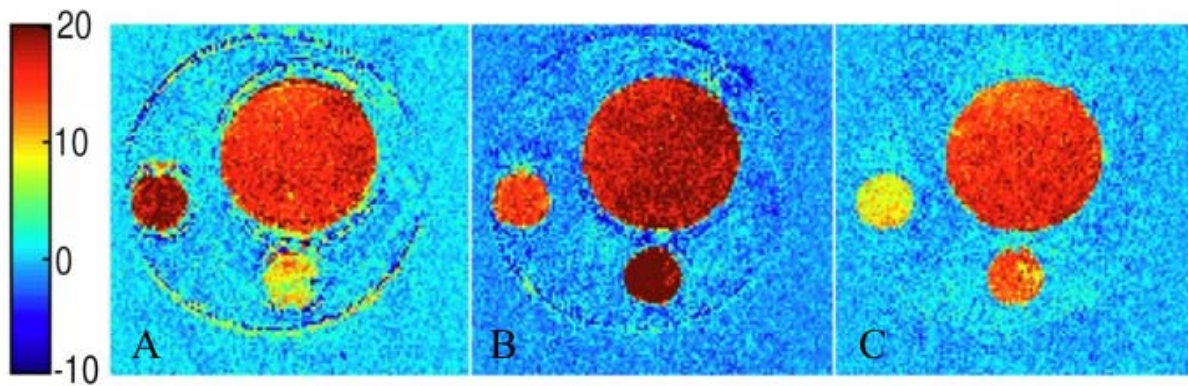


Figure 3-18. Difference images of Eu-2 pH phantom at 14.1 T color enhanced to represent the corresponding CNR. A) CNR map at 53 ppm. B) CNR map at 56 ppm. C) CNR map at 59 ppm.

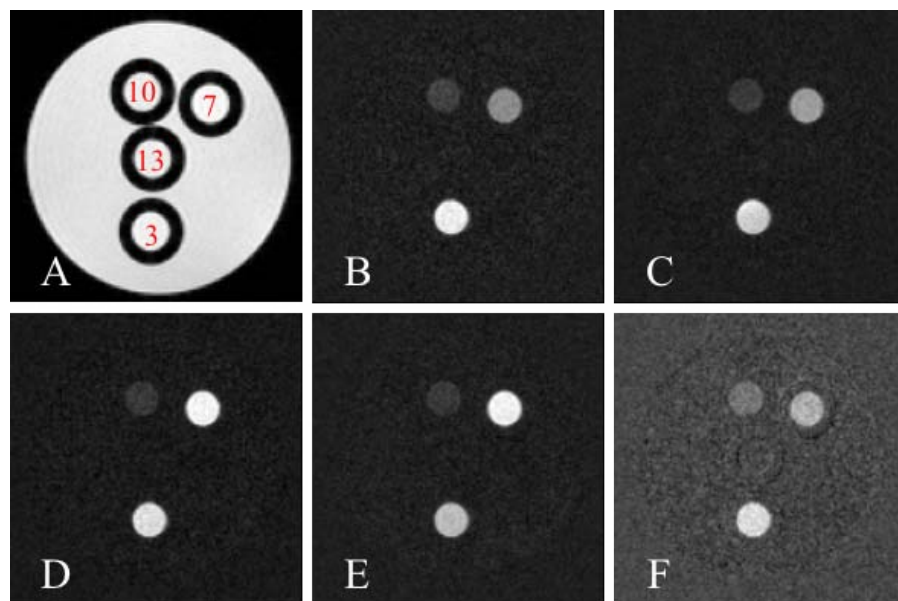


Figure 3-19. Eu-2 at pH values from 3 – 13 at 14.1T. A) Image taken with no presaturation, with pH of 3, 7, 10 and 13 labeled. All solutions were 8 mM Eu-2, and presaturation power was 64  $\mu$ T. Difference images demonstrating change in contrast with presaturation offset for the different pHs at presaturation offsets of B) 51 C) 53 D) 55 E) 57 and F) 59 ppm.

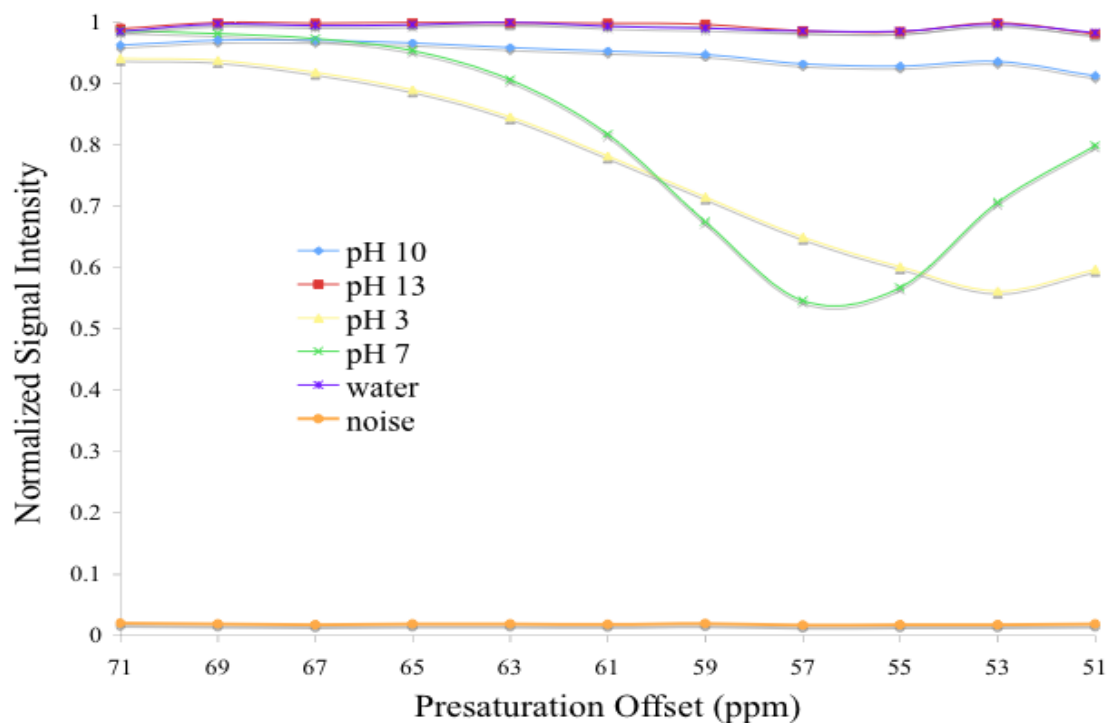


Figure 3-20. Presaturation offset versus normalized signal intensity for Eu-2 at multiple pHs at 14.1 T.

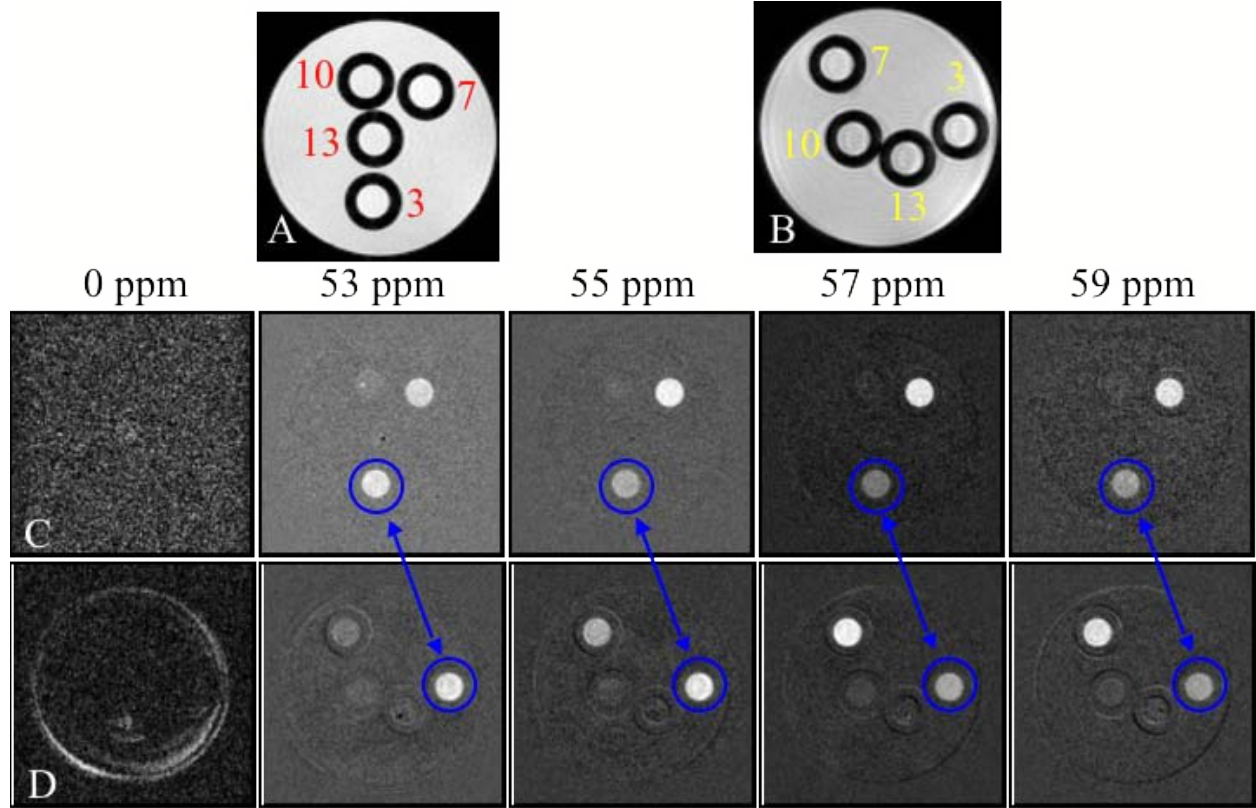
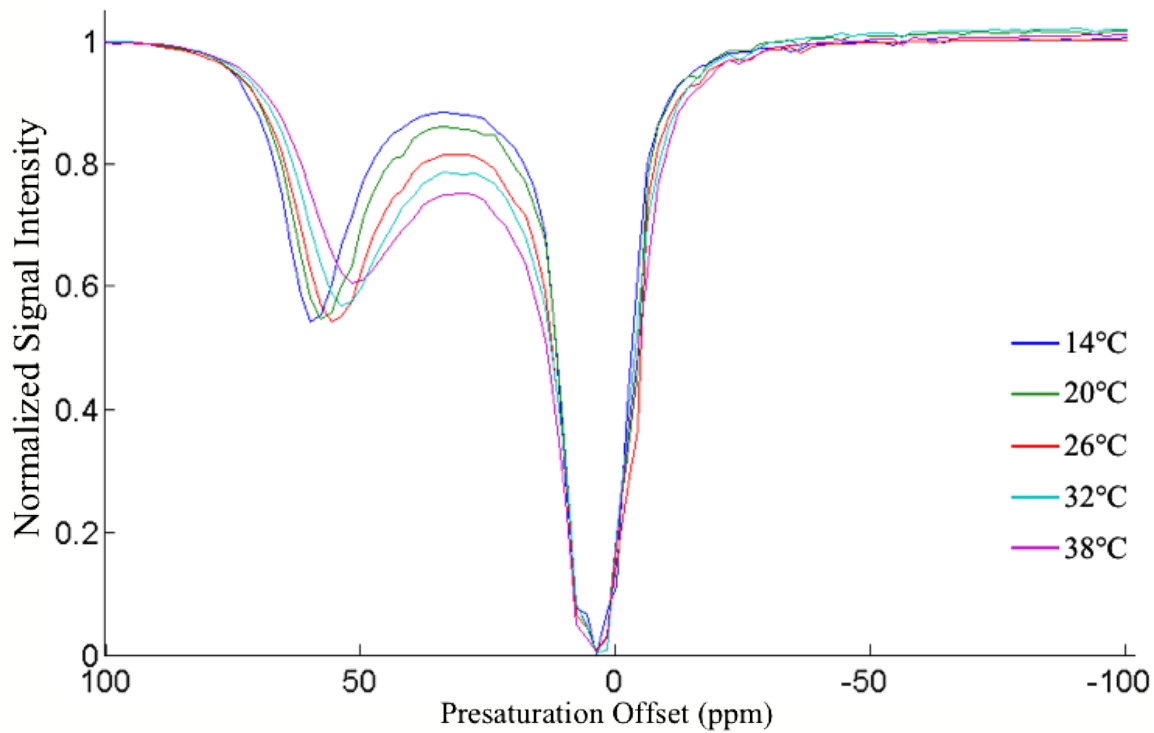
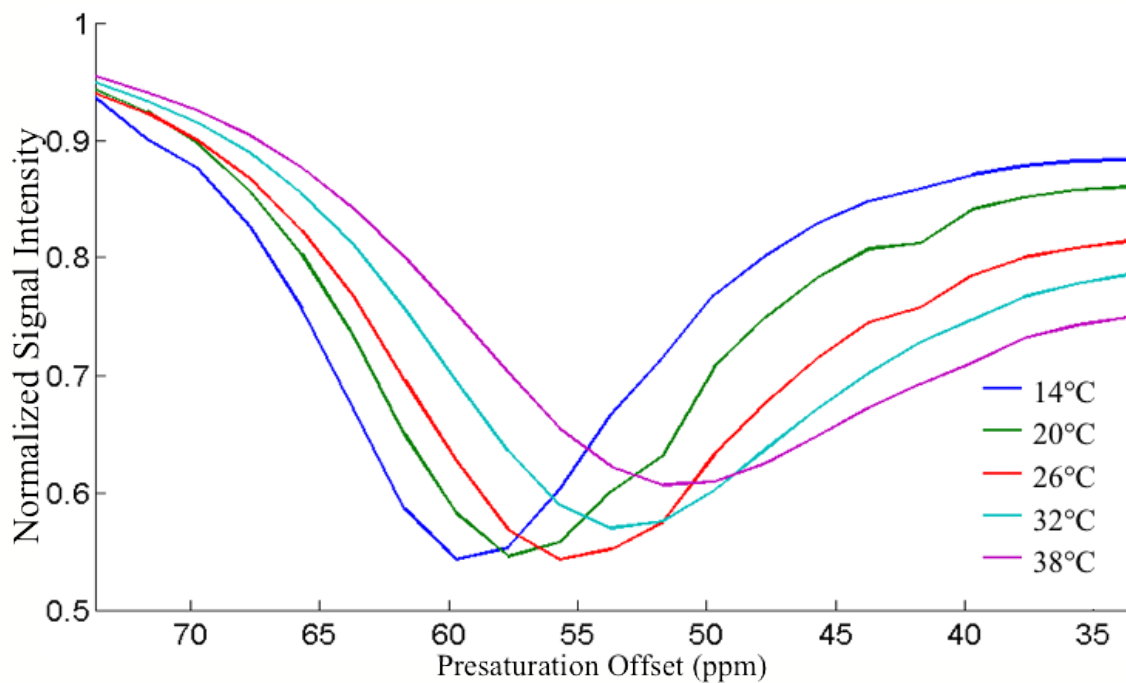


Figure 3-21. Difference images of Eu-2 at multiple pHs at 14.1 and 17.6 T. A) Image without presaturation indicating the location of the samples with pH of 3, 7, 10 and 13 at 14.1 T. B) Image without presaturation indicating the location of the samples with pH of 3, 7, 10 and 13 at 17.6 T. C) Image taken with 32  $\mu$ T presaturation at 0ppm followed by difference images taken 53, 55, 57 and 59 ppm at 14.1 T. D) Image taken with 32  $\mu$ T presaturation at 0ppm followed by difference images taken 53, 55, 57 and 59 ppm at 17.6 T. The blue circles and connecting lines highlight the contrast of pH 3.



A



B

Figure 3-22. CEST spectra for Eu-2 at multiple temperatures. A) Full CEST spectra taken from 100 to -100 ppm, for Eu-2 at 14, 20, 26, 32 and 38 °C. B) A close up of the region from 75 to 35 ppm for Eu-2 showing the shift in maximum contrast potential with offset and temperature.

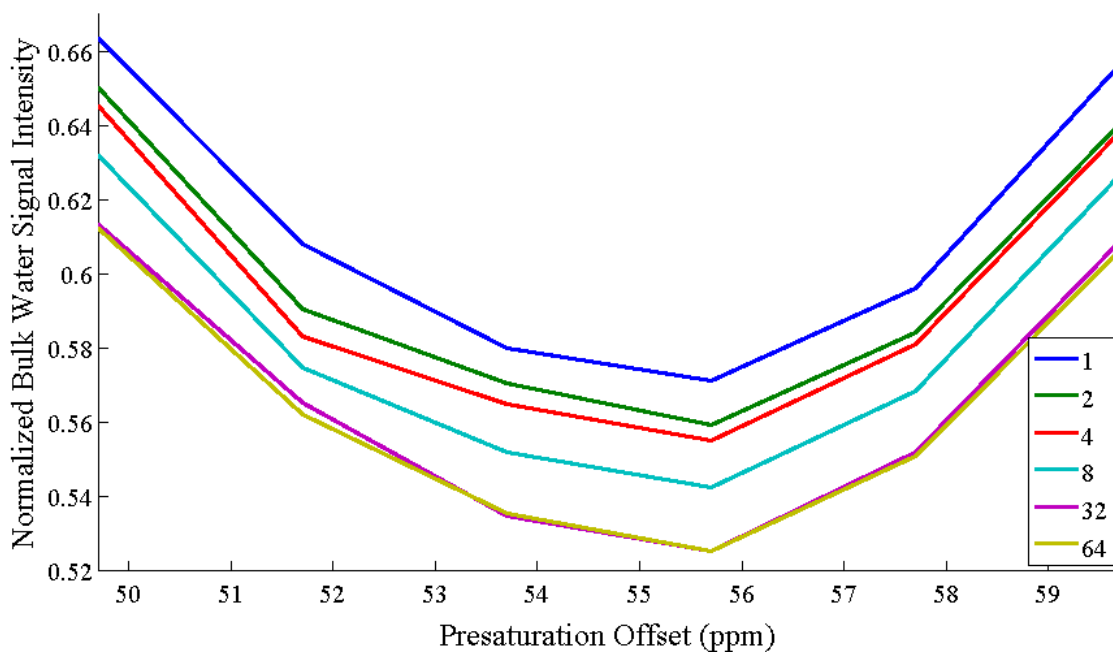
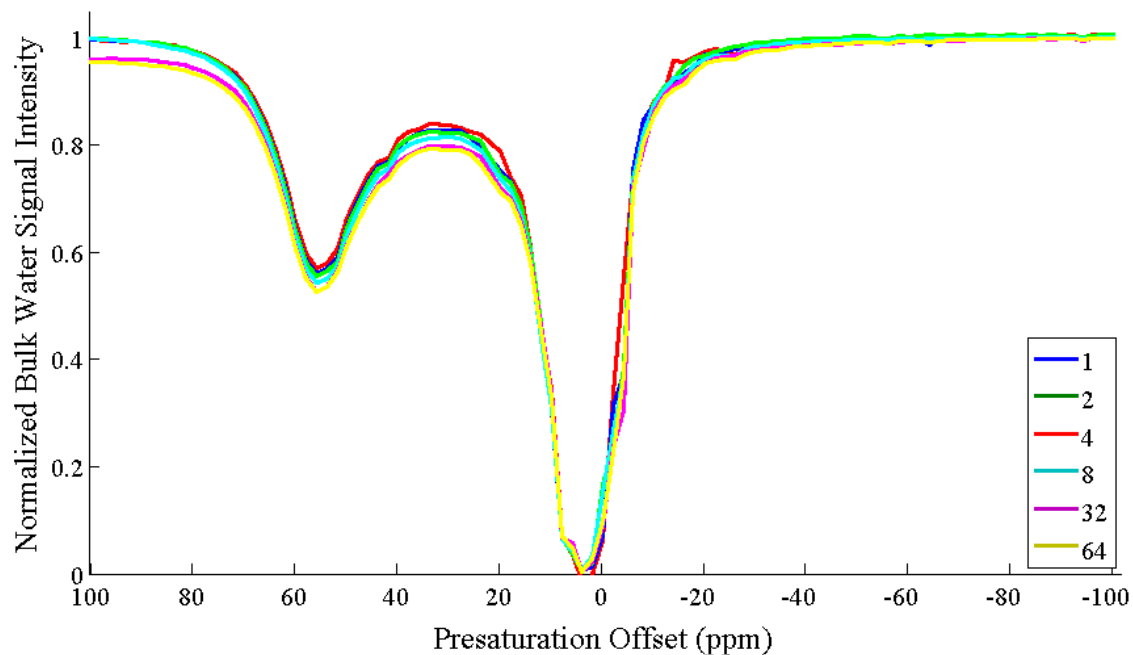


Figure 3-23. CEST spectra for Eu-2 with increasing number of scans. A) Full CEST spectra taken from 100 to -100 ppm, for Eu-2 with 1, 2, 4, 8, 32 and 64 scans. B) A close up of the region from 75 to 35 ppm for Eu-2 showing the change in maximum contrast potential with increasing number of scans.

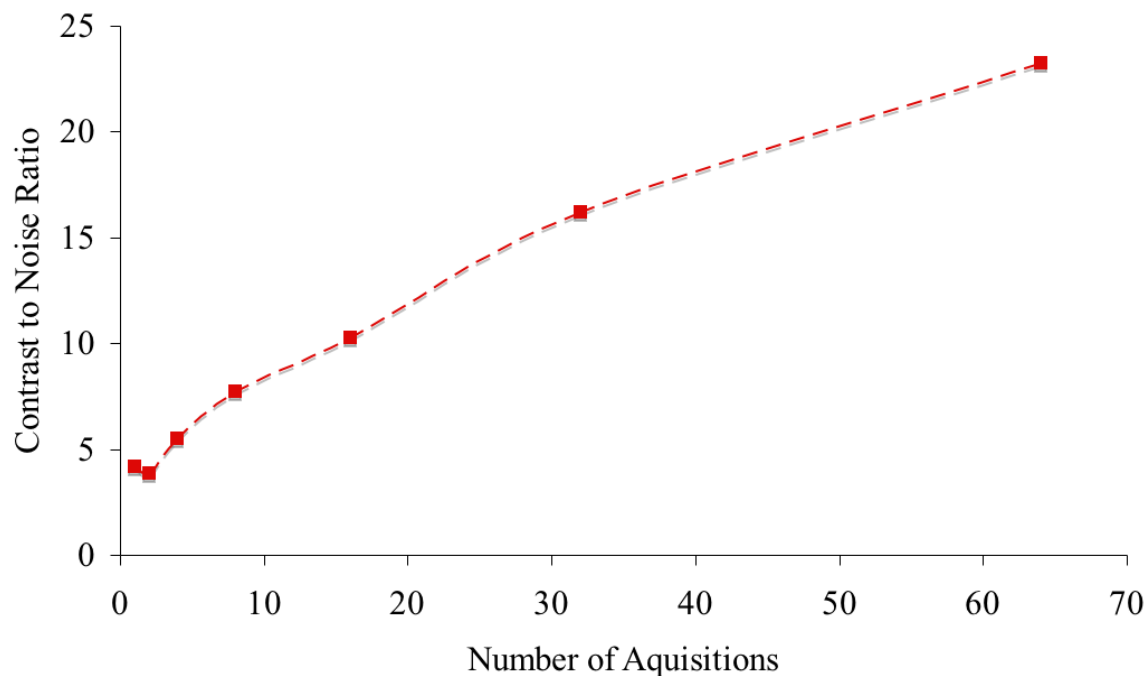


Figure 3-24. Number of acquisitions versus CNR.

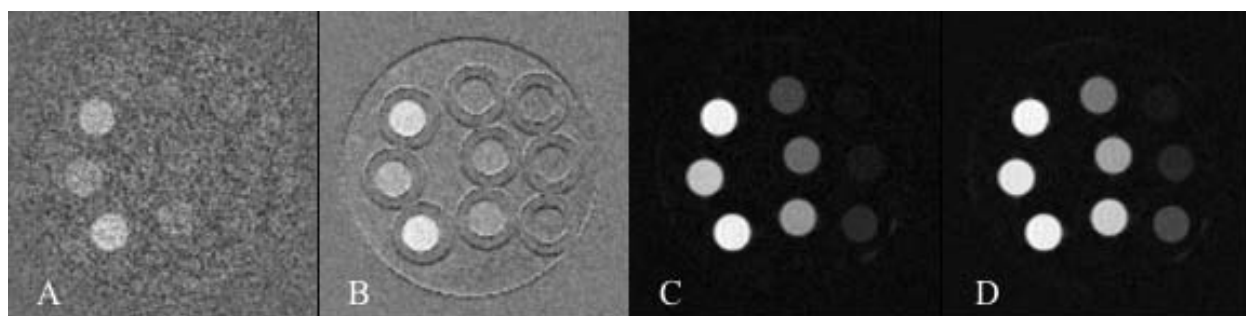


Figure 3-25. Varying presaturation power difference images. The difference images of the serial dilution phantom at 14.1 T, with presaturation offsets of +/- 53 ppm, and a presaturation power of A) 8  $\mu$ T, B) 16  $\mu$ T, C) 64  $\mu$ T and D) 128  $\mu$ T.

Table 3-1.  $T_1$  Relaxation values for 10 mM Eu-2 at multiple temperatures, measured at 14.1 T.

Temperature ( $^{\circ}$ C)	14	20	26	32	38
$T_1$ Relaxation Time (s)	3.1	3.5	4.0	4.4	5.1

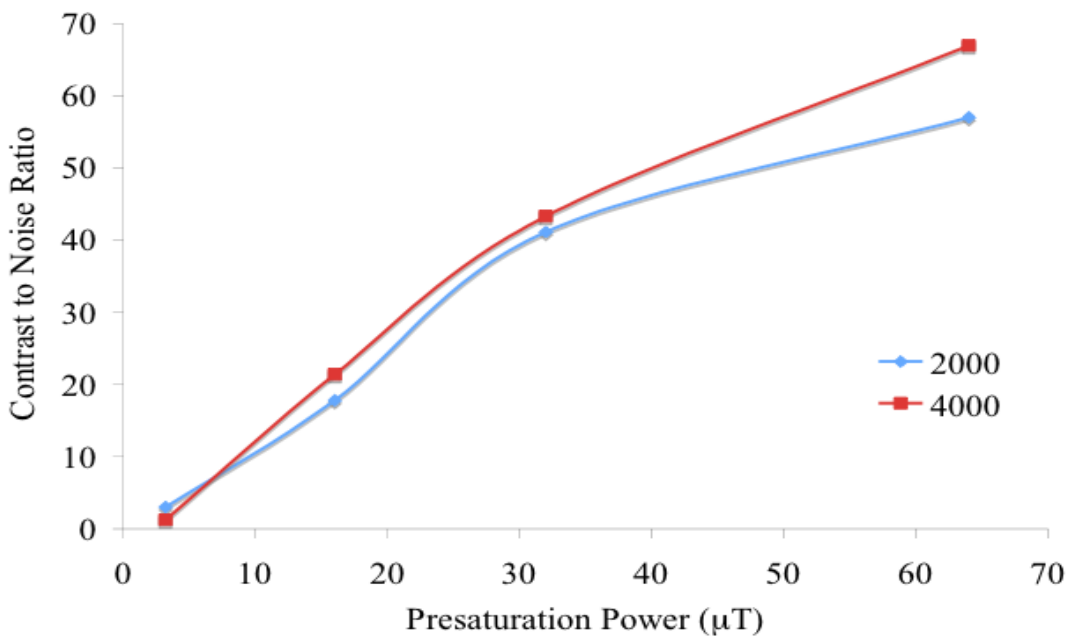


Figure 3-26. Presaturation power versus CNR for serial dilutions of Eu-2 at 14.1 T. The CNR values were calculated from the 100 mM concentration, at 14.1 T, and the number of presaturation pulses was either 2000 (blue) or 4000 (red).

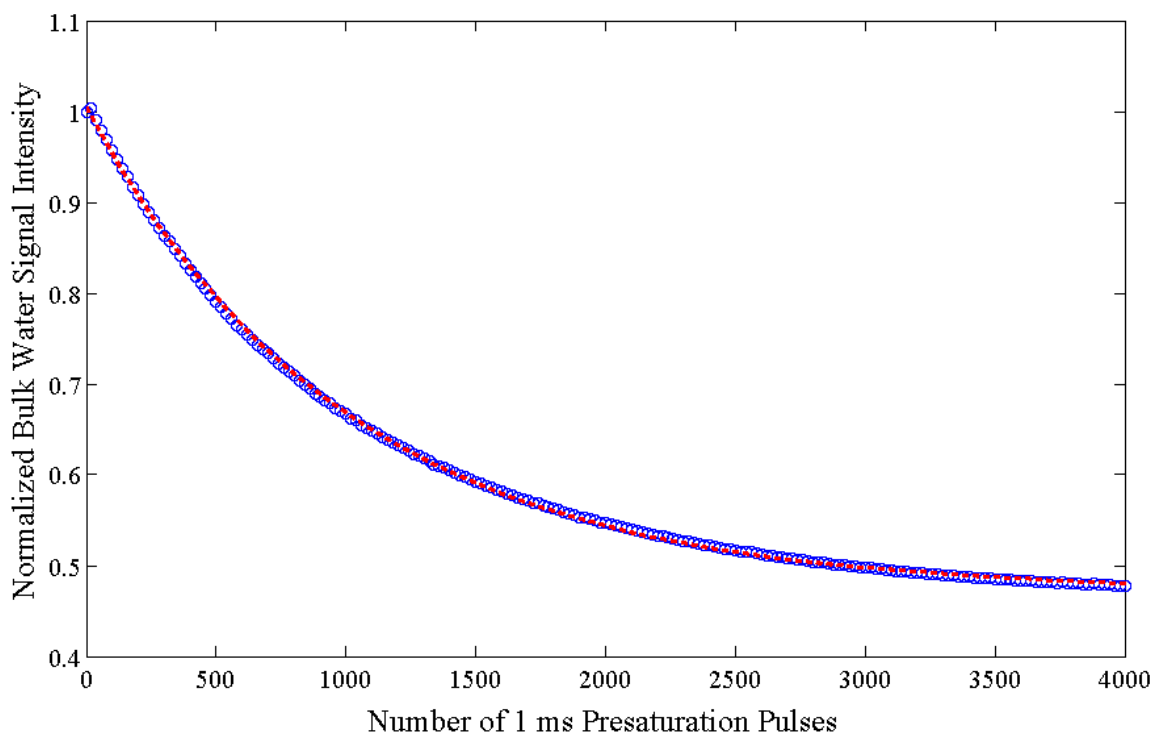


Figure 3-27. Bulk water signal as a function of number of presaturation pulses. The bulk water signal (in blue) was measured with the given number of presaturation pulses at the offset of 53ppm, at 26 °C. The fit to an exponential decay is shown in red.

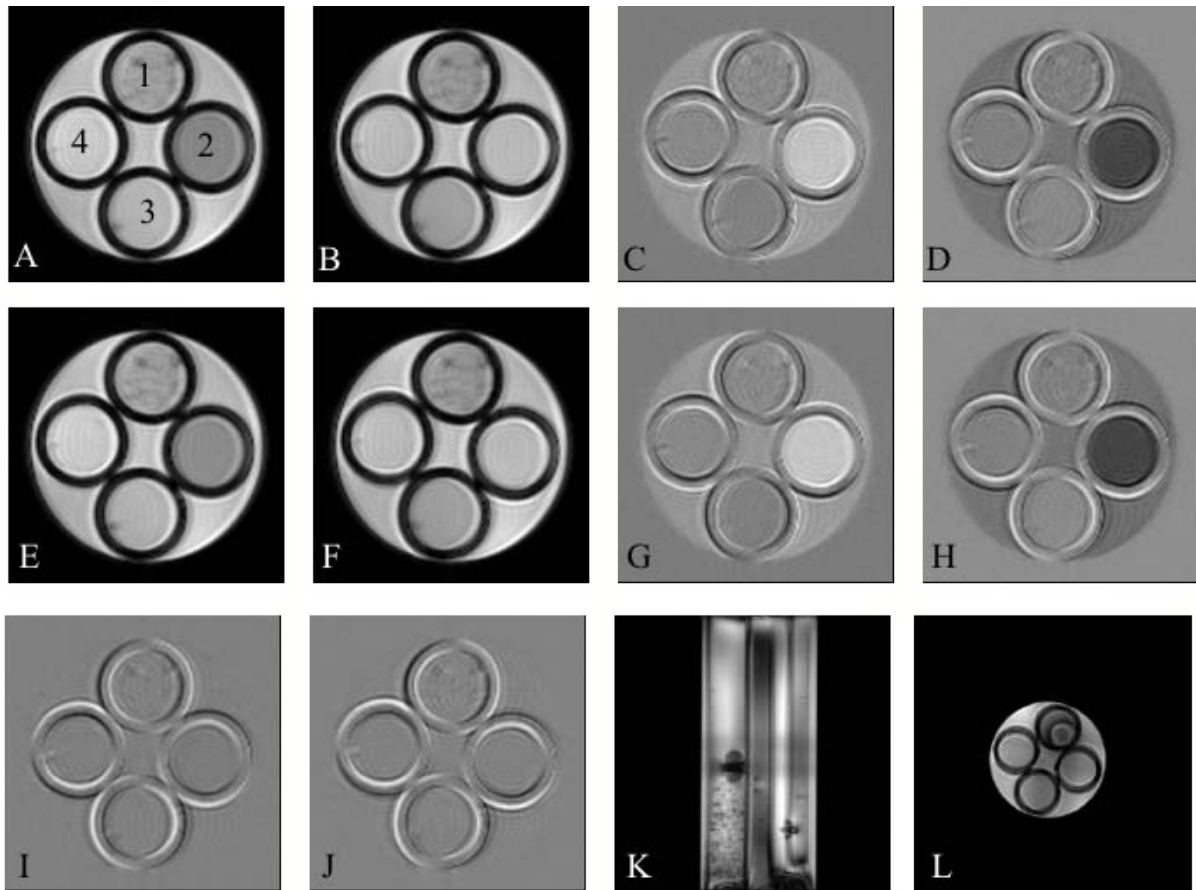


Figure 3-28. Cell labeling image results at 17.6 T. A) Image taken with presaturation offset of 55 ppm, with the tube contents indicated: 1) PARACEST labeled cells 2) labeling media 3) unlabeled cells in agarose and 4) unlabeled media. B) Image taken with presaturation offset of -55 ppm. C) The difference image taken as  $B - A$ . D) The difference image taken as  $A - B$ . E) Image taken with presaturation offset of 57 ppm. F) Image taken with presaturation offset of -57 ppm. G) The difference image taken as  $F - E$ . H) The difference image taken as  $E - F$ . I) Difference image taken as  $A - E$  to show no contrast difference in the surrounding water between 55 and 57 ppm. J) Difference image taken as  $B - F$  to show no contrast difference in the surrounding water between 55 and 57 ppm. K) and L) are tripilot images which validate the tube assignment (1-4) in A.

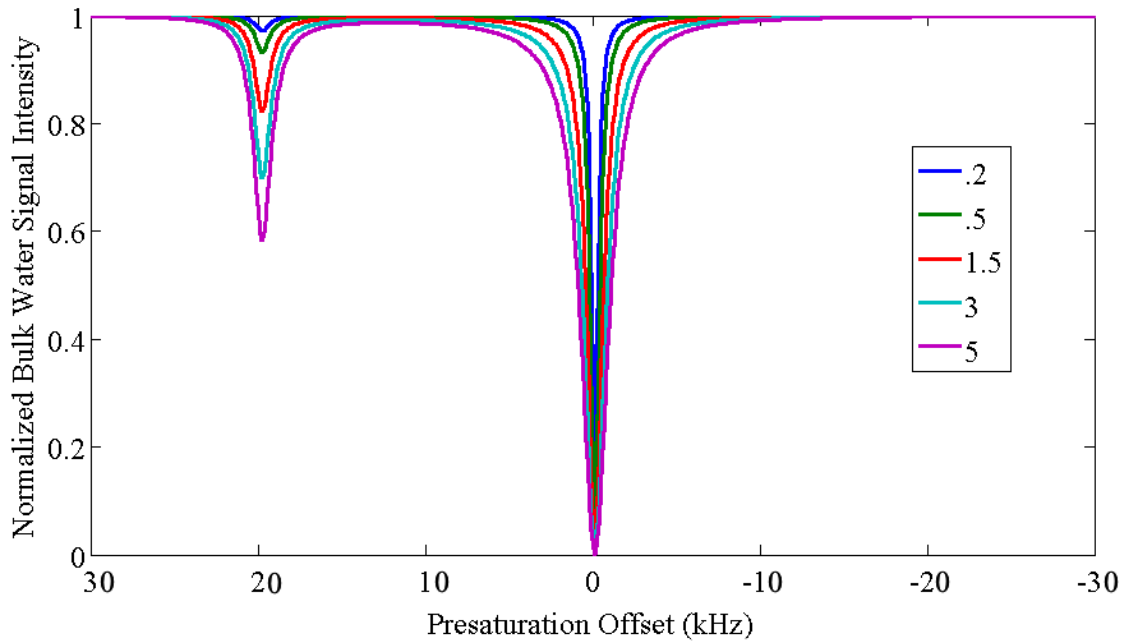


Figure 3-29. Simulated  $T_1$  relaxation variation. The  $T_1$  values are indicated, and show an increase in CEST effect and a broadening of the saturated bulk water with increased  $T_1$ .

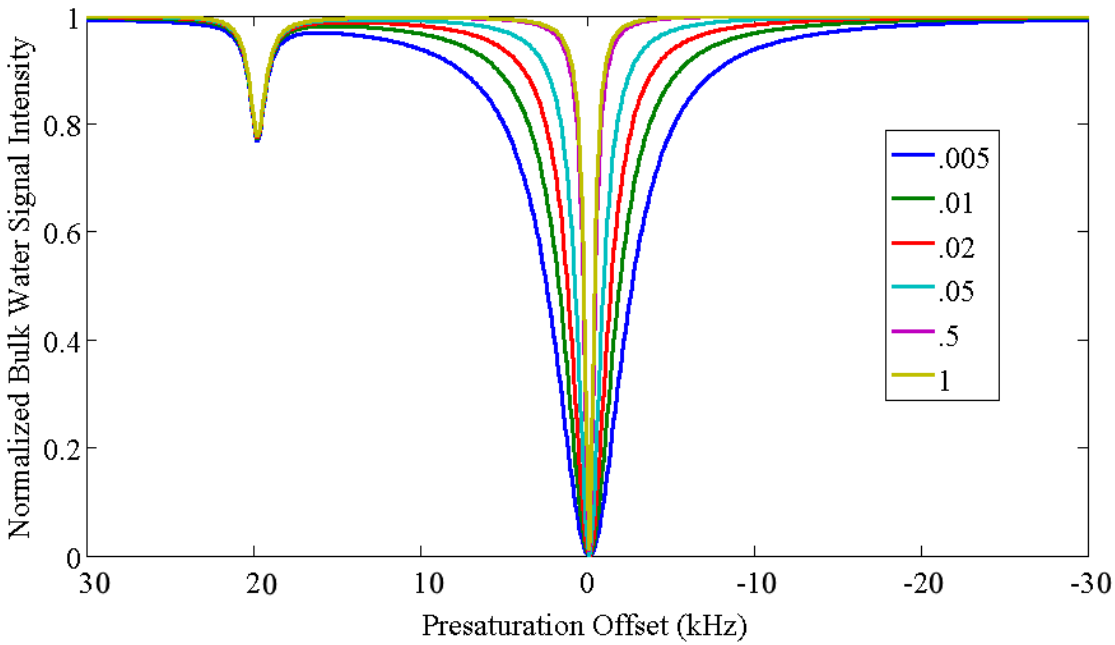


Figure 3-30. Simulated  $T_2$  relaxation variation. The  $T_2$  values are indicated, and show no effect on amount of CEST but show a broadening of the saturated bulk water with decreased  $T_2$ .

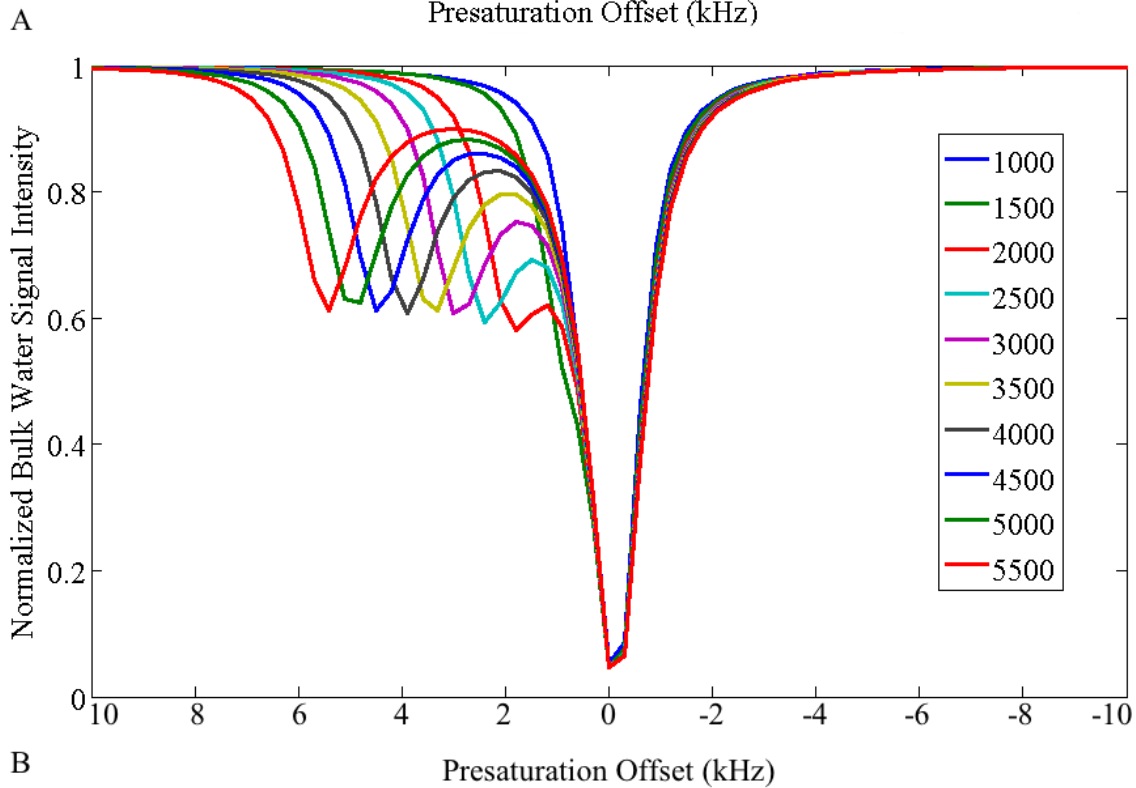
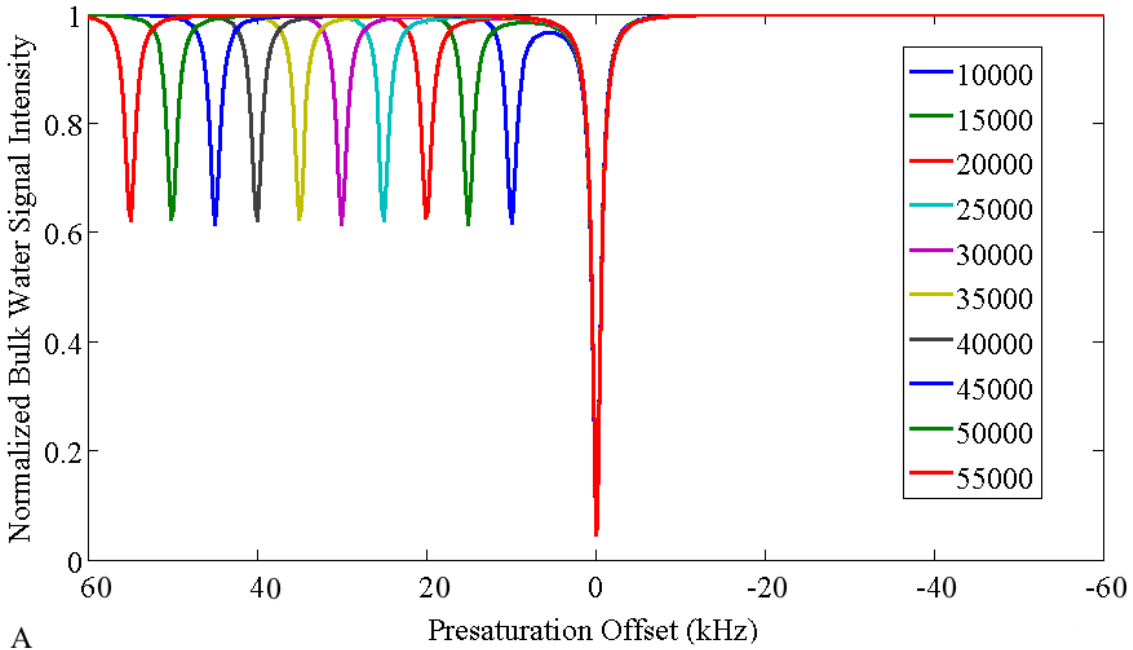


Figure 3-31. Simulated  $\Delta\omega$  variation.  $\Delta\omega$  values indicated (in Hz). A) Values of  $\Delta\omega$  from 10000 to 55000 Hz show a shift away from bulk water with increased  $\Delta\omega$ . B) Values of  $\Delta\omega$  from 1000 to 5500 Hz show a similar shift away from water, but also illustrate the coalescence of the two peaks at low  $\Delta\omega$  values.

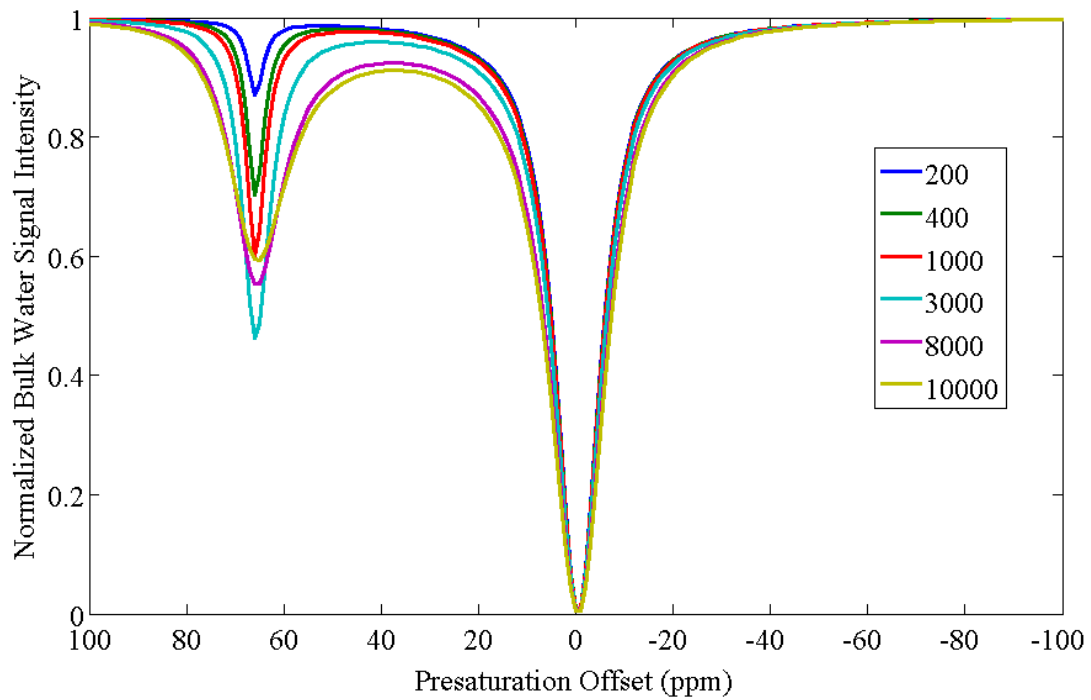


Figure 3-32. Simulated variation in chemical exchange. Transition rate of spins out of the bound pool of protons ( $C_b$ ) indicated. The simulation shows the increase, and then decrease in CEST effect indicating a maximum chemical exchange value.

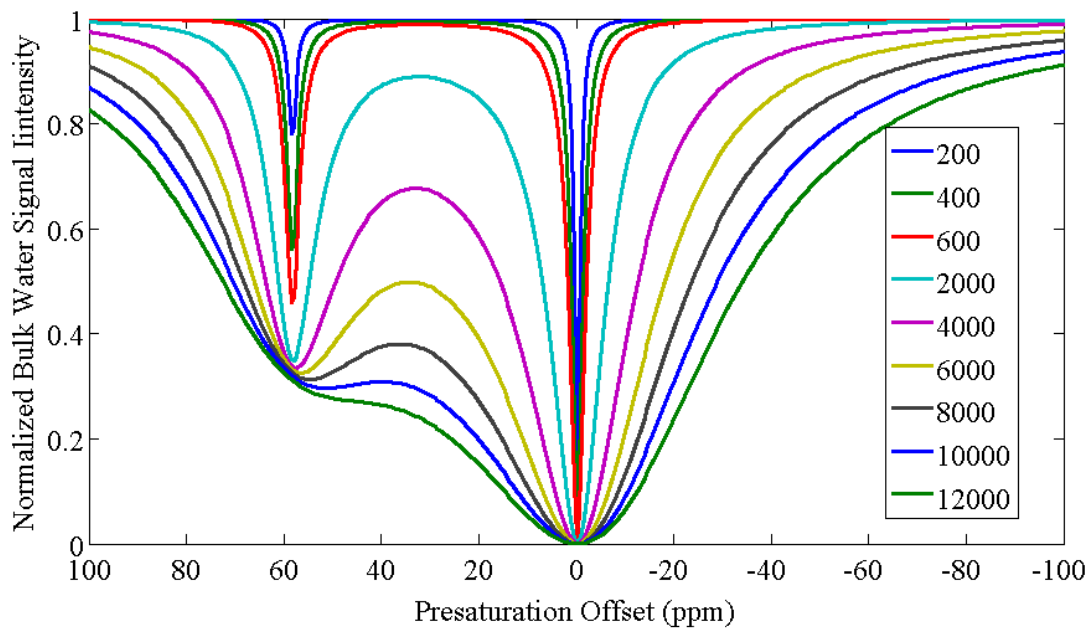


Figure 3-33. Simulated presaturation power variation. Presaturation powers from 200 to 12000 Hz indicated, illustration an increase both in CEST effect and direct saturation of water.

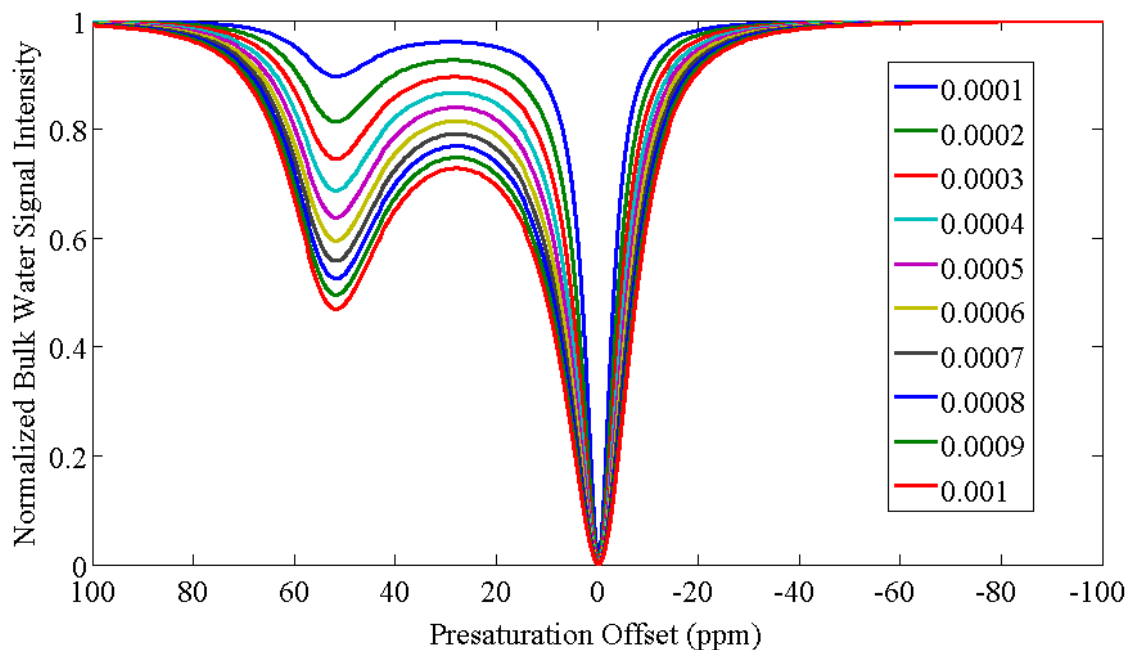


Figure 3-34. Simulated concentration variation. Concentration varied by increasing the ratio of bulk to bound water protons ( $M_0^{\text{bulk/bound}}$ ). The legend indicates the value of  $M_0^{\text{bound}}$  given  $M_0^{\text{bulk}} = 1$ . Increasing concentration shown to increase CEST effect.

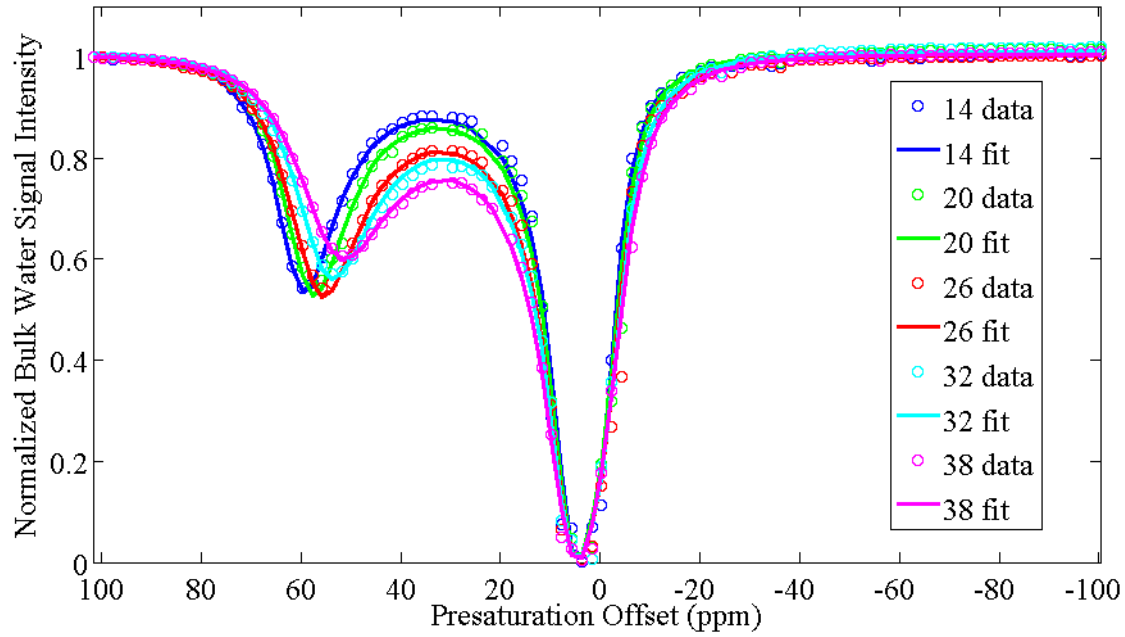


Figure 3-35. Variable temperature data and fit. The fit and the data agree with  $R^2$  values of 0.994, 0.993, 0.991, 0.997 and 0.998 respectively for 14 °C, 20 °C, 26 °C, 32 °C and 38 °C.

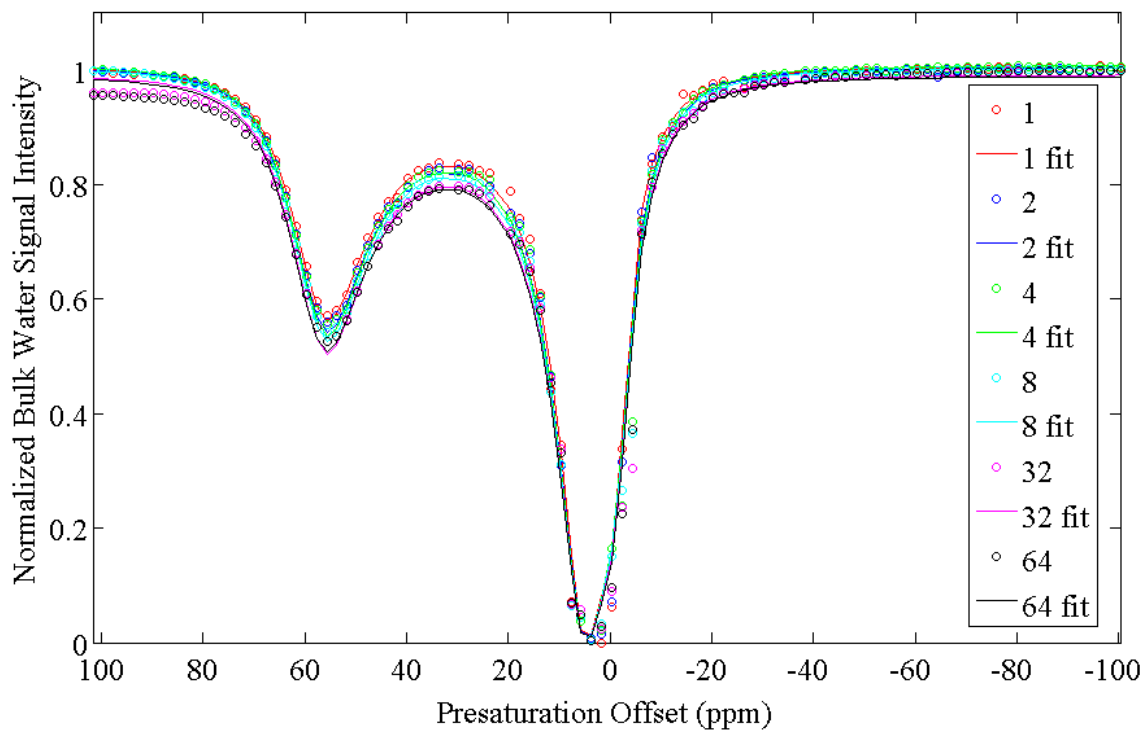


Figure 3-36. Variable number of acquisitions data and fit. The fit and the data agree with  $R^2$  values of 0.994, 0.989, 0.990, 0.991, 0.985 and 0.989 respectively for 1, 2, 4, 8, 32 and 64 scans respectively.

## CHAPTER 4 DISCUSSION

### Relaxation Agents

#### Multimodal Quantum Dots

Gadolinium agents are traditionally used as  $T_1$  relaxation agents; by shortening the  $T_1$  relaxation time of the surrounding water the agents cause positive contrast. At clinical magnetic field strengths (1.5 or 3 T) gadolinium is an effective relaxation agent [56]. However at higher field strengths the  $T_1$  times were shown to increase. This results in a decrease in efficacy of gadolinium quantum dots as  $T_1$  contrast agents with increased field strength. The  $T_1$  relaxation times from dysprosium quantum dots decreased with field strength, indicating an increase in contrast generation potential. However, the observed decrease still resulted in  $T_1$  values at high fields (11 – 21 T) that were comparable to the gadolinium values at low fields (4.7 T). The dysprosium standard decreased the  $T_1$  relaxation times with increased field strength.

The  $T_1$  results indicate a slight advantage for the dysprosium standard as a  $T_1$  relaxation agent at high fields. The contrast generated at high fields with this standard was better than the contrast generated by the gadolinium quantum dots at low fields. However, both quantum dots did not gain significant contrast generation at higher fields. The gadolinium quantum dot actually decreased in contrast generation, and while the dysprosium increased in contrast with increased field strength, it never generated more contrast than the gadolinium quantum dot at 4.7 T.

The results of the spin-spin relaxation measurements generally showed a small to nonexistent decrease in the  $T_2$  and  $T_2^*$  times for all the agents. The dysprosium standard had the largest decrease in both relaxation times, while both quantum dots had only a slight decrease. A decrease in spin-spin relaxation times would indicate an increase in contrast generation potential.

However, iron oxides have already been shown to have the largest effect on relaxation properties per unit metal [93] and would therefore be the more likely choice for  $T_2$  contrast generation.

Overall, the contrast generation of  $T_1$  relaxation agents did not benefit from going to higher magnetic field strengths. The  $T_1$  relaxation properties did not improve for the gadolinium quantum dots, and the dysprosium improvement wasn't significant when compared to gadolinium at low fields. While the gadolinium or dysprosium quantum dots could be used as  $T_2$  relaxation agents at high field strengths, iron oxides would likely be more efficient hence the better choice. At low field strengths, traditional  $T_1$  relaxation contrast agents, including those based on gadolinium, have proven their utility. However to utilize the increase in signal resulting from higher magnetic field strengths, a different type of contrast may prove more useful.

### **Iron Oxides**

Iron oxides have been used for non-targeted contrast generation in clinical studies [65] and also in cell labeling. At lower field strengths there is a minimum number of labeled cells required for detection [94] but at high fields the detection limits are lowered [93] and single cell detection is possible [95,96]. They also benefit from the most change in signal per unit metal [93]. Their contrast generation potential was shown to have little dependence on field strength. Iron oxides are a good choice for contrast agent at high field strengths, but have several ultimate problems for cellular or molecular imaging.

One major problem is that the iron oxides create a negative contrast which appears as a hypointensity on the image. However it may be difficult to distinguish the hypointensity from the iron oxides from other sources of negative image contrast artifacts, e.g., hemorrhage, air, metallic devices [97,98]. One study found that labeled human umbilical vein endothelial cells that were injected post mortem could not be distinguished from other areas of

hemorrhage/microvascular obstruction [66]. This inability to determine the source of the hypointensity can lead to a high incidence of false positives when using iron oxides.

The iron oxide label remains after cell death, which may allow uptake of the label by macrophages. It would become difficult to determine if the hypointensity was due to the living labeled cell or a macrophage. And lastly, even if the label remained in a living cell, cellular division would lead to label dilution or distribution (in the case that the label remained with only one cell).

Despite its negative contrast and other possible problems, due to the magnitude of change in contrast per unit metal, iron oxides remain a viable option for cellular and molecular imaging, including at high field strengths.

## **PARACEST Agents**

### **Multiple Lanthanide Ion Complexes**

The results showed contrast generation for all three europium complexes, with Eu-2 > Eu-1 > Eu-3. Little contrast was shown for the ytterbium and thulium complexes, even at 21.1 T. There are several possible explanations for this observation. First, the predicted values of  $\Delta\omega\tau_M$  at 11.75 T for thulium and ytterbium are relatively low (4.7 and 1.9 respectively) when compared to europium (60.0) [72]. At 21.1 T these values should still be greater, but they are comparatively small, which could explain the low contrast generation of these four complexes even at high fields. Additional factors which may explain the low contrast generation of the ytterbium and thulium complexes is concentration, pH and temperature. Ten mM europium complex solutions exhibited significant contrast generation, but this may not have been significant concentration for the other lanthanide complexes. Increasing the concentration of these agents should increase the contrast generation.

Overall, europium complexes were shown to successfully generate contrast, which increased with field strength. The other lanthanide agents were largely unsuccessful, but this may be attributed to poor optimization. The presaturation, temperatures and concentrations were optimized for europium complexes, and offset was the only factor which was adjusted for the additional complexes. However, both ytterbium and thulium complexes were not predicted to generate as much contrast as europium, for the given parameters. Ytterbium and thulium have both been used by various groups [73,75,99-105] as PARACEST agents for multiple purposes including contrast generation [99-103], pH [73,75] or temperature [104] monitoring, or detection of small molecules [105].

While europium agents yielded the best results in this investigation, other lanthanide agents remain a promising alternative.

### **Field Strength Dependence**

The three europium complexes produced increased contrast with increasing magnetic field strength, in good agreement with theory ( $\Delta\omega\tau_M \geq 1$ ) [72]. The imaging experiments indicated increased CNR with field strength. There was a significant increase in contrast between 4.7 and 17.6 T, and an additional increase at 21.1 T. The greatest amount of contrast generation was produced by Eu-2 which had a 38% increase in CNR between the field strengths of 17.6 and 21.1 T (from 38 to 54) while Eu-3 showed a 48% increase between 17.6 and 21.1 T (from 25 to 37). Eu-1 is unique in that CEST contrast is only evident at the field strengths of 17.6 and 21.1 T (CNR = 8 and 9 respectively) but not at the lower fields that would include clinical field strengths of 1.5 and 3 T. The CEST images at the maximum contrast for each europium complex at 21.1 T are shown in Figure 3, which displays the tunable contrast enhancement

related to the PARACEST agent and saturation offset. The optimal offsets for each agent were 53, 65 and 68 ppm for Eu-2, Eu-1, and Eu-3, respectively.

CEST spectra of all three compounds collected at 11.75, 17.6 and 21.1 T show optimal offsets for each complex: Eu-1 and Eu-3 both have optimal offsets near 65 ppm whereas the optimal presaturation offset for Eu-2 is near 53 ppm. The spectra also demonstrate a distinct difference in contrast generation potential for each agent. At all field strengths, Eu-2 generated the largest CEST contrast, followed by Eu-3 and Eu-1. For each agent, the spectra at the different field strengths show the increase in contrast from 11.75 to 17.6 to 21.1 T. The CEST spectra of Eu-2 at the three field strengths shown on one plot demonstrate the normalized bulk water signal at the offset of bound water decreases from 0.80 (11.75 T) to 0.78 (17.6 T) to 0.75 (21.1 T) (indicating an increase in contrast generation).

Both the decreased water signal in the CEST spectra and increased CNR at higher fields are consistent with expectations that the bound water shifts ( $\Delta\omega$ ) will be larger while the bound lifetimes ( $\tau_M$ ) are unaffected, thus expanding the intermediate exchange requirement,  $\tau_M\Delta\omega \geq 1$ . Most of the existing Eu(III)-based agents have a bound water peak near 50 ppm at room temperature, corresponding to  $\Delta\omega = 10,000$  Hz at 4.7 T and a requirement for  $\tau_M \geq 100$   $\mu$ s. This requirement is rather stringent for lanthanide complexes and consequently only a few Eu(III) complexes meet this condition. However, this same imaging experiment performed at 21.1 T ( $\Delta\omega = 45,000$  Hz) would require a Eu(III)-complex having a  $\tau_M \geq 22$   $\mu$ s, a more accessible value to achieve experimentally. This condition may be the case with Eu-1, which was unable to produce contrast at low field strengths, but generated useful contrast at the higher field strengths.

The results of this study indicate that going to higher fields increases the contrast generation potential for all tested lanthanide complexes.

## **Concentration Dependence**

The serial dilutions of Eu-2 showed an increase in contrast generation with increased concentration. The lowest tested concentration was 0.4 mM, which showed a 5% signal decrease in the CEST spectra and a CNR of 2.2. The increase in contrast generation was nonlinear, and appeared to level out at the highest concentrations. This indicates a maximum contrast generation, which is physically logical because the contrast is a saturation of the water signal, the physical maximum is complete water saturation. With higher power saturation, the lowest concentration was visible. However, the amount of power used will be dependent on several variables, not the least of which is power deposited in the sample.

Concentration was expected to increase the amount of contrast generation because there are more lanthanide ions and therefore more sites for water to bind to, hence more shifted water protons. The results agreed with this expectation and showed that increasing concentration increases the amount of CEST contrast generated. However, concentrations above 25 mM result in over a 50% decrease in signal, which is sufficient for a contrast to noise ratio of over 50 (for a presaturation power of 128  $\mu$ T). This fact could be used to either limit the amount of contrast agent needed, or increase the concentration and lower the power.

## **pH Dependence**

The results of the pH imaging illustrate a shift in the location of the optimal presaturation offset as a function of pH. The results demonstrated the ability of the PARACEST agents to maintain contrast in the presence of other ions (in the labeling media). The pH imaging also indicates a difference in magnitude of contrast at a given offset for different pH values, which has been shown in previous studies [73]. Contrast generation was achieved at pH values of 3, 7, and 10, but not at 13. The optimal range of contrast generation was between pH 3 and 7, both of which resulted in greater than 40% decrease in signal. There was a shift in the optimal offset

between the pH of 3 and 7, with a shift away from water with increasing pH. Although contrast (~5% decrease) was generated at a pH of 10 it was not optimal, and did not increase beyond the 5% threshold. The decrease in contrast generation and the lack of contrast at the pH of 13 suggests a pH dependent chemical change that inhibits the CEST in extremely basic conditions.

It is noteworthy that during the making of the pH sample, the solution was first at pH of 3, then taken to 13, then to 10 and then 7. This is important because it shows the stability of the compound, and its ability to maintain contrast generation even after exposure to basic conditions. It also shows that the basic pH did not destroy the complex (as evidenced by its ability to generate maximum contrast at pH 7), and adds further weight to the argument that the basic pH causes a change in exchange or confirmation rather than complete annihilation of the complex in extremely basic conditions.

The overlap of the contrast generation offsets between pH of 3 and 7 indicate that this europium complex may not be optimal for measurement of pH by itself. This is evidenced by the contrast generation at 55 ppm, where both pH 3 and 7 produced ~40% signal decrease, so it would not be possible to differentiate between the two. However, these results indicate the utility of this complex for contrast generation across a range of pH values, most notably at pH 7, which is the normal pH of most cellular and living systems. Given that it also works at pH 3, this makes it a good possibility for cellular labeling, because often the end location of the label is unknown. If it is endocytosed, it may be put into a compartment with an acidic pH. This complex would still work as a contrast agent in that case, because it has been shown not only to generate contrast in acidic environments, but also to maintain stability.

### **Temperature Dependence**

CEST spectra from temperature studies indicate contrast generation potential at all tested temperatures ranging from 14 °C to 38 °C (287 to 312 K). The CEST spectra also show an

increase in contrast generation at the lower temperatures. They illustrate a broader width of useful presaturation offsets at the higher temperatures, and a shift of the optimal offset with temperature. These results agree with previously documented effects of temperature on PARACEST agents [106].

The results are also consistent with expectations of chemical exchange as a function of temperature. Chemical exchange is expected to increase with temperature, and this would theoretically result in a broadening of the peaks, and a trend towards coalescence. Both of these effects were seen with increased temperature. The last observed effect of temperature was an increase in  $T_1$  relaxation times.

### **Effect of Signal to Noise**

There was increased contrast generation with increased number of acquisitions. The signal to noise ratio is known to increase with the square root of the number of acquisitions [44], so the increase in SNR is expected. CNR would be expected to increase by the same amount (with the square root of the number of acquisitions) as SNR because it is the difference of SNR. The increase in CEST effect is likely due to the increase in SNR with increased number of acquisitions.

The imaging experiments highlight this effect. The results showed an increase in CNR with number of acquisitions. For each number of acquisitions, the observed CNR value was used to calculate the predicted corresponding CNR values for all other number of acquisitions. Figure 4-1 shows that the predicted CNR values are within the  $\pm 2$  of the observed CNR values, indicating that the gains in CNR are due to the gains in SNR obtained by increasing number of acquisitions. The calculations for this experiment are included in Appendix B.

## **Presaturation power and Length**

Increasing the presaturation power clearly resulted in an increase in contrast generation. The results indicated that the gain in contrast was not limited, meaning there was no point at which additional power caused a decrease in contrast. The amount of power was limited by both the imaging system and the amount of heat tolerated by the sample. The amount of sample heating was similar between systems, but the amount each coil was capable of supplying without arcing differed vastly between systems.

The amount of contrast also increased with longer saturation times, as indicated by the decrease in signal with the increase of presaturation pulses. The gain in contrast appeared to approach a maximum (with minimum signal) as the time of presaturation increased. This maximum is expected as the system reaches steady state, at which point any additional bulk water proton saturation will correspond to an earlier saturated proton losing its saturation, resulting in no gain in contrast. The difference between 2000 and 4000 pulses was small in both the imaging and spectral experiments, but in all cases except the image at 4  $\mu$ T 4000 pulses resulted in more contrast generation than 2000 pulses. This indicates that a gain in contrast may be possible by increasing the presaturation time from 2 to 4 seconds. The resultant gain in most cases will not be large enough to justify effectively doubling the total scan time. However in systems which are limited to low powers, increasing presaturation time can be used to achieve comparable contrast.

## **Cell Labeling**

The results of the cell labeling experiments did indicate successful contrast generation. The labeling media was included in the phantom as a positive control to ensure the presaturation was sufficient to generate contrast. The labeling media was easily identifiable, and generated significant contrast. The cells in this phantom were imaged in solution (not agarose) and were

allowed to sink to the bottom of the tube. The cells did not generate significant contrast. There are several reasons this may be the case. The most obvious explanation is that the labeling did not work, and the cells retained no contrast agent. An alternate explanation is that the cells did uptake the label, but once in the cell the contrast agent was no longer able to generate contrast. The ultimate destination of the contrast agent within the cell is unknown, and thus the water exchange is also unknown. As previously discussed, this contrast is highly dependent on the chemical exchange of the contrast agent with its surrounding water. If the cell compartmentalized the contrast agent into an area with extremely restricted water exchange, the contrast would not be generated.

Lastly, there may have been contrast generation, but this contrast is calculated by the difference between the area with the contrast agent and the area without contrast (water). Each phantom is constructed to include ddH<sub>2</sub>O for comparison. In this phantom, the ddH<sub>2</sub>O generated contrast. This indicates a high probability that the labeling media leaked into the surrounding water. Because all of the tubes in this phantom were constructed of open ended capillary tubes closed with clay, there is chance that they all leaked into the surrounding water. In addition to elucidating the possibility of leaking, the contrast in the surrounding water negated the ability to make a CNR, because the SNR<sub>water</sub> was not valid. There may have been some contrast generation in the cells, but the amount was negligible compared to the labeling media and the surrounding water.

Previous studies used Eu-2 to generate contrast in a cell pellet [69]. The same labeling protocol was followed in this study, but the cells were allowed to sink to the bottom rather than creating a cell pellet. There are two possible explanations why this study failed to generate contrast. The first is that each cell contains only a minute amount of contrast agent. Allowing

the cells to remain somewhat dispersed in solution may have caused the contrast to be dispersed as well, which would result in very low concentration of the contrast agent in each the imaging voxel. As shown previously, there is a minimum amount of contrast agent needed to produce detectable contrast, and the cell solution did not meet this threshold. Alternately, the cells may have restricted the amount of chemical exchange possible for the contrast agent, which would also negate its ability to create contrast. The cell pellet formation either localized all the cells increasing the total concentration or possibly destroyed the cells releasing the contrast into solution, allowing for free chemical exchange. In either case, this contrast agent would not be optimal for molecular imaging, as either it does not have a high enough concentration per cell for cellular imaging, or its chemical exchange is no longer favorable within cells. As such, this agent was determined not to be optimal for cell labeling studies.

### **Simulation**

MATLAB simulations were made to see the effect of different variables on the resulting CEST spectra for a PARACEST agent. Each simulation was done allowing only one variable to change, while holding others constant, in order to pinpoint the effect of the initial variable. By evaluating the effect of several variables, the optimal values can be determined. This information can be used for future studies, to determine what agents have the greatest potential.

### **Relaxation Times**

The results of the simulation indicated that an increase in  $T_1$  increases the contrast generation potential. This increase in contrast illustrates the effect of longer  $T_1$  values increasing the efficiency of CEST. This can be derived from the modified Bloch equations resulting in Equation 4-1 [87].

$$Z = \frac{\tau}{T_1 + \tau} \quad (4-1)$$

$Z$  is the equilibrium bulk water magnetization, which is proportional to the observed water signal,  $\tau$  is the lifetime of a proton in the bulk water, and  $T_1$  is the  $T_1$  relaxation time of the bulk water. This equation predicts that longer the  $T_1$ , the lower the magnetization, which would result in a greater decrease in the bulk water signal. This also theoretically makes sense, because the longer  $T_1$  would allow protons to retain their saturation longer, which would allow for longer presaturation times increasing the amount of total saturation.

The simulation of changing  $T_2$  indicated that decreasing  $T_2$  resulted in an increase in width of the bulk water peak in the CEST Spectra, with little effect of the CEST effect. This illustrates that with short  $T_2$  values, there is greater direct saturation of bulk water farther off resonance.

In reality, it is generally not possible to increase or decrease the relaxation values of a given sample/system without the addition of other contrast agents. This could result in a change in the amount of viable contrast generated by PARACEST agents. However, knowing the effect of the relaxation parameters on different contrast agents would allow selection of specific targets or tissues which would most benefit from this type of contrast. For example, knowing that systems with large  $T_1$  values would benefit from PARACEST agents, areas of the brain like the ventricles with documented  $T_1$  values of 2.77 s at 17.6 T [45] would be likely be a better target than tissues with shorter values like the corpus callosum ( $T_1$  of 1.88 s at 17.6 T [45]). Also,  $T_1$  was found to increase with temperature, so if the sample system permits higher temperatures, the CEST effect may be increased with sample heating with careful attention to the effect of temperature on chemical exchange (which also increases). The limited effect of changing  $T_2$  on the amount of CEST contrast generation indicates that tissues with varying  $T_2$  would still be good candidates for PARACEST contrast, however the increased direct saturation of bulk water

with decreased  $T_2$  values indicates that tissues with very short  $T_2$  would need a PARACEST with a larger  $\Delta\omega$  to compensate.

### **Chemical Shift Differences**

The simulation showed that changing  $\Delta\omega$  alone only effected the location of the bound water peak. But the shifts closest to water (Figure 3-31-B) show how could be beneficial. For a contrast agent with a  $\Delta\omega$  close to water, the bulk and bound water peaks may be close enough together so as to be indistinguishable. Going to higher fields will increase  $\Delta\omega$ , and allow the two peaks to be resolved.

### **Chemical Exchange Rates**

Increasing the chemical exchange rate resulted in an increase in contrast generation to a point, and then a decrease. This indicated that there is an optimal value for the chemical exchange, which is consistent with expectations. When the exchange is too slow, the exchange will not meet the requirement that  $\Delta\omega\tau_M \geq 1$ , and no contrast will be generated. Likewise, if the exchange is very slow, it just meets the requirement, and a small amount of contrast will be generated. At this point, increasing the chemical exchange will allow greater contrast to be generated. However, once the chemical exchange can become too fast, which is shown in the simulation by the decrease in CEST with exchange rates of 8000 and 10000. Both of these simulations also show an increase in the width of the bulk water saturation. As the chemical exchange goes from intermediate to fast, the effect of the contrast agent changes. When the exchange is slow to intermediate, the contrast effects only the bound pool of protons, and this pool can exchange with bulk water. However, when the exchange becomes very fast, the effect is then seen as bulk water effect. This bulk water effect can be utilized for other types of contrast generation, as with gadolinium agents which have very fast exchange and are efficient  $T_1$

relaxation agents. But for PARACEST contrast, this increase in chemical exchange rate to fast exchange would be detrimental, as eventually it would no longer be possible to differentiate (and saturate) the bound water pool.

### **Presaturation Power**

In agreement with the findings of the previous section, the simulation showed that an increase in presaturation power resulted in an increase in contrast generation. However the simulation was used to show the results of much higher powers than were actually tested. This highlights one of the main benefits to using computer simulations: the ability to test parameters which may cause damage in real life. The simulation showed that at very high powers, the gain in contrast reaches an approximate maximum. It also shows an overall decrease in signal, signifying broader saturation, and more power deposition into the system. Notably, it may actually indicate an optimal value for the power. The decrease in the CEST effect on the positive side of water levels out, and appears to reach a minimum. However, since most PARACEST contrast is done as a difference image it is important to note that the water signal on the negative side of water is also decreasing, so the difference will actually decrease.

### **Concentration**

The simulation shows an increase in CEST contrast with increasing concentration, in agreement with expectations and previous findings. The concentration was simulated by changing the ratio exchangeable protons to bulk protons. For molecular imaging, the concentration will likely be limited by the amount of contrast agent which can be tolerated in a cell or system. However, the simulation and the data show that contrast will increase with concentration, so the highest possible concentration is desirable.

### **Temperature Fit**

The values for  $T_1$  were measured for each of the temperatures at which data were collected, and these values were used to fit the data. The chemical exchange rate, the  $T_1$  relaxation times, and the  $\Delta\omega$  values were allowed to vary for the temperature fit. The results showed that the fit and the data matched very well, with  $R^2$  values between 0.991 and 0.998. Upon further inspection, the values of the chemical exchange from the fit increase with increasing temperature, and the  $\Delta\omega$  also shifts towards water.

### **Number of Acquisitions Fit**

The number of acquisitions data and fit were in good agreement with  $R^2$  values between 0.985 and 0.994. However, upon closer inspection, the only variable which changed between fits in the simulation was the chemical exchange rate and the RF irradiation. There is no physical reason that an increase in number of acquisitions would increase the chemical exchange rate, and the RF irradiation was not changed between acquisitions. There is also a visible difference between the fit and the data at the points farthest from water, especially with 32 and 64 acquisitions. The simulation assumes approximate steady state, which is likely not actually obtained. The success of this simulation to fit the data shows its versatility, but also illustrates its fallibility, as the values for chemical exchange and irradiation are not accurate. It also illustrates the importance of carefully considering the values of resulting variables for feasibility, before accepting the results.

### **Conclusions**

The overall purpose of this study was to optimize contrast agents for use in high magnetic fields. The results showed several important results, most notably the fact that there is no one perfect contrast agent for high magnetic fields. The best contrast agent will depend on several variables, not just the increased magnetic field strength.

Traditional  $T_1$  contrast agents used in this study were shown to decrease in efficacy at high field strengths. This does not negate their utility, especially at lower magnetic field strengths. Because of their positive contrast and low toxicity profiles, gadolinium based contrast agents will likely remain one of the more prominent contrast agents. However, because of their decreased efficacy at high magnetic fields, they would not be an optimal choice for ultra high field MRI.

Traditional  $T_2$  contrast agents were shown to slightly increase efficacy at high fields, but they will likely suffer from higher susceptibility artifacts at high field strengths and a high incidence of false positives. That being said, iron oxides maintain especially great promise for further use in cellular and molecular imaging, including ultra high field MRI.

PARACEST contrast agents are relatively new type of contrast, but hold great promise, especially at higher field strengths. This study showed an increase in contrast generation for current europium based contrast agents. It also showed the ability of different contrast agents that were unable to generate contrast at lower magnetic field strengths to generate PARACEST contrast at ultra high magnetic fields. There are several other factors contributing to a PARACEST contrast agent's utility for cellular and molecular imaging, which will be discussed further below. However, the overall conclusion is that the PARACEST agents have great potential for use in cellular and molecular imaging using ultra high field MRI.

MRI benefits from increased SNR at high fields. PARACEST contrast enjoys the same benefit, but also the added benefits of increased  $\Delta\omega$ . One study [45] found that ultra high fields increased the  $T_1$  relaxation values in all measured areas of tissue in mouse brain. PARACEST contrast would benefit from this increase in  $T_1$  with increased CEST efficiency. The iron oxides would benefit from the added SNR, but may suffer from increased susceptibility artifacts leading

to image distortion especially in the  $T_2$  weighted images which would best enhance the iron oxide contrast [107].

While PARACEST results in a negative contrast, it is often taken as a difference image with one image taken on the resonance of the bound water pool and the other on the opposite side of the bulk water peak. Areas of hypointensity intrinsic to the image would appear dark in both of the image, and thus cancel out of the difference image. As such, PARACEST agents avoid the inability to differentiate between inherent hypointensity and hypointensity caused by the contrast. In this aspect, PARACEST agents have the advantage over iron oxides.

PARACEST agents are detectable at concentrations down to 0.4 mM and generate greater contrast with increased concentration, but iron oxides maintain the largest contrast generation potential per unit metal. In this sense, for applications with very limited amount of contrast agent, iron oxides would likely be the better candidate.

PARACEST agents are dependent on chemical exchange, which itself is effected by variables including temperature, pH and surrounding chemical environment (presence of small molecules). This leads to a sensitivity of PARACEST agents to these variables, in some cases [73,74,77,79,108-111,104-106] meaning that the contrast agent can be used to monitor those variables. This ability to monitor pH, temperature and small molecules adds physiological information too otherwise purely anatomical images, a good first step towards molecular imaging.

The utility of a given PARACEST agent is going to depend not only on the pH and temperature, but also the field strength (as previously discussed) and the presaturation power and duration. Increased duration of presaturation will initially yield good improvements in contrast (up to  $\sim 2$ s), but eventually will give diminishing returns relative to the increase in time for

imaging. And the power will also give good returns for increased power levels, but is limited by the ability of the system to apply the power efficiently (and homogenously), and by the ability of the sample to tolerate a certain amount of power deposition. Additionally the amount of PARACEST contrast will be highly sensitive to movement. If the contrasted portion of the sample moves at all between scans, the difference image will no longer be valid.

The general conclusion of this study is that iron oxides and PARACEST agents are both viable options for high field MRI. Each has advantages, and should both be considered depending on the intended use. Further discussion for future uses is included in the final chapter of this study.

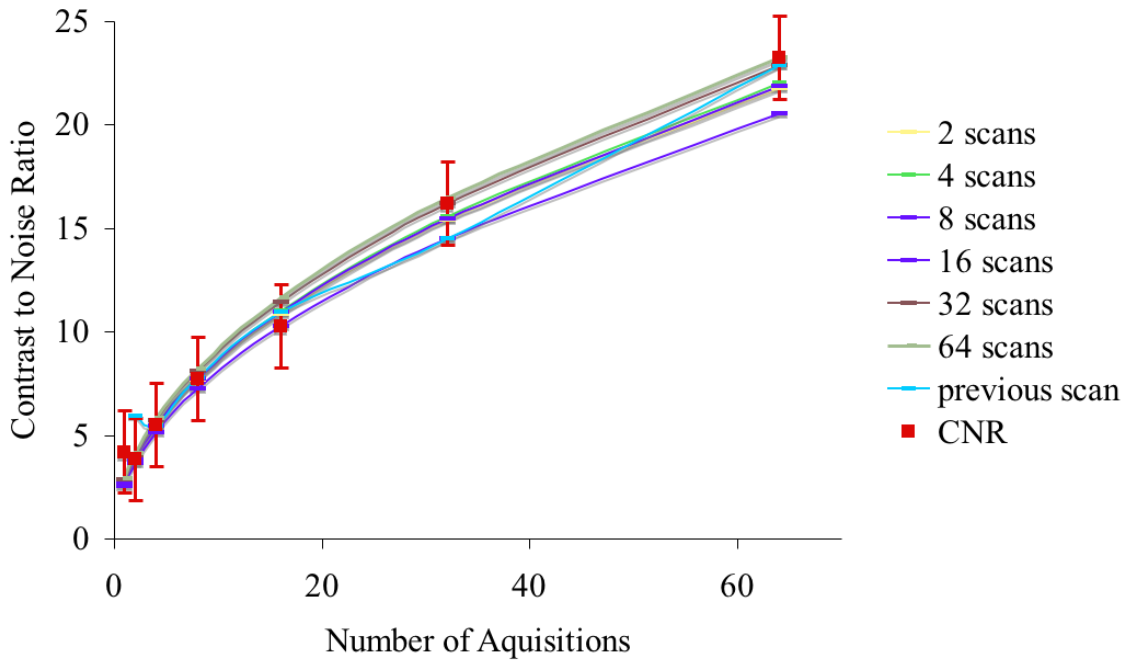


Figure 4-1. Number of acquisitions versus CNR. Each series is the data point indicated, with the other points calculated based on a gain in SNR proportional to the number of acquisitions relative to that point. The error bars illustrate that the predicted gains are within +/- 2 in most cases, which is within the error of the measurement.

## CHAPTER 5 FUTURE PERSPECTIVES

Magnetic Resonance Imaging is both noninvasive and nondestructive. It has proven its utility as a medical imaging modality, and is currently used to diagnose a myriad of conditions ranging from vascular diseases [112-115] to cancers [116-119] (and more). And these studies are all done at 1.5 or 3 T. With the increased resolution afforded by higher magnetic field strengths, it is easy to conclude that higher field imaging could be an even more powerful diagnostic tool. That being said, the contrast agents currently used in medical imaging are optimized for the lower field strengths. As higher fields are becoming more and more available, the need arises to evaluate the current contrast agents at high fields, and investigate possible alternatives.

First, gadolinium has been the gold standard for medical imaging contrast for years. Although recently iron oxides have come into favor for liver imaging [61,64,65], gadolinium remains the choice for pretty much everything else (from brain scans to lumber/thoracic spinal imaging) with an estimated 30% of all MRI scans done with gadolinium based contrast enhancement [47]. It was the obvious starting point for MRI contrast investigation. Unfortunately the contrast of the gadolinium complex did not improve, and in fact decreased in efficacy at higher field strengths.

However, gadolinium still has the benefit to easily obtained positive contrast at lower field strengths. It is therefore is still being investigated by others as a cell labeling contrast agent. One study used poly ethylene glycol (PEG) coated liposomes loaded with Gd<sup>3+</sup> chelates to successfully target inflamed endothelial cells in vitro, and concluded the results implied possible future use for disease diagnosis and therapeutic efficacy tracking [120]. Other studies investigated several routes for cell labeling with gadolinium contrast agents, including via

transfection agents[121], receptor targeting [122,123] and pinocytosis (cells incubated in media with a high concentration of contrast agent) [124,125]. Aime et al. concluded that MRI cell visualization was possible when a minimum concentration of Gd chelates was met ( $10^7$ - $10^8$  chelates/cell) [67]. Gadolinium agents have also been used to evaluate gene therapy for experimental brain tumors [126]. The general conclusion of these studies was that further investigation of cell tracking studies using gadolinium-based agents was warranted.

It is the conclusion of this study that gadolinium agents will still provide an excellent choice for contrast generation at lower fields, but when moving to ultra high fields there will likely be better alternatives, including iron oxides and PARACEST agents.

Ferumoxides are usually used to create a negative contrast, with the previously discussed disadvantages associated with hypointensity, namely the inability to distinguish between hypointensity created by contrast and hypointensity inherent in the sample/patient. However, the greatest signal change per unit metal [93] is a huge advantage, and therefore causes a lot of interest for cell labeling. This study showed that there was some improvement in  $T_2^*$  with increased field strength, so they remain viable options for high field contrast generation.

Multiple groups have stated that iron oxides are the best candidates for molecular imaging via MRI [63,93]; a very strong claim. But there are various studies which seem to back up that claim. Weissleder et al. used iron oxide nano particles conjugated to polyclonal IgG antibody to image induced liver inflammation and cancer *in vivo* [127] and myocardial infarction *ex vivo* [128]. Other groups have found that it is possible to use iron oxides in MRI to target specific processes including apoptosis [129], atherosclerosis [130] and amyloid plaque deposition in Alzheimer's [131]. Zhu et al. used iron oxides to track the migration of neural stem cells and showed that the label had no effect on the ability of the cells to differentiate into

astrocytes and neurons during migration [132]. Several studies have come out investigating the use of monoclonal antibodies for tumor specific iron oxide particles [133-135]. Shapiro et al. has reported single cell detection using iron oxides [96,136,88].

Also, notably several groups have introduced pulses sequence which causes iron oxides to have positive contrast [137-139]. This is accomplished through spectrally selective excitation and refocusing of spins in the vicinity of the SPIO [137], steady state free precession imaging [138] or inversion of the magnetization in conjunction with a spectrally-selective on-resonant saturation of water [139]. They benefit from the hyper intensity, but the resulting signal to noise is not optimal. With work, however, this type of imaging may prove to be a viable alternative to gadolinium at higher fields.

PARACEST agents are relatively new, but this study shows a substantial improvement with increasing field strength. Aime et al. reported cell labeling with multiple PARACEST agents, and showed the ability to highlight contrast in either agent at will [69]. Exogenous europium based agents with two phenylboronate moieties as the ligands have recently been used to monitor the amount of glucose in livers [140]. In addition to detecting enzyme activity [106], Yoo and Pagel have reported protease responsive PARACEST agents [141] and peptide linked PARACEST agents for molecular imaging [142].

There has been increased research in CEST recently, including advances such as 'GLYCOCEST', 'LIPOCEST' and 'DIACEST'. GLYCOCEST uses the hydroxyl groups on glycogen to create CEST contrast as a means to monitor glycogen [143]. LIPOCEST utilizes liposomes to create more favorable exchange rates and chemical shifts in order to have more lanthanide ions available for use in PARACEST contrast [100,144,145]. DIACEST was introduced with a fast screening mechanism to determine viability of polypeptides for CEST

contrast generation, and then demonstrated the ability to highlight each of several polypeptides independently [146]. All of these mechanisms would benefit from increased contrast at higher fields.

Most importantly, the overall goal is a movement towards molecular or cellular imaging. This is beneficial because currently MRI provides fantastic anatomical information, but little to no metabolic information. MRI should be able to provide this dual functional-anatomical information imaging in the future, and optimized contrast agents will likely play a huge role. However, the type of agent is going to depend on the goal of the individual study. This is not new; currently medical doctors choose between gadolinium and iron oxide contrast agents depending on the patient and the area of interest. Scientists have the options for similar choices, even at high fields. There is lot to gain by going to high fields, especially as the larger magnets become more accessible. And at this point, iron oxides and PARACEST agents make the best contrast.

APPENDIX A  
IRON OXIDES DATA

Single slice multi spin multi echo images were taken at constant  $T_R$  of either 400 ms or 2000 s, with variable  $T_E$  in order to calculate  $T_2^*$ . Those images are included in Figures A-1 and A-2 for 4.7 T, Figures A-3 and A-4 for 14.1 T and Figures A-5 and A-6 for 21.1 T. The  $T_E$  values are indicated in the figure caption.

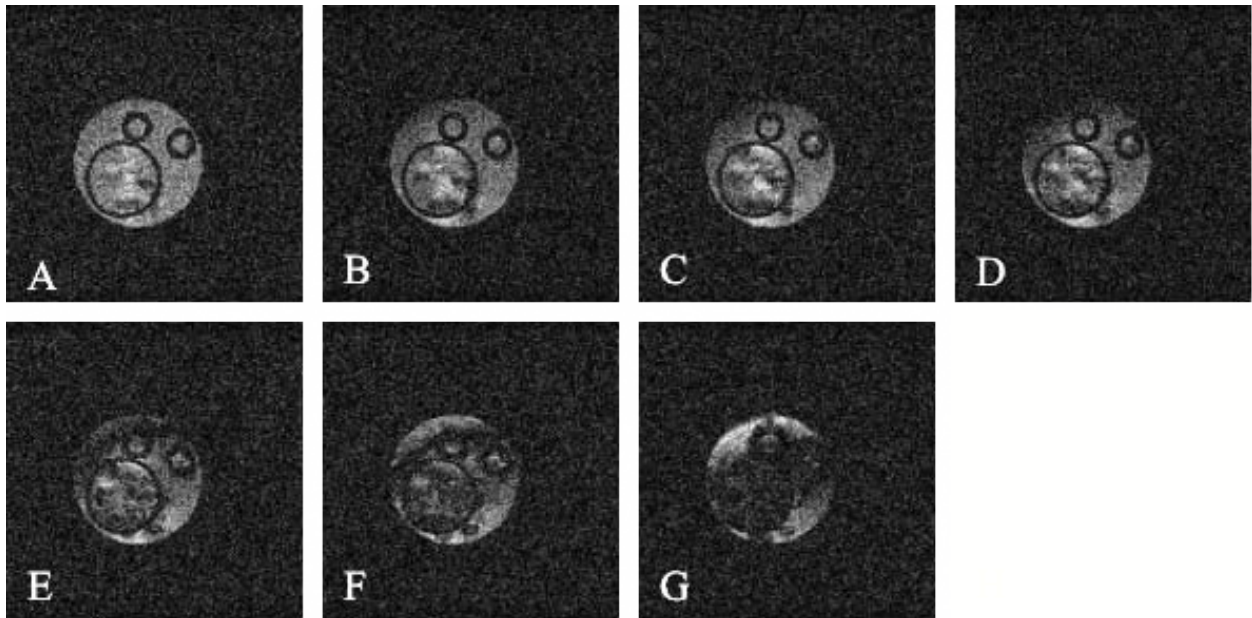


Figure A-1. Iron oxide images at 4.7 T.  $T_R = 400$  ms.  $T_E =$  A) 3.4 ms, B) 9 ms, C) 12 ms, D) 15 ms, E) 30 ms, F) 45 ms and G) 90 ms. The image quality was insufficient to make  $T_2^*$  measurements from.

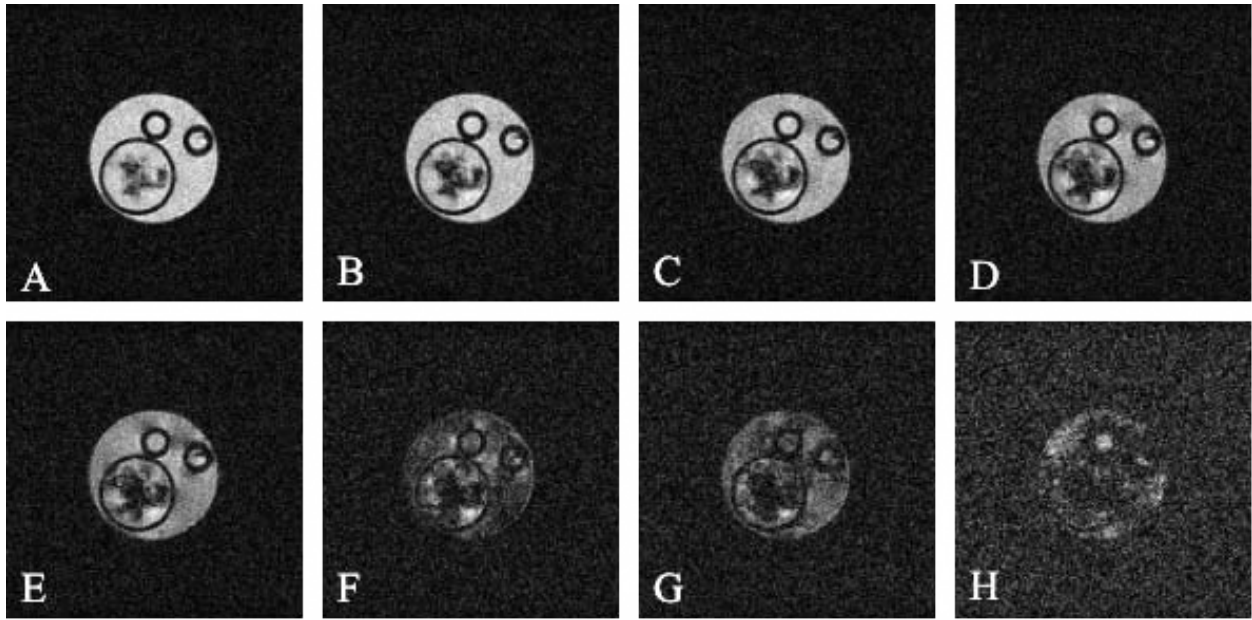


Figure A-2. Iron oxide images at 4.7 T.  $T_R = 2$  s.  $T_E =$  A) 3.4 ms, B) 6 ms, C) 9 ms, D) 12 ms, E) 15 ms, F) 30 ms, G) 45 ms and H) 90 ms. The image quality was insufficient to make  $T_2^*$  measurements from.

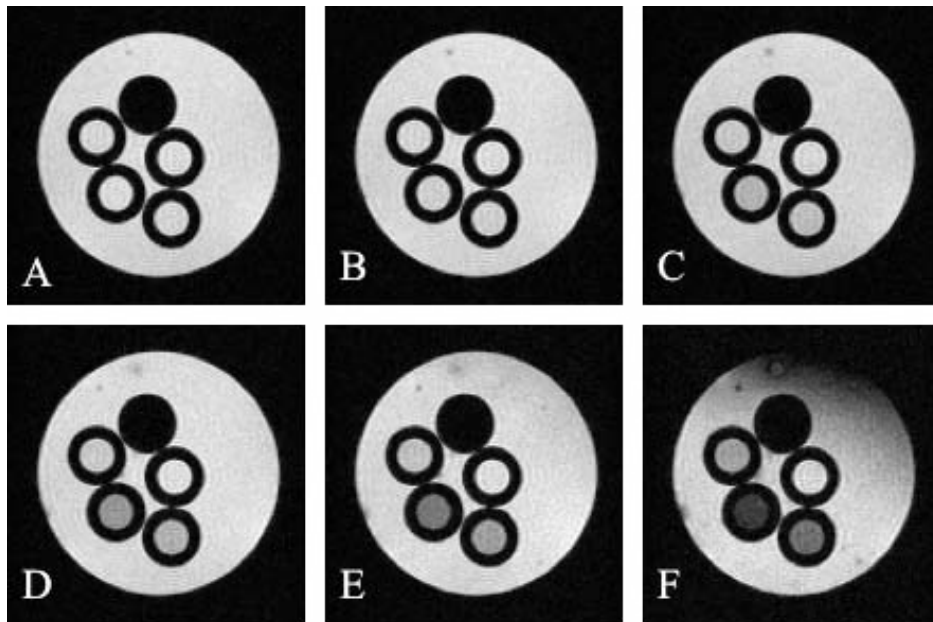


Figure A-3. Iron oxide images at 14.1 T.  $T_R = 400$  ms.  $T_E =$  A) 2.5 ms, B) 5 ms, C) 10 ms, D) 20 ms, E) 30 ms and F) 60 ms. The contents of the tubes are clockwise from top: ferumoxide 1/10 dilution, ddH<sub>2</sub>O, 50 mM ferumoxide, 100 mM ferumoxide, 20 mM ferumoxide.

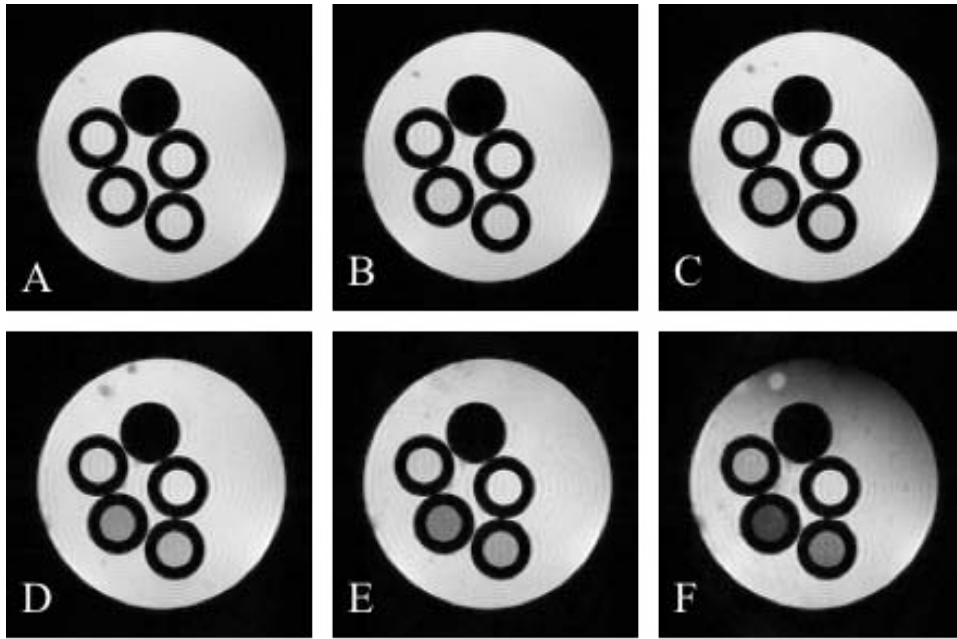


Figure A-4. Iron oxide images at 14.1 T.  $T_R = 2000$  ms.  $T_E =$  A) 2.5 ms, B) 5 ms, C) 10 ms, D) 20 ms, E) 30 ms and F) 60 ms. The contents of the tubes are clockwise from top: ferumoxide 1/10 dilution, ddH<sub>2</sub>O, 50 mM ferumoxide, 100 mM ferumoxide, 20 mM ferumoxide.

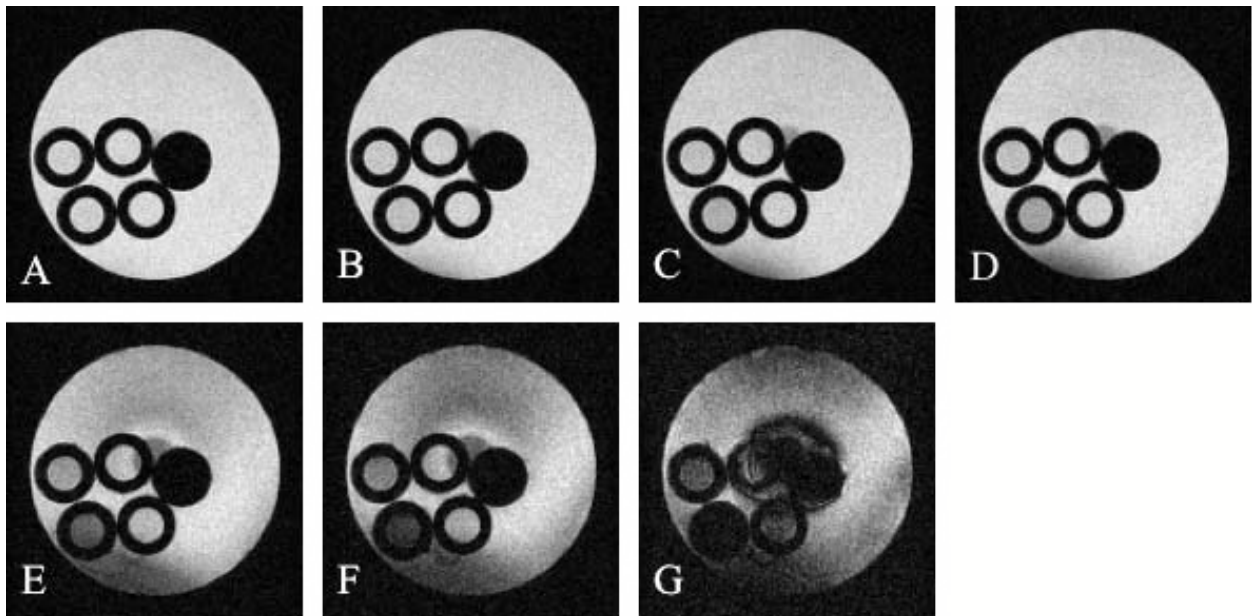


Figure A-5. Iron oxide images at 21.1 T.  $T_R = 400$  ms.  $T_E =$  A) 3 ms, B) 6 ms, C) 9 ms, D) 12 ms, E) 30 ms, F) 45 ms and G) 90 ms. The contents of the tubes are clockwise from right: ferumoxide 1/10 dilution, ddH<sub>2</sub>O, 50 mM ferumoxide, 100 mM ferumoxide, 20 mM ferumoxide.

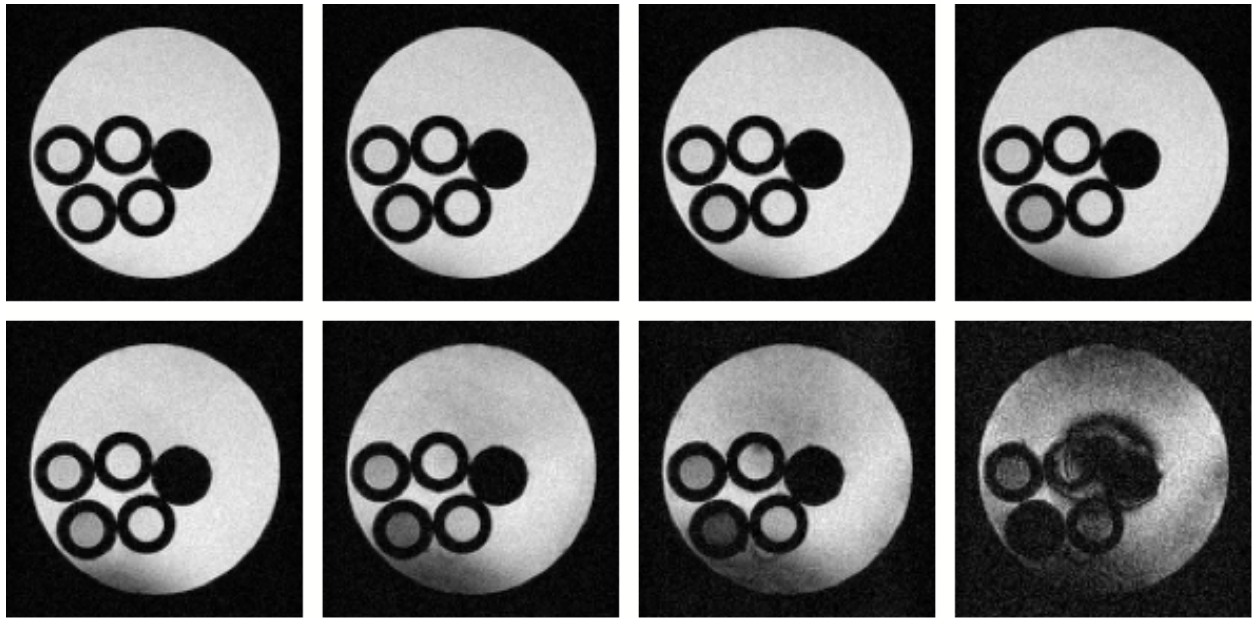


Figure A-6. Iron oxide images at 21.1 T.  $T_R = 2000$  ms.  $T_E =$  A) 3 ms, B) 6 ms, C) 9 ms, D) 12 ms, E) 15 ms, F) 30 ms, G) 45 ms and H) 90 ms. The contents of the tubes are clockwise from right: ferumoxide 1/10 dilution, ddH<sub>2</sub>O, 50 mM ferumoxide, 100 mM ferumoxide, 20 mM ferumoxide.

## APPENDIX B PARACEST AGENTS DATA AND CALCULATIONS

### **Ytterbium, Thulium and Europium PARACEST**

All four ytterbium and thulium complexes were imaged at 14.1 T prior to imaging at 21.1 T. While the results at 900 were very small at best, there were no distinguishable contrasts generated by any of these complexes. Sample images from the region of interest (presaturation on and off the bound water specific to the complex) are included in Figures B-1 – B-6. Three different europium complexes were imaged at various field strengths. The CEST spectrum for all three europium complexes are included in Figure B-7.

### **Europium PARACEST Field Dependence**

To determine the field dependence of the PARACEST agents the phantom containing all three europium agents was imaged field strengths from 4.7 – 21 T and these results are shown in the Results section. The calculations for the CNR values are shown in Tables B-1 – B-4 for 4.7, 11.75, 17.6 and 21.1 T, respectively. This table shows the mean value and standard deviation within each region of interest in the difference image with presaturation at the optimal offset (from which the reported values were taken). The SNR for all non-noise values and the CNR for all non-water values calculated from the mean and standard deviation.

Many of the other phantoms were tested at various field strengths, especially 14.1 and 17.6 T. When the power levels were the same, the results always indicated greater contrast at the higher field strengths. The additional imaging from various field strengths is included in the following appendices, under the type of phantom being imaged.

### **Europium PARACEST Concentration**

The serial dilutions phantom which was presented in the main body of this investigation was imaged many times, at different field strengths. The results indicated similar findings as

were presented, with increasing contrast generation with increased concentration. Figures B-8 – B-10 show the results of these imaging experiments at field strengths of 14.1 T. Figures B-11 and B-12 show the imaging results at 17.6 T. Figures B-13 and B-14 show the imaging results at 21.1 T. The presaturation power ranged from 4 – 128  $\mu$ T as indicated in the figure captions.

Figure B-15 shows the CEST spectrum calculated from the images at 21.1 T. These spectrum suffer from a lot of noise, likely due to the inhomogeneity of the presaturation and the limited number of presaturation offsets.

### **Europium PARACEST pH**

The pH phantoms which were presented in the main body of this investigation were imaged many times, at different field strengths. The results indicated similar findings as were presented, with a shift in optimal presaturation offset with pH, and viable contrast for pH values of 3, 7 and 10. Initial findings indicated no contrast generation at pH 13, but later studies showed contrast, which was attributed to sample degradation or instability in the extremely basic solution. Figures B-16 – B-23 show the results of these imaging experiments at field strengths of 14.1 T, with presaturation power ranging from 4 – 128  $\mu$ T. The presaturation duration was 2 s except for Figures B-22 and B-23. Figures B-24 shows the imaging results at 17.6 T. Figures B-25 and B-26 show the imaging results at 21.1 T. Figure B-27 shows the imaging results at 17.6 T for the pH phantom including the ion rich environment.

### **Europium PARACEST Temperature**

The CEST spectra of a 10 mM Eu-2 sample was taken at 14, 20, 26, 32 and 36 °C. The cumulative results are presented in the main body of the text, but they are individually shown in Figures B-28 – B-32 respectively.

### **Europium PARACEST Signal to Noise**

The individual spectra for each of the multiple acquisition experiments are include as Figures B-33 – B-38 for NS = 1, 2, 4, 8, 32 and 64 respectively.

### **Europium PARACEST Presaturation Power and Duration**

The amount and duration of the applied RF presaturation power was tested on numerous occasions with both the serial dilutions phantom and the second pH phantom. In all cases, when tolerated by the system, higher powers resulted in greater contrast generation. The data was presented in the main body of the text, and also throughout this Appendix (B), as indicated by the labeled presaturation power, or number of presaturation pulses. Figure B-39 shows the effect of increasing power and duration of presaturation on the CNR for the serial dilution phantom, and further illustrates the resulting increase in contrast generation.

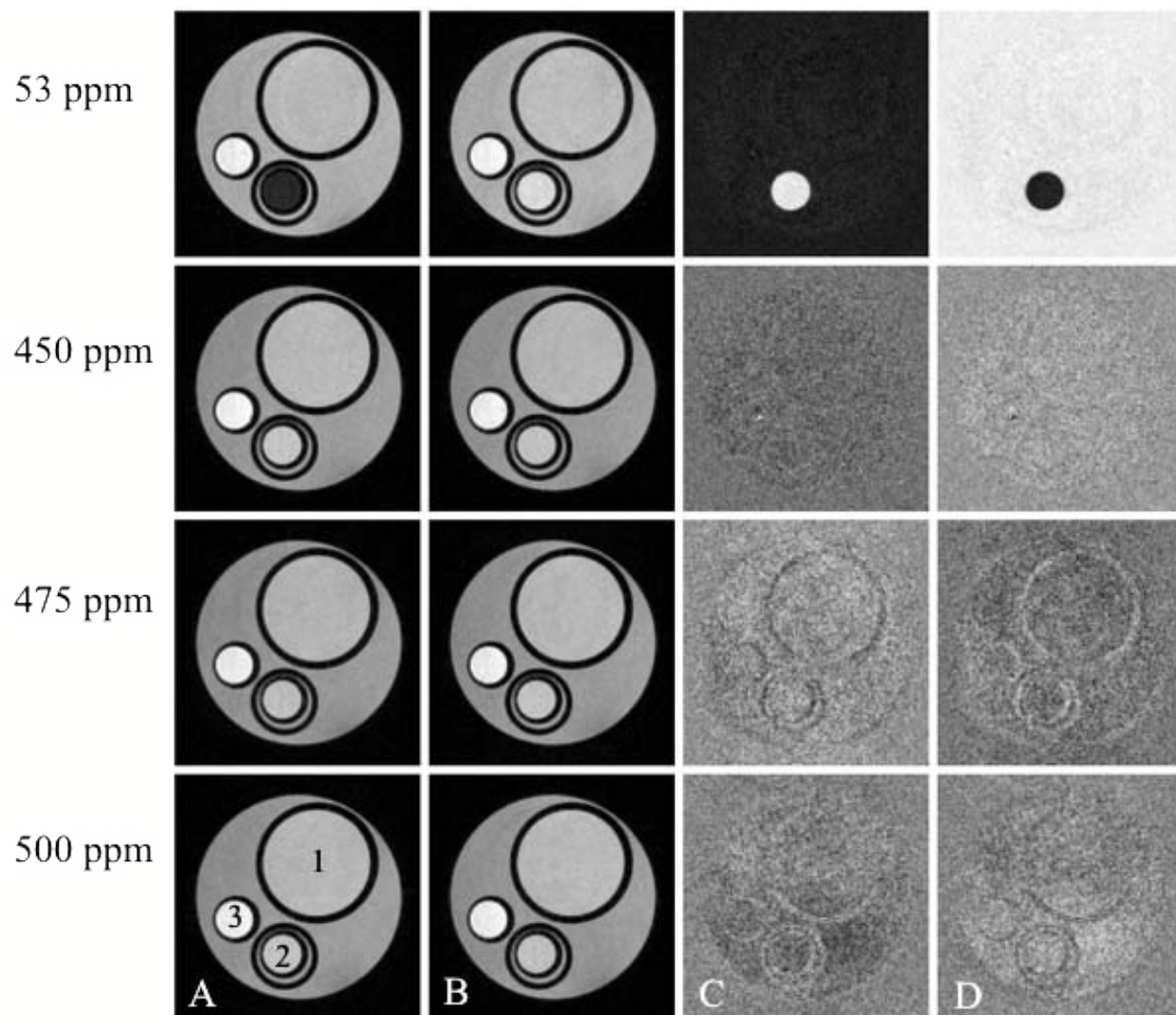


Figure B-1. Thulium complexes at 14.1 T. A) Images taken with the presaturation power applied on the positive side water at the shift listed. B) Images taken with the presaturation power on the opposite side of water at the shift listed. C) Difference images taken to create positive contrast as  $B - A$ . D) Difference images taken to create negative contrast as  $A - B$ . Complexes labeled as 1) Tm-1 10 mM, 2) Tm-2 10 mM and 3) Eu-2 40 mM.

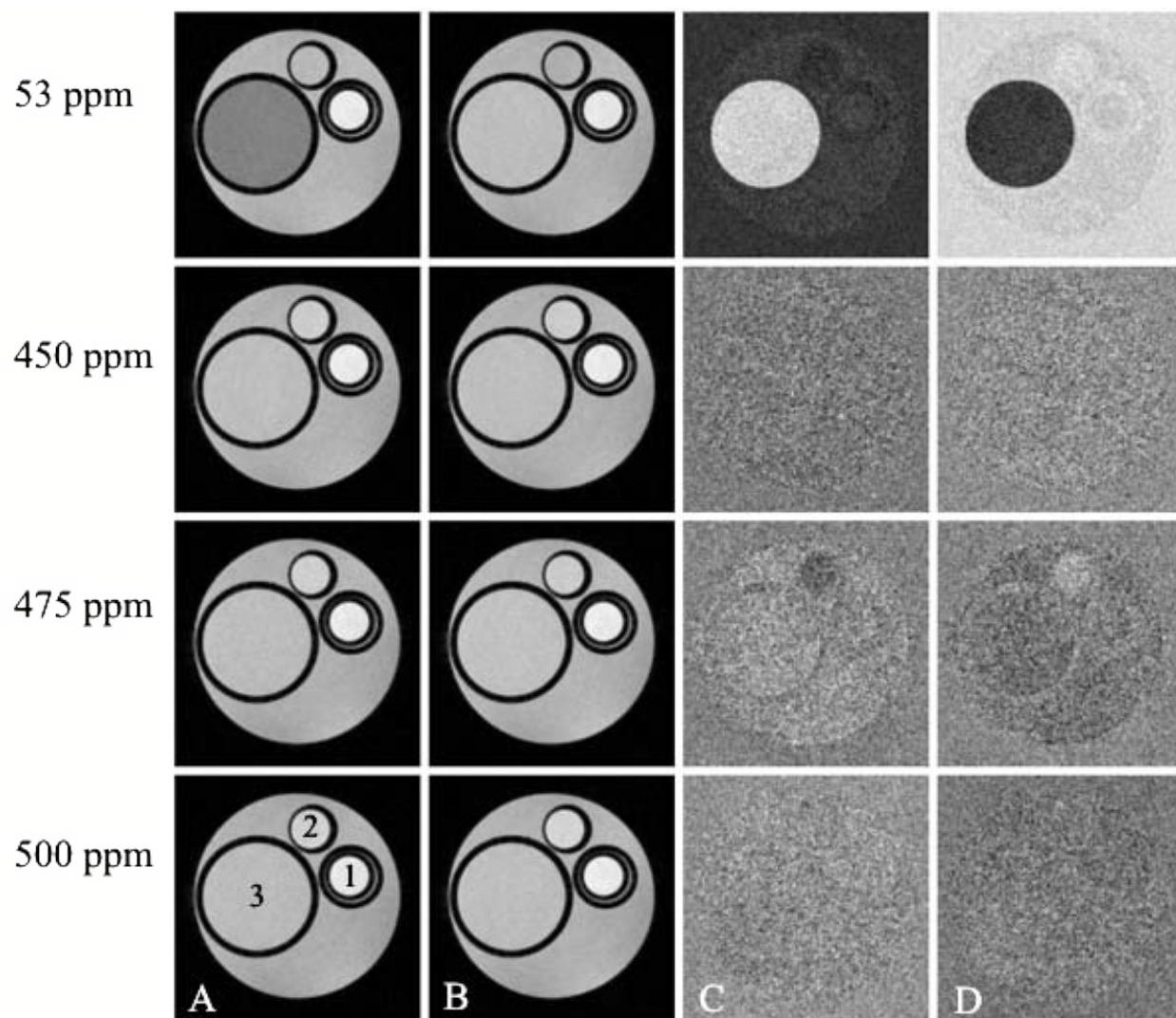


Figure B-2. Ytterbium complexes at 14.1 T. A) Images taken with the presaturation power applied on the positive side water at the shift listed. B) Images taken with the presaturation power on the opposite side of water at the shift listed. C) Difference images taken to create positive contrast as  $B - A$ . D) Difference images taken to create negative contrast as  $A - B$ . Complexes labeled as 1) Yb-1 10 mM, 2) Yb-2 10 mM and 3) Eu-2 10 mM.

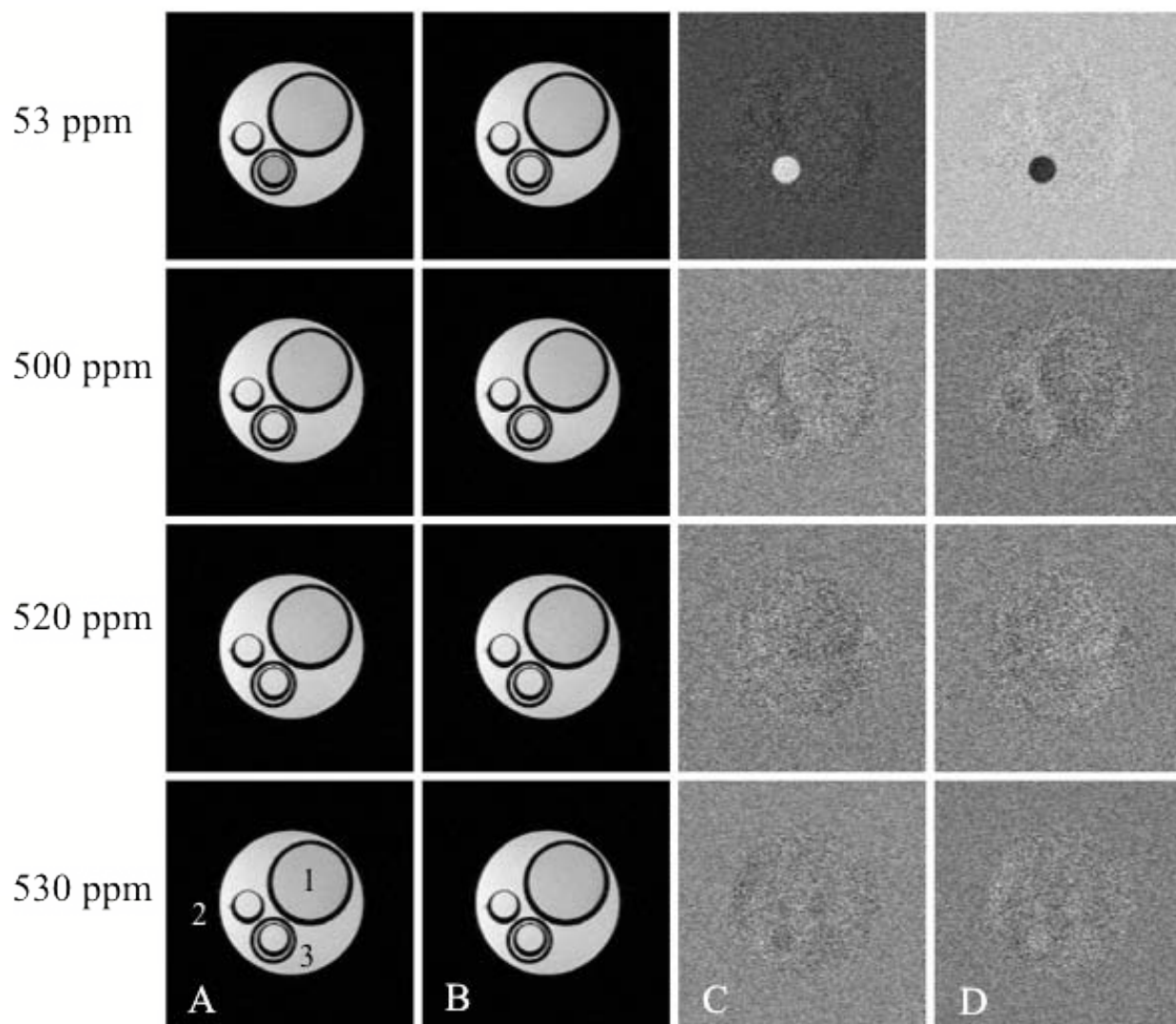


Figure B-3. Thulium complexes at 17.6 T. A) Images taken with the presaturation power applied on the positive side water at the shift listed. B) Images taken with the presaturation power on the opposite side of water at the shift listed. C) Difference images taken to create positive contrast as  $B - A$ . D) Difference images taken to create negative contrast as  $A - B$ . Complexes labeled as 1) Tm-1 10 mM, 2) Tm-2 10 mM and 3) Eu-2 40 mM.

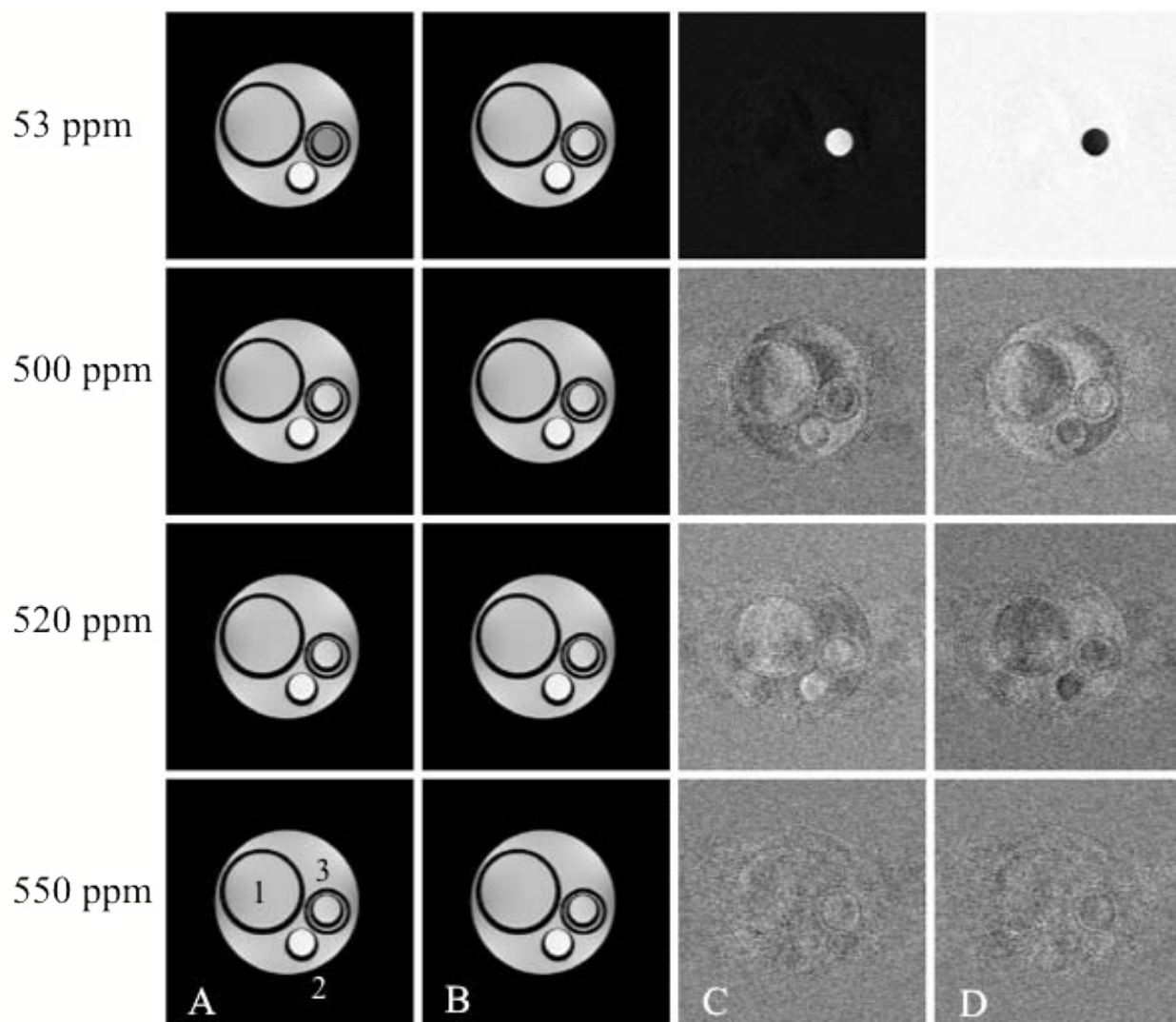


Figure B-4. Thulium complexes at 17.6 T. A) Images taken with the presaturation power applied on the positive side water at the shift listed. B) Images taken with the presaturation power on the opposite side of water at the shift listed. C) Difference images taken to create positive contrast as B – A. C) Difference images taken to create negative contrast as A – B. Complexes labeled as 1) Tm-1 10 mM, 2) Tm-2 10 mM and 3) Eu-2 40 mM.

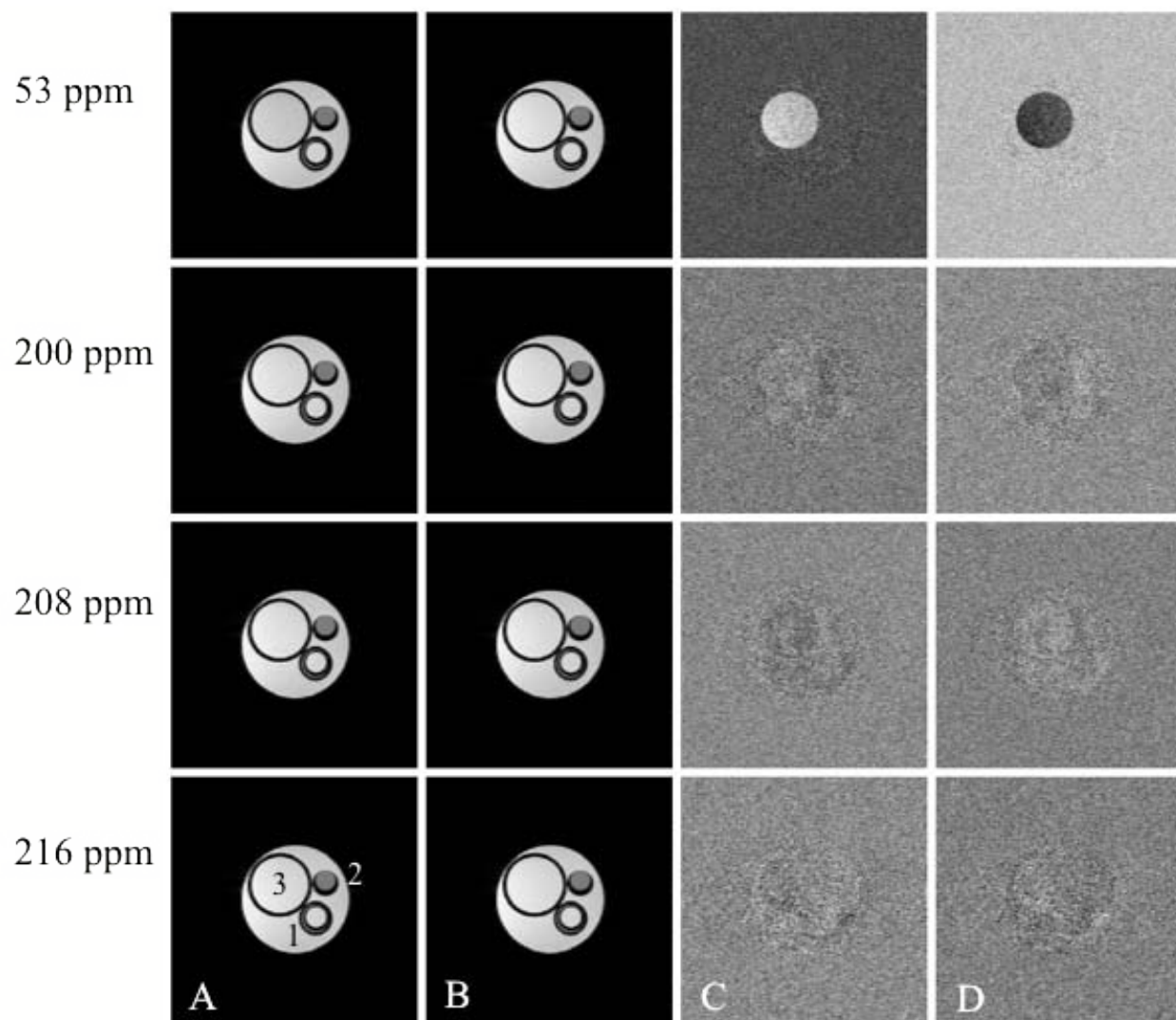


Figure B-5. Ytterbium complexes at 17.6 T. A) Images taken with the presaturation power applied on the positive side water at the shift listed. B) Images taken with the presaturation power on the opposite side of water at the shift listed. C) Difference images taken to create positive contrast as B – A. D) Difference images taken to create negative contrast as A – B. Complexes labeled as 1) Yb-1 10 mM, 2) Yb-2 10 mM and 3) Eu-2 10 mM.

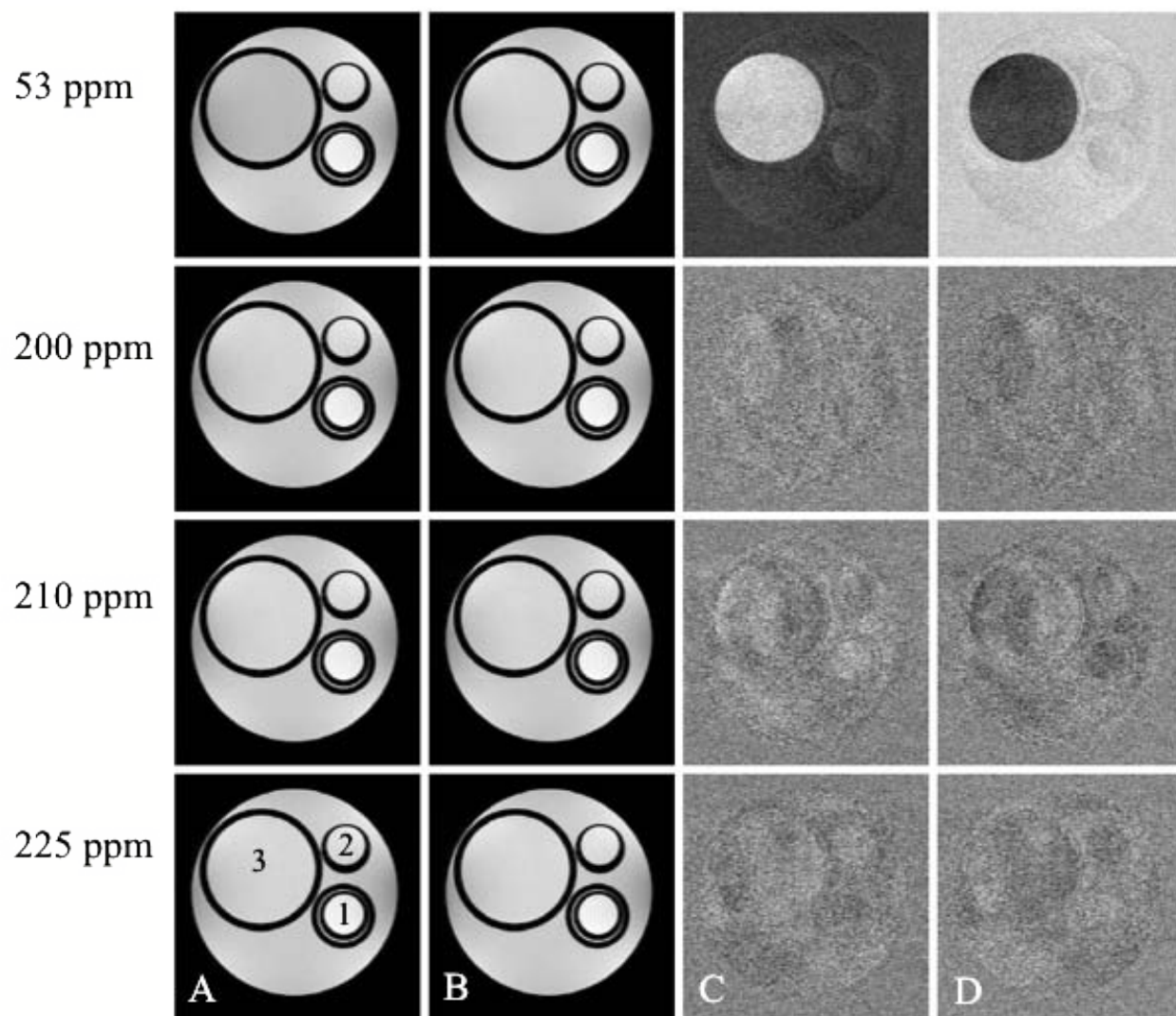


Figure B-6. Ytterbium complexes at 17.6 T. A) Images taken with the presaturation power applied on the positive side water at the shift listed. B) Images taken with the presaturation power on the opposite side of water at the shift listed. C) Difference images taken to create positive contrast as  $B - A$ . D) Difference images taken to create negative contrast as  $A - B$ . Complexes labeled as 1) Yb-1 10 mM, 2) Yb-2 10 mM and 3) Eu-2 10 mM.

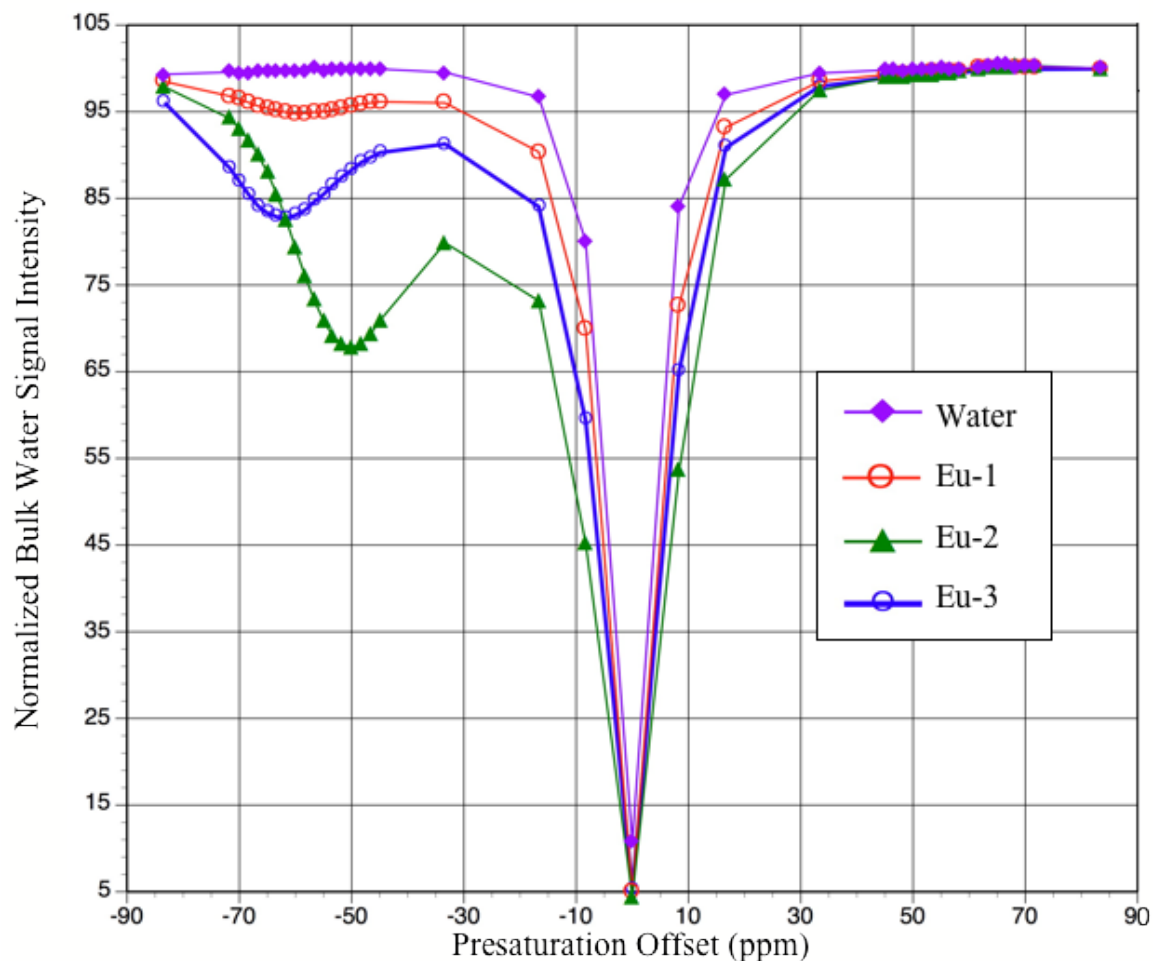


Figure B-7. Europium complexes CEST spectra at 14.1 T. Spectra acquired by taking the signal intensity within regions of interest in images with the presaturation offsets indicated on the x axis.

Table B-1. CNR calculations for 4.7 T.

	offset (ppm)	Mean	Std.Dev.	SNR	CNR	error
Eu-1	65	1086	100157	0	0	1.5
Eu-2	53	-15971	93411	-0.2	0	1
Eu-3	68	69946	10667	1.4	1	1
Water	53	-2919	97646	-0.1		
Water	65	16351	98777	0.2		
Water	68	18202	94921	0.3		
Noise	53	848	70454			
Noise	65	2669	68143			
Noise	68	-1787	74657			

Table B-2. CNR calculations for 17.6 T.

	offset (ppm)	Mean	Std.Dev.	SNR	CNR	error
Eu-1	65	20845	3659	8.4	7.9	1.5
Eu-2	53	91207	4498	39	39	2
Eu-3	68	67368	4116	30	25	2
Water	53	400	3669	0.4		
Water	65	-185	3234	0.5		
Water	68	10761	3414	5.2		
Noise	53	98	1535			
Noise	65	-180	1598			
Noise	68	181	1602			

Table B-3. CNR calculations for 21.1 T.

	offset (ppm)	Mean	Std.Dev.	SNR	CNR	error
Eu-1	65	16099	3320	8.4	8.7	2
Eu-2	53	96201	3202	53	54	1.8
Eu-3	68	70910	2907	37	37	1.5
Water	53	-2982	3038	-1		
Water	65	-111	3301	-0.3		
Water	68	6418	1187	-0.7		
Noise	53	84	1822			
Noise	65	4	1922			
Noise	68	51	1931			

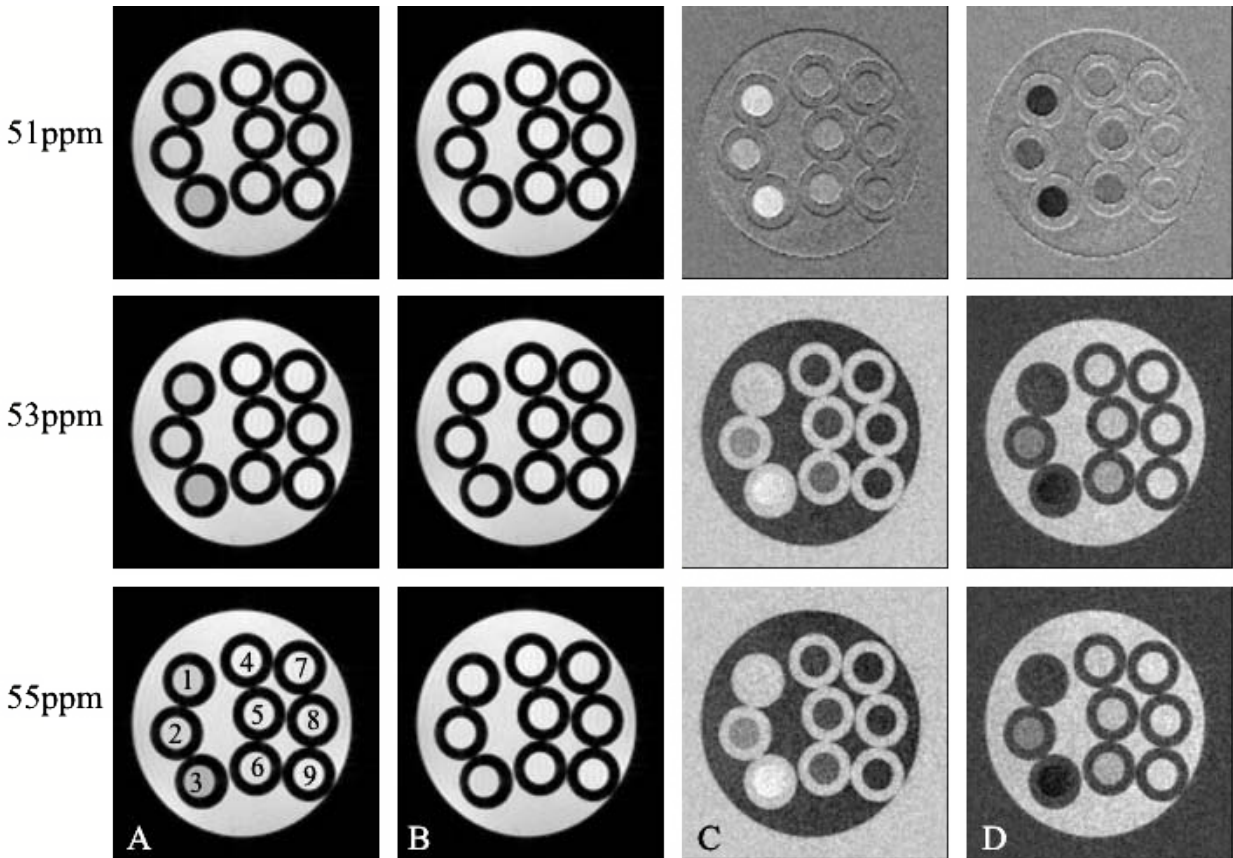


Figure B-8. Serial dilutions at 14.1 T. Presaturation power was  $16 \mu\text{T}$ . A) Images taken with the presaturation power applied on the positive side water at the shift listed. B) Images taken with the presaturation power on the opposite side of water at the shift listed. C) Difference images taken to create positive contrast as  $B - A$ . C) Difference images taken to create negative contrast as  $A - B$ . The concentrations are labeled as 1) 100 mM, 2) 25 mM, 3) 50 mM, 4) 3 mM, 5) 6 mM, 6) 12.5 mM, 7) 0.4 mM, 8) 0.8 mM and 9) 1.6 mM.

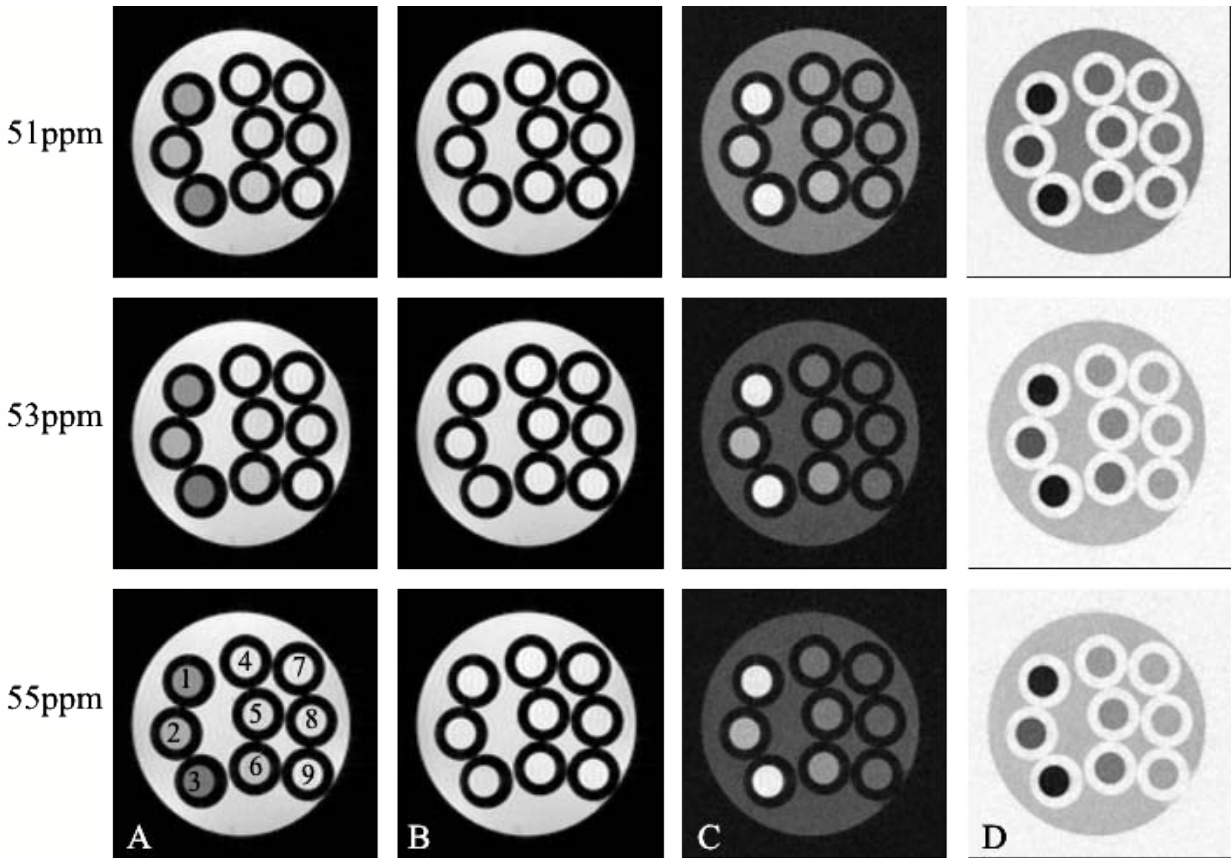


Figure B-9. Serial dilutions at 14.1 T. Presaturation power was  $32 \mu\text{T}$ . A) Images taken with the presaturation power applied on the positive side water at the shift listed. B) Images taken with the presaturation power on the opposite side of water at the shift listed. C) Difference images taken to create positive contrast as  $B - A$ . C) Difference images taken to create negative contrast as  $A - B$ . The concentrations are labeled as 1) 100 mM, 2) 25 mM, 3) 50 mM, 4) 3 mM, 5) 6 mM, 6) 12.5 mM, 7) 0.4 mM, 8) 0.8 mM and 9) 1.6 mM.

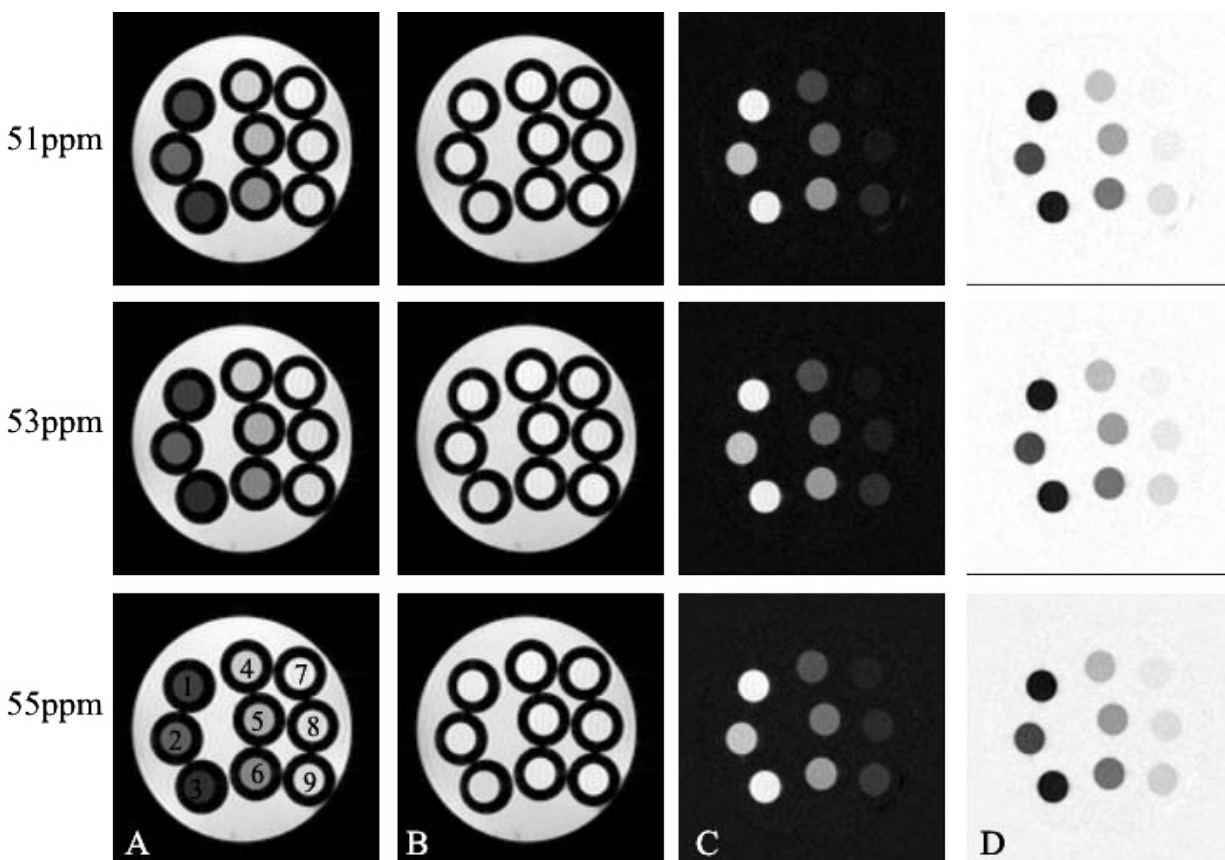


Figure B-10. Serial dilutions at 14.1 T. Presaturation power was  $64 \mu\text{T}$ . A) Images taken with the presaturation power applied on the positive side water at the shift listed. B) Images taken with the presaturation power on the opposite side of water at the shift listed. C) Difference images taken to create positive contrast as  $B - A$ . C) Difference images taken to create negative contrast as  $A - B$ . The concentrations are labeled as 1) 100 mM, 2) 25 mM, 3) 50 mM, 4) 3 mM, 5) 6 mM, 6) 12.5 mM, 7) 0.4 mM, 8) 0.8 mM and 9) 1.6 mM.

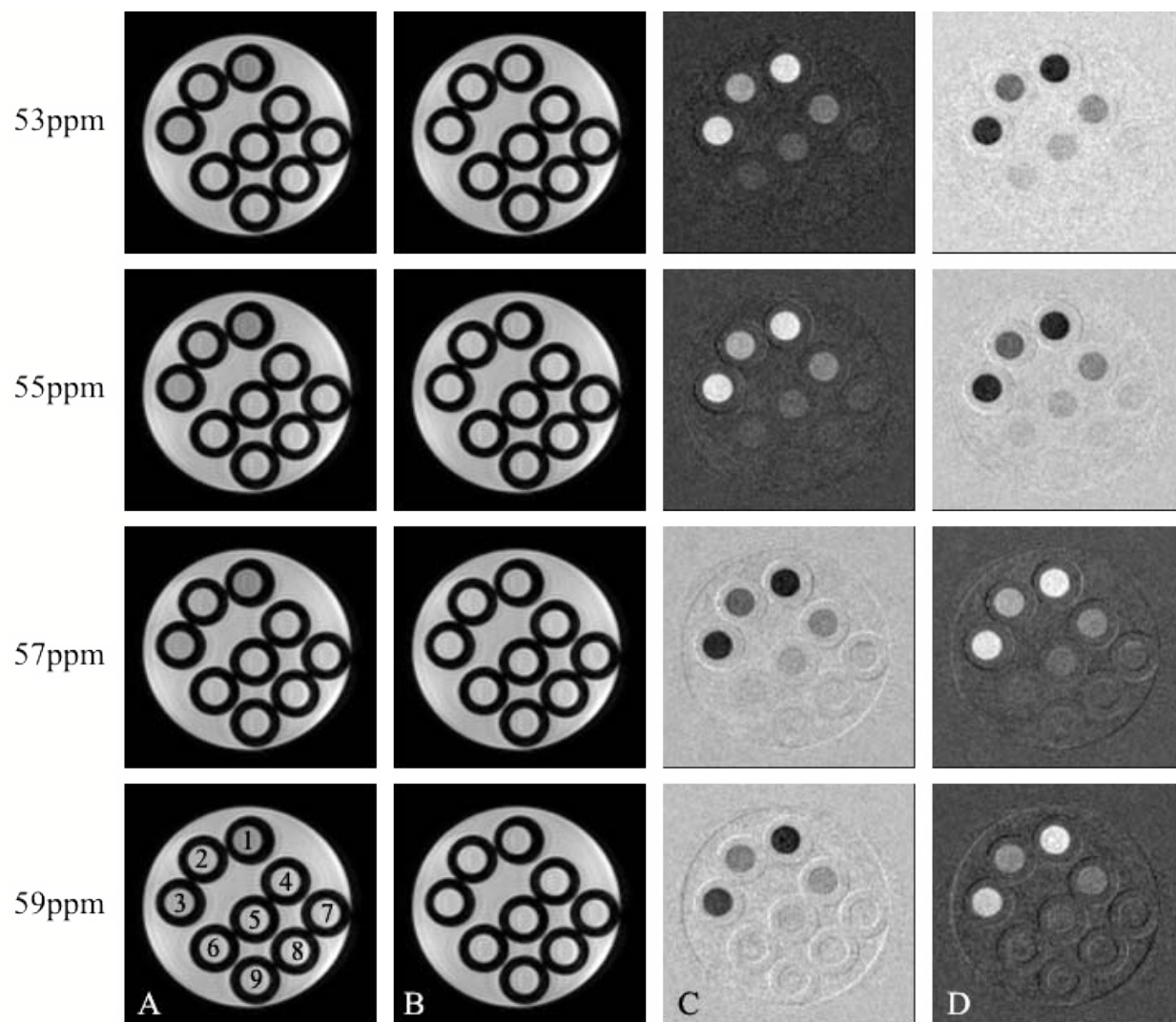


Figure B-11. Serial dilutions at 17.6 T. Presaturation power was 16  $\mu$ T. A) Images taken with the presaturation power applied on the positive side water at the shift listed. B) Images taken with the presaturation power on the opposite side of water at the shift listed. C) Difference images taken to create positive contrast as B – A. C) Difference images taken to create negative contrast as A – B. The concentrations are labeled as 1) 50 mM, 2) 25 mM, 3) 100 mM, 4) 12.5 mM, 5) 6 mM, 6) 3 mM, 7) 1.6 mM, 8) 0.8 mM and 9) 0.4 mM.

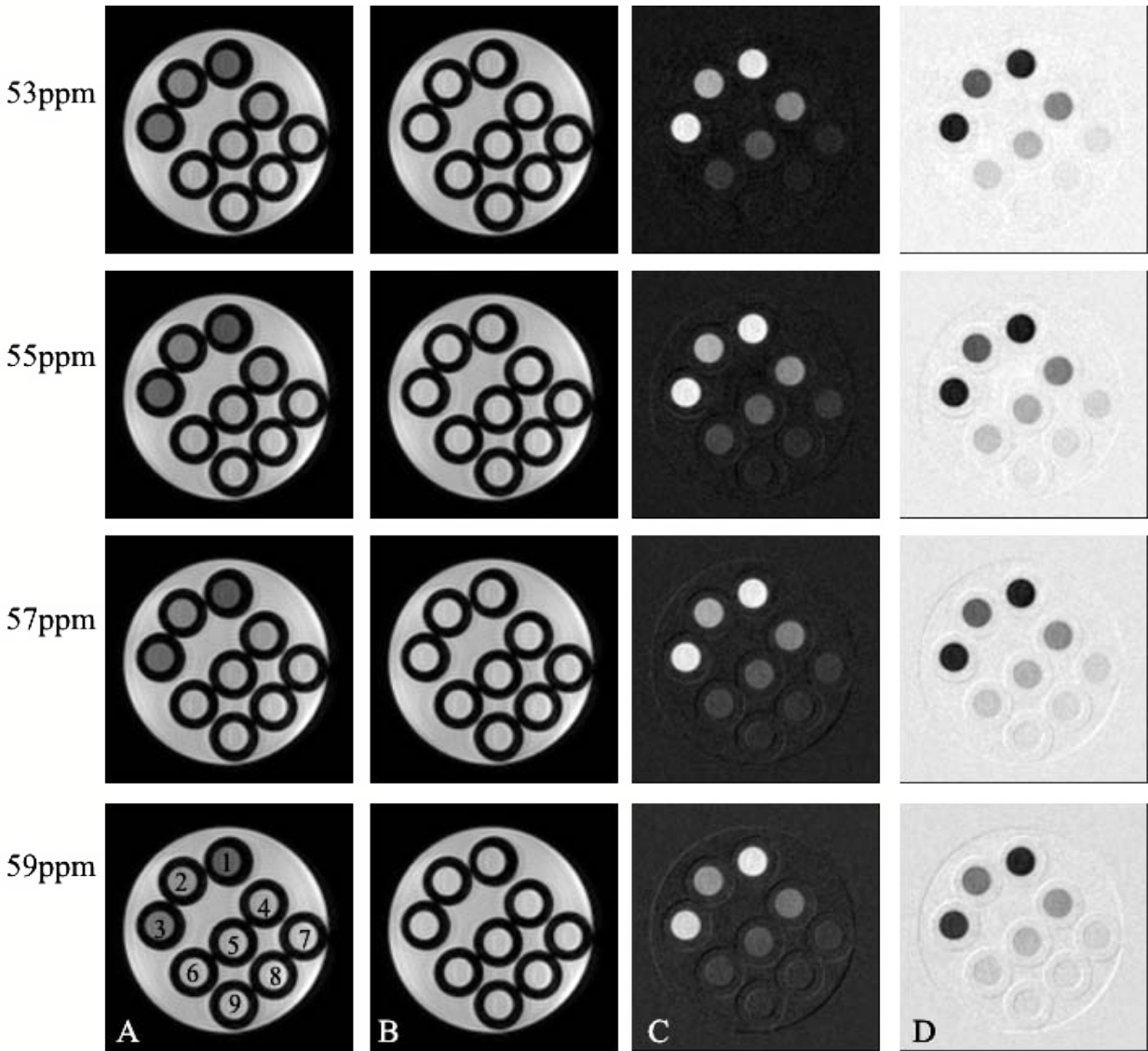


Figure B-12. Serial dilutions at 17.6 T. Presaturation power was  $32 \mu\text{T}$ . A) Images taken with the presaturation power applied on the positive side water at the shift listed. B) Images taken with the presaturation power on the opposite side of water at the shift listed. C) Difference images taken to create positive contrast as  $B - A$ . C) Difference images taken to create negative contrast as  $A - B$ . The concentrations are labeled as 1) 50 mM, 2) 25 mM, 3) 100 mM, 4) 12.5 mM, 5) 6 mM, 6) 3 mM, 7) 1.6 mM, 8) 0.8 mM and 9) 0.4 mM.

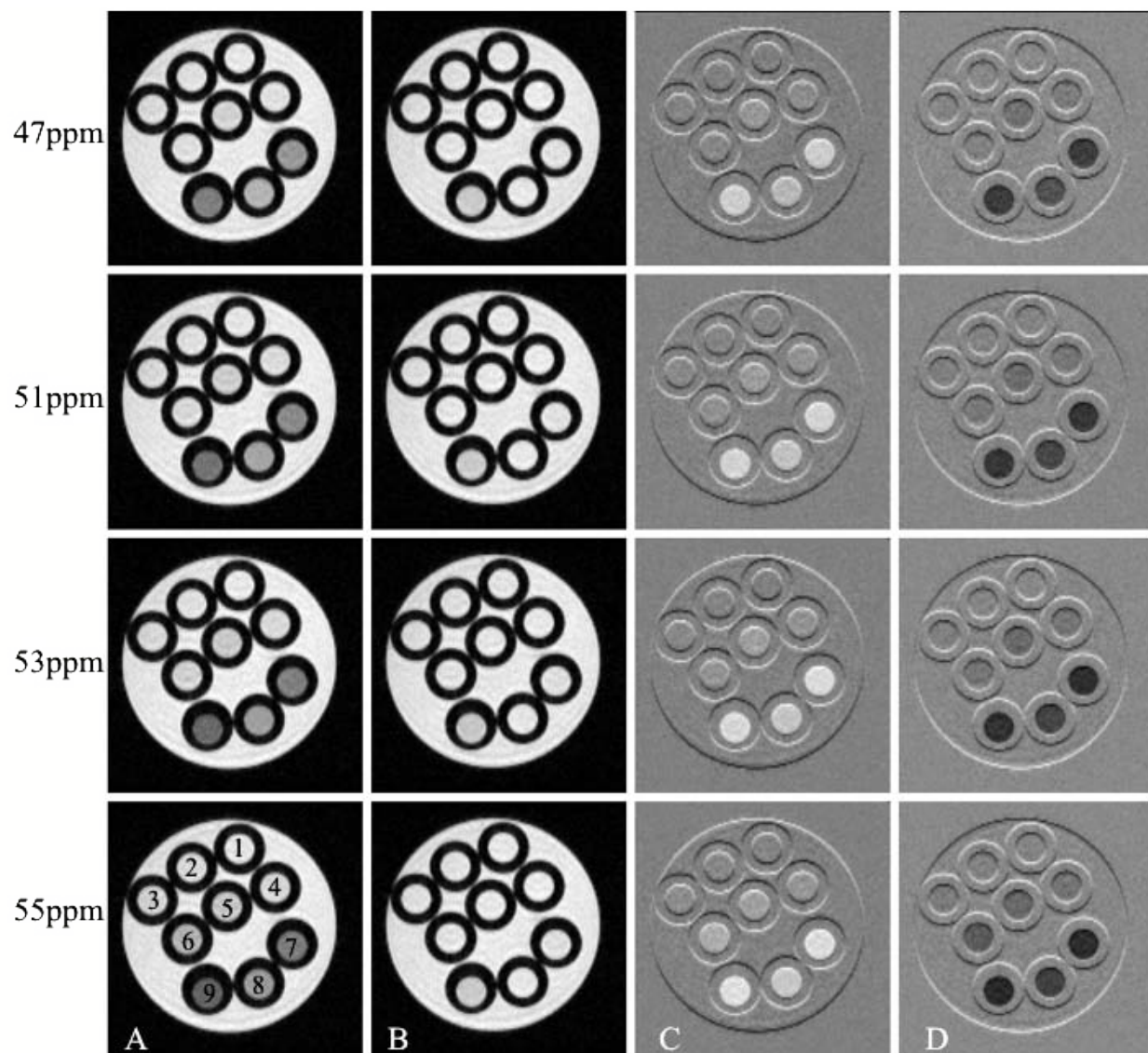


Figure B-13. Serial dilutions at 21.1 T. A) Images taken with the presaturation power applied on the positive side water at the shift listed. B) Images taken with the presaturation power on the opposite side of water at the shift listed. C) Difference images taken to create positive contrast as  $B - A$ . C) Difference images taken to create negative contrast as  $A - B$ . The concentrations are labeled as 1) 0.4 mM, 2) 0.8 mM, 3) 1.6 mM, 4) 3 mM, 5) 6 mM, 6) 12 mM, 7) 100 mM, 8) 25 mM and 9) 50 mM.

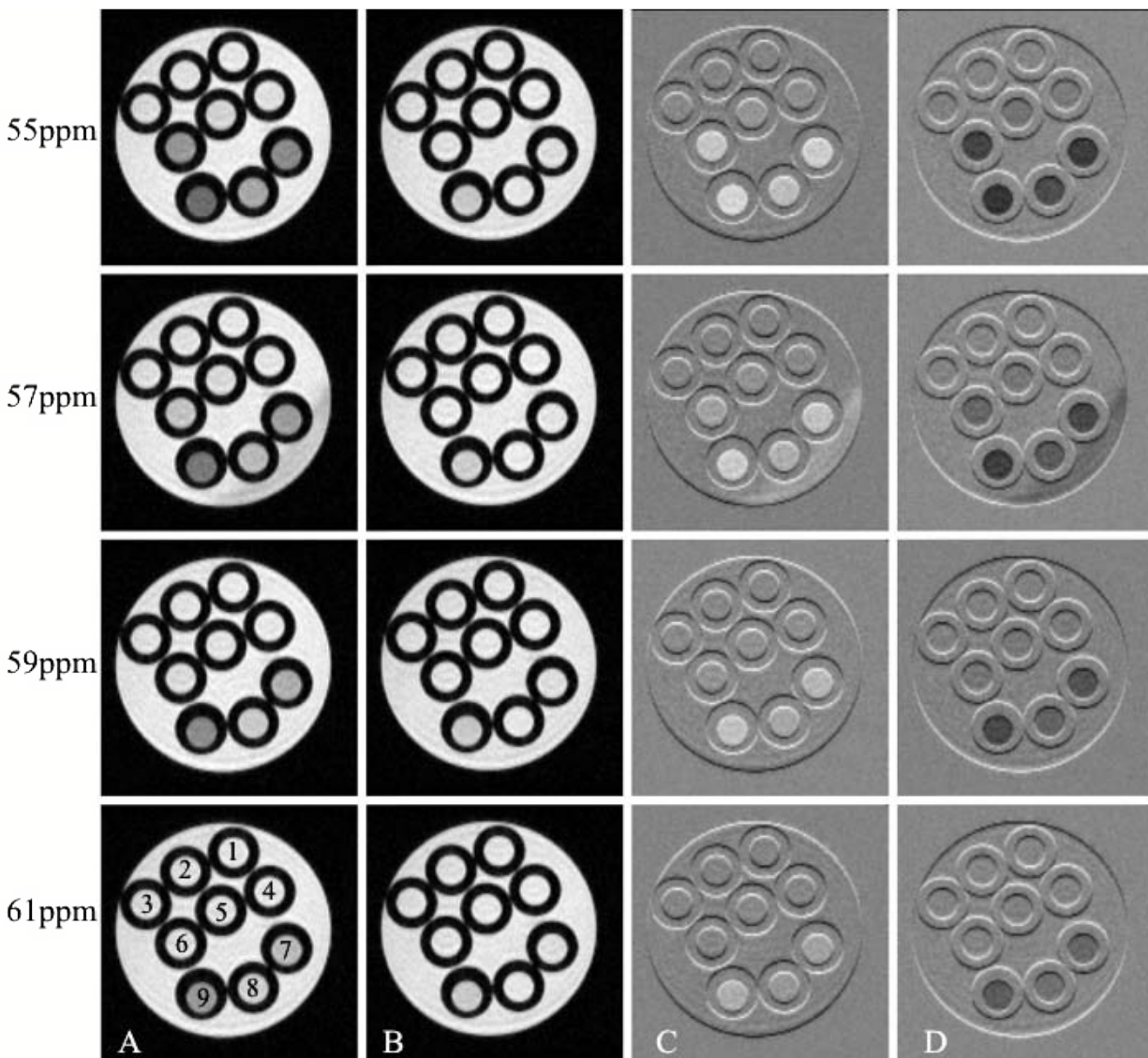


Figure B-14. Serial dilutions at 21.1 T. A) Images taken with the presaturation power applied on the positive side water at the shift listed. B) Images taken with the presaturation power on the opposite side of water at the shift listed. C) Difference images taken to create positive contrast as  $B - A$ . C) Difference images taken to create negative contrast as  $A - B$ . The concentrations are labeled as 1) 0.4 mM, 2) 0.8 mM, 3) 1.6 mM, 4) 3 mM, 5) 6 mM, 6) 12 mM, 7) 100 mM, 8) 25 mM and 9) 50 mM.

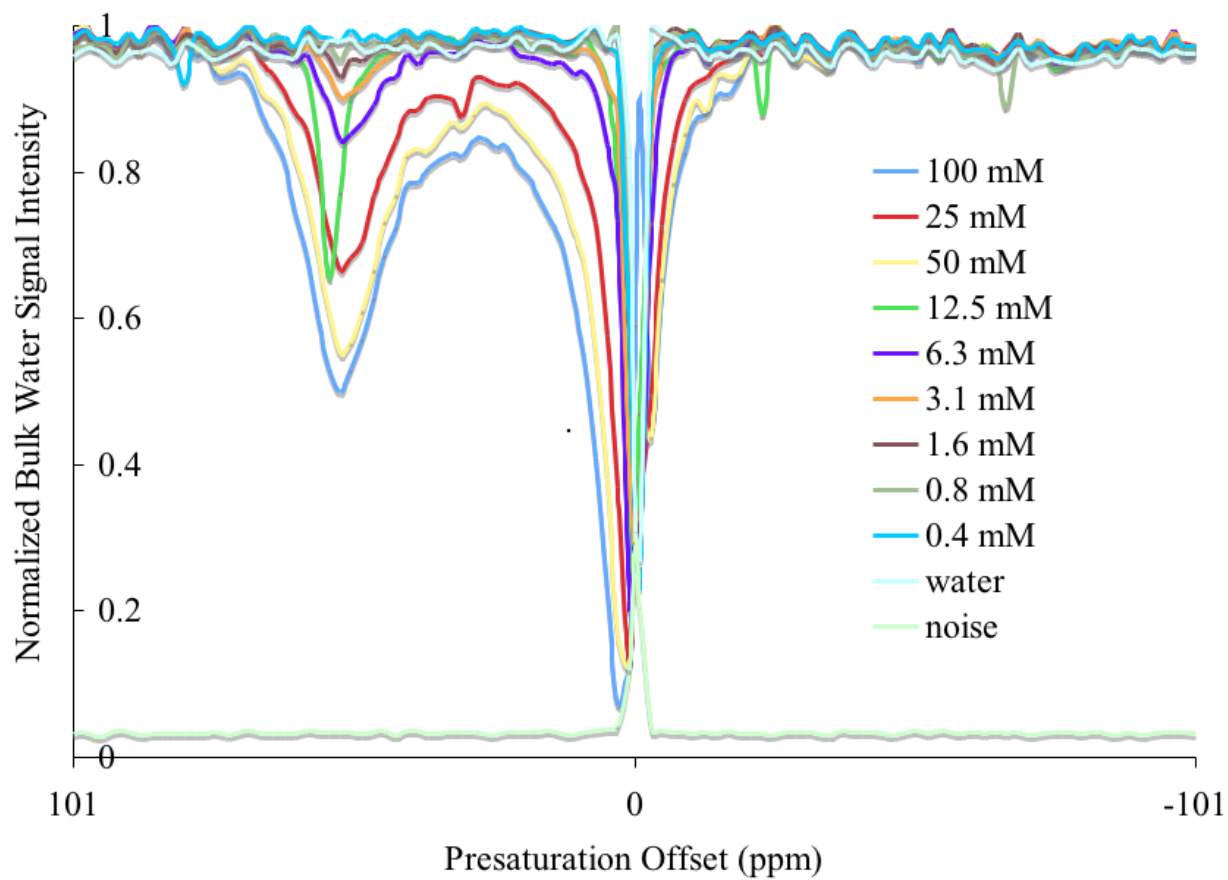


Figure B-15. CEST spectrum of Serial Dilutions at 21.1 T. Spectrum are calculated from images.

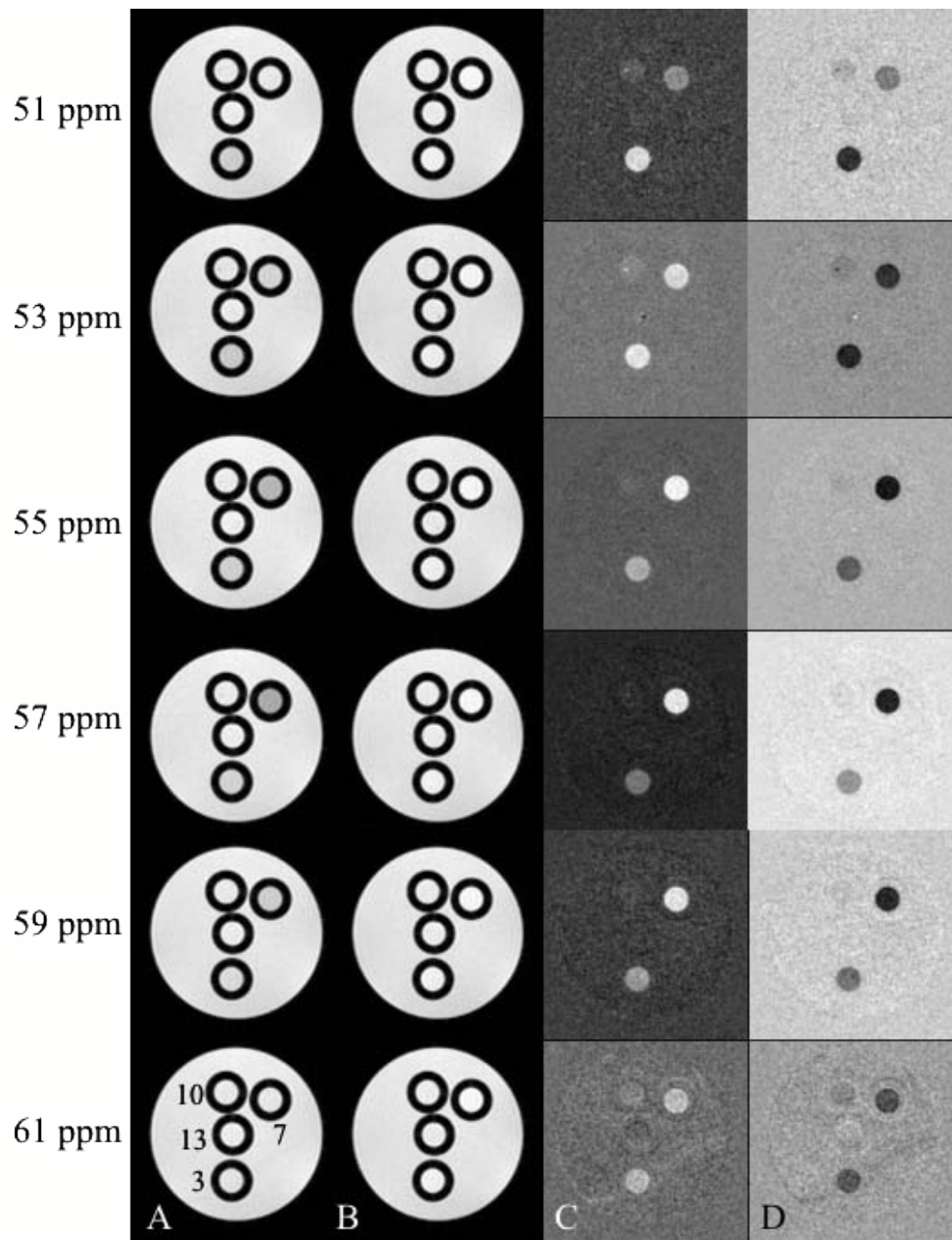


Figure B-16. Variable pH phantom at 14.1 T. Presaturation power was 32  $\mu$ T, presaturation offsets from 51-61 ppm. A) Images taken with the presaturation power applied on the positive side water at the shift listed. B) Images taken with the presaturation power on the opposite side of water at the shift listed. C) Difference images taken to create positive contrast as B - A. C) Difference images taken to create negative contrast as A - B. pH values are labeled.

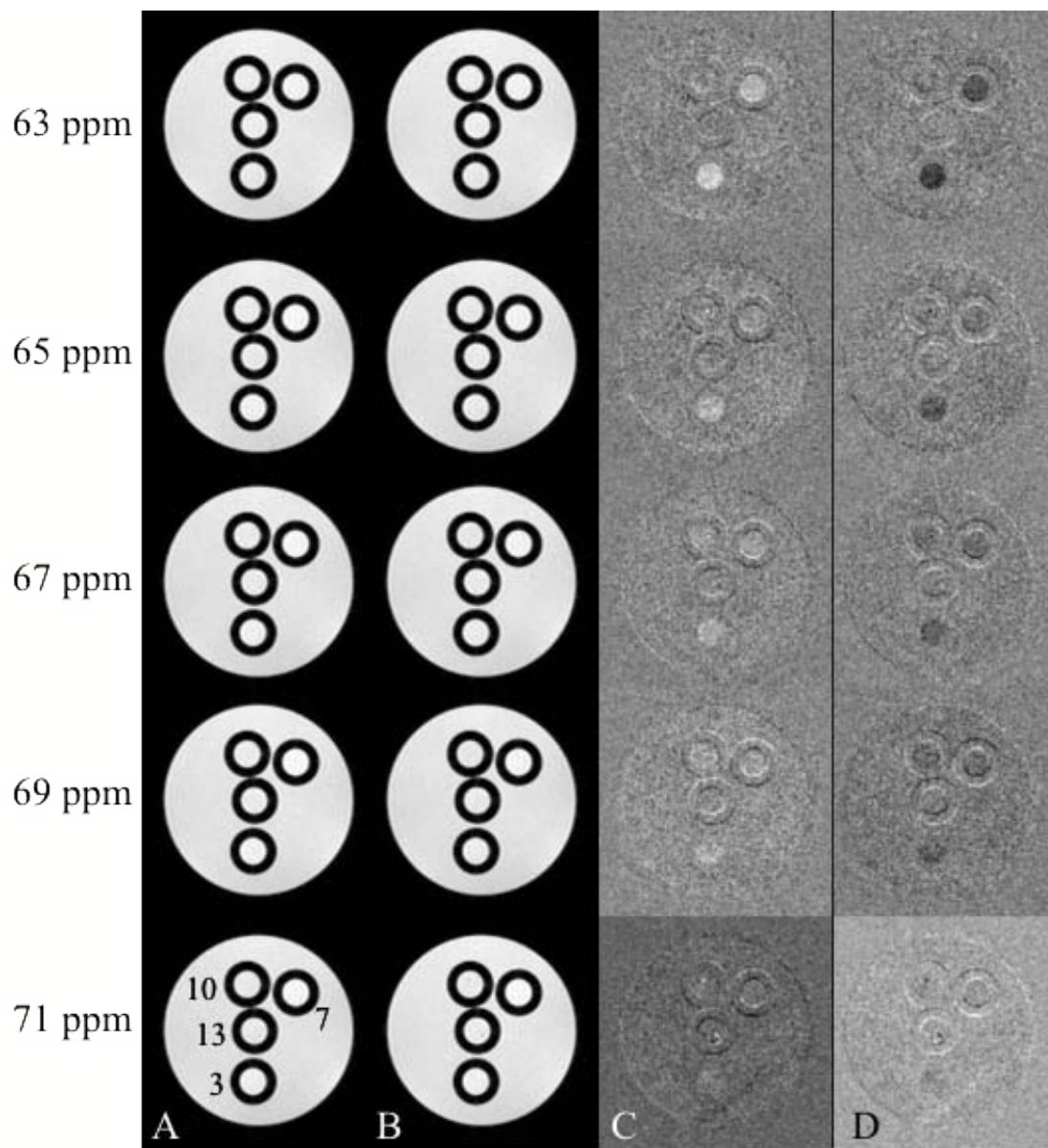


Figure B-17. Variable pH phantom at 14.1 T. Presaturation power  $32 \mu\text{T}$ , presaturation offsets from 65 – 71 ppm. A) Images taken with the presaturation power applied on the positive side water at the shift listed. B) Images taken with the presaturation power on the opposite side of water at the shift listed. C) Difference images taken to create positive contrast as  $B - A$ . D) Difference images taken to create negative contrast as  $A - B$ . pH values are labeled.

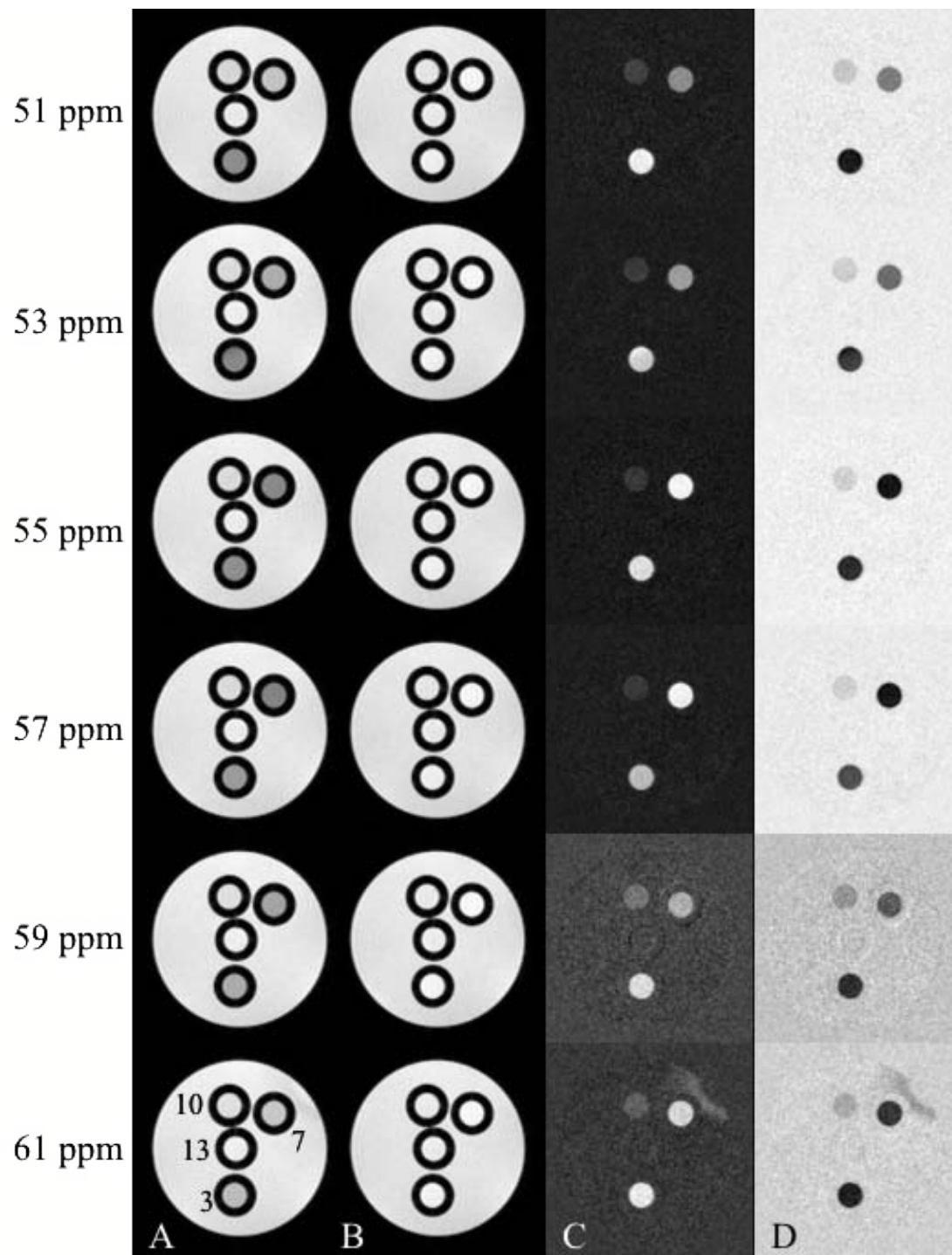


Figure B-18. Variable pH phantom at 14.1 T. Presaturation power  $64 \mu\text{T}$ , presaturation offsets from 51 – 61 ppm. A) Images taken with the presaturation power applied on the positive side water at the shift listed. B) Images taken with the presaturation power on the opposite side of water at the shift listed. C) Difference images taken to create positive contrast as  $B - A$ . D) Difference images taken to create negative contrast as  $A - B$ . pH values are labeled.

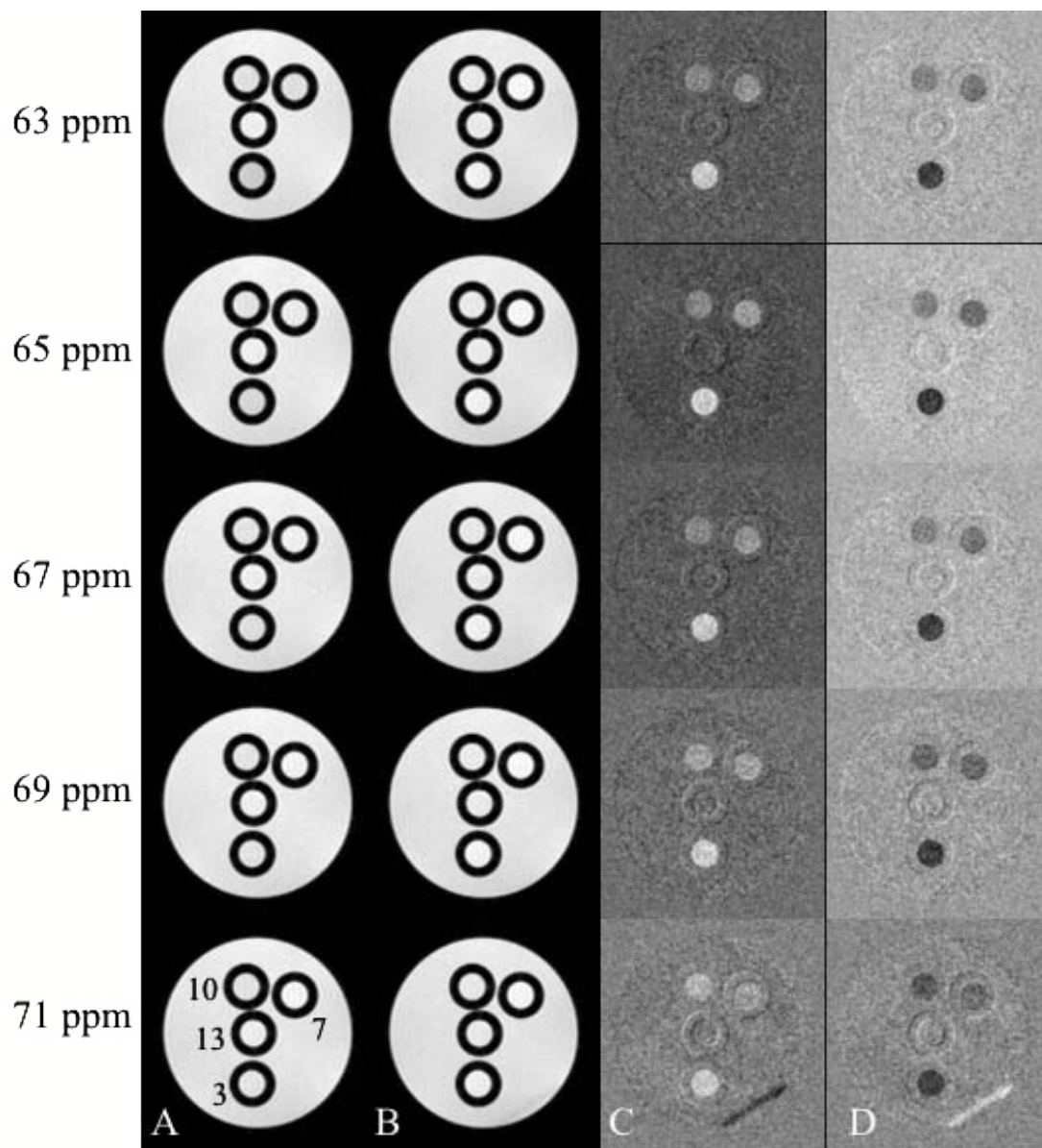


Figure B-19. Variable pH phantom at 14.1 T. Presaturation power  $64 \mu\text{T}$ , presaturation offsets from 65 – 71 ppm. A) Images taken with the presaturation power applied on the positive side water at the shift listed. B) Images taken with the presaturation power on the opposite side of water at the shift listed. C) Difference images taken to create positive contrast as  $B - A$ . D) Difference images taken to create negative contrast as  $A - B$ . pH values are labeled.

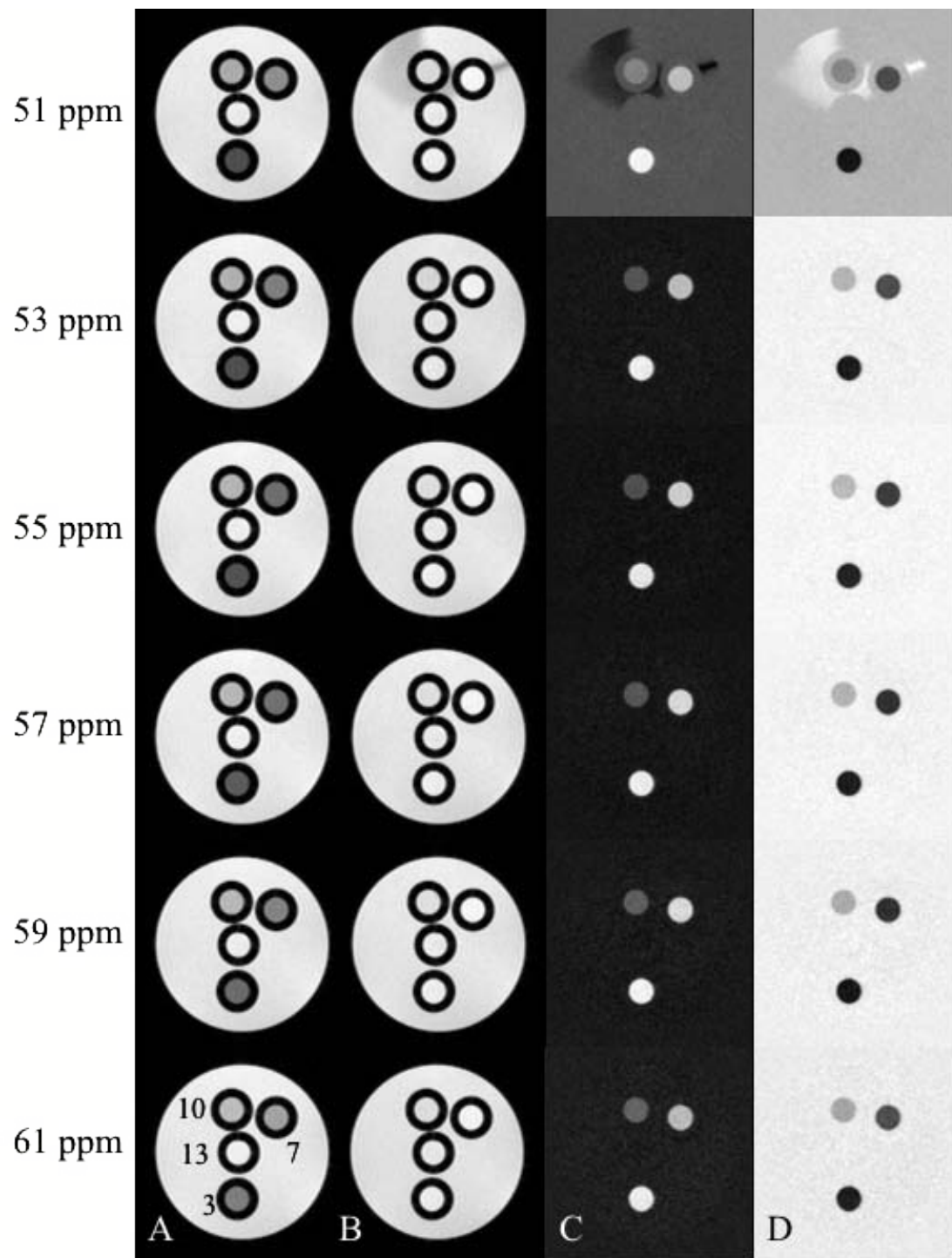


Figure B-20. Variable pH phantom at 14.1 T. Presaturation power 128  $\mu$ T, presaturation offsets from 51 – 61 ppm. A) Images taken with the presaturation power applied on the positive side water at the shift listed. B) Images taken with the presaturation power on the opposite side of water at the shift listed. C) Difference images taken to create positive contrast as B – A. C) Difference images taken to create negative contrast as A – B. pH values are labeled.

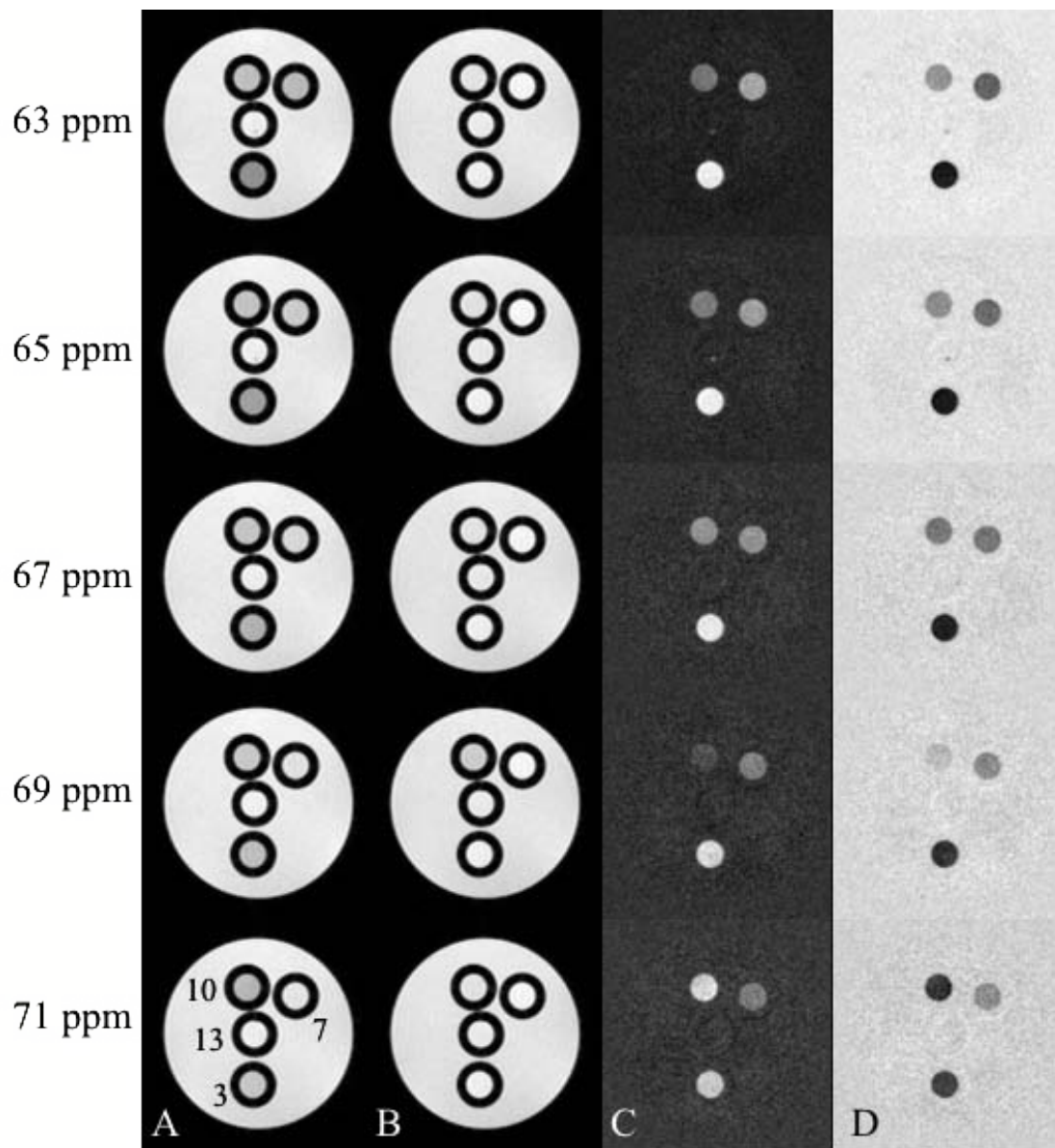


Figure B-21. Variable pH phantom at 14.1 T. Presaturation power 128  $\mu$ T, presaturation offsets from 65 – 71 ppm. A) Images taken with the presaturation power applied on the positive side water at the shift listed. B) Images taken with the presaturation power on the opposite side of water at the shift listed. C) Difference images taken to create positive contrast as B – A. D) Difference images taken to create negative contrast as A – B. pH values are labeled.

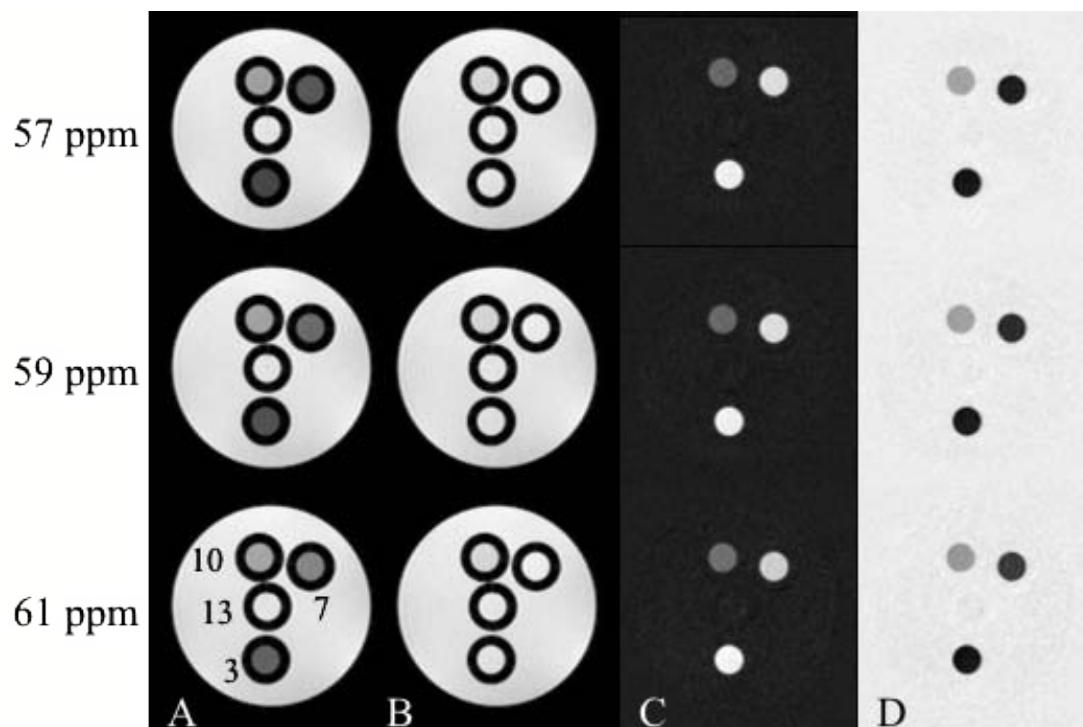


Figure B-22. Variable pH phantom at 14.1 T. Presaturation power  $128 \mu\text{T}$ , presaturation offsets from 51 – 61 ppm, presaturation time 4 s. A) Images taken with the presaturation power applied on the positive side water at the shift listed. B) Images taken with the presaturation power on the opposite side of water at the shift listed. C) Difference images taken to create positive contrast as  $B - A$ . D) Difference images taken to create negative contrast as  $A - B$ . pH values are labeled.

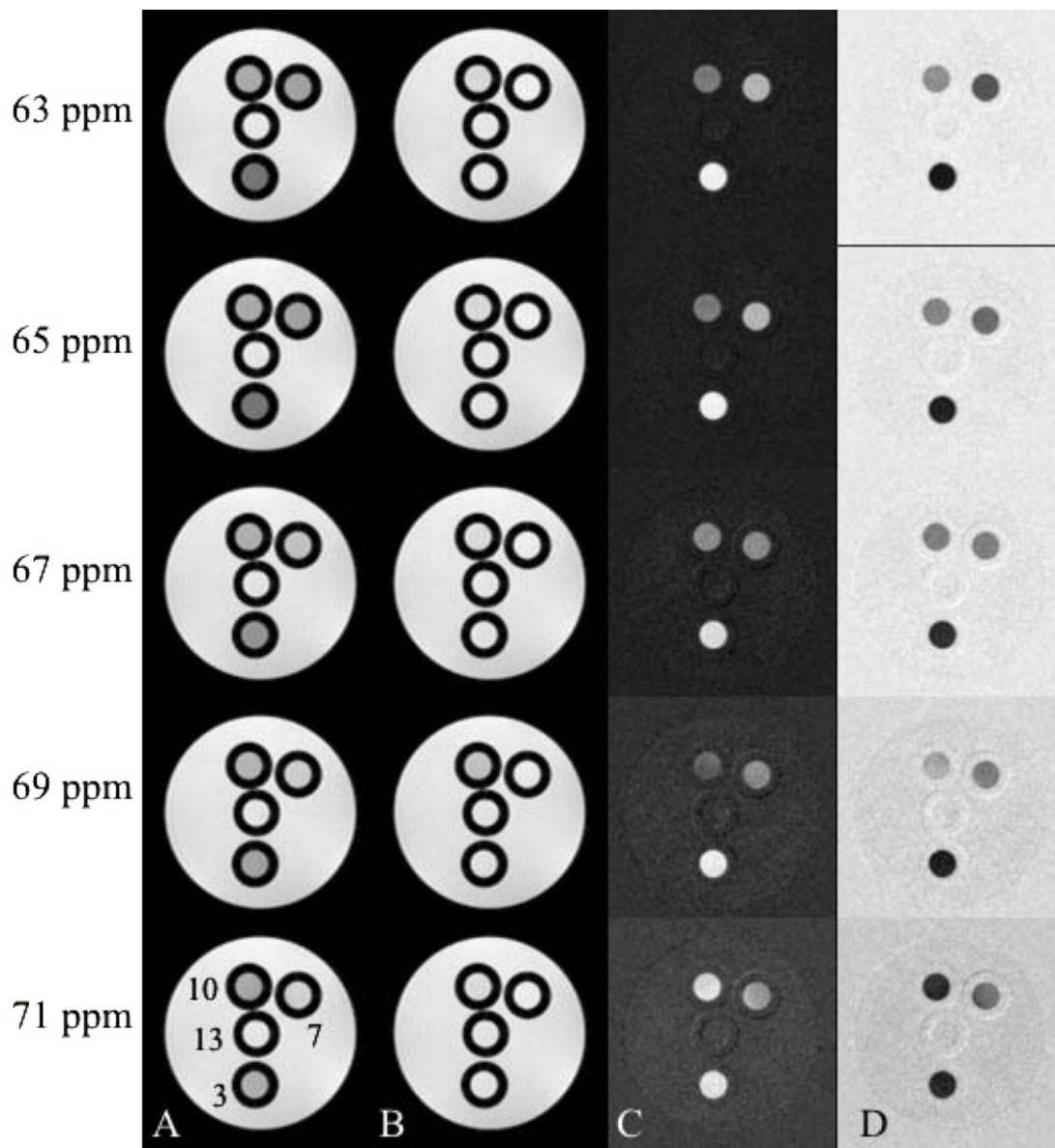


Figure B-23. Variable pH phantom at 14.1 T. Presaturation power  $128 \mu\text{T}$ , presaturation offsets from 65 – 71 ppm, presaturation time 4 s. A) Images taken with the presaturation power applied on the positive side water at the shift listed. B) Images taken with the presaturation power on the opposite side of water at the shift listed. C) Difference images taken to create positive contrast as  $B - A$ . C) Difference images taken to create negative contrast as  $A - B$ . pH values are labeled.

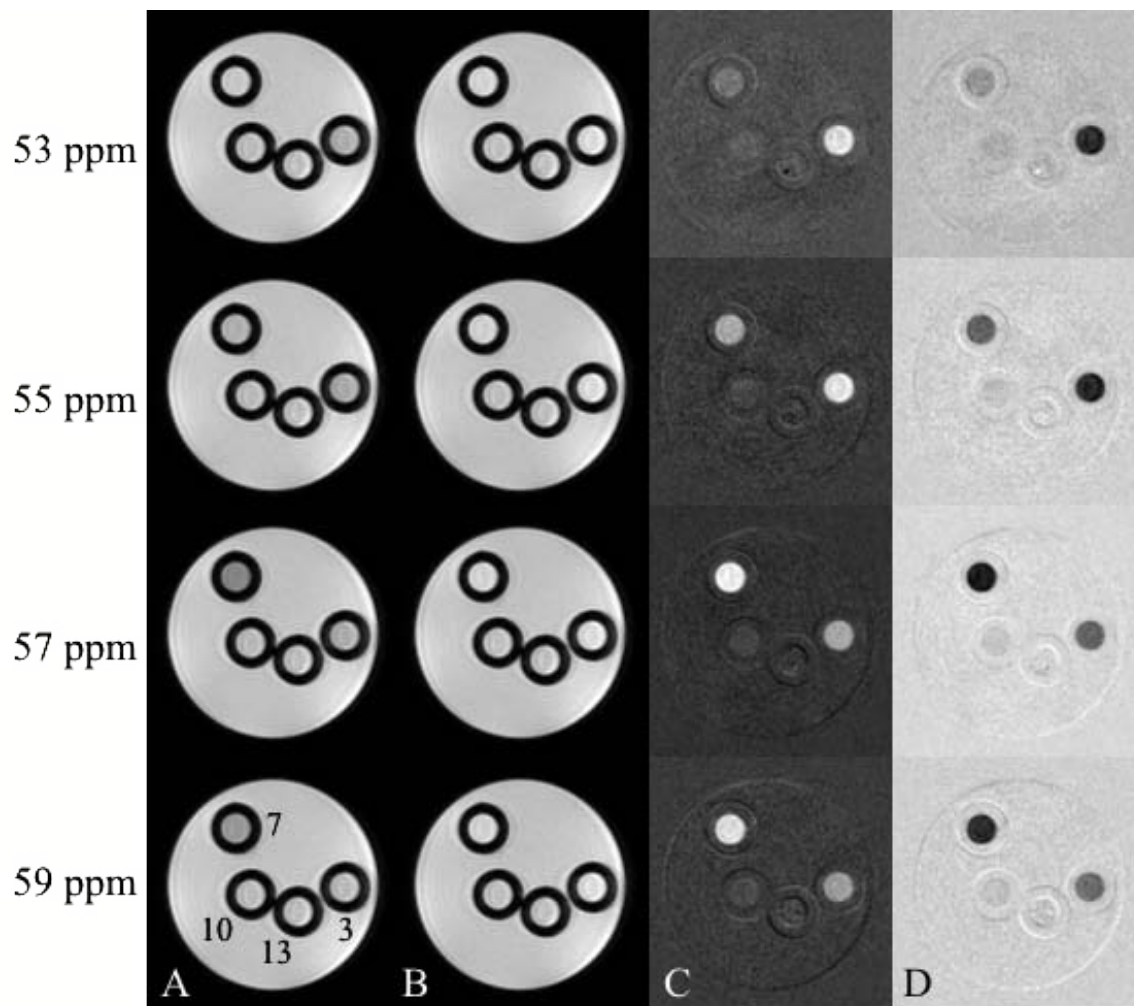


Figure B-24. Variable pH phantom at 17.6 T. Presaturation power  $32 \mu\text{T}$ , presaturation offsets from 53 – 59 ppm. A) Images taken with the presaturation power applied on the positive side water at the shift listed. B) Images taken with the presaturation power on the opposite side of water at the shift listed. C) Difference images taken to create positive contrast as  $B - A$ . D) Difference images taken to create negative contrast as  $A - B$ . pH values are labeled.

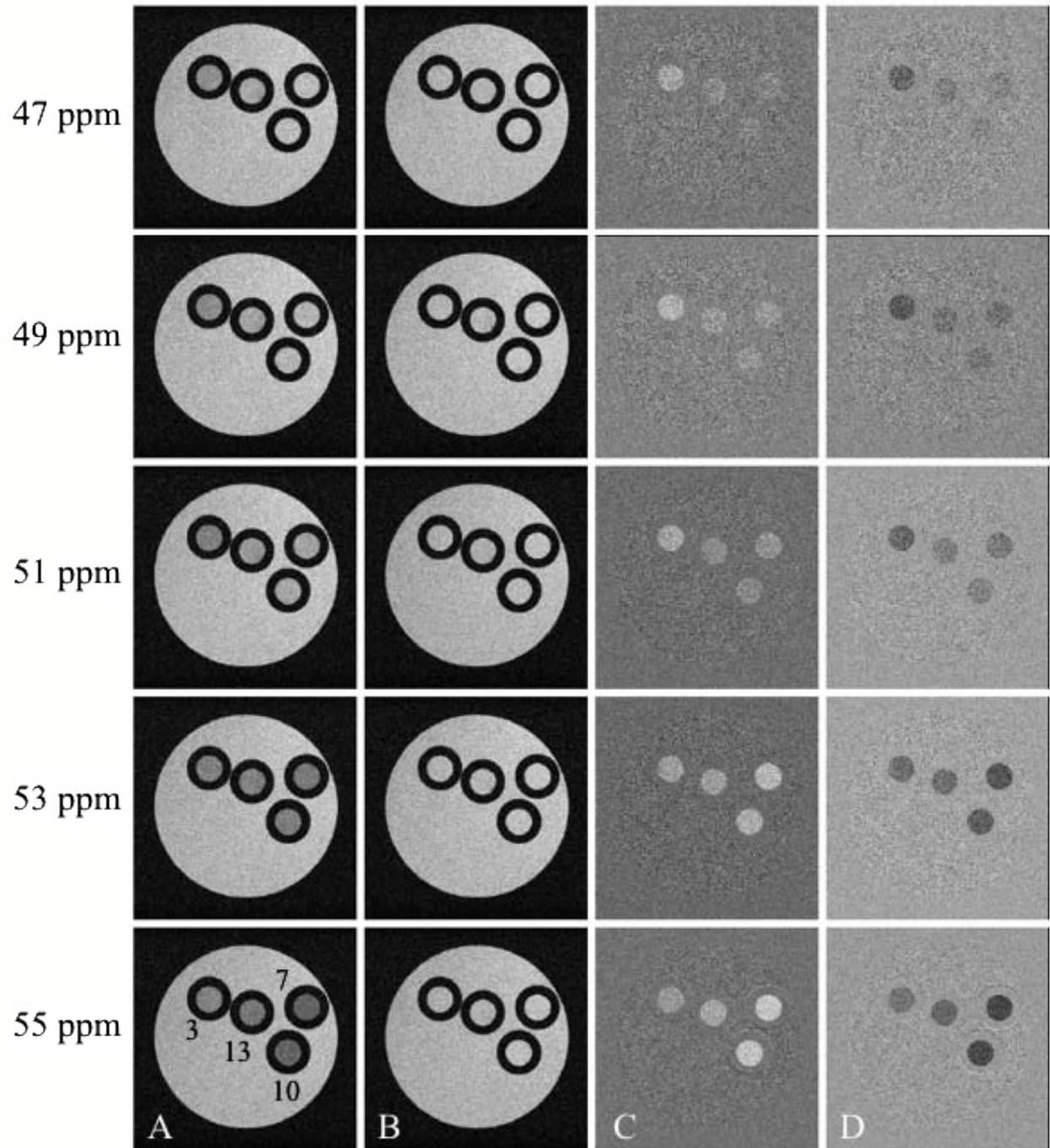


Figure B-25. Variable pH phantom at 21.1 T. Presaturation offsets from 47 – 55 ppm.  
 A) Images taken with the presaturation power applied on the positive side water at the shift listed. B) Images taken with the presaturation power on the opposite side of water at the shift listed. C) Difference images taken to create positive contrast as B – A. D) Difference images taken to create negative contrast as A – B. pH values are labeled.

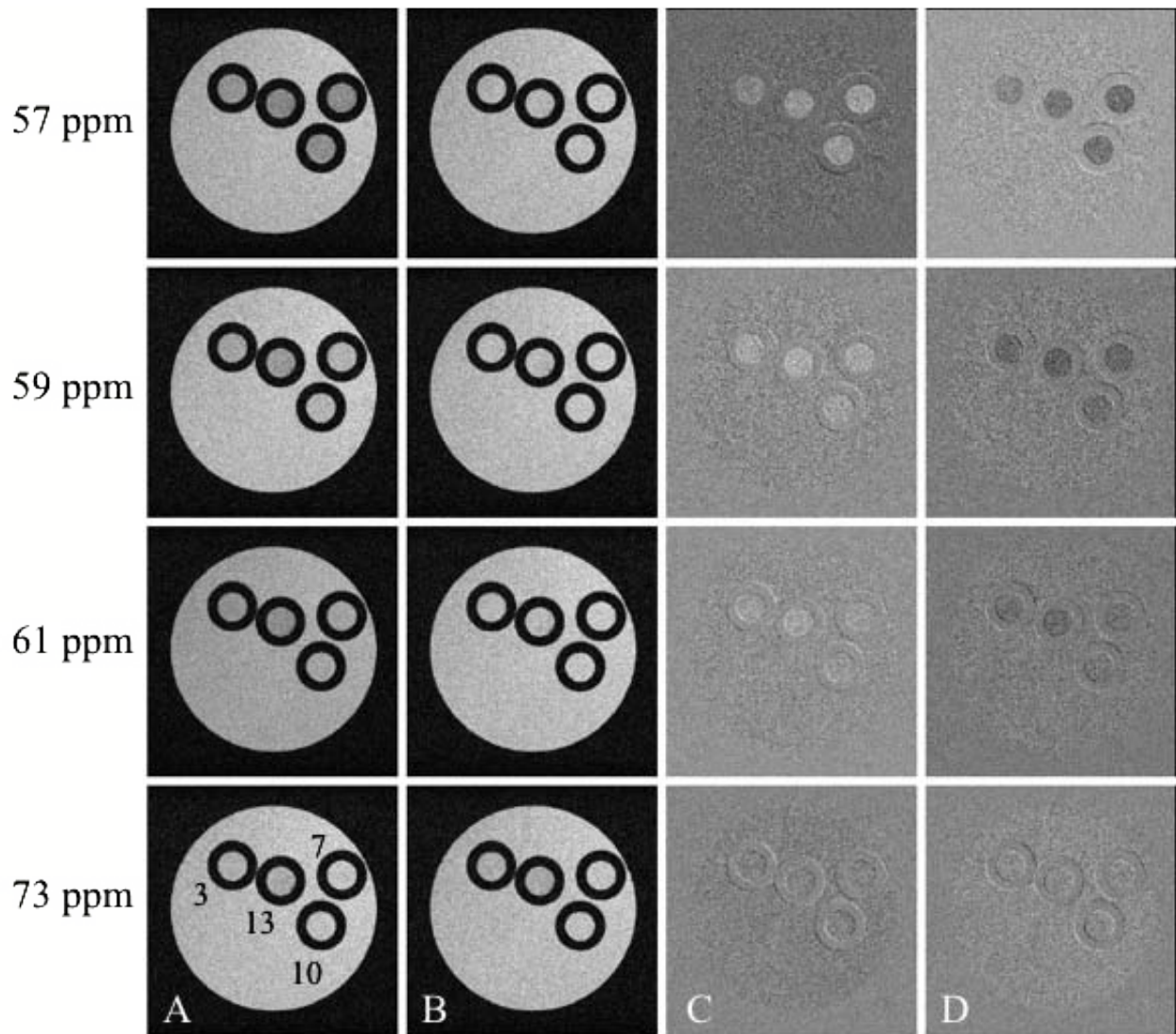


Figure B-26. Variable pH phantom at 21.1 T. Presaturation offsets from 57 – 73 ppm.  
 A) Images taken with the presaturation power applied on the positive side water at the shift listed. B) Images taken with the presaturation power on the opposite side of water at the shift listed. C) Difference images taken to create positive contrast as B – A. D) Difference images taken to create negative contrast as A – B. pH values are labeled.

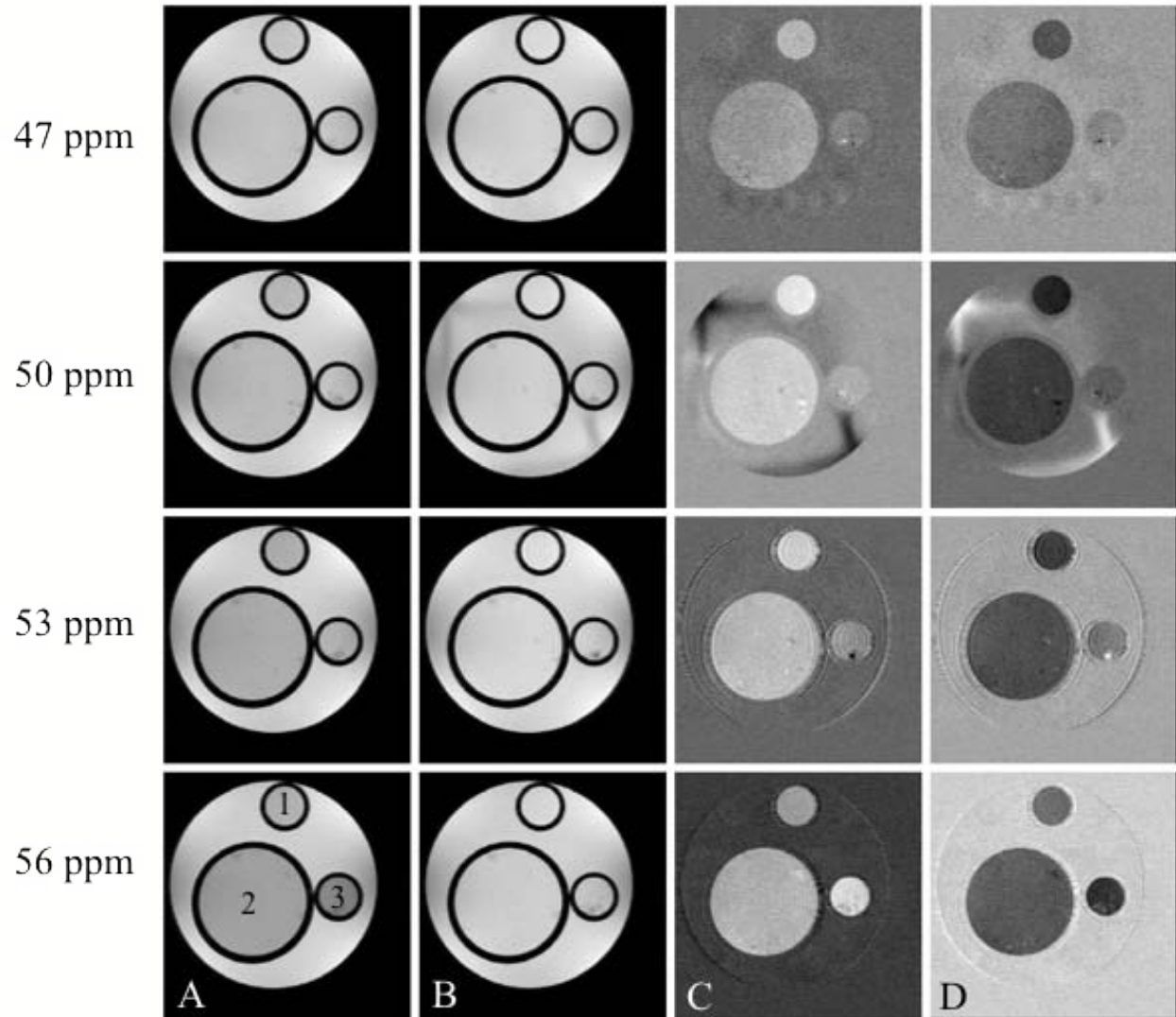


Figure B-27. Variable pH with media phantom at 17.6 T. Presaturation offsets from 47 – 56 ppm. A) Images taken with the presaturation power applied on the positive side water at the shift listed. B) Images taken with the presaturation power on the opposite side of water at the shift listed. C) Difference images taken to create positive contrast as  $B - A$ . D) Difference images taken to create negative contrast as  $A - B$ . pH values are labeled as 1) pH 3, 2) pH 7 in media and 3) pH 7.

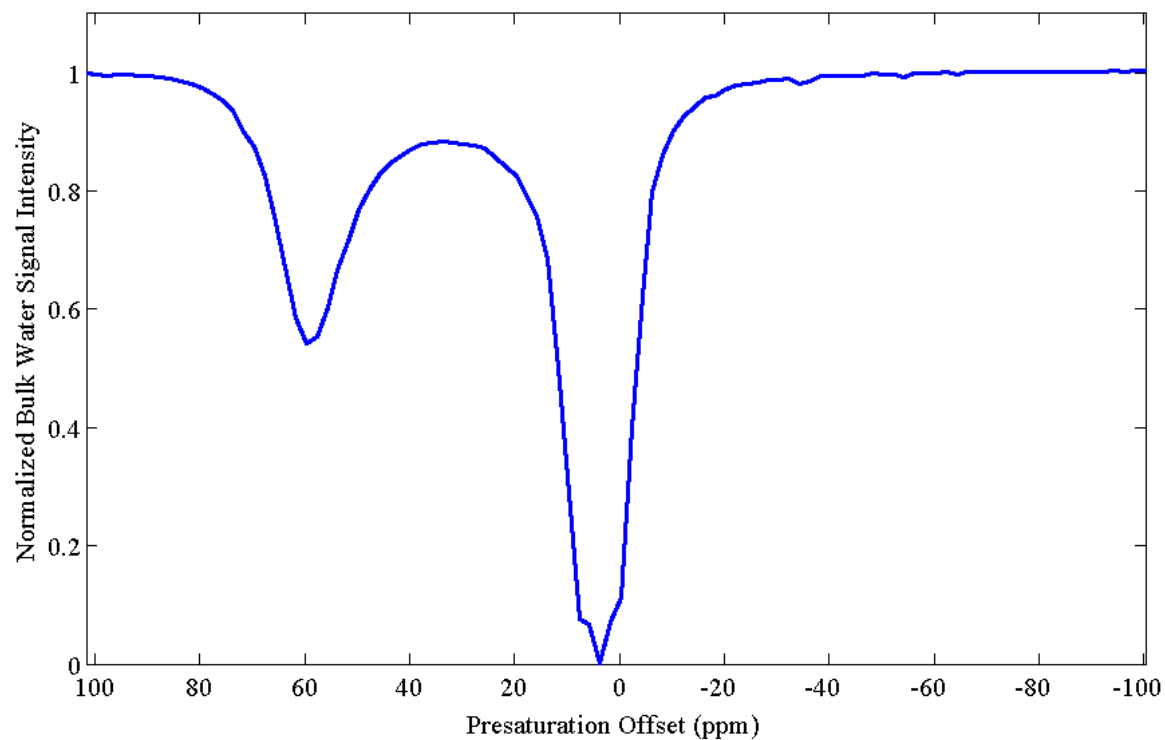


Figure B-28. CEST spectrum of 10 mM Eu-2 at 14 °C.

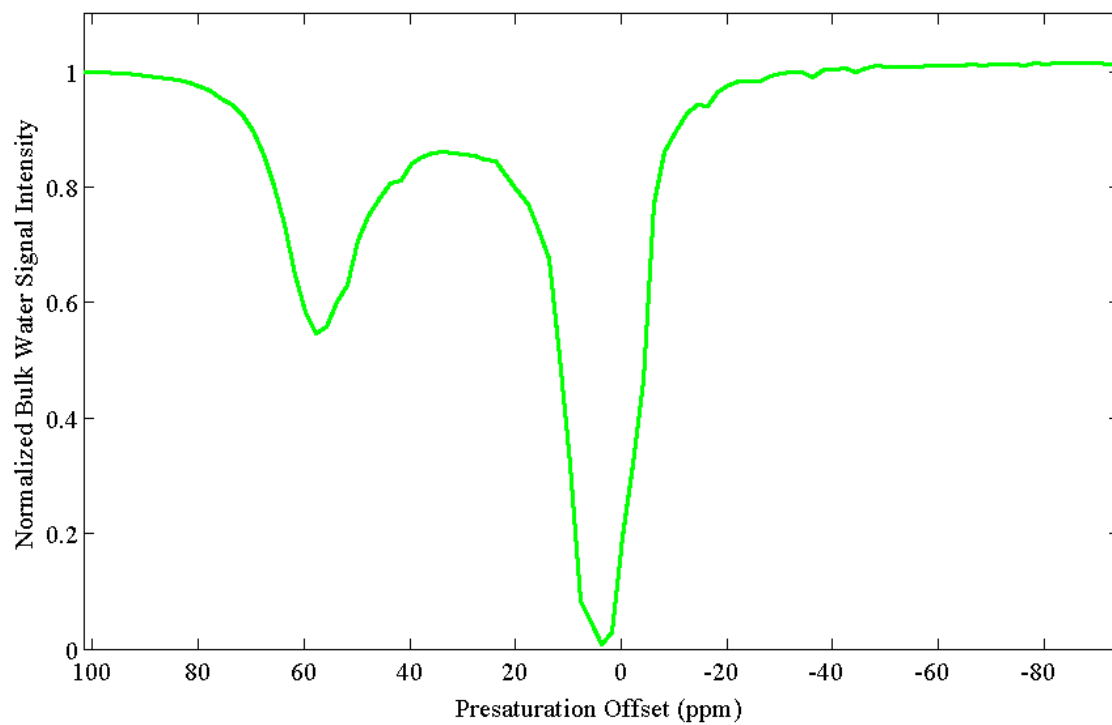


Figure B-29. CEST spectrum of 10 mM Eu-2 at 20 °C.

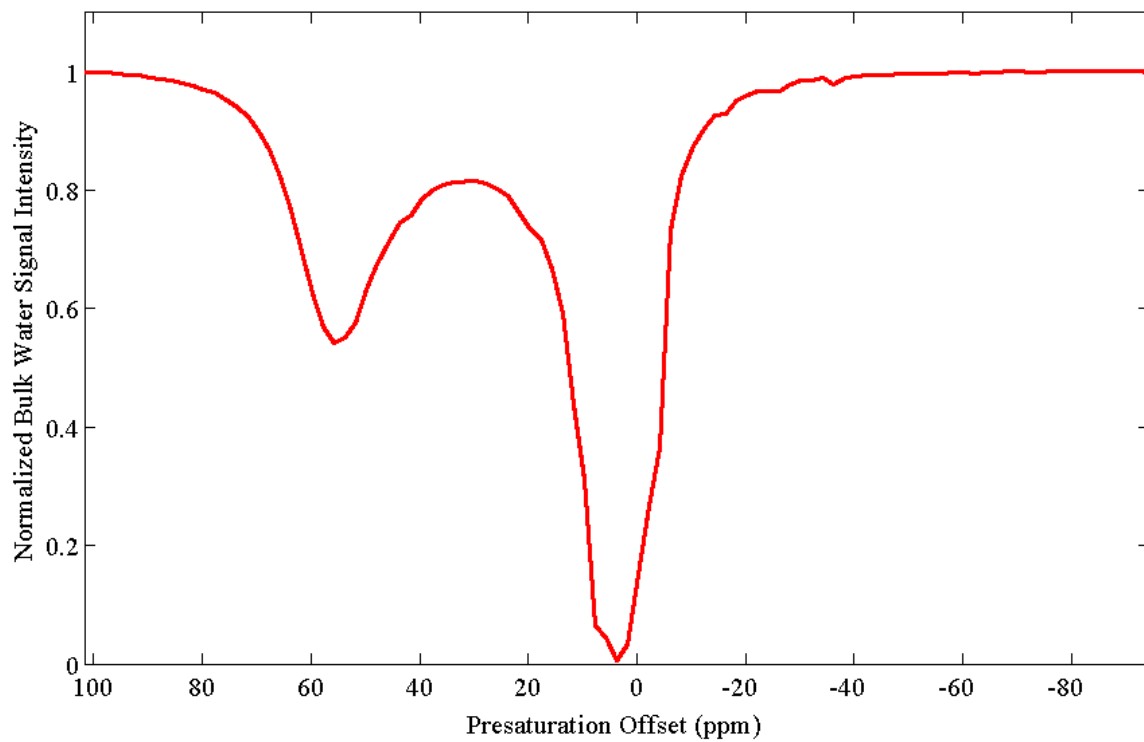


Figure B-30. CEST spectrum of 10 mM Eu-2 at 26 °C.

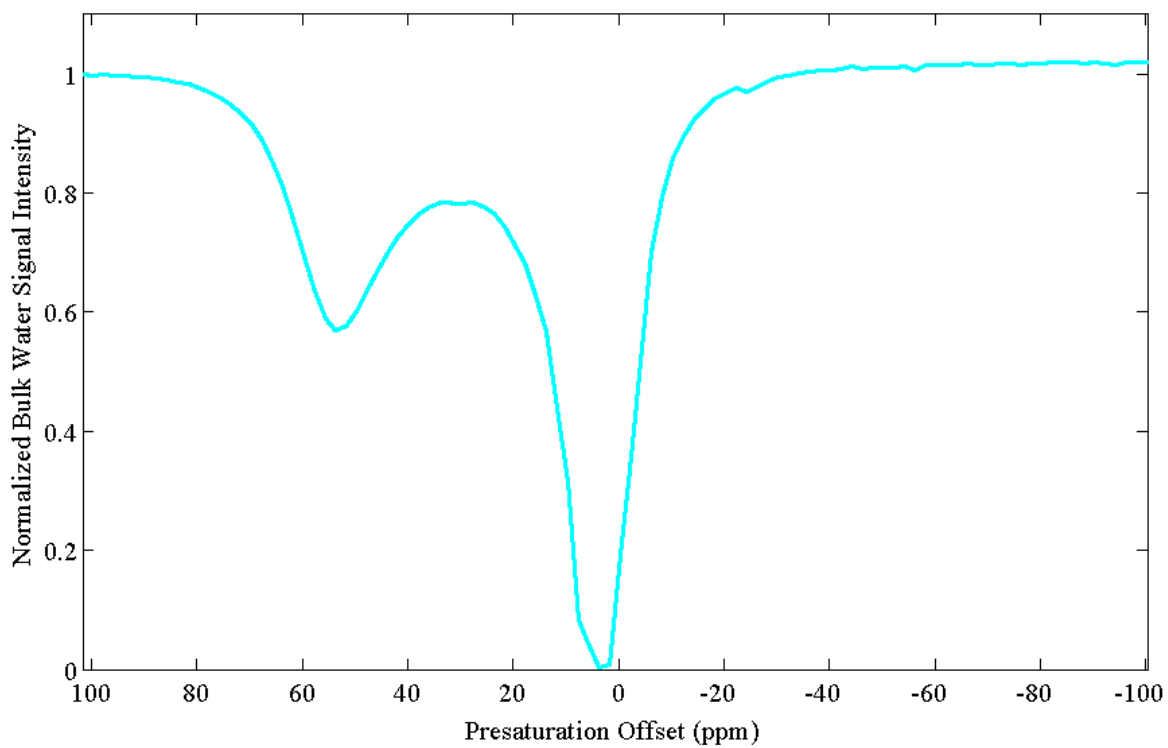


Figure B-31. CEST spectrum of 10 mM Eu-2 at 32 °C.

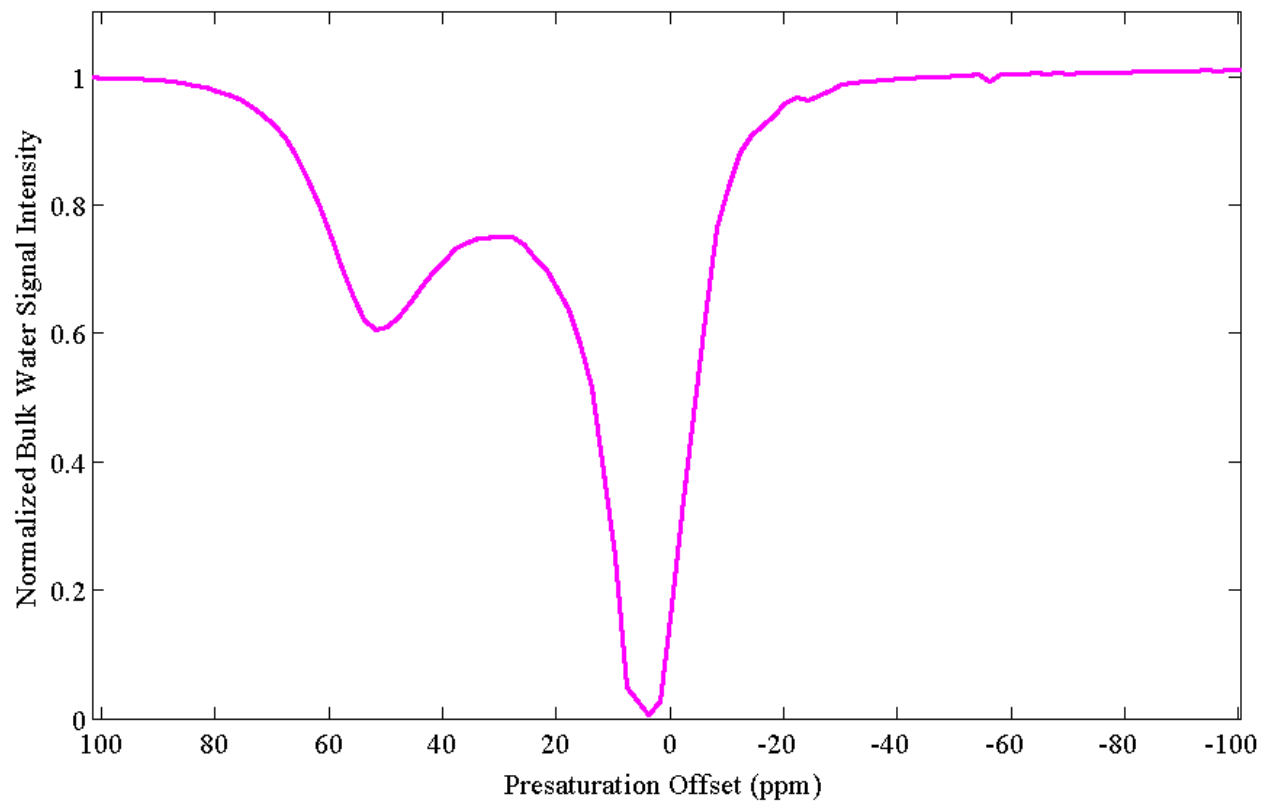


Figure B-32. CEST spectrum of 10 mM Eu-2 at 38 °C.

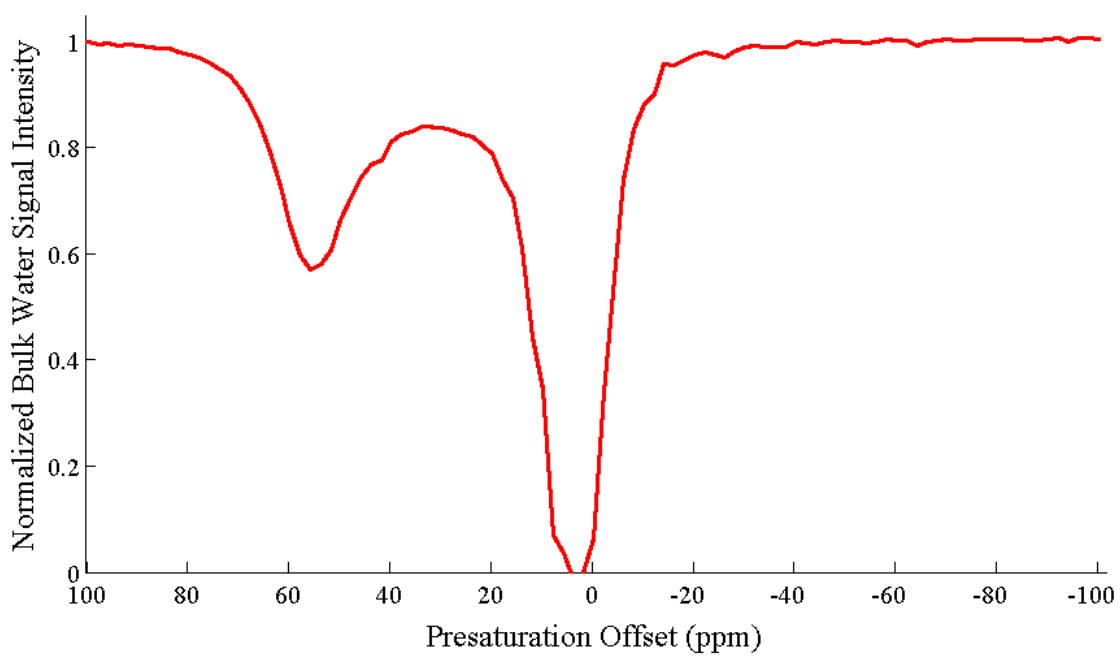


Figure B-33. CEST spectrum of 10 mM Eu-2 for one acquisition.

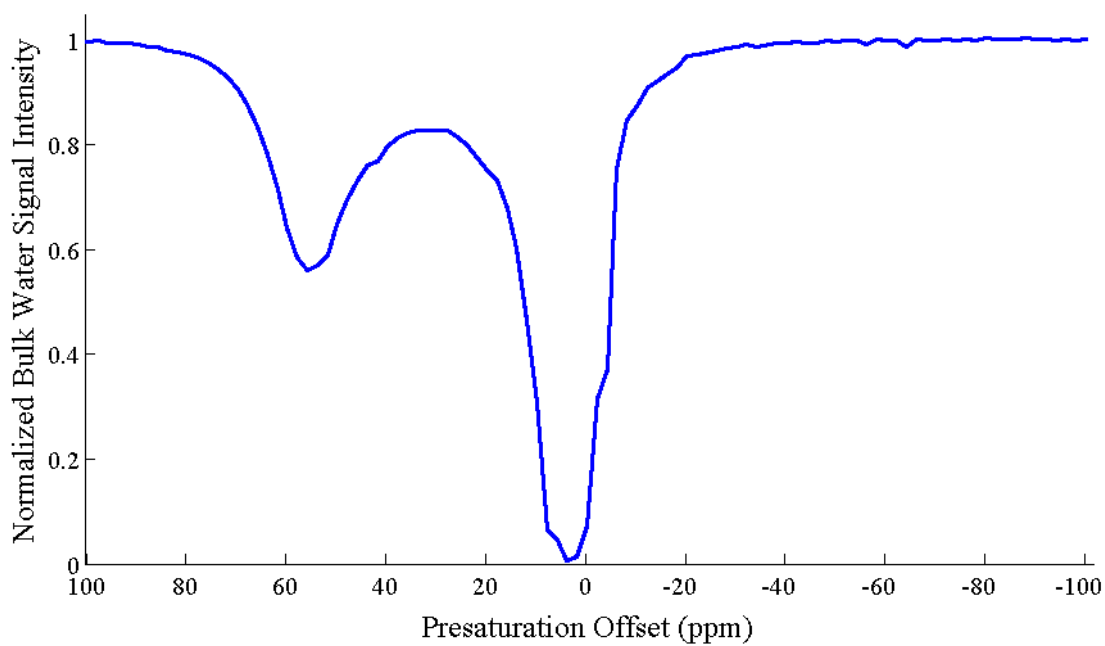


Figure B-34. CEST spectrum of 10 mM Eu-2 for two acquisitions.

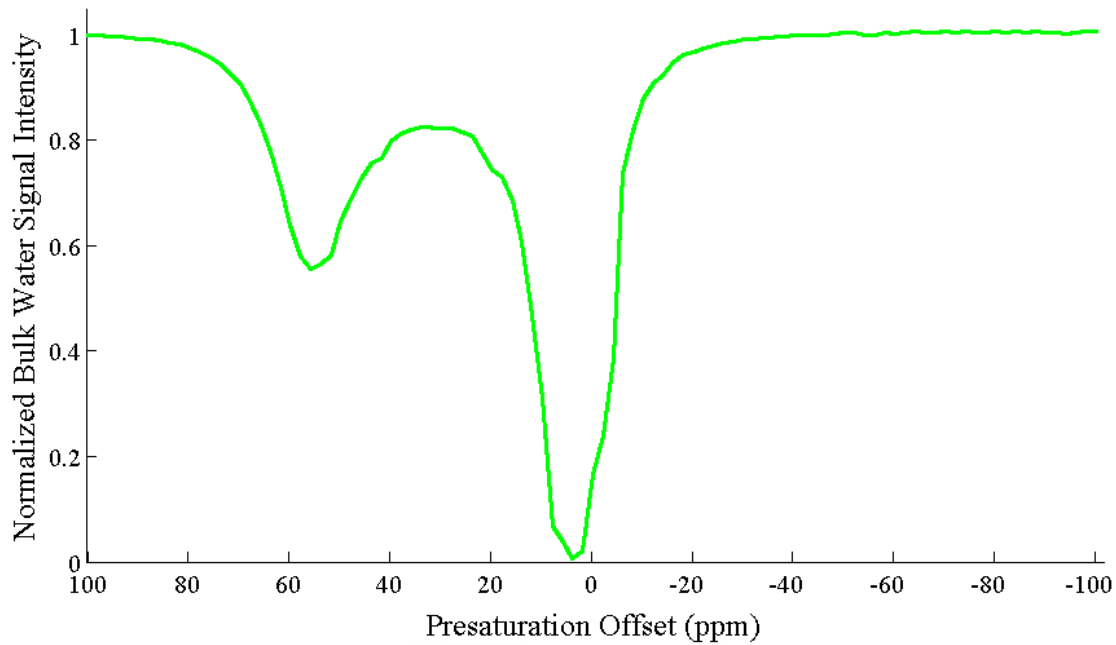


Figure B-35. CEST spectrum of 10 mM Eu-2 for four acquisitions.

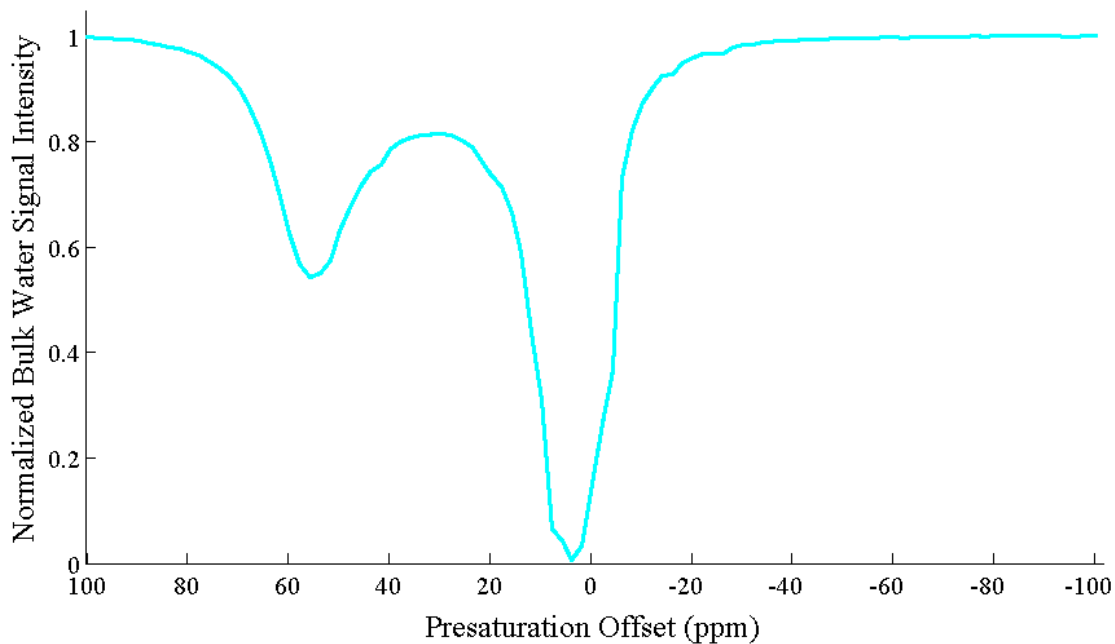


Figure B-36. CEST spectrum of 10 mM Eu-2 for eight acquisitions.

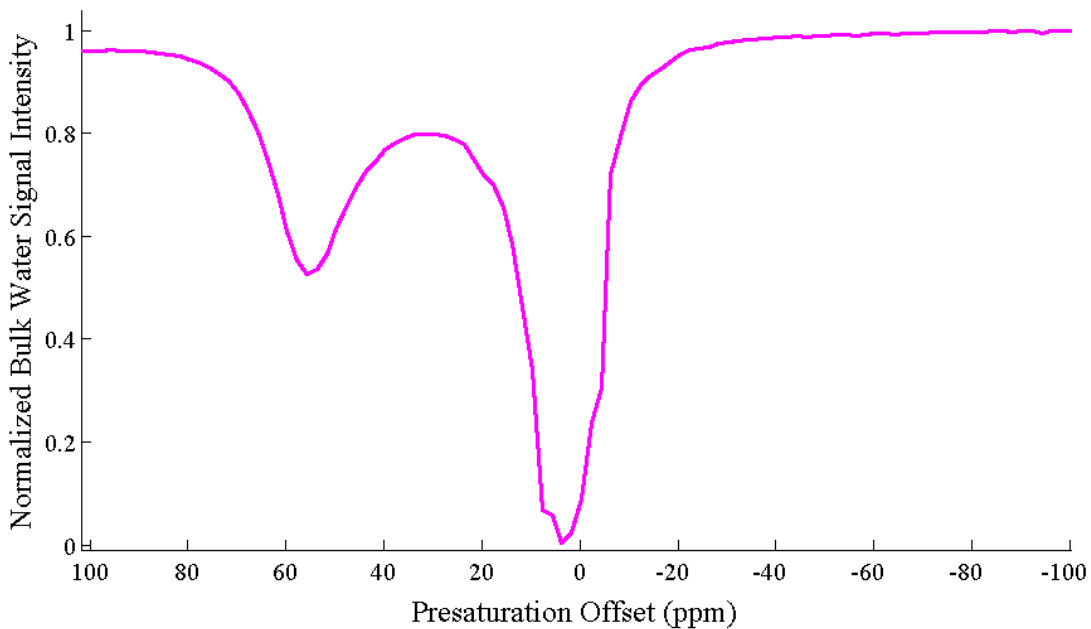


Figure B-37. CEST spectrum of 10 mM Eu-2 for 32 acquisitions.

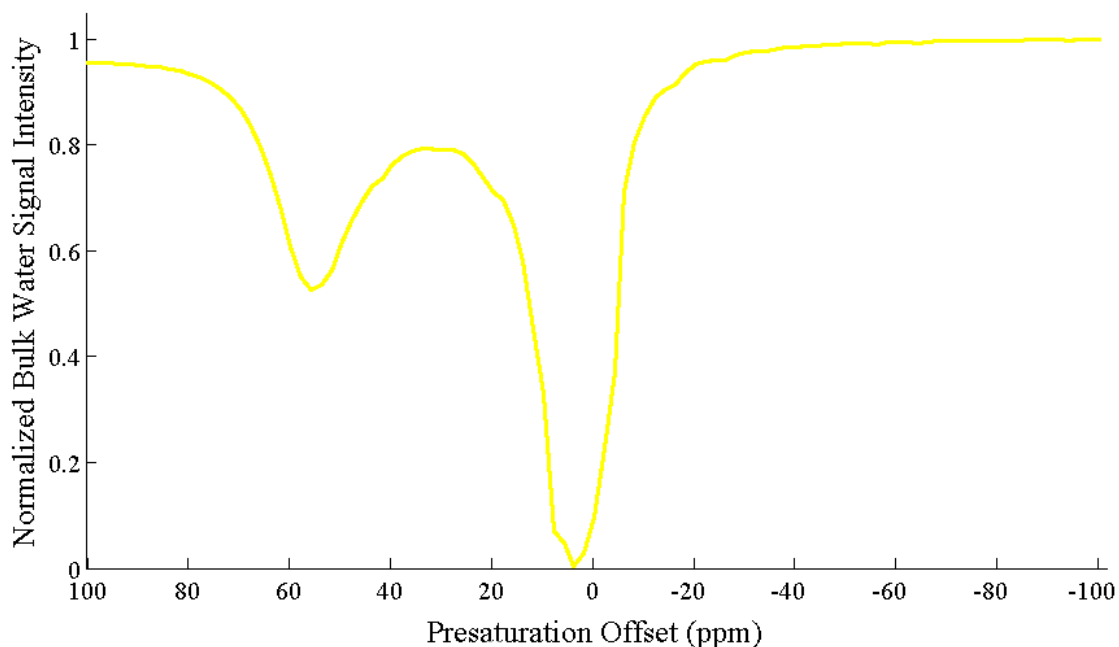


Figure B-38. CEST spectrum of 10 mM Eu-2 for 64 acquisitions.

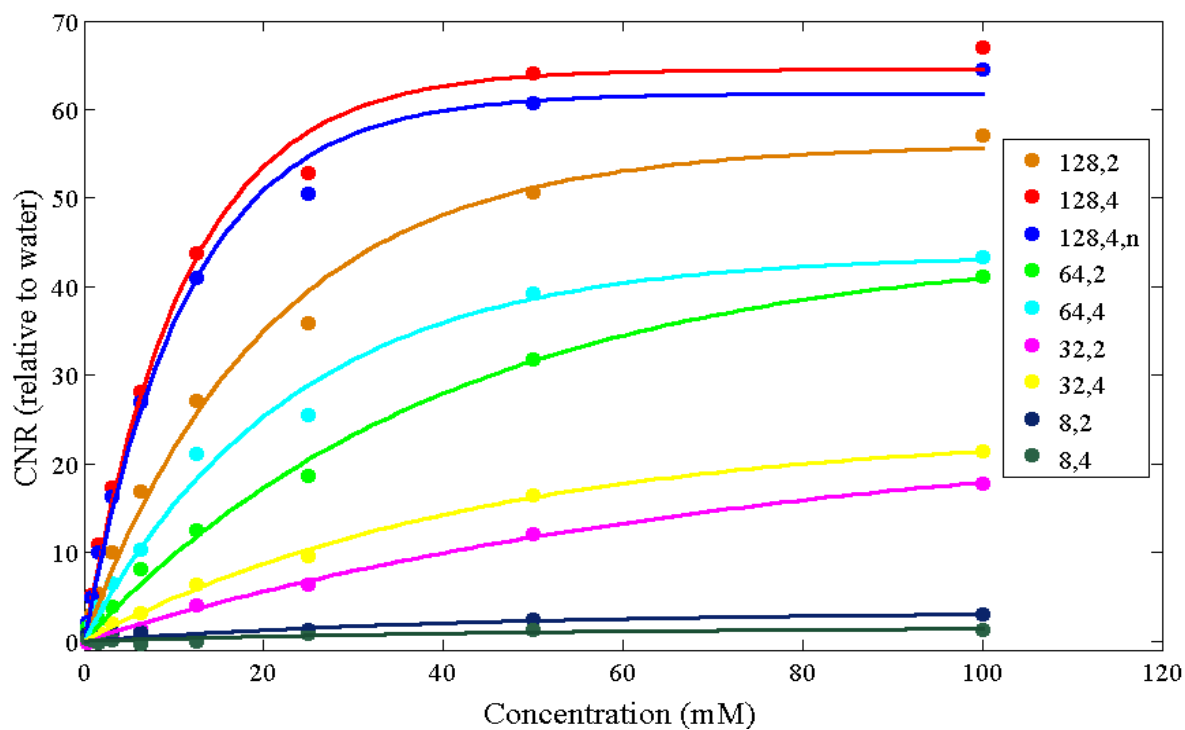


Figure B-39. Presaturation power and duration effect on CNR. The legend indicates the presaturation power ( $\mu\text{T}$ ) followed by the number of 1 ms presaturation pulses ( $2 \times 1000$  or  $4 \times 1000$ ); n indicates that 'derive gains' was set to off to test the power calculation within the Paravision Program.

APPENDIX C  
MATLAB SIMULATION

**MATLAB Code Format**

MATLAB code can be utilized by typing commands directly into the command box, or through scripts, or .m files, which can be edited to run through a series of commands automatically. M files are generally quicker, and can be saved and rerun. They may also refer to other scripts. The MATLAB code used for the simulations was generally in the form of m files. The code is listed as it appears in the m file, and if one script calls another, the additional scripts are included after the first, and are separated by a solid line break.

**Modified Bloch Equations**

The Bloch equation (Eq. C-1) describes the relationship between the change in magnetization ( $dM/dt$ ), the static magnetic field ( $B_0$ ) and the starting magnetization ( $M_0$ ) [147] (in vector notation).

$$\frac{d\vec{M}}{dt} = \gamma \vec{B}_0 \times \vec{M}_0 \quad (C-1)$$

This equation can be modified for chemical exchange to describe the resulting magnetization [87,148,149].

$$\frac{dM_x^{bulk}}{dt} = -(\omega_{bulk} - \omega)M_y^{bulk} - k_{2bulk}M_x^{bulk} + C_{bound}M_x^{bound} \quad (C-2)$$

$$\frac{dM_x^{bound}}{dt} = -(\omega_{bound} - \omega)M_y^{bound} - k_{2bound}M_x^{bound} + C_{bulk}M_x^{bulk} \quad (C-3)$$

$$\frac{dM_y^{bulk}}{dt} = -(\omega_{bulk} - \omega)M_x^{bulk} - k_{2bulk}M_y^{bulk} + C_{bound}M_y^{bound} - \omega_1 M_z^{bulk} \quad (C-4)$$

$$\frac{dM_y^{bound}}{dt} = -(\omega_{bound} - \omega)M_x^{bound} - k_{2bound}M_y^{bound} + C_{bulk}M_y^{bulk} - \omega_1 M_z^{bound} \quad (C-5)$$

$$\frac{dM_z^{bulk}}{dt} = \frac{M_0^{bulk}}{T_1^{bulk}} - k_{1bulk} M_z^{bulk} + C_{bound} M_z^{bound} + \omega_1 M_y^{bulk} \quad (C-6)$$

$$\frac{dM_z^{bound}}{dt} = \frac{M_0^{bound}}{T_1^{bound}} - k_{1bound} M_z^{bound} + C_{bulk} M_z^{bulk} + \omega_1 M_y^{bound} \quad (C-7)$$

Bulk and bound are used to describe the properties of their respective pools of water,  $\omega$  is the frequency of RF irradiation,  $\omega_1$  is the nutation rate of the RF irradiation,  $C_{bulk}$  refers to the transition rate of the spins leaving the bulk pool, and  $C_{bound}$  refers to the transition rate of the spins leaving the bound pool. The transition rates ( $C_{bound}$  or  $C_{bulk}$ ) are equal to  $1/\tau_{(bound\ or\ bulk)}$  where  $\tau$  is the lifetime of a proton in the bound or bulk water pool.  $M_0^{bound}$  and  $M_0^{bulk}$  are proportional to the number of protons in the bound or bulk water pool and refer to the thermal equilibrium z magnetizations. Also for both bound and bulk water proton pools Equations 1-8 and 1-9 apply.

$$k_1 = \frac{1}{T_1} + C \quad (1-8)$$

$$k_2 = \frac{1}{T_2} + C \quad (1-9)$$

$T_1$  and  $T_2$  refer to the spin-lattice and spin-spin relaxation times.

These equations (Eqn.1-2-7), are the basis for the CESTFIT simulation[87]. This program was modified to model and fit the simulations in this appendix. The following code shows the modified Bloch equations (Eqn. 1-2 – 7) for simulating a two pool exchanging system.

```

ss2pool.m
function [Za] = ss2pool(params)
% global data
Za=zeros(1,241); %201
M0a =1;
M0b = .0003636;
M0c = .000;
w1 = 512 * 2 * pi;
wa = -138 * 2 * pi;
wb = 19760 * 2 * pi;
%T1a = 1;

```

```

T2a = .2;
%T1b = .1;
T2b = .1;
Cb=params(3);
Cc=params(4);
Cab=Cb*M0b/M0a;
Cac=Cc*M0c/M0a;
Ca=Cab+Cac;
k1a = (1/params(1)) + Ca;
k2a = (1/T2a) + Ca;
k1b = (1/params(2)) + params(3);
k2b = (1/T2b) + params(3);
wctr=0;
for ww =-30000:250:30000 %-25000
    w=ww * 2 * pi;
    wctr = wctr+1;
    Maxterm = [-k2a params(3) -(wa -w) 0 0 0];
    Mbxterm = [Cab -k2b 0 -(wb -w) 0 0 ];
    Mayterm = [(wa - w) 0 -k2a params(3) -w1 0 ];
    Mbyterm = [0 (wb -w) Cab -k2b 0 -w1 ];
    Mazterm = [0 0 w1 0 -k1a params(3)];
    Mbzterm = [0 0 0 w1 Cab -k1b ];
    blochmat = [Maxterm; Mbxterm; Mayterm; Mbyterm; Mazterm; Mbzterm];
    outvec = [0 0 0 0 -M0a/params(1) -M0b/params(2) ]';
    mags = blochmat\outvec;
    Za(wctr) = mags(5)/M0a;
end

```

The Bloch Equations can be treated in a similar manner to include a third pool of exchanging protons. The resulting equations lend themselves to a similar simulation as follows:

```

ss3.m
function [Za] = ss3(params)
% global data
Za=zeros(1,481);
M0a =1;
M0b = .0003636;
M0c = .0007272;
w1 = 512 * 2 * pi;
wa = -138 * 2 * pi;
wb = params(5) * 2 * pi;
wc = -133* 2 *pi;
T1a = 2;
T2a = .88;
T1b = .1;

```

```

T2b = .5;
T1c = .003;
T2c = .003;
Cb=params(3);
Cc=params(4);
Cab=Cb*M0b/M0a;
Cac=Cc*M0c/M0a;
Ca=Cab+Cac;
k1a = (1/params(1)) + Ca;
k2a = (1/T2a) + Ca;
k1b = (1/params(2)) + params(3);
k2b = (1/T2b) + params(3);
k1c = (1/T1c) + params(4);
k2c = (1/T2c) + params(4);
wctr=0;
for ww =-60000:250:60000
    w=ww * 2 * pi;
    wctr = wctr+1;
    Maxterm = [-k2a params(3) params(4) -(wa -w) 0 0 0 0];
    Mbxterm = [Cab -k2b 0 0 -(wb -w) 0 0 0 0];
    Mcxterm = [Cac 0 -k2c 0 0 -(wc -w) 0 0 0];
    Mayterm = [(wa - w) 0 0 -k2a params(3) params(4) -w1 0 0];
    Mbyterm = [0 (wb -w) 0 Cab -k2b 0 0 -w1 0];
    Mcyterm = [0 0 (wc -w) Cac 0 -k2c 0 0 -w1];
    Mazterm = [0 0 0 w1 0 0 -k1a params(3) params(4)];
    Mbzterm = [0 0 0 0 w1 0 Cab -k1b 0];
    Mczterm = [0 0 0 0 0 w1 Cac 0 -k1c];
    blochmat = [Maxterm; Mbxterm; Mcxterm; Mayterm; Mbyterm; Mcyterm; Mazterm;
Mbzterm; Mczterm];
    outvec = [0 0 0 0 0 -M0a/params(1) -M0b/params(2) -M0c/T1c]';
    mags = blochmat\outvec;
    Za(wctr) = mags(7)/M0a;
end

```

This code was manipulated in order to vary different variables and simulate the effect, and the changes are shown in the remainder of the Appendix.

### Variables Relaxation Time

The effect of varying both  $T_1$  and  $T_2$  relaxation times were simulated using the following code:

```

dot1cestcomp.m
N=[-30000:100:30000];
c = [.2 .2 3000 0];

```

```

M1=ss2ipool(c);
c = [.5 .2 3000 0];
M2=ss2ipool(c);
c = [1.5 .2 3000 0];
M3=ss2ipool(c);
c = [3 .2 3000 0];
M4=ss2ipool(c);
c = [5 .2 3000 0];
M5=ss2ipool(c);
plot(N,M1)
set(gca,'xdir','reverse')
hold all
plot(N,M2)
set(gca,'xdir','reverse')
plot(N,M3)
set(gca,'xdir','reverse')
plot(N,M4)
set(gca,'xdir','reverse')
plot(N,M5)
set(gca,'xdir','reverse')
legend('.2', '.5', '1.5', '3', '5');

```

---

```

ss2ipool.m
function [Za] = ss2ipool(params)
Za=zeros(1,201);
M0a =1;
M0b = .0007272;
M0c = .000;
w1 = 128 * 2 * pi;    % w1/2pi = B1 Hz
wa = -138 * 2 * pi;
wb = 19760 * 2 * pi;
%T1a = 1;
T2a = .1;
%T1b = .1;
T2b = .08;
Cb=params(3);
Cc=params(4);
Cab=Cb*M0b/M0a;
Cac=Cc*M0c/M0a;
Ca=Cab+Cac;
k1a = (1/params(1)) + Ca;
k2a = (1/T2a) + Ca;
k1b = (1/params(2)) + params(3);
k2b = (1/T2b) + params(3);
wctr=0;

```

```

for ww = -30000:100:30000
    w = ww * 2 * pi;
    wctr = wctr + 1;
    Maxterm = [-k2a params(3) -(wa - w) 0 0 0];
    Mbxterm = [Cab -k2b 0 -(wb - w) 0 0];
    Mayterm = [(wa - w) 0 -k2a params(3) -w1 0];
    Mbyterm = [0 (wb - w) Cab -k2b 0 -w1];
    Mazterm = [0 0 w1 0 -k1a params(3)];
    Mbzterm = [0 0 0 w1 Cab -k1b];
    blochmat = [Maxterm; Mbxterm; Mayterm; Mbyterm; Mazterm; Mbzterm];
    outvec = [0 0 0 0 -M0a/params(1) -M0b/params(2) ]';
    mags = blochmat \ outvec;
    Za(wctr) = mags(5)/M0a;
end

```

```

dot2cestcomp.m
N = [-30000:100:30000];
d = [.005 .1 3000 0];
M1 = ss2iipool(d);
d = [.01 .1 3000 0];
M2 = ss2iipool(d);
d = [.02 .1 3000 0];
M3 = ss2iipool(d);
d = [.05 .1 3000 0];
M4 = ss2iipool(d);
d = [.5 .1 3000 0];
M5 = ss2iipool(d);
d = [1 .1 3000 0];
M6 = ss2iipool(d);
plot(N, M1)
set(gca, 'xdir', 'reverse')
hold all
plot(N, M2)
set(gca, 'xdir', 'reverse')
plot(N, M3)
set(gca, 'xdir', 'reverse')
plot(N, M4)
set(gca, 'xdir', 'reverse')
plot(N, M5)
set(gca, 'xdir', 'reverse')
plot(N, M6)
set(gca, 'xdir', 'reverse')
legend('.005', '.01', '.02', '.05', '.5', '1');

```

---

```

ss2iipool.m
function [Za] = ss2iipool(params)

```

```

Za=zeros(1,201);
M0a =1;
M0b = .0007272;
M0c = .000;
w1 = 128 * 2 * pi;    % w1/2pi = B1 Hz
wa = -138 * 2 * pi;
wb = 19760 * 2 * pi;
T1a = 2;
T2a = params(1);
%T1b = .1;
T2b = .08;
Cb=params(3);
Cc=params(4);
Cab=Cb*M0b/M0a;
Cac=Cc*M0c/M0a;
Ca=Cab+Cac;
k1a = (1/T1a) + Ca;
k2a = (1/T2a) + Ca;
k1b = (1/params(2)) + params(3);
k2b = (1/T2b) + params(3);
wctr=0;
for ww =-30000:100:30000
    w=ww * 2 * pi;
    wctr = wctr+1;
    Maxterm = [-k2a params(3) -(wa -w) 0 0 0];
    Mbxterm = [Cab -k2b 0 -(wb -w) 0 0 ];
    Mayterm = [(wa - w) 0 -k2a params(3) -w1 0 ];
    Mbyterm = [0 (wb -w) Cab -k2b 0 -w1 ];
    Mazterm = [0 0 w1 0 -k1a params(3)];
    Mbzterm = [0 0 0 w1 Cab -k1b ];
    blochmat = [Maxterm; Mbxterm; Mayterm; Mbyterm; Mazterm; Mbzterm];
    outvec = [0 0 0 0 -M0a/T1a -M0b/params(2) ]';
    mags = blochmat\outvec;
    Za(wctr) = mags(5)/M0a;
end

```

### Variable Chemical Shift Difference

The effect of changing chemical shift difference ( $\Delta\omega$ ) was simulated using the following code.

```

doomegavary.m
%A small amount of different offsets
figure('name','varying omega b')

```

```

N=[-60000:300:60000];
e = [3 .5 3000 100 10000];
M1=ssthreepool(e);
e = [3 .5 3000 100 15000];
M2=ssthreepool(e);
e = [3 .5 3000 100 20000];
M3=ssthreepool(e);
e = [3 .5 3000 100 25000];
M4=ssthreepool(e);
e = [3 .5 3000 100 30000];
M5=ssthreepool(e);
e = [3 .5 3000 100 35000];
M6=ssthreepool(e);
e = [3 .5 3000 100 40000];
M7=ssthreepool(e);
e = [3 .5 3000 100 45000];
M8=ssthreepool(e);
e = [3 .5 3000 100 50000];
M9=ssthreepool(e);
e = [3 .5 3000 100 55000];
M10=ssthreepool(e);
plot(N,M1)
hold all
plot(N,M2)
plot(N,M3)
plot(N,M4)
plot(N,M5)
plot(N,M6)
plot(N,M7)
plot(N,M8)
plot(N,M9)
plot(N,M10)
set(gca,'xdir','reverse')
legend('10000', '15000', '20000', '25000', '30000','35000','40000','45000','50000','55000');

```

---

```

% for close up:
figure('name','varying omega b')
N=[-60000:300:60000];
e = [3 .5 3000 100 500];
M1=ssthreepool(e);
e = [3 .5 3000 100 1000];
M2=ssthreepool(e);
e = [3 .5 3000 100 2000];
M3=ssthreepool(e);
e = [3 .5 3000 100 2500];

```

```

M4=ssthreepool(e);
e = [3 .5 3000 100 3000];
M5=ssthreepool(e);
e = [3 .5 3000 100 3500];
M6=ssthreepool(e);
e = [3 .5 3000 100 4000];
M7=ssthreepool(e);
e = [3 .5 3000 100 4500];
M8=ssthreepool(e);
e = [3 .5 3000 100 5000];
M9=ssthreepool(e);
e = [3 .5 3000 100 5500];
M10=ssthreepool(e);
plot(N,M1)
hold all
plot(N,M2)
plot(N,M3)
plot(N,M4)
plot(N,M5)
plot(N,M6)
plot(N,M7)
plot(N,M8)
plot(N,M9)
plot(N,M10)
set(gca,'xdir','reverse')
axis([-10000 10000 0 1.1])
legend('1000', '1500', '2000', '2500', '3000','3500','4000','4500','5000','5500');

```

ssthreepool.m

```

function [Za] = ssthreepool(params)
Za=zeros(1,101);
M0a =1;
M0b = .0003636;
M0c = .0007272;
w1 = 256*2*pi; % switch to params(6) * 2 * pi if power variable;
wa = -138 * 2 * pi;
wb = params(5) * 2 * pi;
wc = -133* 2 *pi;
%T1a = 2;
T2a = .88;
%T1b = .1;
T2b = .5;
T1c = .003;
T2c = .003;
Cb=params(3);
Cc=params(4);

```

```

Cab=Cb*M0b/M0a;
Cac=Cc*M0c/M0a;
Ca=Cab+Cac;
k1a = (1/params(1)) + Ca;
k2a = (1/T2a) + Ca;
k1b = (1/params(2)) + params(3);
k2b = (1/T2b) + params(3);
k1c = (1/T1c) + params(4);
k2c = (1/T2c) + params(4);
wctr=0;
for ww =-60000:300:60000
    w=ww * 2 * pi;
    wctr = wctr+1;
    Maxterm = [-k2a params(3) params(4) -(wa -w) 0 0 0 0];
    Mbxterm = [Cab -k2b 0 0 -(wb -w) 0 0 0 0];
    Mcxterm = [Cac 0 -k2c 0 0 -(wc -w) 0 0 0];
    Mayterm = [(wa - w) 0 0 -k2a params(3) params(4) -w1 0 0];
    Mbyterm = [0 (wb -w) 0 Cab -k2b 0 0 -w1 0];
    Mcyterm = [0 0 (wc -w) Cac 0 -k2c 0 0 -w1];
    Mazterm = [0 0 0 w1 0 0 -k1a params(3) params(4)];
    Mbzterm = [0 0 0 0 w1 0 Cab -k1b 0];
    Mczterm = [0 0 0 0 0 w1 Cac 0 -k1c];
    blochmat = [Maxterm; Mbxterm; Mcxterm; Mayterm; Mbyterm; Mcyterm; Mazterm;
Mbzterm; Mczterm];
    outvec = [0 0 0 0 0 -M0a/params(1) -M0b/params(2) -M0c/T1c]';
    mags = blochmat\outvec;
    Za(wctr) = mags(7)/M0a;
end

```

## Variable Chemical Exchange

The effect of changing chemical exchange rates, effectively simulating various PARACEST compounds, was simulated by changing Cb and Ca using the following code.

```

varyCb.m
N=[-100:1:100];
paramss = [2 .1 200 0];
M1=ss2pool(paramss);
paramss = [2 .1 400 0];
M2=ss2pool(paramss);
paramss = [2 .1 1000 0];
M3=ss2pool(paramss);
paramss = [2 .1 3000 0];
M4=ss2pool(paramss);
paramss = [2 .1 8000 0];

```

```

M5=ss2pool(paramss);
paramss = [2 .1 10000 0];
M6=ss2pool(paramss);
plot(N,M1)
hold all
plot(N,M2)
plot(N,M3)
plot(N,M4)
plot(N,M5)
plot(N,M6)
set(gca,'xdir','reverse')
legend('200', '400', '1000', '3000', '8000', '10000');

```

---

### ss2pool.m

```

function [Za] = ss2pool(params)
Za=zeros(1,201);
M0a =1;
M0b = .0003636;
M0c = .000;
w1 = 512 * 2 * pi;
wa = -138 * 2 * pi;
wb = 19760 * 2 * pi;
%T1a = 1;
T2a = .2;
%T1b = .1;
T2b = .1;
Cb=params(3);
Cc=params(4);
Cab=Cb*M0b/M0a;
Cac=Cc*M0c/M0a;
Ca=Cab+Cac;
k1a = (1/params(1)) + Ca;
k2a = (1/T2a) + Ca;
k1b = (1/params(2)) + params(3);
k2b = (1/T2b) + params(3);
wctr=0;
for ww =-30000:300:30000
    w=ww * 2 * pi;
    wctr = wctr+1;
    Maxterm = [-k2a params(3) -(wa -w) 0 0 0];
    Mbxterm = [Cab -k2b 0 -(wb -w) 0 0 ];
    Mayterm = [(wa - w) 0 -k2a params(3) -w1 0 ];
    Mbyterm = [0 (wb -w) Cab -k2b 0 -w1 ];
    Mazterm = [0 0 w1 0 -k1a params(3)];
    Mbzterm = [0 0 0 w1 Cab -k1b ];
    blochmat = [Maxterm; Mbxterm; Mayterm; Mbyterm; Mazterm; Mbzterm];

```

```

outvec = [0 0 0 0 -M0a/params(1) -M0b/params(2) ]';
mags = blochmat\outvec;
Za(wctr) = mags(5)/M0a;
end

```

### Variable Presaturation Power

The presaturation power was increased from 200 to 12000 Hz using the following code.

```

dopowervary.m
%varying power
figure('name','varying power')
hold all
n=(-100:0.5:100);
for h=[200:200:600]
    e=[2 .1 3000 100 35000 h];
    m=ssthreepool(e);
    plot(n,m)
end
for h=[2000:2000:12000]
    ctr=ctr+1;
    e=[2 .1 3000 100 35000 h];
    m=ssthreepool(e);
    plot(n,m)
end
set(gca,'xdir','reverse')
legend ('200','400','600','2000','4000','6000','8000','10000','12000','Location','SouthEast')

```

---

```

ssthreepool.m
function [Za] = ssthreepool(params)
%params6 = power
Za=zeros(1,101);
M0a =1;
M0b = .0003636;
M0c = .0007272;
w1 = params(6) * 2 * pi; %switch to 512 if power not variable
wa = -138 * 2 * pi;
wb = params(5) * 2 * pi;
wc = -133 * 2 * pi;
%T1a = 2;
T2a = .88;
%T1b = .1;
T2b = .5;
T1c = .003;
T2c = .003;
Cb=params(3);
Cc=params(4);

```

```

Cab=Cb*M0b/M0a;
Cac=Cc*M0c/M0a;
Ca=Cab+Cac;
k1a = (1/params(1)) + Ca;
k2a = (1/T2a) + Ca;
k1b = (1/params(2)) + params(3);
k2b = (1/T2b) + params(3);
k1c = (1/T1c) + params(4);
k2c = (1/T2c) + params(4);
wctr=0;
for ww =-60000:300:60000
    w=ww * 2 * pi;
    wctr = wctr+1;
    Maxterm = [-k2a params(3) params(4) -(wa -w) 0 0 0 0 0];
    Mbxterm = [Cab -k2b 0 0 -(wb -w) 0 0 0 0];
    Mcxterm = [Cac 0 -k2c 0 0 -(wc -w) 0 0 0];
    Mayterm = [(wa - w) 0 0 -k2a params(3) params(4) -w1 0 0];
    Mbyterm = [0 (wb -w) 0 Cab -k2b 0 0 -w1 0];
    Mcyterm = [0 0 (wc -w) Cac 0 -k2c 0 0 -w1];
    Mazterm = [0 0 0 w1 0 0 -k1a params(3) params(4)];
    Mbzterm = [0 0 0 0 w1 0 Cab -k1b 0];
    Mczterm = [0 0 0 0 0 w1 Cac 0 -k1c];
    blochmat = [Maxterm; Mbxterm; Mcxterm; Mayterm; Mbyterm; Mcyterm; Mazterm;
Mbzterm; Mczterm];
    outvec = [0 0 0 0 0 0 -M0a/params(1) -M0b/params(2) -M0c/T1c]';
    mags = blochmat\outvec;
    Za(wctr) = mags(7)/M0a;
end

```

### Variable Concentration Simulation

For the simulation, the concentration was by changing the ratio of  $M_0^{\text{bound}}$  and  $M_0^{\text{bulk}}$ .

$M_0^{\text{bulk}}$  was kept at 1, while  $M_0^{\text{bound}}$  was increased incrementally from 0.0001 to 0.001 using the

following code.

```

doconcvary.m
figure('name','varying concentration')
title('Varying concentration, concentration increase as the CESTffect gets bigger ')
hold all
n=[-100:1:100];
for h=[.0001:.0001:.001]
    ctr=ctr+1;
    e=[2 .1 30000 15000 31800 800 h .00072];
    m=ssthreepoolconc(e);
    plot(n,m)

```

```

end
set(gca,'xdir','reverse')
legend
('0.0001','0.0002','0.0003','0.0004','0.0005','0.0006','0.0007','0.0008','0.0009','0.001','Location','SouthEast')

```

---

ssthreepoolconc.m

```

function [Za] = ssthreepoolconc(params)
% global data
%params1= t1a not variable
%params2=t1b
%params3=Cb
%params4=Cc
%params5 = bound water shift
%Params6=power w1
%params7=M0b
%params8=M0c
Za=zeros(1,101);
M0a =1;
M0b = params(7);
M0c = params(8);
w1 = params(6) * 2 * pi; %switch to 512 if power not variable
wa = -138 * 2 * pi;
wb = params(5) * 2 * pi;
wc = -133* 2 *pi;
%T1a = 2;
T2a = .88;
%T1b = .1;
T2b = .5;
T1c = .003;
T2c = .003;
Cb=params(3);
Cc=params(4);
Cab=Cb*M0b/M0a;
Cac=Cc*M0c/M0a;
Ca=Cab+Cac;
k1a = (1/params(1)) + Ca;
k2a = (1/T2a) + Ca;
k1b = (1/params(2)) + params(3);
k2b = (1/T2b) + params(3);
k1c = (1/T1c) + params(4);
k2c = (1/T2c) + params(4);
wctr=0;
for ww =-60000:600:60000
    w=ww * 2 * pi;
    wctr = wctr+1;

```

```

Maxterm = [-k2a params(3) params(4) -(wa -w) 0 0 0 0];
Mbxterm = [Cab -k2b 0 0 -(wb -w) 0 0 0 0];
Mcxterm = [Cac 0 -k2c 0 0 -(wc -w) 0 0 0];
Mayterm = [(wa - w) 0 0 -k2a params(3) params(4) -w1 0 0];
Mbyterm = [0 (wb -w) 0 Cab -k2b 0 0 -w1 0];
Mcyterm = [0 0 (wc -w) Cac 0 -k2c 0 0 -w1];
Mazterm = [0 0 0 w1 0 0 -k1a params(3) params(4)];
Mbzterm = [0 0 0 0 w1 0 Cab -k1b 0];
Mczterm = [0 0 0 0 0 w1 Cac 0 -k1c];
blochmat = [Maxterm; Mbxterm; Mcxterm; Mayterm; Mbyterm; Mcyterm; Mazterm;
Mbzterm; Mczterm];
outvec = [0 0 0 0 0 0 -M0a/params(1) -M0b/params(2) -M0c/T1c]';
mags = blochmat\outvec;
Za(wctr) = mags(7)/M0a;
end

```

### Temperature Fit MATLAB Code

Data was acquired on the 14.1 T magnetic of a 10 mM solution of Eu-2 at five different temperatures. That data was input in MATLAB, and fit to the modified Bloch Equations using `fminsearch.m` (an unconstrained nonlinear minimization (Nelder-Mead) program) which is included in the MATLAB software. This function was used inside of the following code.

```

dotemp14 38.m
close all
clear all
load m050508tcorr %pre processed data from the 14.1 T
%define variables for fit for T=14
xdata=(a14(:,1));
ydata14=(a14(:,2));
ydata=ydata14;
%For T=14
T1=3.1;
%abc=fmincon('expfitcest120808',[2.6 3000 200 1000 59],[[],[],[],[],[0 0 0 0 45],[10 10000
10000 3000 75],[[],[],xdata,T1, ydata);
abc=fminsearch('expfitcest120808',[3.1 3000 200 100 55],[[],[],xdata,T1,ydata);
%to get error
[err,R2]=expfitcest120808(abc,xdata,T1, ydata);
%plot with points and fit
figure('name','Temperature fit')
hold all
plot(xdata,ydata,'bo');
plot(xdata,y_fit,'b-');
set(gca,'xdir','reverse')

```

```

axis([xdata(xval) xdata(1) 0 1.1])
abc14=abc;
yfit14=y_fit;
err14=err;
R2_14=R2;
%14 values: [3.0687,20778.0708,6935.4489,860.8371,59.7442]

%define variables for fit for T=20
xdata=(a20(:,1));
ydata20=(a20(:,2));
ydata=ydata20;
T1=3.5;
abc=fminsearch('expfitcest120808',[3.0687 20778.0708 6935.4489 860.8371
59.7442],[],xdata,T1,ydata);
abc=fminsearch('expfitcest120808',abc,[],xdata,T1,ydata);
%to get error
[err,R2]=expfitcest120808(abc,xdata,T1, ydata);
%plot with points and fit
plot(xdata,ydata,'go');
plot(xdata,y_fit,'g-');
set(gca,'xdir','reverse')
axis([xdata(xval) xdata(1) 0 1.1])
%legend ('20 data','20 fit','Location','SouthEast')
abc20=abc;
yfit20=y_fit;
err20=err;
R2_20=R2;

%define variables for fit for T=26
xdata=(a26(:,1));
ydata26=(a26(:,2));
ydata=ydata26;
T1=4.0;
abc=fminsearch('expfitcest120808',[3.0687 20778.0708 6935.4489 860.8371
59.7442],[],xdata,T1,ydata);
abc=fminsearch('expfitcest120808',abc,[],xdata,T1,ydata);
%to get error
[err,R2]=expfitcest120808(abc,xdata,T1, ydata);
%plot with points and fit
plot(xdata,ydata,'ro');
plot(xdata,y_fit,'r-');
set(gca,'xdir','reverse')
axis([xdata(xval) xdata(1) 0 1.1])
%legend ('26 data','26 fit','Location','SouthEast')
abc26=abc;
yfit26=y_fit;

```

```

err26=err;
R2_26=R2;

%define variables for fit for T=32
xdata=(a32(:,1));
ydata32=(a32(:,2));
ydata=ydata32;
T1=4.4;
abc=fminsearch('expfitcest120808',[3.0687 20778.0708 6935.4489 860.8371
59.7442],[],xdata,T1,ydata);
abc=fminsearch('expfitcest120808',abc,[],xdata,T1,ydata);
%to get error
[err,R2]=expfitcest120808(abc,xdata,T1, ydata);
%plot with points and fit
plot(xdata,ydata,'co');
plot(xdata,y_fit,'c-');
set(gca,'xdir','reverse')
axis([xdata(xval) xdata(1) 0 1.1])
%legend ('32 data','32 fit','Location','SouthEast')
abc32=abc;
yfit32=y_fit;
err32=err;
R2_32=R2;

%define variables for fit for T=38
xdata=(a38(:,1));
ydata38=(a38(:,2));
ydata=ydata38;
%For T=38
T1=5.1;
abc=fminsearch('expfitcest120808',[3.0687 20778.0708 6935.4489 860.8371
59.7442],[],xdata,T1,ydata);
abc=fminsearch('expfitcest120808',abc,[],xdata,T1,ydata);
%to get error
[err,R2]=expfitcest120808(abc,xdata,T1, ydata);
%plot with points and fit
plot(xdata,ydata,'mo');
plot(xdata,y_fit,'m-');
set(gca,'xdir','reverse')
axis([xdata(xval) xdata(1) 0 1.1])
legend ('14 data', '14 fit', '20 data', '20 fit', '26 data', '26 fit', '32 data', '32 fit', '38 data', '38
fit','Location','SouthEast')
abc38=abc;
yfit38=y_fit;
err38=err;
R2_38=R2;

```

```
title(['14degC. Rsquared value is ',num2str(R2_14), ' 20degC. Rsquared value is ',
num2str(R2_20) ' 26degC. Rsquared value is ', num2str(R2_26) ' 32degC. Rsquared value is ',
num2str(R2_32) ' 38degC. Rsquared value is ', num2str(R2_38)])
```

---

expfitcest120808.m

```
function [ err, R2 ] = expfitcest120808(args, xdata, T1a, ydata)
a=args(1);
b=args(2);
c=args(3);
d=args(4);
e=args(5);
A=[a b c d e];
y_fit=fit(A,xdata,T1a); %was ssthreepoolfit, but changed to fit for temp data)
err=norm(ydata-y_fit);
fitval = sum((y_fit-ydata).^2);
ybar=mean(ydata);
SStot = sum((ydata-ybar).^2);
R2=1-fitval/SStot;
assignin('base','y_fit',y_fit);
```

---

fit.m

```
function [Za] = fit(params,xdata,T1) %was ssthreepool
%params = t1a not variable
%params1=t1b
%params2=Cb
%params3=Cc
%params4 = w1
%Params5=bound water shift in ppm
%%%%params6=M0b
%%%%params7=MOc
Za=(xdata(:));
Za(:)=0;
numx=(xdata(:));
numx(:)=1;
xval=sum(numx(:));
assignin('base','xval', xval);
M0a =1;
M0b = .0003636;
M0c = .0007272;
w1 = params(4) * 2 * pi;
wa = 4.7*600*2*pi;
wb = params(5) * 600 * 2 * pi;
wc = -133* 2 *pi;
T1a = T1;
T2a = .88;
%T1b = .1;
```

```

T2b = .5;
T1c = .003;
T2c = .003;
Cb=params(2);
Cc=params(3);
Cab=Cb*M0b/M0a;
Cac=Cc*M0c/M0a;
Ca=Cab+Cac;
k1a = (1/T1a) + Ca;
k2a = (1/T2a) + Ca;
k1b = (1/params(1)) + params(2);
k2b = (1/T2b) + params(2);
k1c = (1/T1c) + params(3);
k2c = (1/T2c) + params(3);
wctr=0;
%for 101.7ppm to -100.3 in -2 steps at 600MHz
for i=(1:1:xval)
    ww = 600*xdata(i);
    w=ww * 2 * pi;
    wctr = wctr+1;
    Maxterm = [-k2a params(2) params(3) -(wa -w) 0 0 0 0];
    Mbxterm = [Cab -k2b 0 0 -(wb -w) 0 0 0 0];
    Mcxterm = [Cac 0 -k2c 0 0 -(wc -w) 0 0 0];
    Mayterm = [(wa - w) 0 0 -k2a params(2) params(3) -w1 0 0];
    Mbyterm = [0 (wb -w) 0 Cab -k2b 0 0 -w1 0];
    Mcyterm = [0 0 (wc -w) Cac 0 -k2c 0 0 -w1];
    Mazterm = [0 0 0 w1 0 0 -k1a params(2) params(3)];
    Mbzterm = [0 0 0 0 w1 0 Cab -k1b 0];
    Mczterm = [0 0 0 0 0 w1 Cac 0 -k1c];
    blochmat = [Maxterm; Mbxterm; Mcxterm; Mayterm; Mbyterm; Mcyterm; Mazterm;
    Mbzterm; Mczterm];
    outvec = [0 0 0 0 0 0 -M0a/params(1) -M0b/params(1) -M0c/T1c];
    mags = blochmat\outvec;
    Za(wctr) = mags(7)/M0a;

```

### Number of Acquisitions Fit MATLAB Code

Data were acquired on the 14.1 T magnetic of a 10 mM solution of Eu-2 with 1, 2, 4, 8, 32 and 64 scans. The data was input in MATLAB, and fit to the modified Bloch Equations. The data and the fits for each individual set are shown in Figures C-1, C-2, C-3, C-4, C-5, C-6 for 1, 2, 4, 8, 32 and 64 scans respectively. The fits and the figures were created using the following code.

NS050508.m

%create NS spectra graphs and recall processed data

clear all

load m050508\_NScorr2

figure('name','Z spec increasing NS study')

hold all

plot(a1(:,1),a1(:,2),'r-','linewidth',2);

plot(a2(:,1),a2(:,2),'b-','linewidth',2);

plot(a4(:,1),a4(:,2),'g-','linewidth',2);

plot(a8(:,1),a8(:,2),'c-','linewidth',2);

plot(a32(:,1),a32(:,2),'m-','linewidth',2);

plot(a64(:,1),a64(:,2),'y-','linewidth',2);

set(gca,'xdir','reverse')

axis([-101.7 100.3 0 1.05])

legend('1','2','4','8','32','64','Location','East')

%and for the close up

figure('name','Close up NS study')

hold all

plot(a1(22:27,1),a1(22:27,2))

plot(a2(22:27,1),a2(22:27,2))

plot(a4(22:27,1),a4(22:27,2))

plot(a8(22:27,1),a8(22:27,2))

plot(a32(22:27,1),a32(22:27,2))

plot(a64(22:27,1),a64(22:27,2))

axis([49.7 59.7 0.54 0.67])

legend('1','2','4','8','32','64','Location','SouthEast')

%All expts performed at 26deg C so:

T1=4.0;

%define variables for fit for NS=1

xdata=(a1(:,1));

ydata1=(a1(:,2));

ydata=ydata1;

%For NS=1

%abc=fmincon('expfitcest120808',[2.6 3000 200 1000 59],[[],[],[],[]],[0 0 0 0 45],[10 10000 10000 3000 75],[[],[],xdata,T1, ydata);

abc=fminsearch('expfitcest120808',[3.9561 24930.5981 5903.144 822.1845 56.3058],[[],xdata,T1,ydata);

%to get error

[err,R2]=expfitcest120808(abc,xdata,T1, ydata);

%plot with points and fit

figure('name','NS=1 fit')

title(['NS=1. Rsquared value is ',num2str(R2)])

hold all

plot(xdata,ydata,'ro');

plot(xdata,y\_fit,'r-');

```

set(gca,'xdir','reverse')
axis([xdata(xval) xdata(1) 0 1.05])
legend('NS 1 data','NS 1 fit','Location','SouthEast')
abc1=abc;
yfit1=y_fit;
err1=err;
R2_1=R2;
% I values: [3.9561,24930.5981,5903.144,822.1845,56.3058;]

%define variables for fit for NS=2
xdata=(a2(:,1));
ydata2=(a2(:,2));
ydata=ydata2;
%For NS=2
abc=fminsearch('expfitcest120808',[3.9561 24930.5981 5903.144 822.1845
56.3058],[],xdata,T1,ydata);
%to get error
[err,R2]=expfitcest120808(abc,xdata,T1,ydata);
%plot with points and fit
figure('name','NS=2 fit')
title(['NS=2. Rsquared value is ',num2str(R2)])
hold all
plot(xdata,ydata,'bo');
plot(xdata,y_fit,'b-');
set(gca,'xdir','reverse')
axis([xdata(xval) xdata(1) 0 1.05])
legend('NS 2 data','NS 2 fit','Location','SouthEast')
abc2=abc;
yfit2=y_fit;
err2=err;
R2_2=R2;

%define variables for fit for NS=4
xdata=(a4(:,1));
ydata4=(a4(:,2));
ydata=ydata4;
%For NS=4
abc=fminsearch('expfitcest120808',[3.9561 24930.5981 5903.144 822.1845
56.3058],[],xdata,T1,ydata);
%to get error
[err,R2]=expfitcest120808(abc,xdata,T1,ydata);
%plot with points and fit
figure('name','NS=4 fit')
title(['NS=4. Rsquared value is ',num2str(R2)])
hold all
plot(xdata,ydata,'go');

```

```

plot(xdata,y_fit,'g-');
set(gca,'xdir','reverse')
axis([xdata(xval) xdata(1) 0 1.05])
legend('NS 4 data','NS 4 fit','Location','SouthEast')
abc4=abc;
yfit4=y_fit;
err4=err;
R2_4=R2;

%define variables for fit for NS=8
xdata=(a8(:,1));
ydata8=(a8(:,2));
ydata=ydata8;
%For NS=8
abc=fminsearch('expfitcest120808',[3.9561 24930.5981 5903.144 822.1845
56.3058],[],xdata,T1,ydata);
%to get error
[err,R2]=expfitcest120808(abc,xdata,T1,ydata);
%plot with points and fit
figure('name','NS=8 fit')
title(['NS=8. Rsquared value is ',num2str(R2)])
hold all
plot(xdata,ydata,'co');
plot(xdata,y_fit,'c-');
set(gca,'xdir','reverse')
axis([xdata(xval) xdata(1) 0 1.05])
legend('NS 8 data','NS 8 fit','Location','SouthEast')
abc8=abc;
yfit8=y_fit;
err8=err;
R2_8=R2;

%define variables for fit for NS=32
xdata=(a32(:,1));
ydata32=(a32(:,2));
ydata=ydata32;
%For NS=32
abc=fminsearch('expfitcest120808',[3.9561 24930.5981 5903.144 822.1845
56.3058],[],xdata,T1,ydata);
%to get error
[err,R2]=expfitcest120808(abc,xdata,T1,ydata);
%plot with points and fit
figure('name','NS=32 fit')
title(['NS=32. Rsquared value is ',num2str(R2)])
hold all
plot(xdata,ydata,'mo');

```

```

plot(xdata,y_fit,'m-');
set(gca,'xdir','reverse')
axis([xdata(xval) xdata(1) 0 1.05])
legend('NS 32 data','NS 32 fit','Location','SouthEast')
abc32=abc;
yfit32=y_fit;
err32=err;
R2_32=R2;

%define variables for fit for NS=64
xdata=(a64(:,1));
ydata64=(a64(:,2));
ydata=ydata64;
%For NS=64
abc=fminsearch('expfitcest120808',[3.9561 24930.5981 5903.144 822.1845
56.3058],[],xdata,T1,ydata);
%to get error
[err,R2]=expfitcest120808(abc,xdata,T1,ydata);
%plot with points and fit
figure('name','NS=64 fit')
title(['NS=64. Rsquared value is ',num2str(R2)])
hold all
plot(xdata,ydata,'yo');
plot(xdata,y_fit,'y-');
set(gca,'xdir','reverse')
axis([xdata(xval) xdata(1) 0 1.05])
legend('NS 64 data','NS 64 fit','Location','SouthEast')
abc64=abc;
yfit64=y_fit;
err64=err;
R2_64=R2;

figure('name','number of scans fit data')
title('Number of scans data and fit')
hold all
plot(a1(:,1),a1(:,2),'ro')%,'linewidth',1.5)
plot(a1(:,1),yfit1,'r-')
plot(a2(:,1),a2(:,2),'bo')%,'linewidth',1.5)
plot(a2(:,1),yfit2,'b-')
plot(a4(:,1),a4(:,2),'go')%,'linewidth',1.5)
plot(a4(:,1),yfit4,'g-')
plot(a8(:,1),a8(:,2),'co')%,'linewidth',1.5)
plot(a8(:,1),yfit8,'c-')
plot(a32(:,1),a32(:,2),'mo')%,'linewidth',1.5)
plot(a32(:,1),yfit32,'m-')
plot(a64(:,1),a64(:,2),'yo')%,'linewidth',1.5)

```

```
plot(a64(:,1),yfit64,'y-')
set(gca,'xdir','reverse')
axis([-100.3 101.7 0 1.1])
legend ('1','1 fit','2','2 fit','4','4 fit','8','8 fit','32','32 fit','64','64 fit','Location','SouthEast')
```

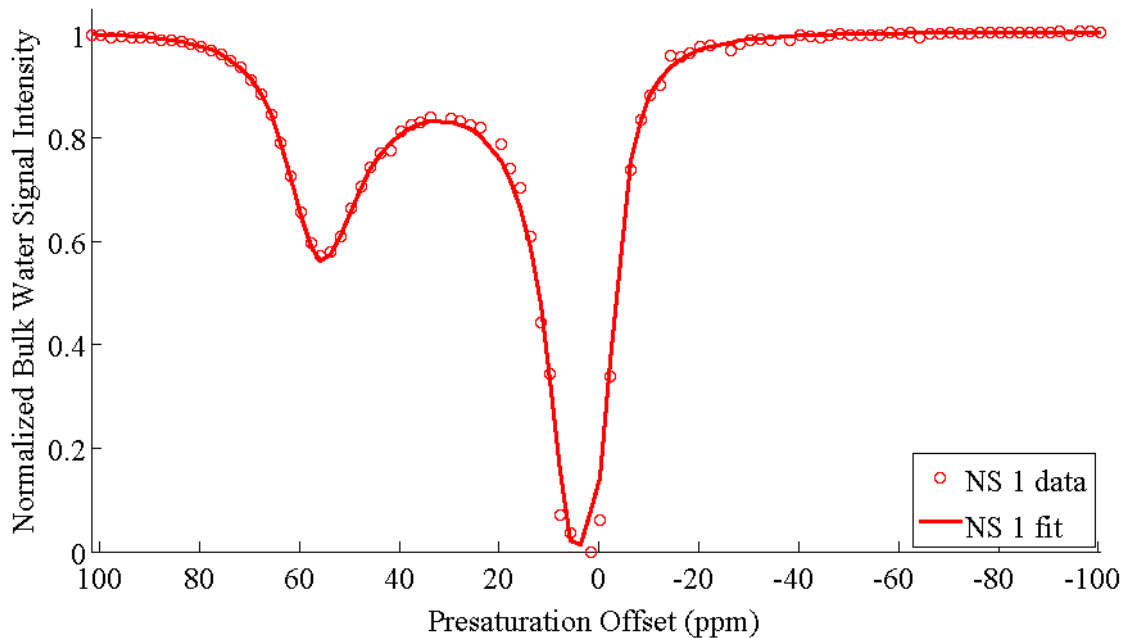


Figure C-1. CEST spectrum and fit for one scan.  $R^2 = 0.995$ .

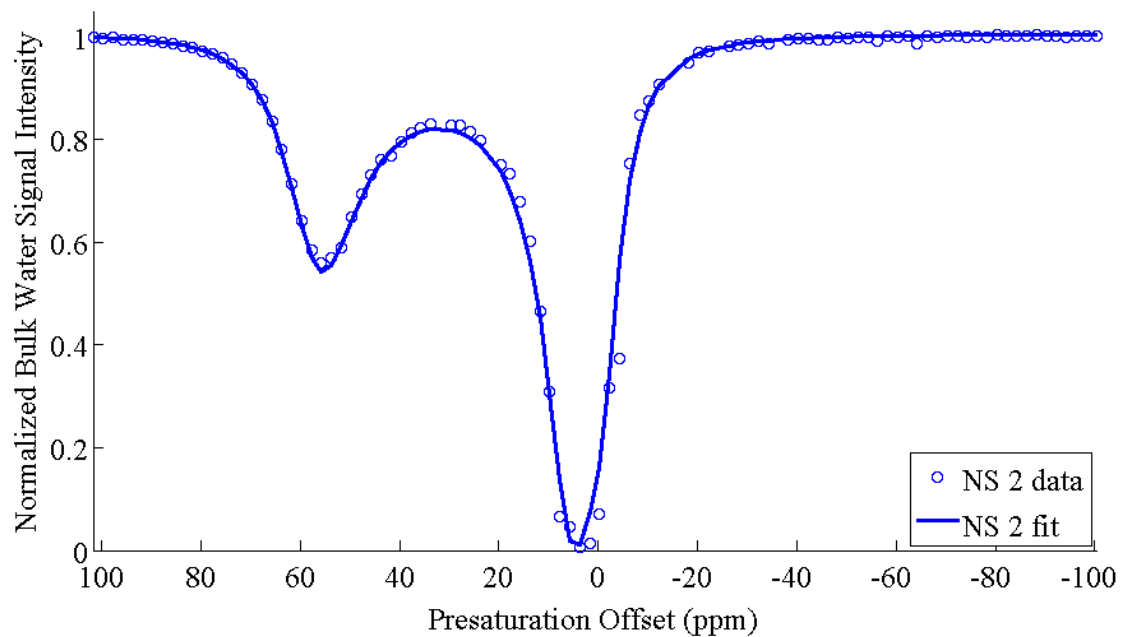


Figure C-2. CEST spectrum and fit for two scans.  $R^2 = 0.989$ .

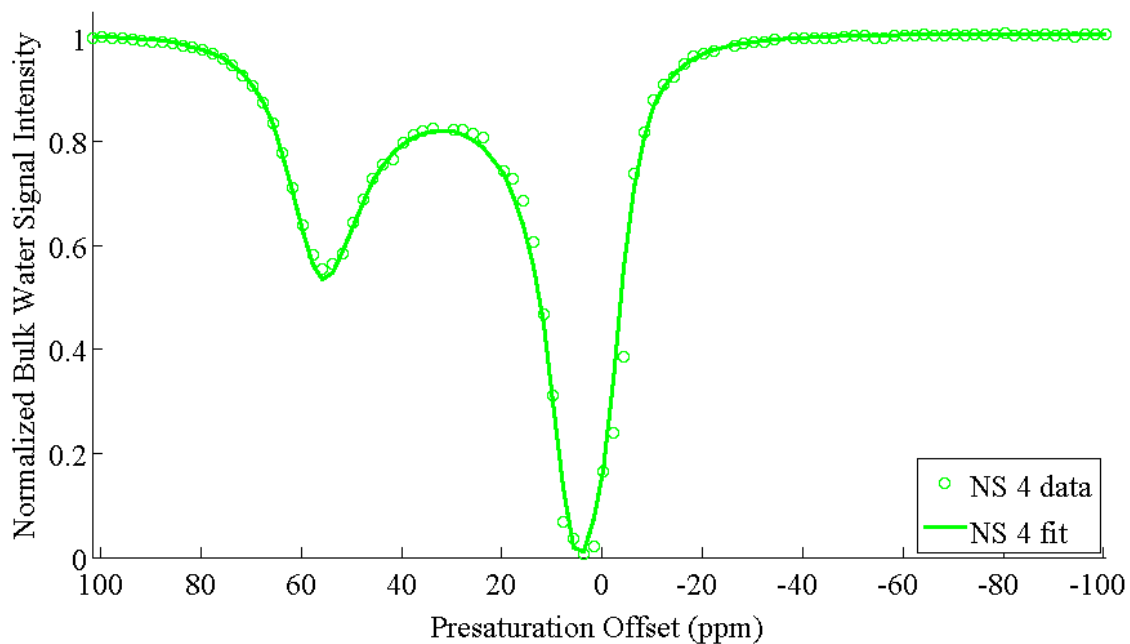


Figure C-3. CEST spectrum and fit for four scans.  $R^2 = 0.990$ .

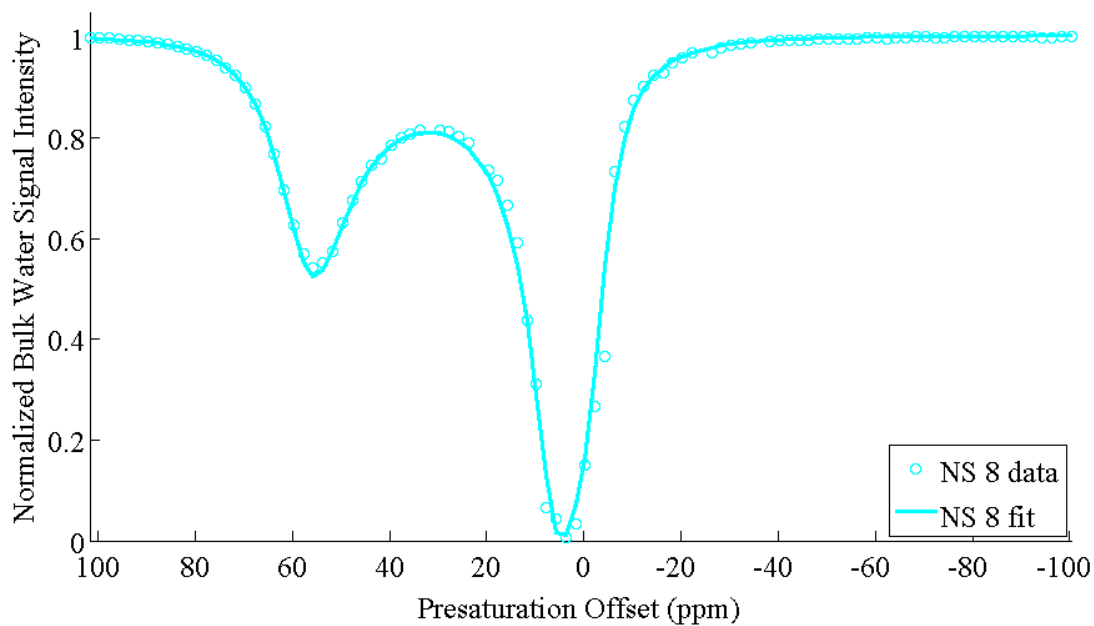


Figure C-4. CEST spectrum and fit for eight scans.  $R^2 = 0.991$ .

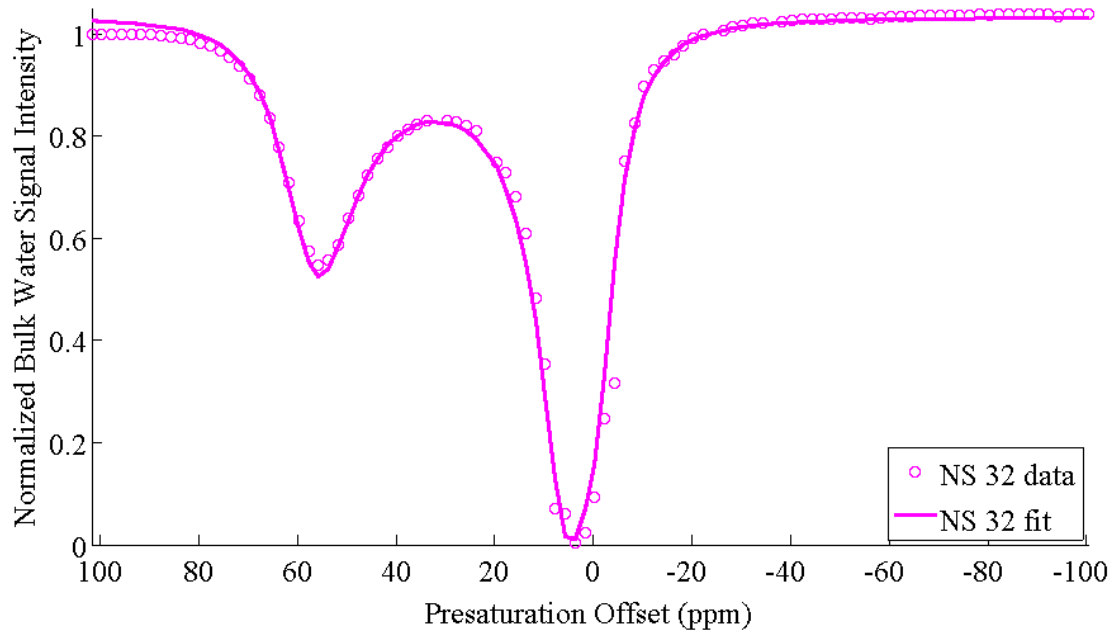


Figure C-5. CEST spectrum and fit for 32 scans.  $R^2 = 0.985$ .

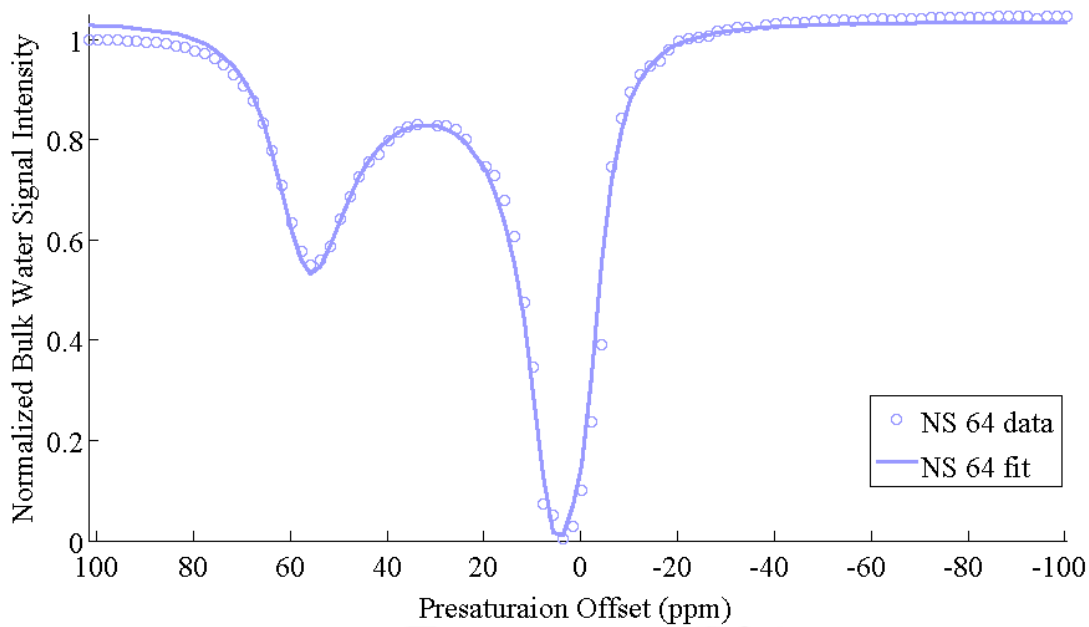


Figure C-6. CEST spectrum and fit for 64 scans.  $R^2 = 0.989$ .

## LIST OF REFERENCES

- [1] D.B. Murphy, *Fundamentals of Light Microscopy and Electronic Imaging*, New York: Wiley-Liss, Inc., 2001.
- [2] I. Pirko, S.T. Fricke, A.J. Johnson, M. Rodriguez, and S.I. Macura, "Magnetic resonance imaging, microscopy, and spectroscopy of the central nervous system in experimental animals," *NeuroRx: The Journal of the American Society for Experimental NeuroTherapeutics*, vol. 2, Apr. 2005, pp. 250-264.
- [3] T.G. Rochow and P.A. Tucker, *Introduction to Microscopy by means of light, electrons, x rays, or acoustics*, New York: Plenum Press, 1994.
- [4] D.J. Goldstein, *Understanding the Light Microscope*, London: Academic Press, 1999.
- [5] *Basic Methods in Microscopy: Protocols and Concepts from Cells: A Laboratory Manual*, Cold Spring Harbor, N.Y: Cold Spring Harbor Laboratory Press, 2006.
- [6] D.J. Brenner and E.J. Hall, "Computed Tomography -- An Increasing Source of Radiation Exposure," *N Engl J Med*, vol. 357, Nov. 2007, pp. 2277-2284.
- [7] R. Felix, E. Kazner, and O.H. Wegener, eds., *Contrast Media in Computed Tomography (International workshop Berlin, January 14-17, 1981)*, New York: Elsevier North-Holland Inc., 1981.
- [8] J.T. Bushberg, J.A. Seibert, E.M. Leidholdt, Jr, and J.M. Boone, *The Essential Physics of Medical Imaging*, Lippincott Williams & Wilkins, 2002.
- [9] T. Schertler, T. Frauenfelder, P. Stolzmann, H. Scheffel, L. Desbiolles, B. Marincek, V. Kaplan, N. Kucher, and H. Alkadhi, "Triple rule-out CT in patients with suspicion of acute pulmonary embolism: findings and accuracy," *Academic Radiology*, vol. 16, Jun. 2009, pp. 708-717.
- [10] A. Webb, *Introduction to Biomedical Imaging*, Hoboken, New Jersey: John Wiley & Sons, Ltd, 2003.
- [11] G. Antoch, L.S. Freudenberg, T. Beyer, A. Bockisch, and J.F. Debatin, "To Enhance or Not to Enhance? 18F-FDG and CT Contrast Agents in Dual-Modality 18F-FDG PET/CT," *Journal of Nuclear Medicine*, vol. 45, 2004, p. 56.
- [12] M. Amiel, ed., *Contrast Media in Radiology*, New York: Springer-Verlag, 1982.
- [13] E. Mittra and A. Quon, "Positron emission tomography/computed tomography: the current technology and applications," *Radiologic Clinics of North America*, vol. 47, Jan. 2009, pp. 147-160.

- [14] A. Berrington de González and S. Darby, "Risk of cancer from diagnostic X-rays: estimates for the UK and 14 other countries," *Lancet*, vol. 363, Jan. 2004, pp. 345-351.
- [15] "Sources and effects of ionizing radiation: United Nations Scientific Committee on the Effects of Atomic Radiation: UNSCEAR 2000 report to the General Assembly.," 2000.
- [16] Jay K. Harness and Dennis B. Wisher, eds., *Ultrasound in Surgical Practice : Basic Principles and Clinical Applications*, New York: Wiley-Liss, Inc., 2001.
- [17] Armin Ernst and David J. Feller-Kopman, eds., *Ultrasound-Guided Procedures and Investigations : A Manual for the Clinician*, New York: Taylor & Francis Group, LLC, 2006.
- [18] M.J. Blomley, J.C. Cooke, E.C. Unger, M.J. Monaghan, and D.O. Cosgrove, "Microbubble contrast agents: a new era in ultrasound," *BMJ (Clinical Research Ed.)*, vol. 322, May. 2001, pp. 1222-5.
- [19] J.R. Lindner, "Evolving applications for contrast ultrasound," *The American Journal of Cardiology*, vol. 90, Nov. 2002, pp. 72J-80J.
- [20] E. Unger, T. Matsunaga, P. Schumann, and R. Zutshi, "Microbubbles in Molecular Imaging Therapy," *MedicaMundi*, vol. 47, Apr. 2003, pp. 58-65.
- [21] S.A. Wickline and G.M. Lanza, "Molecular imaging, targeted therapeutics, and nanoscience," *Journal of Cellular Biochemistry. Supplement*, vol. 39, 2002, pp. 90-7.
- [22] I. Rabi, J. Zacharias, S. Millman, and P. Kusch, "A New Method of Measuring Nuclear Magnetic Moment," *Physical Review*, vol. 53, 1938, p. 318.
- [23] F. Bloch, W. Hansen, and M. Packard, "Nuclear Induction," *Physical Review*, vol. 69, 1946, p. 127.
- [24] E. Purcell, H. Torrey, and R. Pound, "Resonance Absorption by Nuclear Magnetic Moments," *Physical Review*, vol. 69, 1946, pp. 37-38.
- [25] R.W. Darbeau, "Nuclear Magnetic Resonance (NMR) Spectroscopy: A Review and a Look at Its Use as a Probative Tool in Deamination Chemistry," *Applied Spectroscopy Reviews*, vol. 41, 2006, pp. 401-425.
- [26] R. Freeman, "A short history of NMR," *Chemistry of Heterocyclic Compounds*, vol. 31, 1995, pp. 1004-1005.
- [27] J. Mattson, *The Pioneers of NMR and Magnetic Resonance in Medicine: The Story of MRI*, Ramat Gan, Israel: Bar-Ilan University Press, 1996.

- [28] P.C. LAUTERBUR, "Image Formation by Induced Local Interactions: Examples Employing Nuclear Magnetic Resonance," *Nature*, vol. 242, Mar. 1973, pp. 190-191.
- [29] P. Callaghan, "Imaging and diffraction: the mansfield legacy," *Magnetic Resonance Materials in Physics, Biology and Medicine*, vol. 9, Dec. 1999, pp. 109-111.
- [30] P. Mansfield and P.K. Grannell, "'Diffraction" and microscopy in solids and liquids by NMR," *Physical Review B*, vol. 12, Nov. 1975, p. 3618.
- [31] A.E. Merbach and E. Toth, eds., *The Chemistry of Contrast Agents in Medical Magnetic Resonance Imaging*, West Sussex, England: John Wiley & Sons, Ltd, 2001.
- [32] A. Moelker and P.M.T. Pattynama, "Acoustic noise concerns in functional magnetic resonance imaging," *Human Brain Mapping*, vol. 20, Nov. 2003, pp. 123-141.
- [33] C.K. Mechefske, R. Geris, J.S. Gati, and B.K. Rutt, "Acoustic noise reduction in a 4 T MRI scanner," *Magma (New York, N.Y.)*, vol. 13, Jan. 2002, pp. 172-176.
- [34] M. McJury and F.G. Shellock, "Auditory noise associated with MR procedures: a review," *Journal of Magnetic Resonance Imaging: JMRI*, vol. 12, Jul. 2000, pp. 37-45.
- [35] P.A. Gowland, "Present and future magnetic resonance sources of exposure to static fields," *Progress in Biophysics and Molecular Biology*, vol. 87, Apr. 2005, pp. 175-183.
- [36] H.E. Möller and D.Y. von Cramon, "[Survey of risks related to static magnetic fields in ultra high field MRI]," *RöFo: Fortschritte Auf Dem Gebiete Der Röntgenstrahlen Und Der Nuklearmedizin*, vol. 180, Apr. 2008, pp. 293-301.
- [37] J.F. Schenck, "Safety of strong, static magnetic fields," *Journal of Magnetic Resonance Imaging: JMRI*, vol. 12, Jul. 2000, pp. 2-19.
- [38] G. Franco, R. Perduri, and A. Murolo, "[Health effects of occupational exposure to static magnetic fields used in magnetic resonance imaging: a review]," *La Medicina Del Lavoro*, vol. 99, Feb. 2008, pp. 16-28.
- [39] R.L. Magin, J.K. Lee, A. Klintsova, K.I. Carnes, and F. Dunn, "Biological effects of long-duration, high-field (4 T) MRI on growth and development in the mouse," *Journal of Magnetic Resonance Imaging: JMRI*, vol. 12, Jul. 2000, pp. 140-149.
- [40] J.F. Schenck, "MR safety at high magnetic fields," *Magnetic Resonance Imaging Clinics of North America*, vol. 6, Nov. 1998, pp. 715-730.
- [41] F.G. Shellock and E. Kanal, "Guidelines and recommendations for MR imaging safety and patient management. III. Questionnaire for screening patients before MR procedures. The SMRI Safety Committee," *Journal of Magnetic Resonance Imaging: JMRI*, vol. 4, Oct. 1994, pp. 749-751.

- [42] M. Bottrill, L. Kwok, and N.J. Long, "Lanthanides in magnetic resonance imaging," *Chemical Society Reviews*, vol. 35, Jun. 2006, pp. 557-71.
- [43] M.H. Levitt, *Spin Dynamics: Basics of Nuclear Magnetic Resonance*, West Sussex, England: John Wiley & Sons, Ltd, 2001.
- [44] E. Mark Haacke, Brown, Robert Robert, Michael R. Thompson, and Ramesh Venkatesan, *Magnetic Resonance Imaging: Physical Principles and Sequence Design*, New York: J. Wiley & Sons, 1999.
- [45] R.C.V.D. Ven, B. Hogers, A.M.V.D. Maagdenberg, H.J.D. Groot, M.D. Ferrari, R.R. Frants, R.E. Poelmann, L.V.D. Weerd, and S.R. Kiihne, "T1 relaxation in in vivo mouse brain at ultra-high field," *Magnetic Resonance in Medicine*, vol. 58, 2007, pp. 390-395.
- [46] Lauterbur, Paul C., Mendoca Dias, H, and Rudin, A.M., "Augmentation of tissue proton spin-lattice relaxation rates by in vivo addition of paramagnetic ions," *Frontiers of Biological Energetics*, New York, NY: Academic Press, 1978, pp. 752-759.
- [47] P. Caravan, J.J. Ellison, T.J. McMurry, and R.B. Lauffer, "Gadolinium(III) Chelates as MRI Contrast Agents: Structure, Dynamics, and Applications," *Chemical Reviews*, vol. 99, Sep. 1999, pp. 2293-352.
- [48] H. Ersoy and F.J. Rybicki, "Biochemical safety profiles of gadolinium-based extracellular contrast agents and nephrogenic systemic fibrosis," *Journal of Magnetic Resonance Imaging: JMRI*, vol. 26, Nov. 2007, pp. 1190-1197.
- [49] J.C. Bousquet, S. Saini, D.D. Stark, P.F. Hahn, M. Nigam, J. Wittenberg, and J.T. Ferrucci, "Gd-DOTA: characterization of a new paramagnetic complex," *Radiology*, vol. 166, Mar. 1988, pp. 693-698.
- [50] S. Zhang, M. Merritt, D.E. Woessner, R.E. Lenkinski, and A.D. Sherry, "PARACEST agents: modulating MRI contrast via water proton exchange," *Accounts of Chemical Research*, vol. 36, Oct. 2003, pp. 783-90.
- [51] A.N. Oksendal and P.A. Hals, "Biodistribution and toxicity of MR imaging contrast media," *Journal of Magnetic Resonance Imaging: JMRI*, vol. 3, Feb. 1993, pp. 157-165.
- [52] M. Mitka, "MRI Contrast Agents May Pose Risk for Patients With Kidney Disease," *JAMA*, vol. 297, Jan. 2007, pp. 252-253.
- [53] G. Schneider, L. Grazioli, and S. Saini, *MRI of the Liver*, Verlag, Italy: Springer, 2003.
- [54] G.J. Strijkers, W.J.M. Mulder, G.A.F. van Tilborg, and K. Nicolay, "MRI contrast agents: current status and future perspectives," *Anti-Cancer Agents in Medicinal Chemistry*, vol. 7, May. 2007, pp. 291-305.

- [55] M. Querol and A. Bogdanov, "Amplification strategies in MR imaging: activation and accumulation of sensing contrast agents (SCAs)," *Journal of Magnetic Resonance Imaging: JMRI*, vol. 24, Nov. 2006, pp. 971-82.
- [56] P. Caravan, "Strategies for increasing the sensitivity of gadolinium based MRI contrast agents," *Chemical Society Reviews*, vol. 35, Jun. 2006, pp. 512-23.
- [57] D. Baleriaux, T. Metens, and W.G. Bradley, "MRI Contrast for the new Millennium: Contrast-Enhanced MRI of CNS (CME)," *Applied Radiology, the Journal of Practical Medical Imaging and Management*, vol. 32, Apr. 2003, pp. Supplement pp1-50.
- [58] "Multihance(R) (gadopentate dimeglumine) Injection," *U.S. Food and Drug Administration*, Sep. 2007.
- [59] "MAGNEVIST(R) (brand of gadopentate dimeglumine (Injection)," *U.S. Food and Drug Administration*, Sep. 2007.
- [60] P. Caravan, C.T. Farrar, L. Frullano, and R. Uppal, "Influence of molecular parameters and increasing magnetic field strength on relaxivity of gadolinium- and manganese-based T1 contrast agents," *Contrast Media & Molecular Imaging*, vol. 4, Mar. 2009, pp. 89-100.
- [61] M. Bellin, "MR contrast agents, the old and the new," *European Journal of Radiology*, vol. 60, Dec. 2006, pp. 314-323.
- [62] P.R. Ros, P.C. Freeny, S.E. Harms, S.E. Seltzer, P.L. Davis, T.W. Chan, A.E. Stillman, L.R. Muroff, V.M. Runge, and M.A. Nissenbaum, "Hepatic MR imaging with ferumoxides: a multicenter clinical trial of the safety and efficacy in the detection of focal hepatic lesions," *Radiology*, vol. 196, Aug. 1995, pp. 481-488.
- [63] Y. Gossuin, P. Gillis, A. Hocq, Q.L. Vuong, and A. Roch, "Magnetic resonance relaxation properties of superparamagnetic particles," *Wiley Interdisciplinary Reviews: Nanomedicine and Nanobiotechnology*, vol. 1, Jun. 2009, pp. 299-310.
- [64] R. Weissleder, "Liver MR imaging with iron oxides: toward consensus and clinical practice," *Radiology*, vol. 193, 1994, p. 593.
- [65] E.J. Rummeny, P. Reimer, H. Daldrup, and P.E. Peters, "[Detection of liver tumors]," *Der Radiologe*, vol. 35, Nov. 1995, pp. S252-258.
- [66] E.J. van den Bos, T. Baks, A.D. Moelker, W. Kerver, R. van Geuns, W.J. van der Giessen, D.J. Duncker, and P.A. Wielopolski, "Magnetic resonance imaging of haemorrhage within reperfused myocardial infarcts: possible interference with iron oxide-labelled cell tracking?," *Eur Heart J*, vol. 27, Jul. 2006, pp. 1620-1626.

- [67] S. Aime, A. Barge, C. Cabella, S.G. Crich, and E. Gianolio, "Targeting Cells with MR Imaging Probes Based on Paramagnetic Gd(III) Chelates," *Current Pharmaceutical Biotechnology*, vol. 5, Dec. 2004, pp. 509-518.
- [68] S. Zhang, P. Winter, K. Wu, and A.D. Sherry, "A novel europium(III)-based MRI contrast agent," *Journal of the American Chemical Society*, vol. 123, Feb. 2001, pp. 1517-8.
- [69] S. Aime, C. Carrera, D. Delli Castelli, S. Geninatti Crich, and E. Terreno, "Tunable imaging of cells labeled with MRI-PARACEST agents," *Angewandte Chemie (International Ed. in English)*, vol. 44, Mar. 2005, pp. 1813-5.
- [70] K.M. Ward, A.H. Aletras, and R.S. Balaban, "A new class of contrast agents for MRI based on proton chemical exchange dependent saturation transfer (CEST)," *Journal of Magnetic Resonance (San Diego, Calif.: 1997)*, vol. 143, Mar. 2000, pp. 79-87.
- [71] J. Peters, J. Huskens, and D. Raber, "Lanthanide induced shifts and relaxation rate enhancements," *Progress in Nuclear Magnetic Resonance Spectroscopy*, vol. 28, 1996, pp. 283-350.
- [72] S. Zhang and A.D. Sherry, "Physical characteristics of lanthanide complexes that act as magnetization transfer (MT) contrast agents," *Journal of Solid State Chemistry*, vol. 171, pp. 38-43.
- [73] S. Aime, A. Barge, D. Delli Castelli, F. Fedeli, A. Mortillaro, F.U. Nielsen, and E. Terreno, "Paramagnetic lanthanide(III) complexes as pH-sensitive chemical exchange saturation transfer (CEST) contrast agents for MRI applications," *Magnetic Resonance in Medicine: Official Journal of the Society of Magnetic Resonance in Medicine / Society of Magnetic Resonance in Medicine*, vol. 47, Apr. 2002, pp. 639-48.
- [74] K. Ward and R. Balaban, "Determination of pH using water protons and chemical exchange dependent saturation transfer (CEST)," *Magnetic Resonance in Medicine*, vol. 44, 2000, pp. 799-802.
- [75] N. Raghunand, C. Howison, A.D. Sherry, S. Zhang, and R.J. Gillies, "Renal and systemic pH imaging by contrast-enhanced MRI," *Magnetic Resonance in Medicine: Official Journal of the Society of Magnetic Resonance in Medicine / Society of Magnetic Resonance in Medicine*, vol. 49, Feb. 2003, pp. 249-57.
- [76] S. Aime, D. Delli Castelli, and E. Terreno, "Novel pH-reporter MRI contrast agents," *Angewandte Chemie (International Ed. in English)*, vol. 41, Nov. 2002, pp. 4334-6.
- [77] S. Zhang, K. Wu, M.C. Biewer, and A.D. Sherry, "<sup>1</sup>H and (<sup>17</sup>O) NMR detection of a lanthanide-bound water molecule at ambient temperatures in pure water as solvent," *Inorganic Chemistry*, vol. 40, Aug. 2001, pp. 4284-90.

- [78] A.X. Li, F. Wojciechowski, M. Suchy, C.K. Jones, R.H.E. Hudson, R.S. Menon, and R. Bartha, "A sensitive PARACEST contrast agent for temperature MRI: Eu<sup>3+</sup>-DOTAM-glycine (Gly)-phenylalanine (Phe)," *Magnetic Resonance in Medicine: Official Journal of the Society of Magnetic Resonance in Medicine / Society of Magnetic Resonance in Medicine*, vol. 59, Feb. 2008, pp. 374-81.
- [79] S. Zhang, C.R. Malloy, and A.D. Sherry, "MRI thermometry based on PARACEST agents," *Journal of the American Chemical Society*, vol. 127, Dec. 2005, pp. 17572-3.
- [80] S.D. Wolff and R.S. Balaban, "Magnetization transfer imaging: practical aspects and clinical applications," *Radiology*, vol. 192, Sep. 1994, pp. 593-599.
- [81] S.D. Wolff and R.S. Balaban, "Magnetization transfer contrast (MTC) and tissue water proton relaxation in vivo," *Magnetic Resonance in Medicine: Official Journal of the Society of Magnetic Resonance in Medicine / Society of Magnetic Resonance in Medicine*, vol. 10, Apr. 1989, pp. 135-144.
- [82] J. Zhou and P.C.M. Van Zijl, "Chemical exchange saturation transfer imaging and spectroscopy," *Progress in Nuclear Magnetic Resonance Spectroscopy*, vol. 48, May. 2006, pp. 109-136.
- [83] P. Mansfield, P. Morris, and J. Waugh, eds., *NMR imaging in biomedicine*, New York, NY: Academic Press, 1982.
- [84] W.A. Edelstein, G.H. Glover, C.J. Hardy, and R.W. Redington, "The intrinsic signal-to-noise ratio in NMR imaging," *Magnetic Resonance in Medicine: Official Journal of the Society of Magnetic Resonance in Medicine / Society of Magnetic Resonance in Medicine*, vol. 3, Aug. 1986, pp. 604-618.
- [85] H. Yang, S. Santra, G. Walter, and P. Holloway, "Gd(III) Functionalized Fluorescent Quantum Dots as Multimodal Imaging Probes," *Advanced Materials*, vol. 18, 2006, pp. 2890-2894.
- [86] K. Wu, S. Zhang, Z. Kovacs, and A.D. Sherry, "Doat-amide derivatives with extended arms form lanthanide complexes with unusual kinetic inertness.," *Journal of Nuclear Medicine*, vol. 41, May. 2000, p. 246P Suppl. S .
- [87] D.E. Woessner, S. Zhang, M.E. Merritt, and A.D. Sherry, "Numerical solution of the Bloch equations provides insights into the optimum design of PARACEST agents for MRI," *Magnetic Resonance in Medicine: Official Journal of the Society of Magnetic Resonance in Medicine / Society of Magnetic Resonance in Medicine*, vol. 53, Apr. 2005, pp. 790-9.
- [88] E.M. Shapiro, S. Skrtic, and A.P. Koretsky, "Sizing it up: cellular MRI using micron-sized iron oxide particles," *Magnetic Resonance in Medicine: Official Journal of the Society of Magnetic Resonance in Medicine / Society of Magnetic Resonance in Medicine*, vol. 53, Feb. 2005, pp. 329-38.

- [89] C.F.G.C. Geraldes and S. Laurent, "Classification and basic properties of contrast agents for magnetic resonance imaging," *Contrast Media & Molecular Imaging*, vol. 4, pp. 1-23.
- [90] F. Deckers, B. Corthouts, Y. Nackaerts, O. Ozsarlak, P.M. Parizel, and A.M. De Schepper, "The influence of MR field strength on the detection of focal liver lesions with superparamagnetic iron oxide," *European Radiology*, vol. 7, 1997, pp. 887-892.
- [91] P.M. Parizel, B. Van Riet, B.A. van Hasselt, J.W. Van Goethem, L. van den Hauwe, H.A. Dijkstra, P.J. van Wiechen, and A.M. De Schepper, "Influence of magnetic field strength on T2\* decay and phase effects in gradient echo MRI of vertebral bone marrow," *Journal of Computer Assisted Tomography*, vol. 19, Jun. 1995, pp. 465-471.
- [92] M.T. McMahon, A.A. Gilad, J. Zhou, P.Z. Sun, J.W.M. Bulte, and P.C.M. van Zijl, "Quantifying exchange rates in chemical exchange saturation transfer agents using the saturation time and saturation power dependencies of the magnetization transfer effect on the magnetic resonance imaging signal (QUEST and QUESP): Ph calibration for poly-L-lysine and a starburst dendrimer," *Magnetic Resonance in Medicine: Official Journal of the Society of Magnetic Resonance in Medicine / Society of Magnetic Resonance in Medicine*, vol. 55, Apr. 2006, pp. 836-47.
- [93] J.W.M. Bulte and D.L. Kraitchman, "Iron oxide MR contrast agents for molecular and cellular imaging," *NMR in Biomedicine*, vol. 17, Nov. 2004, pp. 484-99.
- [94] N.K. Chang, Y.Y. Jeong, J.S. Park, H.S. Jeong, S. Jang, M.J. Jang, J.H. Lee, S.S. Shin, W. Yoon, T.W. Chung, and H.K. Kang, "Tracking of neural stem cells in rats with intracerebral hemorrhage by the use of 3T MRI," *Korean Journal of Radiology: Official Journal of the Korean Radiological Society*, vol. 9, pp. 196-204.
- [95] C. Heyn, C.V. Bowen, B.K. Rutt, and P.J. Foster, "Detection threshold of single SPIO-labeled cells with FIESTA," *Magnetic Resonance in Medicine: Official Journal of the Society of Magnetic Resonance in Medicine / Society of Magnetic Resonance in Medicine*, vol. 53, Feb. 2005, pp. 312-20.
- [96] E.M. Shapiro, S. Skrtic, K. Sharer, J.M. Hill, C.E. Dunbar, and A.P. Koretsky, "MRI detection of single particles for cellular imaging," *Proceedings of the National Academy of Sciences of the United States of America*, vol. 101, Jul. 2004, pp. 10901-6.
- [97] J.W.M. Bulte and D.L. Kraitchman, "Monitoring cell therapy using iron oxide MR contrast agents," *Current Pharmaceutical Biotechnology*, vol. 5, Dec. 2004, pp. 567-84.
- [98] D.L. Kraitchman and J.W.M. Bulte, "Imaging of stem cells using MRI," *Basic Research in Cardiology*, vol. 103, Mar. 2008, pp. 105-13.

- [99] M. Suchý, A.X. Li, R. Bartha, and R.H.E. Hudson, "Analogues of Eu<sup>3+</sup> DOTAM-Gly-Phe-OH and Tm<sup>3+</sup> DOTAM-Gly-Lys-OH: synthesis and magnetic properties of potential PARACEST MRI contrast agents," *Bioorganic & Medicinal Chemistry*, vol. 16, Jun. 2008, pp. 6156-66.
- [100] E. Terreno, A. Barge, L. Beltrami, G. Cravotto, D.D. Castelli, F. Fedeli, B. Jebasingh, and S. Aime, "Highly shifted LIPOCEST agents based on the encapsulation of neutral polynuclear paramagnetic shift reagents," *Chemical Communications (Cambridge, England)*, Feb. 2008, pp. 600-2.
- [101] E. Vinogradov, S. Zhang, A. Lubag, J.A. Balschi, A.D. Sherry, and R.E. Lenkinski, "On-resonance low B1 pulses for imaging of the effects of PARACEST agents," *Journal of Magnetic Resonance (San Diego, Calif.: 1997)*, vol. 176, Sep. 2005, pp. 54-63.
- [102] D. Burdinski, J. Lub, J.A. Pikkemaat, D. Moreno Jalón, S. Martial, and C. Del Pozo Ochoa, "Triethylenetetramine penta- and hexa-acetamide ligands and their ytterbium complexes as paraCEST contrast agents for MRI," *Dalton Transactions (Cambridge, England: 2003)*, Aug. 2008, pp. 4138-51.
- [103] J.A. Pikkemaat, R.T. Wegh, R. Lamerichs, R.A. van de Molengraaf, S. Langereis, D. Burdinski, A.Y.F. Raymond, H.M. Janssen, B.F.M. de Waal, N.P. Willard, E.W. Meijer, and H. Grüll, "Dendritic PARACEST contrast agents for magnetic resonance imaging," *Contrast Media & Molecular Imaging*, vol. 2, Sep. 2007, pp. 229-39.
- [104] S.K. Hekmatyar, P. Hopewell, S.K. Pakin, A. Babsky, and N. Bansal, "Noninvasive MR thermometry using paramagnetic lanthanide complexes of 1,4,7,10-tetraazacyclododecane- $\alpha,\alpha',\alpha'',\alpha'''$ -tetramethyl-1,4,7,10-tetraacetic acid (DOTMA4-)," *Magnetic Resonance in Medicine: Official Journal of the Society of Magnetic Resonance in Medicine / Society of Magnetic Resonance in Medicine*, vol. 53, Feb. 2005, pp. 294-303.
- [105] G. Liu, Y. Li, and M.D. Pagel, "Design and characterization of a new irreversible responsive PARACEST MRI contrast agent that detects nitric oxide," *Magnetic Resonance in Medicine: Official Journal of the Society of Magnetic Resonance in Medicine / Society of Magnetic Resonance in Medicine*, vol. 58, Dec. 2007, pp. 1249-56.
- [106] B. Yoo and M.D. Pagel, "A PARACEST MRI contrast agent to detect enzyme activity," *Journal of the American Chemical Society*, vol. 128, Nov. 2006, pp. 14032-3.
- [107] P. Robitaille and L. Berliner, *Ultra High Field Magnetic Resonance Imaging*, Springer, 2006.
- [108] S. Aime, D. Delli Castelli, F. Fedeli, and E. Terreno, "A paramagnetic MRI-CEST agent responsive to lactate concentration," *Journal of the American Chemical Society*, vol. 124, Aug. 2002, pp. 9364-5.

- [109] T. Chauvin, P. Durand, M. Bernier, H. Meudal, B. Doan, F. Noury, B. Badet, J. Beloeil, and E. Tóth, "Detection of enzymatic activity by PARACEST MRI: a general approach to target a large variety of enzymes," *Angewandte Chemie (International Ed. in English)*, vol. 47, 2008, pp. 4370-2.
- [110] M. Woods, S. Zhang, V.H. Ebron, and A.D. Sherry, "pH-sensitive modulation of the second hydration sphere in lanthanide(III) tetraamide-DOTA complexes: a novel approach to smart MR contrast media," *Chemistry (Weinheim an Der Bergstrasse, Germany)*, vol. 9, Oct. 2003, pp. 4634-40.
- [111] S. Zhang, R. Trokowski, and A.D. Sherry, "A paramagnetic CEST agent for imaging glucose by MRI," *Journal of the American Chemical Society*, vol. 125, Dec. 2003, pp. 15288-9.
- [112] E. Agabiti-Rosei, M.L. Muiesan, and M. Salvetti, "New approaches to the assessment of left ventricular hypertrophy," *Therapeutic Advances in Cardiovascular Disease*, vol. 1, Dec. 2007, pp. 119-128.
- [113] G. Gold, "Defining the neuropathological background of vascular and mixed dementia and comparison with magnetic resonance imaging findings," *Frontiers of Neurology and Neuroscience*, vol. 24, 2009, pp. 86-94.
- [114] K.H. Nelson, T. Li, and L. Afonso, "Diagnostic approach and role of MRI in the assessment of acute myocarditis," *Cardiology in Review*, vol. 17, Feb. 2009, pp. 24-30.
- [115] X. Zhao, Z.E. Miller, and C. Yuan, "Atherosclerotic plaque imaging by carotid MRI," *Current Cardiology Reports*, vol. 11, Jan. 2009, pp. 70-77.
- [116] A.L. Dancey, B.S. Mahon, and S.S. Rayatt, "A review of diagnostic imaging in melanoma," *Journal of Plastic, Reconstructive & Aesthetic Surgery: JPRAS*, vol. 61, Nov. 2008, pp. 1275-1283.
- [117] K. Kimura, N. Tanigawa, M. Matsuki, T. Nohara, M. Iwamoto, K. Sumiyoshi, S. Tanaka, Y. Takahashi, and Y. Narumi, "High-resolution MR lymphography using ultrasmall superparamagnetic iron oxide (USPIO) in the evaluation of axillary lymph nodes in patients with early stage breast cancer: preliminary results," *Breast Cancer (Tokyo, Japan)*, Jul. 2009.
- [118] N. Lawrentschuk and N. Fleshner, "The role of magnetic resonance imaging in targeting prostate cancer in patients with previous negative biopsies and elevated prostate-specific antigen levels," *BJU International*, vol. 103, Mar. 2009, pp. 730-733.
- [119] E.L. Trimble, "Cervical cancer state-of-the-clinical-science meeting on pretreatment evaluation and prognostic factors, September 27-28, 2007: proceedings and recommendations," *Gynecologic Oncology*, vol. 114, Aug. 2009, pp. 145-150.

- [120] W.J.M. Mulder, G.J. Strijkers, A.W. Griffioen, L. van Bloois, G. Molema, G. Storm, G.A. Koning, and K. Nicolay, "A liposomal system for contrast-enhanced magnetic resonance imaging of molecular targets," *Bioconjugate Chemistry*, vol. 15, Aug. 2004, pp. 799-806.
- [121] S.A. Anderson, K.K. Lee, and J.A. Frank, "Gadolinium-fullerenol as a paramagnetic contrast agent for cellular imaging," *Investigative Radiology*, vol. 41, Mar. 2006, pp. 332-8.
- [122] D. Artemov, N. Mori, R. Ravi, and Z.M. Bhujwala, "Magnetic resonance molecular imaging of the HER-2/neu receptor," *Cancer Research*, vol. 63, Jun. 2003, pp. 2723-7.
- [123] G. Digilio, V. Catanzaro, F. Fedeli, E. Gianolio, V. Menchise, R. Napolitano, C. Gringeri, and S. Aime, "Targeting exofacial protein thiols with Gd(III) complexes. An efficient procedure for MRI cell labelling," *Chemical Communications (Cambridge, England)*, Feb. 2009, pp. 893-5.
- [124] L. Biancone, S.G. Crich, V. Cantaluppi, G.M. Romanazzi, S. Russo, E. Scalabrino, G. Esposito, F. Figliolini, S. Beltramo, P.C. Perin, G.P. Segoloni, S. Aime, and G. Camussi, "Magnetic resonance imaging of gadolinium-labeled pancreatic islets for experimental transplantation," *NMR in Biomedicine*, vol. 20, Feb. 2007, pp. 40-8.
- [125] J. Hsiao, C. Tsai, T. Chung, Y. Hung, M. Yao, H. Liu, C. Mou, C. Yang, Y. Chen, and D. Huang, "Mesoporous silica nanoparticles as a delivery system of gadolinium for effective human stem cell tracking," *Small (Weinheim an Der Bergstrasse, Germany)*, vol. 4, Sep. 2008, pp. 1445-52.
- [126] S. Benedetti, B. Pirola, B. Pollo, L. Magrassi, M.G. Bruzzone, D. Rigamonti, R. Galli, S. Selleri, F. Di Meco, C. De Fraja, A. Vescovi, E. Cattaneo, and G. Finocchiaro, "Gene therapy of experimental brain tumors using neural progenitor cells," *Nat Med*, vol. 6, Apr. 2000, pp. 447-450.
- [127] R. Weissleder, A.S. Lee, A.J. Fischman, P. Reimer, T. Shen, R. Wilkinson, R.J. Callahan, and T.J. Brady, "Polyclonal human immunoglobulin G labeled with polymeric iron oxide: antibody MR imaging," *Radiology*, vol. 181, Oct. 1991, pp. 245-9.
- [128] R. Weissleder, A.S. Lee, B.A. Khaw, T. Shen, and T.J. Brady, "Antimyosin-labeled monocrystalline iron oxide allows detection of myocardial infarct: MR antibody imaging," *Radiology*, vol. 182, Feb. 1992, pp. 381-5.
- [129] M. Zhao, D.A. Beauregard, L. Loizou, B. Davletov, and K.M. Brindle, "Non-invasive detection of apoptosis using magnetic resonance imaging and a targeted contrast agent," *Nature Medicine*, vol. 7, Nov. 2001, pp. 1241-4.

- [130] F.A. Jaffer, M. Nahrendorf, D. Sosnovik, K.A. Kelly, E. Aikawa, and R. Weissleder, "Cellular imaging of inflammation in atherosclerosis using magnetofluorescent nanomaterials," *Molecular Imaging: Official Journal of the Society for Molecular Imaging*, vol. 5, Jun. 2006, pp. 85-92.
- [131] Y.Z. Wadghiri, Einar M. Sigurdsson, Marcin Sadowski, James I. Elliott, Yongsheng Li, Henrieta Scholtzova, Cheuk Ying Tang, Gilbert Aguinaldo, Miguel Pappolla, Karen Duff, Thomas Wisniewski, and Daniel H. Turnbull, "Detection of Alzheimer's amyloid in transgenic mice using magnetic resonance microimaging," *Magnetic Resonance in Medicine*, vol. 50, 2003, pp. 293-302.
- [132] W. Zhu, X. Li, J. Qi, Z. Tang, W. Wang, L. Wei, and H. Lei, "Experimental study of cell migration and functional differentiation of transplanted neural stem cells co-labeled with superparamagnetic iron oxide and BrdU in an ischemic rat model," *Biomedical and Environmental Sciences: BES*, vol. 21, Oct. 2008, pp. 420-4.
- [133] L.G. Remsen, C.I. McCormick, S. Roman-Goldstein, G. Nilaver, R. Weissleder, A. Bogdanov, I. Hellström, R.A. Kroll, and E.A. Neuwelt, "MR of carcinoma-specific monoclonal antibody conjugated to monocrystalline iron oxide nanoparticles: the potential for noninvasive diagnosis," *AJNR. American Journal of Neuroradiology*, vol. 17, Mar. 1996, pp. 411-8.
- [134] L.X. Tiefenauer, A. Tschirky, G. Kühne, and R.Y. Andres, "In vivo evaluation of magnetite nanoparticles for use as a tumor contrast agent in MRI," *Magnetic Resonance Imaging*, vol. 14, 1996, pp. 391-402.
- [135] L.X. Tiefenauer, G. Kühne, and R.Y. Andres, "Antibody-magnetite nanoparticles: in vitro characterization of a potential tumor-specific contrast agent for magnetic resonance imaging," *Bioconjugate Chemistry*, vol. 4, pp. 347-52.
- [136] E.M. Shapiro, K. Sharer, S. Skrtic, and A.P. Koretsky, "In vivo detection of single cells by MRI," *Magnetic Resonance in Medicine: Official Journal of the Society of Magnetic Resonance in Medicine / Society of Magnetic Resonance in Medicine*, vol. 55, Feb. 2006, pp. 242-9.
- [137] P. Balchandani, M. Yamada, J. Pauly, P. Yang, and D. Spielman, "Self-refocused spatial-spectral pulse for positive contrast imaging of cells labeled with SPIO nanoparticles," *Magnetic Resonance in Medicine: Official Journal of the Society of Magnetic Resonance in Medicine / Society of Magnetic Resonance in Medicine*, vol. 62, Jul. 2009, pp. 183-192.
- [138] N. Mascheri, R. Dharmakumar, Z. Zhang, T. Paunesku, G. Woloschak, and D. Li, "Fast low-angle positive contrast steady-state free precession imaging of USPIO-labeled macrophages: theory and in vitro experiment," *Magnetic Resonance Imaging*, Jun. 2009.

- [139] M. Stuber, W.D. Gilson, M. Schär, D.A. Kedziorek, L.V. Hofmann, S. Shah, E. Vonken, J.W.M. Bulte, and D.L. Kraitchman, "Positive contrast visualization of iron oxide-labeled stem cells using inversion-recovery with ON-resonant water suppression (IRON)," *Magnetic Resonance in Medicine: Official Journal of the Society of Magnetic Resonance in Medicine / Society of Magnetic Resonance in Medicine*, vol. 58, Nov. 2007, pp. 1072-7.
- [140] J. Ren, R. Trokowski, S. Zhang, C.R. Malloy, and A.D. Sherry, "Imaging the tissue distribution of glucose in livers using a PARACEST sensor," *Magnetic Resonance in Medicine: Official Journal of the Society of Magnetic Resonance in Medicine / Society of Magnetic Resonance in Medicine*, vol. 60, Nov. 2008, pp. 1047-55.
- [141] B. Yoo, M.S. Raam, R.M. Rosenblum, and M.D. Pagel, "Enzyme-responsive PARACEST MRI contrast agents: a new biomedical imaging approach for studies of the proteasome," *Contrast Media & Molecular Imaging*, vol. 2, Jul. 2007, pp. 189-98.
- [142] B. Yoo and M.D. Pagel, "Peptidyl molecular imaging contrast agents using a new solid-phase peptide synthesis approach," *Bioconjugate Chemistry*, vol. 18, pp. 903-11.
- [143] P.C.M. van Zijl, C.K. Jones, J. Ren, C.R. Malloy, and A.D. Sherry, "MRI detection of glycogen in vivo by using chemical exchange saturation transfer imaging (glycoCEST)," *Proceedings of the National Academy of Sciences of the United States of America*, vol. 104, Mar. 2007, pp. 4359-64.
- [144] S. Aime, D. Delli Castelli, and E. Terreno, "Highly sensitive MRI chemical exchange saturation transfer agents using liposomes," *Angewandte Chemie (International Ed. in English)*, vol. 44, Aug. 2005, pp. 5513-5.
- [145] J.M. Zhao, Y. Har-el, M.T. McMahon, J. Zhou, A.D. Sherry, G. Sgouros, J.W.M. Bulte, and P.C.M. van Zijl, "Size-induced enhancement of chemical exchange saturation transfer (CEST) contrast in liposomes," *Journal of the American Chemical Society*, vol. 130, Apr. 2008, pp. 5178-84.
- [146] M.T. McMahon, A.A. Gilad, M.A. DeLiso, S.M.C. Berman, J.W. Bulte, and P.C. van Zijl, "New "multi color" polypeptide diamagnetic chemical exchange saturation transfer (DIACEST) contrast agents for MRI," *Magnetic Resonance in Medicine*, vol. 60, 2008, pp. 803-812.
- [147] F. Bloch, "Nuclear Induction," *Physical Review*, vol. 70, Oct. 1946, p. 460.
- [148] H.M. McConnell, "Reaction Rates by Nuclear Magnetic Resonance," *The Journal of Chemical Physics*, vol. 28, Mar. 1958, pp. 430-431.
- [149] D.E. Woessner, "Nuclear Transfer Effects in Nuclear Magnetic Resonance Pulse Experiments," *The Journal of Chemical Physics*, vol. 35, Jul. 1961, pp. 41-48.

## BIOGRAPHICAL SKETCH

Heather Cornell graduated from Atlantic Community High School in the International Baccalaureate Program in 1999, and earned the Bright Futures and National Merit Scholarships. Heather Cornell earned a Bachelor of Science in chemistry and a Bachelor of Science in chemical engineering from the University of Florida in 2004. While in graduate school she earned a UF Alumni fellowship and several scholarships and stipends including the Tillie, Jennie and Harold Schwartz Foundation Scholarship in Biomedical Engineering and the ISMRM-ESMRMB Educational Stipend. She worked as a teaching assistant for several graduate level courses in the Department of Biomedical Engineering and also as a teaching assistant for physical exam courses at the Harrell Professional Development Center in the College of Medicine at UF. Through her course of study she presented her work on contrast agents at several conferences, and gave invited oral presentations including her talk " Characterization of Paramagnetic Lanthanide Ion complexes as MRI Contrast Agents as a Function of Magnetic Field Strength" which was given at the Joint Annual International Society for Magnetic Resonance in Medicine and European Society for Magnetic Resonance in Medicine and Biology conference in Berlin, Germany in May 2007. She earned a Master of Engineering in biomedical engineering from the University of Florida in 2007, and a Doctor of Philosophy in biomedical engineering from the University of Florida in 2009.